

BEAM DYNAMICS STUDIES OF THE ISOLDE  
POST-ACCELERATOR FOR THE HIGH INTENSITY  
AND ENERGY UPGRADE

A THESIS SUBMITTED TO THE UNIVERSITY OF MANCHESTER  
FOR THE DEGREE OF DOCTOR OF PHILOSOPHY (PHD) IN THE  
FACULTY OF ENGINEERING AND PHYSICAL SCIENCES

2011

MATTHEW ALEXANDER FRASER

SCHOOL OF PHYSICS AND ASTRONOMY

# CONTENTS

<b>Abstract</b>	<b>15</b>
<b>Declaration</b>	<b>16</b>
<b>Copyright</b>	<b>17</b>
<b>The Author</b>	<b>18</b>
<b>Acknowledgements</b>	<b>19</b>
<b>Nomenclature</b>	<b>21</b>
<b>1 Introduction to Radioactive Ion Beam Facilities</b>	<b>26</b>
1.1 Physics Motivation . . . . .	27
1.2 ISOL vs. In-flight . . . . .	29
1.3 Post-acceleration of Radioactive Beams . . . . .	30
1.4 Present and ‘Next Generation’ RIB Facilities . . . . .	31
1.5 Thesis Overview . . . . .	35
<b>2 Radioactive Ion Beams at CERN</b>	<b>37</b>
2.1 ISOLDE . . . . .	38
2.2 REX . . . . .	39
2.3 HIE-ISOLDE . . . . .	47
2.4 HIE Linac (SC-REX Linac) . . . . .	50
<b>3 Linac Beam Dynamics</b>	<b>57</b>
3.1 Resonance Linear Accelerators . . . . .	57

---

3.2	Accelerating Cavities . . . . .	59
3.3	Longitudinal Beam Dynamics . . . . .	68
3.4	Transverse Beam Dynamics . . . . .	84
3.5	Sources of Emittance Growth . . . . .	100
3.6	Beam Dynamics Simulation Codes . . . . .	102
<b>4</b>	<b>Investigation of the REX Linac</b>	<b>103</b>
4.1	Radio Frequency Quadrupole (RFQ) . . . . .	105
4.2	Rebuncher (ReB) . . . . .	109
4.3	20-gap IH Structure (IHS) . . . . .	110
4.4	7-gap Split-ring Cavities (7GX) . . . . .	125
4.5	9-gap IH Cavity (9GP) . . . . .	126
4.6	Beam Emittance . . . . .	129
4.7	Summary of End-to-end Beam Dynamics Simulations . . . . .	132
<b>5</b>	<b>Longitudinal Emittance Measurements</b>	<b>139</b>
5.1	Experimental Overview . . . . .	139
5.2	Theory of Three-gradient Emittance Measurement . . . . .	142
5.3	Spectrometer . . . . .	147
5.4	Simulations of the Measurement . . . . .	150
5.5	Effect of Resolution . . . . .	154
5.6	ReB Measurements . . . . .	155
5.7	7G3 Measurements . . . . .	158
5.8	Longitudinal Phase Space Distribution . . . . .	161
5.9	Summary . . . . .	165
<b>6</b>	<b>Beam Dynamics Design Studies of the HIE-ISOLDE Linac</b>	<b>167</b>
6.1	Lattice Design . . . . .	167
6.2	Suppression of Longitudinal-Transverse Coupling . . . . .	171
6.3	Matching Sections . . . . .	177
6.4	Compensation of Beam-steering . . . . .	183
6.5	Compensation of Transverse Asymmetry . . . . .	189

6.6	Removal of Cavity Noses . . . . .	192
6.7	Misalignment and Error Studies . . . . .	192
6.8	Deceleration in Low Energy Section . . . . .	210
6.9	Summary of Beam Parameters . . . . .	218
<b>7</b>	<b>Development of a Silicon Detector for Phasing the HIE Linac</b>	<b>225</b>
7.1	Longitudinal Beam Diagnostics . . . . .	225
7.2	Diagnostic System Setup . . . . .	226
7.3	Control of Beam Intensity . . . . .	229
7.4	Resolution . . . . .	233
7.5	Phasing with Energy . . . . .	237
7.6	Phasing with Time-of-Flight . . . . .	238
7.7	Summary . . . . .	239
<b>8</b>	<b>Conclusion</b>	<b>240</b>
8.1	Summary . . . . .	240
8.2	Future of HIE-ISOLDE . . . . .	242
	<b>Bibliography</b>	<b>243</b>
<b>A</b>	<b>REX-ISOLDE Time Structure</b>	<b>257</b>
<b>B</b>	<b>Second-order Transit-Time Factors</b>	<b>259</b>
B.1	Derivation of $T^{(2)}$ for a Two-gap Resonator . . . . .	260
B.2	Derivation of $T_s^{(2)}$ for a Two-gap Resonator . . . . .	260
B.3	$T^{(2)}$ and $T_s^{(2)}$ for a Single Gap Resonator . . . . .	264
B.4	Standard Integrals . . . . .	264
<b>C</b>	<b>Longitudinal Transfer Matrices for Buncher Cavities</b>	<b>267</b>
C.1	Thin Lens Buncher Cavity . . . . .	268
C.2	Multi-gap Buncher Cavity . . . . .	268
<b>D</b>	<b>ReB and 7G3 Calibrations</b>	<b>272</b>
D.1	Setting the Synchronous Phase . . . . .	273

---

D.2	Pick-up Calibration . . . . .	274
<b>E</b>	<b>Phase Space Tomography</b>	<b>275</b>
E.1	7G3 Measurement . . . . .	276
<b>F</b>	<b>Cavity Variants</b>	<b>277</b>
F.1	Modification to the Drift-Tubes . . . . .	278
F.2	High- $\beta$ Cavity with Beam Port Noses Removed . . . . .	279
<b>G</b>	<b>Misalignment in the Matrix Description</b>	<b>282</b>
<b>H</b>	<b>Matched Linac Parameters</b>	<b>286</b>
H.1	Stage 1 and 2a . . . . .	288
H.2	Stage 2b . . . . .	289
<b>I</b>	<b>HEBT</b>	<b>292</b>
I.1	Stage 1: 5.9 MeV/u - Experiment Station 1 . . . . .	293
I.2	Stage 1: 5.9 MeV/u - Experiment Station 2 . . . . .	294
I.3	Stage 2b: 10 MeV/u - Experiment Station 1 . . . . .	295
I.4	Stage 2b: 10 MeV/u - Experiment Station 2 . . . . .	296
I.5	Stage 2b: 0.45 MeV/u - Experiment Station 1 . . . . .	297

## LIST OF FIGURES

1.1	Radionuclides available at ISOLDE . . . . .	27
1.2	Schematic of post-acceleration at an ISOL facility . . . . .	30
1.3	Worldwide overview of current radioactive nuclear beam facilities. . . . .	33
1.4	Summary of the NuPECC Long Range Plan 2010 . . . . .	34
2.1	The CERN accelerator complex . . . . .	37
2.2	Layout of the ISOLDE facility . . . . .	38
2.3	The REX post-accelerator . . . . .	40
2.4	Schematic layout of the REX charge breeder . . . . .	41
2.5	The Miniball array . . . . .	45
2.6	Schematic of a Coulomb excitation reaction . . . . .	46
2.7	Schematic of the T-REX detector inside the Miniball array . . . . .	46
2.8	The HIE-ISOLDE post-accelerator . . . . .	47
2.9	The Linac4 injector . . . . .	48
2.10	Installation stages of the superconducting HIE linac . . . . .	49
2.11	Geometries of the low and high- $\beta$ quarter-wave cavities . . . . .	53
2.12	Energy gain and transit-time factors in the HIE cavities . . . . .	53
2.13	Preparation of the first prototype high- $\beta$ cavity . . . . .	54
2.14	Prototype high- $\beta$ cavity before and after sputtering . . . . .	54
3.1	Schematic of the Wideröe concept. . . . .	58
3.2	Schematic of the REX IHS. . . . .	62
3.3	Schematic of the fields in the quarter-wave resonator . . . . .	64
3.4	Electromagnetic fields on the beam axis of the quarter-wave resonator . . . . .	65

3.5	Co-moving coordinate system . . . . .	68
3.6	Transit-time factors of the HIE-ISOLDE low- $\beta$ cavity . . . . .	75
3.7	Schematic illustrating the concept of phase focusing . . . . .	77
3.8	Longitudinal phase space separatrix and potential . . . . .	79
3.9	First KONUS period of the REX IHS . . . . .	80
3.10	Rebuncher section of the REX IHS . . . . .	81
3.11	Second KONUS period of the REX IHS . . . . .	82
3.12	Longitudinal dynamics through the stationary separatrix of an independent cavity linac . . . . .	83
3.13	Electromagnetic fields in the vicinity of the beam axis of the HIE linac high- $\beta$ cavity . . . . .	85
3.14	Definition of $y_0$ in the quarter-wave resonator. . . . .	86
3.15	Analytic calculation of the beam-steering in the high- $\beta$ cavity . . . . .	87
3.16	Stability regions of the Mathieu-Hill equation . . . . .	93
3.17	The definition of the phase space ellipse . . . . .	95
3.18	Definition of the acceptance . . . . .	99
4.1	The REX linac juxtaposed with the HIE linac to illustrate the emittance measurement campaign . . . . .	104
4.2	Simulated beam phase space distribution after the REX RFQ . . . . .	106
4.3	Summary of the beam dynamics in the REX RFQ . . . . .	107
4.4	Energy spread measurements after the REX RFQ vs. simulation . . . . .	108
4.5	REX RFQ transmission measurements vs. simulation . . . . .	109
4.6	Simulated REX ReB electromagnetic fields and emittance growth . . . . .	110
4.7	REX IHS geometry implemented in HFSS . . . . .	111
4.8	Photos documenting the bead-pull measurement . . . . .	113
4.9	Schematic of the bead-pull measurement apparatus . . . . .	114
4.10	Schematic of the tuner actuator for the IHS. . . . .	115
4.11	Analysis of the phase noise in the bead-pull measurement . . . . .	115
4.12	Baseline tracking algorithm used in the bead-pull measurement software . . . . .	117
4.13	REX IHS gap voltage distribution . . . . .	118

4.14	REX IHS accelerating field . . . . .	119
4.15	REX IHS output energy as a function of phase . . . . .	120
4.16	Measured REX IHS output energy as a function of phase with variation of voltage and input beam energy vs. simulation . . . . .	121
4.17	Simulated dipole steering of the beam centroid in the REX IHS . . . . .	121
4.18	Benchmarking of beam dynamics codes simulating the REX IHS . . . . .	122
4.19	Longitudinal acceptance of the REX IHS . . . . .	123
4.20	Simulated longitudinal emittance growth in the REX IHS surveyed as a function of the input Twiss parameters . . . . .	124
4.21	Effect of rf jitter on the longitudinal emittance in the REX IHS . . . . .	125
4.22	Benchmarking of beam dynamics codes simulating the REX 9GP . . . . .	127
4.23	Energy spread measurements after the REX 9GP vs. simulation . . . . .	127
4.24	Bunch length profiles as a function of the REX 9GP phase . . . . .	128
4.25	Summary of the transverse emittance measurements at REX . . . . .	129
4.26	Summary of existing energy spread data useful for REX longitudinal emittance estimates . . . . .	130
4.27	TRACE 3-D model of the REX linac . . . . .	133
4.28	Summary of end-to-end LANA simulations of the REX linac . . . . .	134
4.29	Simulated beam phase space distribution at the exit of the REX 9GP . . . . .	137
4.30	Simulated beam phase space distribution at the exit of the REX IHS . . . . .	138
5.1	Simulated longitudinal emittance at output to the RFQ as a function of the input transverse emittance . . . . .	141
5.2	Beam diagnostics systems at REX . . . . .	142
5.3	Energy spread calculations downstream of the ReB and 7G3 cavities . . . . .	146
5.4	TRACE 3-D of the REX spectrometer . . . . .	148
5.5	An energy spread measurement with the REX spectrometer . . . . .	149
5.6	TRAVEL simulations of the energy spread reconstruction technique . . . . .	152
5.7	TRAVEL simulations assessing the effect of perturbing the REX switch- yard magnet on the resolution . . . . .	152
5.8	TRAVEL simulations of the emittance measurement . . . . .	153

5.9	Effect of a finite energy resolution on the measurement . . . . .	154
5.10	Energy spread measured as a function of the ReB voltage . . . . .	156
5.11	Raw data for the ReB measurement . . . . .	157
5.12	Energy spread measured as a function of the 7G3 voltage . . . . .	159
5.13	Bunch length measured downstream of the 7G3 as a function of voltage .	160
5.14	Raw data taken during the bunch length measurements . . . . .	161
5.15	Indirect measurement of the longitudinal phase space distribution . . . . .	162
5.16	Longitudinal phase space distributions measured with the ReB: measure- ment vs. simulation . . . . .	163
5.17	Longitudinal phase space distributions measured with the 7G3: measure- ment vs. simulation . . . . .	163
5.18	MENT beam tomography analysis for the ReB measurement . . . . .	164
5.19	Contour plot from MENT beam tomography analysis for the ReB mea- surement . . . . .	164
6.1	Schematic of the lattice of the HIE linac . . . . .	168
6.2	TRACE 3-D model of the HIE linac . . . . .	170
6.3	Parametric resonance observed in simulations of the HIE linac . . . . .	173
6.4	Simulated transverse emittance growth in Stage 2a: LANA vs. TRACK . .	174
6.5	Parametric resonance peak in the HIE linac simulations . . . . .	174
6.6	Summary of LANA simulations of the HIE linac . . . . .	176
6.7	Longitudinal acceptance of Stage 2b of the HIE linac . . . . .	178
6.8	Longitudinal acceptance of Stage 1 of the HIE linac . . . . .	179
6.9	TRACE 3-D model matching REX to Stage 1 and 2a . . . . .	181
6.10	TRACE 3-D model matching REX to Stage 2b . . . . .	182
6.11	Analytic calculation of the beam-steering in the high- $\beta$ cavity including compensation with the rf (de)focusing force . . . . .	184
6.12	Schematic of the circular and racetrack apertures . . . . .	184
6.13	Beam-steering in the HIE cavities: analytical vs. numerical calculations .	185
6.14	Survey to assess optimum beam port height and beam offset . . . . .	187
6.15	Beam-steering optimisation routine vs. TRACK simulations . . . . .	187

6.16	Definition of the nose offset $\Delta$ . . . . .	188
6.17	Effect on the beam-steering from offsetting the noses . . . . .	189
6.18	Cross-section of the high- $\beta$ cavity at the beam axis . . . . .	190
6.19	Asymmetry of the rf (de)focusing force in the HIE cavities . . . . .	190
6.20	Beam envelope in each section of the HIE linac with different modifica- tions to the cavity geometry . . . . .	191
6.21	Beam envelope along the entire HIE linac with different modifications to the cavity geometry in the vicinity of the beam axis. . . . .	192
6.22	Transfer matrices of the linearised beam dynamics in high energy section	195
6.23	Effect of cold steerers in the orbit correction routine . . . . .	197
6.24	Centroid trajectory in the presence of cavity misalignment . . . . .	198
6.25	Centroid trajectory in the presence of solenoid misalignment . . . . .	199
6.26	Centroid trajectory with BPM errors in the presence of cavity and solenoid misalignment . . . . .	200
6.27	Survey of the loss in acceptance in Stage 2a as a function of the error tolerance . . . . .	202
6.28	An example of the emittance growth with cavity misalignments . . . . .	203
6.29	Probability of emittance growth with transverse misalignments of the cav- ities . . . . .	204
6.30	Probability of emittance growth with longitudinal misalignments of the cavities . . . . .	204
6.31	Probability of emittance growth with transverse misalignments of the solenoids . . . . .	205
6.32	Time-averaged longitudinal emittance growth in Stage 2a as a function of the rf jitter . . . . .	206
6.33	Time-averaged longitudinal emittance growth in Stage 2a as a function of cavity number . . . . .	206
6.34	Design of the compact warm inter-cryomodule corrector magnet . . . . .	207
6.35	Design of the high energy cryomodule . . . . .	208
6.36	Orbit excursion in the low energy section: warm vs. cold steerers . . . . .	209

6.37	Transit time factors of the low- $\beta$ cavity: realistic field vs. the square-wave approximation . . . . .	212
6.38	Phasing the low- $\beta$ cavity for deceleration . . . . .	214
6.39	Energy loss in the low energy section during deceleration . . . . .	214
6.40	$\Delta W$ vs. $\phi$ for deceleration with $A/q = 4.5$ . . . . .	215
6.41	$\Delta W$ vs. $\phi$ for deceleration with $A/q = 3$ . . . . .	216
6.42	Beam-steering in the low energy section during deceleration . . . . .	217
6.43	Simulated beam phase space distribution at exit to Stage 1 at 5.9 MeV/u .	220
6.44	Simulated beam phase space distribution at exit to Stage 2b at 10 MeV/u .	221
6.45	Simulated beam phase space distribution at exit to Stage 2b at 0.45 MeV/u	222
6.46	HEBT layout . . . . .	223
7.1	The 300 $\mu\text{m}$ and 50 $\text{mm}^2$ PIPS detector . . . . .	227
7.2	Schematic of the silicon detector electronics and data acquisition system.	227
7.3	Demonstration of pile-up and baseline correction. . . . .	228
7.4	Probing the time structure of the extracted EBIS pulse . . . . .	230
7.5	Attenuator foils made with various transmissions . . . . .	231
7.6	Example beam spectra taken with the silicon detector . . . . .	232
7.7	Simulated phasing curves for the first and last cavities. . . . .	233
7.8	$\alpha$ -source detector resolution measurements . . . . .	234
7.9	Beam-based estimation of the resolution of the silicon detectors . . . . .	235
7.10	Measured time structure of the REX beam 9.5 m downstream of the 9-gap structure . . . . .	237
7.11	Proof-of-principle of phasing the 7G3 with the energy signal from the silicon detector . . . . .	238
7.12	Proof-of-principle of phasing the 7G3 with the time signal from the silicon detector . . . . .	239
A.1	REX beam time structure . . . . .	258
D.1	Beam-based phasing of 7G3 . . . . .	273
D.2	Calibration curves for the ReB and 7G3 pick-up ports . . . . .	274

---

E.1	MENT beam tomography analysis for the 7G3 measurement . . . . .	276
E.2	Contour plot from MENT beam tomography analysis for the 7G3 measurement . . . . .	276
F.1	Modifications to the drift-tubes of the low and high- $\beta$ cavities . . . . .	278
F.2	A comparison of the accelerating field and shunt impedance of the high- $\beta$ cavity, with and without noses . . . . .	280
F.3	A comparison of the rf (de)focusing and beam-steering in the high- $\beta$ cavity with and without beam ports . . . . .	280
I.1	HEBT to Experiment Station 1 at 5.9 MeV/u . . . . .	293
I.2	HEBT to Experiment Station 1 at 5.9 MeV/u with rebuncher . . . . .	293
I.3	HEBT to Experiment Station 2 at 5.9 MeV/u . . . . .	294
I.4	HEBT to Experiment Station 2 at 5.9 MeV/u with rebuncher . . . . .	294
I.5	HEBT to Experiment Station 1 at 10 MeV/u . . . . .	295
I.6	HEBT to Experiment Station 1 at 10 MeV/u with rebuncher . . . . .	295
I.7	HEBT to Experiment Station 2 at 10 MeV/u . . . . .	296
I.8	HEBT to Experiment Station 2 at 10 MeV/u with rebuncher . . . . .	296
I.9	HEBT to Experiment Station 1 at 0.45 MeV/u . . . . .	297

## LIST OF TABLES

1.1	Comparison between ISOL and In-flight production techniques . . . . .	30
1.2	Selection of worldwide ISOL facilities in operation today . . . . .	32
2.1	Parameters of the REX linac structures . . . . .	43
2.2	Requested beam characteristics at HIE-ISOLDE . . . . .	51
2.3	Basic design parameters for the HIE linac . . . . .	51
2.4	HIE cavity design parameters . . . . .	55
2.5	HIE solenoid design parameters . . . . .	56
3.1	Properties of the 4-dimensional Gaussian and Waterbag distributions . . .	98
3.2	Summary of beam dynamics codes . . . . .	102
4.1	Summary of the simulated horizontal REX beam parameters . . . . .	135
4.2	Summary of the simulated vertical REX beam parameters . . . . .	135
4.3	Summary of the simulated longitudinal REX beam parameters . . . . .	136
5.1	Parameters of the REX switchyard magnet . . . . .	147
5.2	Spectrometer settings for $A/q = 4$ and $W_0 = 300 \text{ keV}/u$ . . . . .	150
5.3	Qualitative effect of the energy resolution on the Twiss parameters reconstructed through a three-gradient emittance measurement . . . . .	155
5.4	Summary of the longitudinal emittance measurements with the ReB (0.3 MeV/ $u$ ) and the 7G3 (1.92 MeV/ $u$ ) . . . . .	166
6.1	HIE linac lattice parameters . . . . .	169
6.2	Summary of the optimisation of $y_0$ and $\delta$ in the high energy section. . . .	186
6.3	Summary of the results of the beam-steering optimisation study. . . . .	189

6.4	RMS emittance growth in end-to-end simulations of Stage 2b in the presence of misalignment and rf jitter. . . . .	210
6.5	Summary of the simulated horizontal HIE beam parameters . . . . .	219
6.6	Summary of the simulated vertical HIE beam parameters . . . . .	219
6.7	Summary of the simulated longitudinal HIE beam parameters . . . . .	219
7.1	Calibration of attenuator foils . . . . .	232
F.1	Basic Parameters of the Modification to the High- $\beta$ Cavity. . . . .	279
F.2	Parameters of the high- $\beta$ cavity without beam port noses . . . . .	279
H.1	Linac settings for the high energy section in stage 1 and 2a, $A/q = 4.5$ and $E_{in} = 2.8$ MeV/u. . . . .	288
H.2	Linac settings for the high energy section in stage 1 and 2a, $A/q = 2.5$ and $E_{in} = 3.0$ MeV/u. . . . .	288
H.3	Linac settings for the low energy section, $A/q = 4.5$ and $E_{in} = 1.2$ MeV/u. . . . .	289
H.4	Linac settings for the low energy section, $A/q = 2.5$ and $E_{in} = 1.2$ MeV/u. . . . .	289
H.5	Linac settings for the high energy section, $A/q = 4.5$ and $E_{in} = 3.6$ MeV/u. . . . .	290
H.6	Linac settings for the high energy section, $A/q = 2.5$ and $E_{in} = 5.2$ MeV/u. . . . .	290
H.7	Solenoid settings and matched beam parameters for the complete stage 2b linac . . . . .	291

## ABSTRACT

The High Intensity and Energy (HIE) project represents a major upgrade of the ISOLDE (On-Line Isotope Mass Separator) nuclear facility at CERN with a mandate to significantly increase the energy, intensity and quality of the radioactive nuclear beams provided to the European nuclear physics community for research at the forefront of topics such as nuclear structure physics and nuclear astrophysics. The HIE-ISOLDE project focuses on the upgrade of the existing Radioactive ion beam EXperiment (REX) post-accelerator with the addition of a 40 MV superconducting linac comprising 32 niobium sputter-coated copper quarter-wave cavities operating at 101.28 MHz and at an accelerating gradient close to 6 MV/m. The energy of post-accelerated radioactive nuclear beams will be increased from the present ceiling of 3 MeV/ $u$  to over 10 MeV/ $u$ , with full variability in energy, and will permit, amongst others, Coulomb interaction and few-nucleon transfer reactions to be carried out on the full inventory of radionuclides available at ISOLDE.

In this thesis the beam dynamics of the superconducting linac is studied with a focus on identifying and mitigating the sources of beam emittance dilution. Highlights include the suppression of a parametric resonance, compensation of the beam-steering effect intrinsic to quarter-wave cavities and a study of the energy change in the cavities well below their geometric velocity using second-order transit-time factors. The studies lead to the specification and tolerances for the linac components. An extensive investigation of REX was also carried out involving rf and beam measurements that facilitated the benchmarking of the beam dynamics codes that were used to design the matching sections and ensure the compatibility of the upgrade. In addition, a solid-state diagnostics system was developed as a tool to aid the quick and eventually automated tuning of the large number of cavities that will accompany the upgrade.

# DECLARATION

The University of Manchester

*PhD Candidate Declaration*

**Candidate Name:** Matthew Alexander Fraser

**Faculty:** Engineering and Physical Sciences

**Thesis Title:** Beam Dynamics Studies of the ISOLDE Post-accelerator for the High Intensity and Energy Upgrade

**Declaration to be completed by the candidate:**

I declare that no portion of this work referred to in this thesis has been submitted in support of an application for another degree or qualification of this or any other university or other institute of learning.

Signed:



Date: December 31, 2011

## COPYRIGHT

The author of this thesis (including any appendices and/or schedules to this thesis) owns any copyright in it (the "Copyright")<sup>1</sup> and s/he has given The University of Manchester the right to use such Copyright for any administrative, promotional, educational and/or teaching purposes.

Copies of this thesis, either in full or in extracts, may be made only in accordance with the regulations of the John Rylands University Library of Manchester. Details of these regulations may be obtained from the Librarian. This page must form part of any such copies made.

The ownership of any patents, designs, trade marks and any and all other intellectual property rights except for the Copyright (the "Intellectual Property Rights") and any reproductions of copyright works, for example graphs and tables ("Reproductions"), which may be described in this thesis, may not be owned by the author and may be owned by third parties. Such Intellectual Property Rights and Reproductions cannot and must not be made available for use without the prior written permission of the owner(s) of the relevant Intellectual Property Rights and/or Reproductions.

Further information on the conditions under which disclosure, publication and exploitation of this thesis, the Copyright and any Intellectual Property Rights and/or Reproductions described in it may take place is available from the Head of School of Physics and Astronomy (or the Vice-President) and the Dean of the Faculty of Engineering and Physical Sciences, for Faculty of Engineering and Physical Sciences candidates.

---

<sup>1</sup>This excludes material already printed in academic journals, for which the copyright belongs to said journal and publisher.

## THE AUTHOR

The author grew up in Berkhamsted, England, attending Ashlyns School before moving to Manchester in 2004 to read physics at the University of Manchester. During the summer of 2007 the author received a scholarship from CERN in Geneva to work and study with the Beta-beam Task Group inside the EURISOL Design Study. The work focused on an optimisation study of the CERN accelerator complex and an investigation of radionuclides with the potential of creating monochromatic beta-beams [1], which served as an introduction to the physics of accelerators and beams.<sup>1</sup> After graduating with a master's degree in physics, MPhys (Hons) first class, from the University of Manchester in 2008, the author returned to Geneva for a period of three years to pursue a PhD degree within the CERN Doctoral Student Programme affiliated with the University of Manchester and the Cockcroft Institute of Accelerator Science and Technology, Daresbury.

---

<sup>1</sup>The beta-beam is a concept for creating intense and pure beams of neutrinos from the beta-decay of radioactive ions stored at relativistic energies in a decay ring [2].

## ACKNOWLEDGEMENTS

Firstly, I would like to thank my supervisors, Roger Jones and Matteo Pasini, for their encouragement and support throughout the last three and a half years. I am particularly grateful for Matteo's tutorship and patience during my first few months at CERN. Without Matteo's dedication to the HIE-ISOLDE project it would certainly not be in the strong position that it finds itself today. I gratefully acknowledge Roger's interest in the HIE-ISOLDE project and his work to involve the Cockcroft Institute. I would also like to thank my advisor Fred Loebinger for his infinite wisdom on matters regarding university life and the HIE-ISOLDE project leader Yacine Kadi for his enthusiasm, which proved an important motivation to finish this thesis.

I thank all my colleagues in both Manchester and Geneva for their interest and guidance with my research, especially Alessandro D'Elia, Piero Posocco and Francesca Zocca. I extend my gratitude to everyone at REX-ISOLDE for helping to make the linac development work possible, namely Emiliano Piselli, Didier Voulot and Fredrik Wenander. I thank Giovanni De Michele for helping to adapt his bead-pull measurement set-up to the REX beam line and for his company during the years that we shared an office together in Building 18 at CERN. I also extend my thanks to all the members, past and present, of the Manchester Electrodynamics and Wakefields group for our weekly meetings and discussions. I would also like to thank the directorate staff, namely Anne Morrow from the University of Manchester and Liz Kennedy from the Cockcroft Institute.

Over the last few years I received bursaries to attend three international conferences: *PAC'09*, *SRF'09* and *LINAC'10*, and I would like to thank the respective organising committees for giving me these opportunities. As a consequence, I was able to meet and collaborate with various international organisations and their distinguished members. I

would like to thank Jean Delayen of JLAB and ODU, Bob Laxdal of TRIUMF, and Peter Ostroumov of ANL for all their advice that added to my knowledge, which helped me to put together this thesis. I would like to thank Bob Laxdal for his hospitality and welcome to the HIE-ISOLDE team during the first cold tests of the high- $\beta$  cavity prototype in Vancouver. A special thanks goes to Dmitry Gorelov and Brahim Mustapha for their help to implement the ISOLDE post-accelerator in the LANA and TRACK beam dynamics simulation codes, respectively.

I acknowledge the funding support of the ISOLDE Collaboration and the Cockcroft Institute, and I would like to express my appreciation of the lecture series on accelerator physics and technology that is made available by the Cockcroft Institute and for making it possible for me to attend the CAS and JUAS accelerator schools.

Finally, I would like to give thanks to my friends and family to whom this thesis is dedicated. To the friends that made Geneva a place to love: Alex and Sara, thank you! To the friends who kept coming back to CERN over the years: Byeong-No, Gareth, Gastón, Jinhwan, John, Laura, Loek, Mark, Martin, Vik, and Xabier, thank you and keep coming back! To Harry, thanks for being there for me in Manchester! And to all the friends who came to visit me in Geneva: Dan, John, James, Katie, Nick, Ste, thank you! To my family: Sam and Lauren, and especially my Mum and Dad who got rather lumbered with proof-reading, thank you for your love and support! Last, but by no means least, I thank Isabel for her love from close and from afar; it would have been a lot harder without you!

## NOMENCLATURE

### Acronyms/Abbreviations

ac	Alternating current	DSSSD	Double-Sided Silicon Strip Detector
AD	Antiproton Decelerator, CERN	DTL	Drift-Tube Linac
ANL	Argonne National Laboratory, USA	EBIS	Electron Beam Ion Source
ARIEL	Advanced Rare IsotopE Laboratory, TRIUMF	ECR	Electron Cyclotron Resonance
BNL	Brookhaven National Laboratory, USA	EPAC	European Particle Accelerator Conference
BPM	Beam Position Monitor	EURISOL	European Isotope Separator Online
CD	Compact Disc	EXCYT	Exotics with Cyclotron and Tandem, LNS-INFN
CERN	Organisation Européenne pour la Recherche Nucléaire (European Organisation for Nuclear Research), Geneva, Switzerland	FAIR	Facility for Antiproton and Ion Research
CNGS	CERN Neutrinos to Gran Sasso	FRIB	Facility for Rare Isotope Beams, MSU
CRC	Cyclotron Research Centre, UCL	FWHM	Full Width at Half Maximum
cw	Continuous wave	GANIL	Grand Accélérateur National d'Ions Lourds (National Large Heavy Ion Accelerator), Caen, France
CYCLOTRONS	Conference on Cyclotrons and their Application	GPS	General Purpose Separator, ISOLDE
dc	Direct current	GSI	Heavy Ion Research Centre, Darmstadt, Germany
DIPAC	Workshop for Beam Diagnostics and Instrumentation for Particle Accelerators	HCI	High Current Injector, MPIK

HEBT	High Energy Beam Transfer Line	LANL	Los Alamos National Laboratory, USA
HIE	High Intensity and Energy, ISOLDE		
HLI	HochLadungsInjektor (High Charge-state Injektor), GSI	LHC	Large Hadron Collider, CERN
HRIBF	Holifield Radioactive Ion Beam Facility, Oak Ridge, USA	LINAC	Linear Accelerator Conference
HRS	High Resolution Separator, ISOLDE	Linac	Linear accelerator
IAB	International Advisory Board	LNL-INFN	Laboratori Nazionali di Legnaro (Legnaro National Laboratory), Legnaro, Italy
IAP	Institute of Applied Physics, University of Frankfurt, Germany	LNS-INFN	Laboratori Nazionali del Sud (Southern National Laboratory), Catania, Italy
IF	Intermediate Frequency		
IH	Interdigital H-mode	LORASR	LONGitudinale und Radiale Strahldynamikrechnungen mit Raumladung (Longitudinal and Radial Beam Dynamics Calculations Including Space Charge)
INFN	Instituto Nazionale di Fisica Nucleare (National Institute of Nuclear Physics), Italy		
INR	Institute for Nuclear Research, RAS	MAFF	Munich Accelerator for Fission Fragments, Munich
IPAC	International Particle Accelerator Conference	MCA	Multi-Channel Analyser
ISAC	Isotope Separator and ACcelerator, TRIUMF	MPIK	Max-Planck-Institut für Kernphysik (Max Planck Institute for Nuclear Physics), Heidelberg
ISCOOL	ISOLDE COOLer and buncher	MSU	Michigan State University, East Lansing, USA
ISOL	Isotope Separation On-Line	MT	Conference on Magnet Technology
ISOLDE	On-Line Isotope Mass Separator, CERN	NBI	Niels Bohr Institute, Copenhagen, Denmark
JLAB	Thomas Jefferson National Accelerator Facility, USA	NC	Normal Conducting
KONUS	Kombinierte Null Grad Struktur (Combined Zero Degree Structure)	NESR	New Experimental Storage Ring, FAIR
LANA	Linear Accelerators Numerical Analysis		

NIM	Nuclear Instrumentation Module	RFQ	Radiofrequency Quadrupole
NMR	Nuclear Magnetic Resonance	RIB	Radioactive Ion Beam
NuPECC	Nuclear Physics European Col- laboration Committee	RIBF	Radioactive Ion Beam Facility, RIKEN
NuSTAR	Nuclear Structure, Astrophysics and Reactions, FAIR	RIKEN	Rikagaku Kenkyūjo (Institute of Physical and Chemical Research), Japan
ODU	Old Dominion University, USA	RILIS	Resonance Ionisation Laser Ion Source, ISOLDE
OECD	Organisation for Economic Co-operation and Development	rms	Root mean square
ORNL	Oak Ridge National Laboratory, Knoxville, USA	SC	Superconducting
PAC	Particle Accelerator Conference	SPES	Selective Production of Exotic Species, LNL-INFN
PARMTEQ	Phase and Radial Motion in a Transverse Electric Quadrupole	SPIRAL	Système de Production d'Ions Radioactifs Accélérés en Ligne (Sys- tem for Producing Online Acceler- ated Radioactive Ions), GANIL
PCI	Peripheral Component Interconnect	SRF	Conference on RF Superconductiv- ity
PIMS	Pi-Mode Accelerating Structure, Linac4	SRIM	Stopping Range of Ions in Matter
PIPS	Passivated Implanted Planer Silicon	SuperFRS	Super Fragment Separator, FAIR
PS	Proton Synchrotron, CERN	T-REX	Transfer reactions at REX
PSB	PS Booster, CERN	TDC	Time-to-Digital Converter
PSI	Paul Scherrer Institute, Switzerland	TE	Transverse Electric
QWR	Quarter-Wave Resonator	TM	Transverse Magnetic
RAS	Russian Academy of Sciences, Moscow, Russia	ToF	Time-of-flight
REX	Radioactive Ion Beam EXperiment, ISOLDE	TRIUMF	National Laboratory for Particle and Nuclear Physics, Vancouver, Canada
REXEBS	REX Electron Beam Ion Source, ISOLDE	VME	Versa Module Europa
REXTRAP	REX Penning TRAP, ISOLDE		
rf	Radio frequency		

<b>Variables/Constants</b>			
		$f_{\text{rms}}$	RMS emittance growth factor
$\tilde{\alpha}$	Twiss $\alpha$ -function	$\gamma$	Relativistic Lorentz factor
$A$	Nucleon or mass number	$\tilde{\gamma}$	Twiss $\gamma$ -function
$\tilde{\beta}$	Twiss $\beta$ -function	$g$	Gap length
$\vec{\beta}$	Reduced velocity	$I$	Beam current or intensity
$\beta_0$	Reduced velocity of reference particle	$i = \sqrt{-1}$	Unit imaginary number
$\beta_g$	Geometric velocity	$\kappa_B, \kappa_E$	Normalised and integrated transverse field component
$\beta_{\text{opt}}$	Optimum velocity, i.e. $\frac{\partial T(\beta_{\text{opt}})}{\partial \beta} = 0$	$K$	Cyclotron $K$ -value
$\beta_s$	Reduced velocity of synchronous particle	$k_{l,s}$	Smoothed longitudinal wavenumber
$\vec{B}$	Magnetic field vector	$k_{t,s}$	Smoothed transverse wavenumber
$B_{\text{pk}}$	Peak magnetic field	$\lambda$	Rf wavelength
$c$	Speed of light, $2.998 \times 10^8 \text{ ms}^{-1}$	$L_a$	Active length
$\Delta$	Offset of cavity noses with respect to beam port centre	$m$	Rest mass
$\delta_{\text{comp}}$	Beam offset in aperture for steering compensation	$\mu_0$	Permeability of free space, $4\pi \times 10^{-7} \text{ N A}^{-2}$
$\epsilon_0$	Permittivity of free space, $8.854 \times 10^{-12} \text{ C}^2 \text{ N}^{-1} \text{ m}^{-2}$	$\mu_L$	Longitudinal phase advance per focusing period
$\epsilon_L$	Longitudinal beam emittance	$\mu_T$	Transverse phase advance per focusing period
$\epsilon_T$	Transverse beam emittance	$N$	Neutron number
$e$	Elementary charge, $1.602 \times 10^{-19} \text{ C}$	$\Psi, \tilde{\Psi}$	Phase functions
$eV$	Electronvolt, $1.602 \times 10^{-19} \text{ J}$	$P$	Power lost on cavity walls
$\vec{E}$	Electric field vector	$\Phi_0$	Amplitude of small longitudinal oscillations
$E_0$	Equivalent dc average gradient	$\phi_s$	Synchronous phase
$E_{\text{acc}}$	Average accelerating gradient	$\vec{p}$	Momentum
$E_{\text{pk}}$	Peak electric field	$Q$	Unloaded quality factor
$F$	Packing factor	$q$	Charge state or Mathieu equation
$f$	Rf frequency		

	parameter
$Q_L$	Loaded quality factor
$R_{ij}$	Transfer matrix element
$R_0$	Shunt impedance
$R_{\text{eff}}$	Effective shunt impedance
$R'_p$	Specific shunt impedance
$R_s$	Rf surface resistance
$\sigma$	Second moment or rms of a distribution
$\tau$	Normalised longitudinal coordinate
$T$	Transit-time factor
$T^{(2)}, T_s^{(2)}$	Second-order transit-time factors
$U$	Stored energy
$u$	Atomic mass unit, $\frac{1}{12}m(^{12}\text{C atom}) = 1.661 \times 10^{-27} \text{ kg} = 931.494 \text{ MeV}/u$
$V_0$	Equivalent dc voltage
$V_{\text{eff}}$	Effective voltage
$W$	Kinetic energy
$\omega_c$	Cyclotron frequency
$\omega_L$	Larmor frequency
$y_0$	Height of centre of beam port in QWR
$Z$	Proton number
$Z_0$	Shunt impedance per unit length
$Z_{\text{eff}}$	Effective shunt impedance per unit length

## INTRODUCTION TO RADIOACTIVE ION BEAM FACILITIES

Since the inception of modern radioactive nuclear beam science some 60 years ago, when a cyclotron providing 11 MeV deuterons was used to induce the fission of uranium and the production of neutron-rich krypton isotopes at NBI in Copenhagen [3], the production of radioactive ion beams at large-scale accelerator facilities has led to significant advances in the fields of nuclear structure physics and nuclear astrophysics [4]. The success of radioactive ion beams in the study of nuclear physics lies in the variety of beams that can now be produced from across the entire nuclear landscape and very far from stability. For example, the CERN On-line Isotope Mass Separator facility (ISOLDE) [5] has spearheaded the development of target and ion source systems over the last 45 years, and today offers the most diverse range of nuclei available in the world, numbering over 800 isotopes, see Figure 1.1. With currently over 3600 radioactive nuclides having been produced worldwide from an estimated total of 6000, the production of radioactive ion beams at dedicated multi-user facilities is providing an unparalleled tool for probing the diverse behaviours of exotic nuclear matter away from the familiar ‘valley of stability’, and is pushing the development of the theoretical understanding of nuclei through the discovery of new and often unexpected phenomenon. The advances made in beam preparation and accelerator technology at these large-scale facilities have gone hand-in-hand with scientific advancements and the link between the two will remain crucial for the future progress of nuclear physics research. For a comprehensive introduction to the ‘how’ and ‘why’ of radioactive beam research the reader is referred to [6].

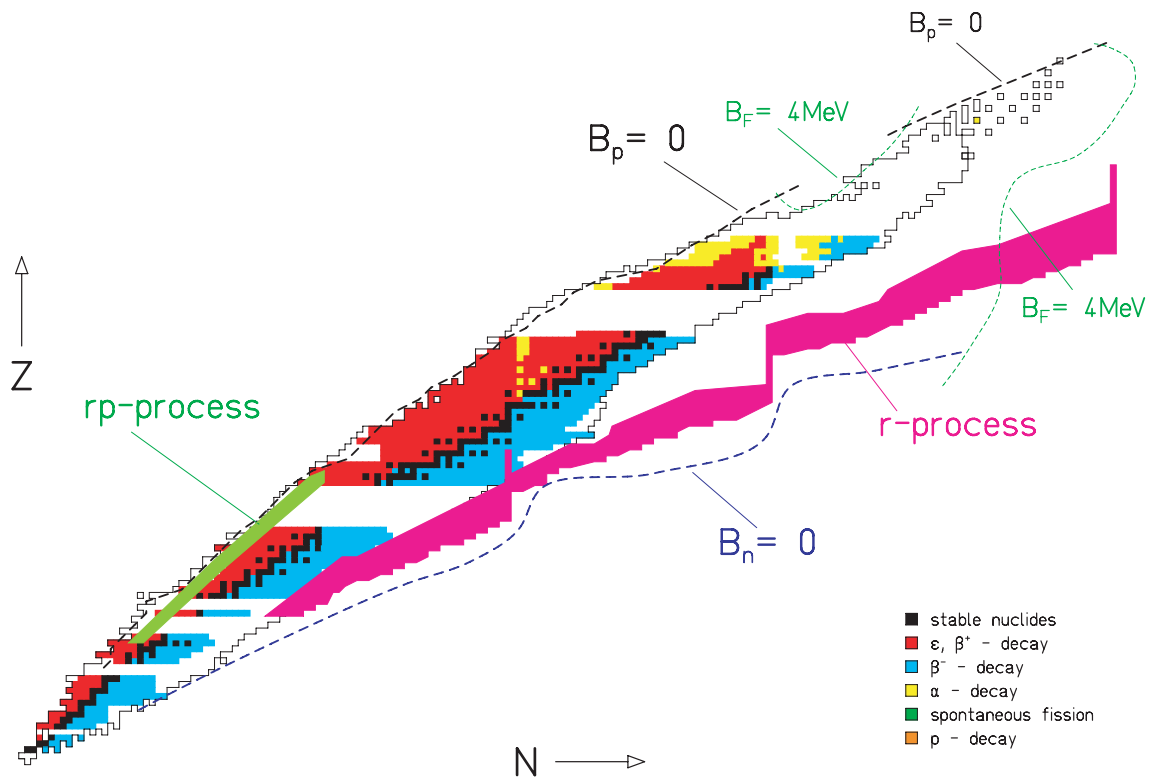


Figure 1.1: Table of radionuclides showing those from  ${}^6\text{He}$  to  ${}^{232}\text{Ra}$  that can be synthesised at ISOLDE. The rp- and r-process pathways thought to have created elements during explosive stellar events, and the expected limits of stability at the neutron, proton and spontaneous fission drip lines are shown. Figure courtesy of T. Nilsson.

## 1.1 Physics Motivation

The two main research areas that exploit radioactive beams are nuclear structure physics and nuclear astrophysics, but beams are also used at the forefront of research into fundamental and condensed matter physics, along with applications in the life sciences and medical physics. The scientific motivations for the development of radioactive nuclear beam facilities are outlined at length in the Appendix to the Organisation for Economic Co-operation and Development (OECD) Megascience Forum Report of the Working Group on Nuclear Physics [7]. Some of the questions that radioactive ion beam facilities strive to answer are:

- What is the origin of the elements that we find in the Universe today?
- What are the limits of nuclear existence?
- What is the nature of nuclear matter away from stability?

The nucleus is a complicated many-body quantal system composed of protons and neutrons on the cusp of what can be treated purely classically or purely quantum mechanically, existing through a balance of many competing interactions including the electromagnetic, nuclear (strong) and weak forces. The large number of degrees of freedom present in the nucleus has been, and continues to be, challenging to understand in a general theoretical framework, and is at the heart of the research being carried out using radioactive nuclear beams.

The nuclear astrophysical processes, e.g. Big Bang nucleosynthesis and supernovae explosions, that led to the production of the elements that we see today are thought to have involved nuclei far from stability, which although existing only fleetingly, played an important role in the formation of matter as we know it. By synthesising exotic nuclei on Earth and measuring their properties, including their reaction and decay characteristics, it is hoped that the mechanisms behind these astrophysical processes and others observed in the cosmos, such as hydrogen burning cycles in stars and X-ray bursters, can be illuminated. Indeed, significant discoveries have already been made, see e.g. [8].

Of particular interest in nuclear structure physics are the limits of nuclear existence, near the proton and neutron drip lines, i.e. at large proton number ( $Z$ ) or neutron number ( $N$ ), respectively, or at very large mass number ( $A$ ). Presently, the drip lines have only been reached for the lightest elements, however in these regions of the nuclear chart new phenomenon have already been observed, such as proton radioactivity [9] for proton-heavy nuclei and dilute neutron halos [10] close to the neutron drip line, as well as resonant states existing outside of the drip lines [11]. The limits of superheavy nuclei have also been probed with elements up to  $Z = 118$  being the heaviest nuclei ever observed, and significant modifications to the single-particle shell model and magic numbers have been measured in nuclei far from stability [12]. It is at the limits of the available experimental parameter space where significant discoveries are being made, which in turn demands more advanced facilities with increased flexibility so as to provide exotic beams of better quality and higher intensity.

## 1.2 ISOL vs. In-flight

For a comprehensive overview of the two main methods by which radioactive nuclides are produced the reader is referred to the review articles [13, 14]. The Isotope Separation On-line (ISOL) and In-flight techniques are broadly summarised in Table 1.1 and below:

- **ISOL** - radioactive nuclides are formed inside a thick, heated target material by spallation, fusion evaporation, fragmentation or fission induced by the impingement of an intense high energy beam of light stable nuclei, e.g. typically H or D.
- **In-flight** - a thin production target is used to initiate the fragmentation or fission of an intense high energy beam of stable heavy nuclei, e.g. typically nuclei up to  $^{238}\text{U}$ , to form radioactive nuclides.

The two methods are largely complementary because of the properties of their secondary beams. The ISOL radioactive nuclides require extraction from the target before they can be ionised, accelerated and separated by magnetic analysis, and as a result the time lag introduced from the diffusion and effusion of the radioactive nuclides out of the target prevents access to beams of very short-living nuclides, and half-lives are limited to longer than about 1 ms. ISOL beams after post-acceleration are characterised with low energy and good optical quality. In-flight beams are produced directly by fragmentation on a thin target and the forward momentum of the nuclear fragments passes them on very quickly through a fragment separator to the experiment without the need for re-acceleration, which allows access to beams of very short-lived isotopes with half-lives down to 1  $\mu\text{s}$ . In-flight beams are characterised by higher energy, poorer optical quality and larger energy spread with respect to ISOL beams.

There are no rigid differences in the physics that can be probed with either facility and the technical advances being made are closing the gap between the quality and energy of the secondary beams. There are plans to re-accelerate ISOL beams to much higher energies so that fragmentation and fission reactions can be induced, and cooling techniques are being developed to improve the optical quality of beams produced by the In-flight method. Aside from these improvements, the focus for the future of these facilities is on the type and intensity of radionuclides that can be produced and delivered to experiments.

Table 1.1: Comparison between typical properties of ISOL and In-flight production

Property	ISOL	In-flight
Primary beam	light ions	heavy ions
Target	thick, complicated	thin, simple
Production cross-section <sup>a</sup>	high	low
Secondary beam energy	$10^{-6}$ eV to 50 MeV/u	0.1 to 2 GeV/u
Half-life reach	$\gtrsim 1$ ms	$\gtrsim 1$ $\mu$ s
Transverse normalised emittance	$0.3 \pi$ mm mrad	$30 \pi$ mm mrad

<sup>a</sup> However, ISOL efficiencies are typically lower due to e.g. extraction, ionisation and decay losses.

### 1.3 Post-acceleration of Radioactive Beams

Since ISOL beams were first post-accelerated at CRC, Louvain-la-Neuve over 20 years ago, there has been worldwide interest in providing high quality re-accelerated beams of radionuclides for nuclear physics research. The typical stages in the production of a post-accelerated radioactive ISOL beam are summarised in the schematic of Figure 1.2.

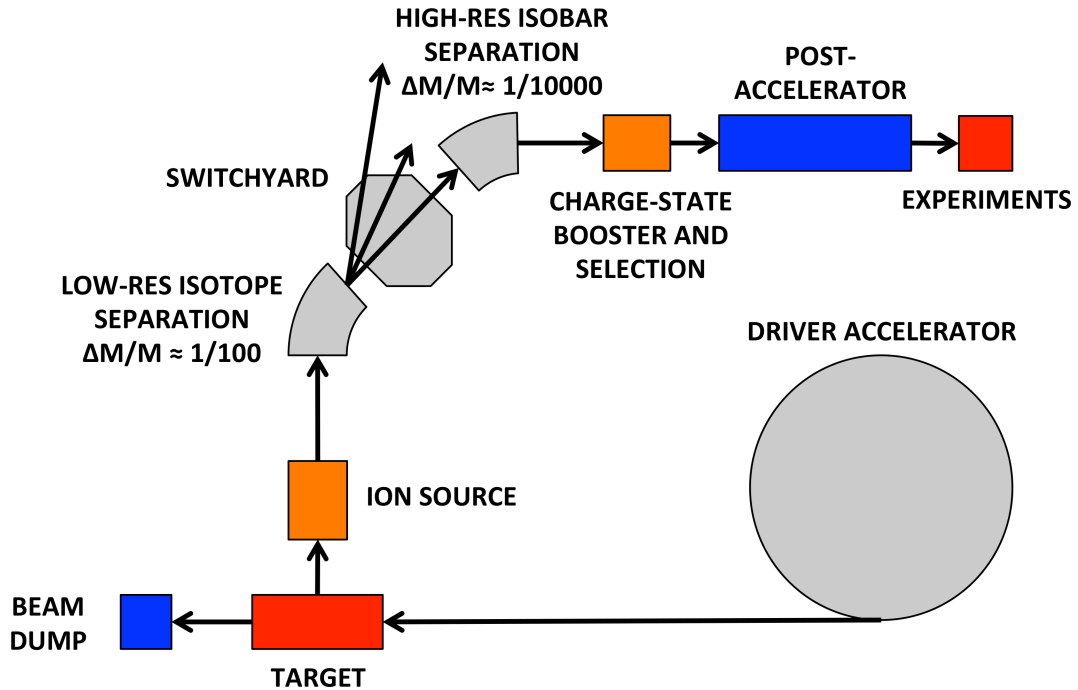


Figure 1.2: Schematic of post-acceleration at an ISOL facility. Reproduced with permission from Figure 1 of [13].

After isotope and isobaric magnetic analysis, the beams are charge-booster before acceleration to the experimental targets. The secondary radioactive beams are diverse, covering a large range of  $A$ , and typically have very low intensity, therefore efficiency, transmission and flexibility are key considerations in the design of post-accelerators [15].

In contrast to the driver accelerator, the beam dynamics in a post-accelerator is characterised by negligible space-charge forces and a lack of beam loading in the accelerating structures. Charge boosting techniques are critical in making the post-accelerator cost-efficient and for allowing the available accelerating potential to be well exploited. A review of the charge breeding techniques currently employed worldwide can be found in [16].

A wide variety of accelerator technology is in use today for post-accelerators, namely electrostatic systems such as tandems and time-varying rf systems such as cyclotrons and linacs, delivering beam energies at or above the Coulomb barrier of a few MeV/*u*. Although the beam quality from tandems is excellent and the output beam energy is fully flexible, the requirement that the beams be negatively charged for acceleration limits the achievable charge-state and therefore the accelerating efficiency. In addition, the maximum accelerating voltage is limited by electrical breakdown of the high-voltage terminals. Rf linear accelerators deliver better quality beams with more energy flexibility than cyclotrons, however at a greater cost. Cyclotrons have the advantage that the mass-to-charge state of the accelerated species is naturally selected, whereas a dedicated mass-separator must be added to the injector of a linac. Linear accelerators can provide a good compromise between operational flexibility and beam quality, with the possibility of staged construction a very attractive feature.

## **1.4 Present and ‘Next Generation’ RIB Facilities**

As a result of the complimentary nature of ISOL and In-flight production both are in widespread use at institutes across the world, and some facilities even employ both to produce their radioactive beams [17–21]. A worldwide summary of radioactive beam institutes and their facilities is collected in Figure 1.3 and, in step with the theme of this thesis, other institutes employing superconducting linear accelerators, albeit for application with stable beams, are also shown. The summary is by no means meant to be comprehensive but merely representative. For the purposes of this thesis, the relevant accelerator technologies and important beam characteristics of a selection of ISOL facilities are summarised in Table 1.2, with In-flight facilities omitted.

Table 1.2: A selection of worldwide ISOL facilities in operation today

Facility (Institute, Location)	First beams	Driver accelerator <sup>a</sup>	Average beam power [kW]	Post-accelerator <sup>a</sup>	Secondary beam energy <sup>b</sup> [MeV/ $u$ ]
CRC [22] (UCL, Louvain-la-Neuve)	1989	cyclotron ( $K = 30$ ) (protons)	15	cyclotrons ( $K = 44, 110$ )	0.5 - 8
HRIBF [23] (ORNL, Knoxville)	1997	cyclotron ( $K = 100$ ) (protons and light ions)	1	25 MV tandem	$\leq 12$
ISAC I/II [24] (TRIUMF, Vancouver)	2000	cyclotron ( $K = 520$ ) (protons)	50	normal and superconducting linacs	0.15 - 6.5
REX-ISOLDE [25] (CERN, Geneva)	2001	synchrotron (PS Booster) (1.4 GeV protons)	2.8	normal conducting linac	0.3 - 3
SPIRAL <sup>c</sup> [26] (GANIL, Caen)	2001	coupled cyclotrons ( $K = 30, 380, 380$ ) ( $\leq 95$ MeV/ $u$ light and heavy ions)	6	cyclotron ( $K = 265$ )	1.2 - 25
EXCYT <sup>c</sup> [27] (LNS-INFN, Catania)	2004	superconducting cyclotron ( $K = 800$ ) ( $\leq 100$ MeV/ $u$ light and heavy ions)	0.15	15 MV tandem	$\leq 7$

<sup>a</sup>  $K$  classifies the cyclotron through the kinetic energy reach of protons in [MeV] (in the non-relativistic limit).

<sup>b</sup> The secondary beam energy depends on the mass-to-charge ratio that can be attained, which is limited for very heavy ions.

<sup>c</sup> These facilities also offer In-flight production with heavy ions.

ISOL facilities operating today are often named ‘first generation’, with ‘intermediate generation’ facilities only just starting to come online, and are characterised with driver accelerators capable of delivering kW beam power onto production targets, with modest secondary beam intensities and post-acceleration capabilities. The most common choice for the driver is the cyclotron, which can provide intense high energy beams for a reasonable cost.

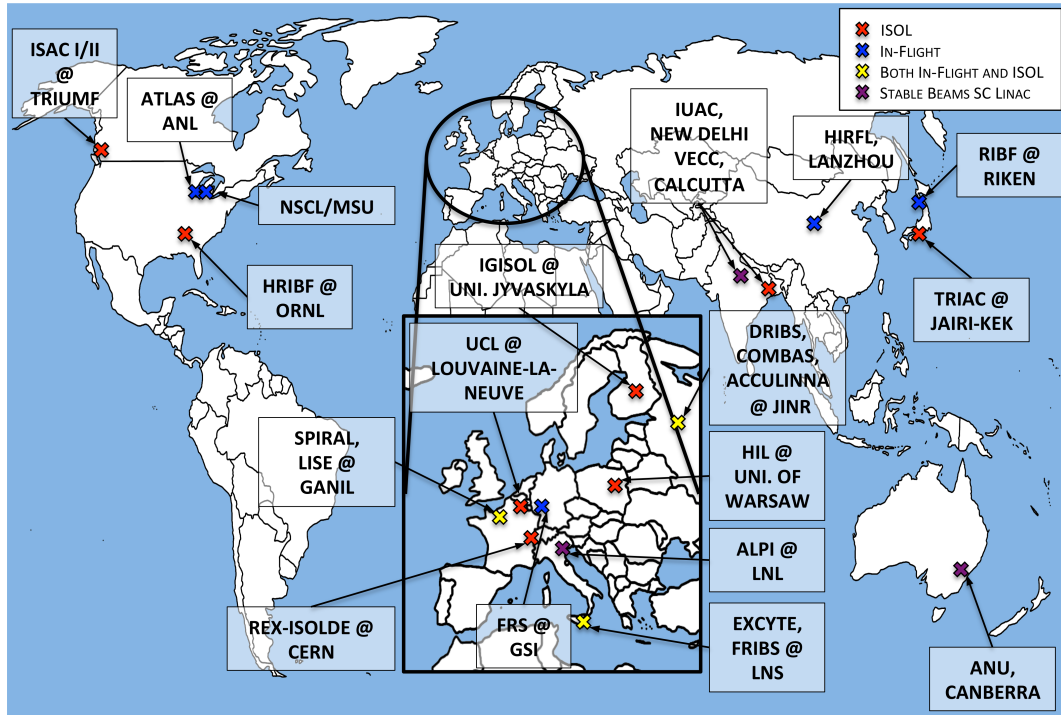


Figure 1.3: Worldwide overview of current radioactive nuclear beam facilities.

ISOLDE finds itself with a unique high energy proton driver but limited post-acceleration capability. This thesis will focus on the improvements to the ISOLDE post-accelerator that will deliver beams with a wide range of energy up to 10 MeV/ $u$  through the construction of a new superconducting linac as part of the High Intensity and Energy (HIE) upgrade of ISOLDE.

With a general consensus amongst the nuclear physics community that radioactive beams are the most effective means to advance the field, a large effort has been invested in planning future facilities with a many orders of magnitude increase in radioactive beam intensity and experimental sensitivity, see [28, 29]. Two complementary large-scale facilities will be constructed in Europe, each based separately on the In-flight and ISOL techniques, respectively:

- FAIR
- EURISOL

Europe is not alone in its ambition to develop 'next generation' facilities, with large-scale upgrades undergoing design studies in North America for FRIB [30] at MSU and ARIEL [31] at TRIUMF, and in Asia for RIBF [32] at RIKEN.

The NuPECC Roadmap to New Large Scale Facilities is summarised in Figure 1.4. With the highest priority is the construction of FAIR, based around an upgrade of the existing In-flight facility at GSI [33], which is imminent and planned to be operational within the next 5 years. The upgrade will include an increase of between 2 and 3 orders of magnitude in the intensity of the 1 - 2 GeV/u primary beams, resulting in an increase of up to 4 orders of magnitude in the secondary radioactive beam intensity. A much improved fragment separator will deliver beams to storage rings at high energy and to cooler rings capable of cooling and decelerating beams, along with an array of cutting-edge experiments.

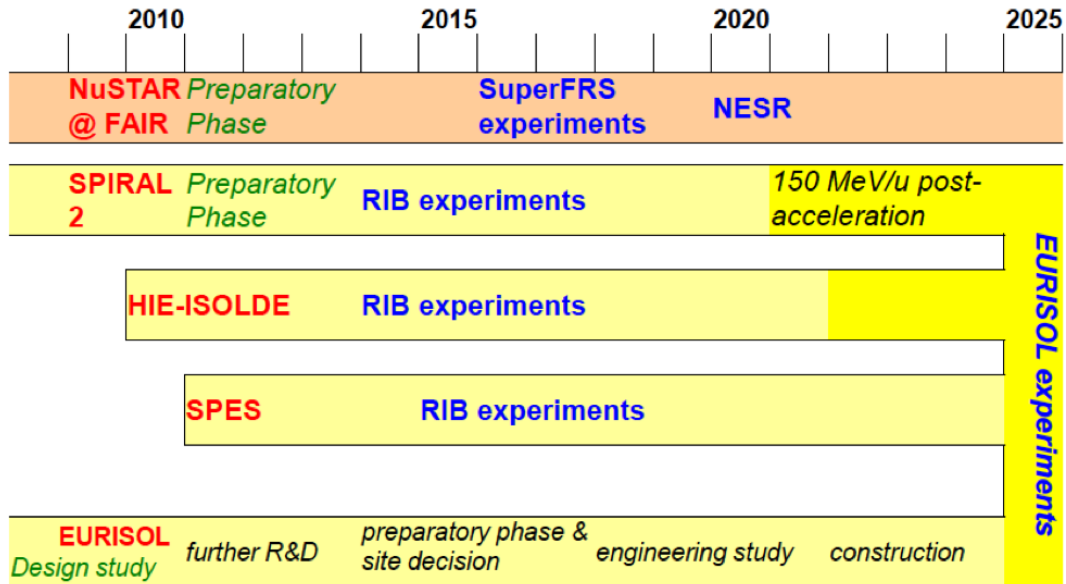


Figure 1.4: Summary of the NuPECC Long Range Plan 2010 [29]. Figure courtesy of Y. Kadi and Y. Blumenfeld.

After FAIR, the EURISOL project is given the next highest priority and envisaged as a state-of-the-art ISOL facility to be operational within the next 15 years, employing a 1 GeV proton driver capable of simultaneously sharing its 5 MW beam power with multiple production targets. A design study was successfully completed in 2009 [34] and a

roadmap created with the aim of overcoming the technical challenges needed to realise such a facility [29]. Inside the roadmap ‘intermediate generation’ facilities are seen as necessary stepping stones in achieving the technical expertise in target, ion source, beam manipulation, charge breeding, accelerator and instrumentation technologies, as well as safety and radiation protection [35]. Alongside other European ‘intermediate generation’ projects, e.g. SPES [36] and SPIRAL2 [37], which are currently under construction and are to become fully operational in the coming years, the HIE-ISOLDE project takes its place as an important step towards the realisation of EURISOL, as shown in the roadmap of Figure 1.4. The HIE-ISOLDE project will act as a test bed for targets and beam manipulation, including cooling and charge breeding, along with the post-accelerator technology and its accompanying instrumentation and diagnostics.

## 1.5 Thesis Overview

The ISOLDE facility and the Radioactive ion beam EXperiment (REX) are described in the next chapter before the HIE-ISOLDE upgrade is set out in detail. Linear resonance accelerators are introduced in Chapter 3 and the relevant formalisms that underlie their beam dynamics design are outlined, including a summary of the effects that degrade the beam quality, which form the focus of this thesis. An investigation of the REX linac is summarised in Chapter 4; this brings together rf and beam-based measurements with the results of simulations that were made to understand the working points of the machine and to identify sources of emittance growth, readying REX for its role as an injector to the superconducting HIE linac. For example, the energy gain as a function of rf phase of the 20-gap Interdigital H-mode Structure (IHS) was simulated using the measured accelerating field profile and compared to beam measurements. Chapter 5 focuses on the longitudinal emittance measurements made either side of the IHS in order to assess its performance. For the measurements using a 7-gap split-ring resonator an analytic formalism was developed and published [38] to describe multi-gap buncher cavities used in emittance measurements where the buncher cannot be modelled as a thin lens. In Chapter 6 the design studies of the superconducting HIE-ISOLDE linac, which were published in [39], are documented. For example, an analytic second-order formalism is investigated

to calculate the energy change in a cavity when the velocity change of the beam inside it is significant; the formalism proved particularly useful at low velocity when calculating the energy range of the linac during deceleration. Chapter 6 also includes the specification of the solenoid focusing system, the orbit correctors, the misalignment tolerances and the level to which the rf jitter must be controlled to minimise the emittance degradation and beam losses, all of which contributed to the design of the cryomodule and other linac components currently being prototyped. The chapter is concluded with the specification of the beam parameters after tracking the realistic particle phase space distribution from the exit of the RFQ through the linac in the presence of errors. Before the thesis is concluded in Chapter 8, the development and characterisation of a solid-state longitudinal diagnostic system, which will be eventually used to automatically tune the large number of cavities accompanying the upgrade, is summarised in Chapter 7 and published in [40].

RADIOACTIVE ION BEAMS AT CERN

CERN [41] is an intergovernmental organisation dedicated to scientific research into fundamental physics using the world’s largest accelerator complex that involves some of the most advanced particle accelerator and detector technologies. Home of its champion the Large Hadron Collider (LHC) [42], CERN sits on the Franco-Swiss border in Geneva and is a European joint-venture that was founded in 1954 and today involves 20 member states and over 10,000 users. The ISOLDE [5] facility, shown in the context of the vast CERN

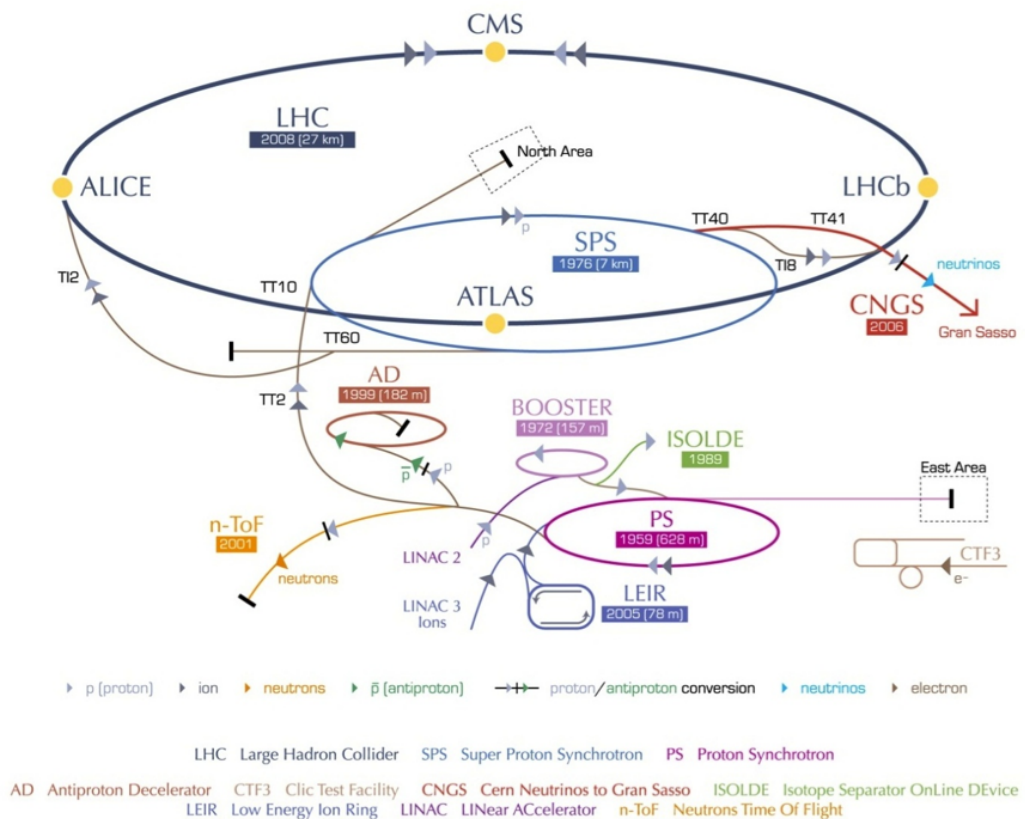


Figure 2.1: A schematic of the CERN accelerator complex. ISOLDE is shown in green. For more information see [41].

accelerator complex in Figure 2.1, is a long-running radioactive nuclear beam facility that has been operating at CERN in one form or another since 1967.

## 2.1 ISOLDE

The ISOLDE facility is shown schematically in Figure 2.2. Following the completion of the Proton Synchrotron Booster (PSB) ISOLDE upgrade in 1992, radioactive beams are produced by impinging high intensity bunches of protons accelerated in the PSB up to between 1 - 1.4 GeV onto thick, heated ISOL targets located at either of two target stations: the General Purpose Separator (GPS) or High Resolution Separator (HRS) targets. The facility has a long history of target and ion source development, which can be found reviewed in [43]. ISOLDE is the heaviest user of the PSB and is able to take beam from the CERN accelerator complex in a parasitic mode whilst the Proton Synchrotron (PS) is ramping and accelerating beams destined for the numerous other experimental areas shown in Figure 2.1. Nominally, ISOLDE takes about half of all PSB batches in any

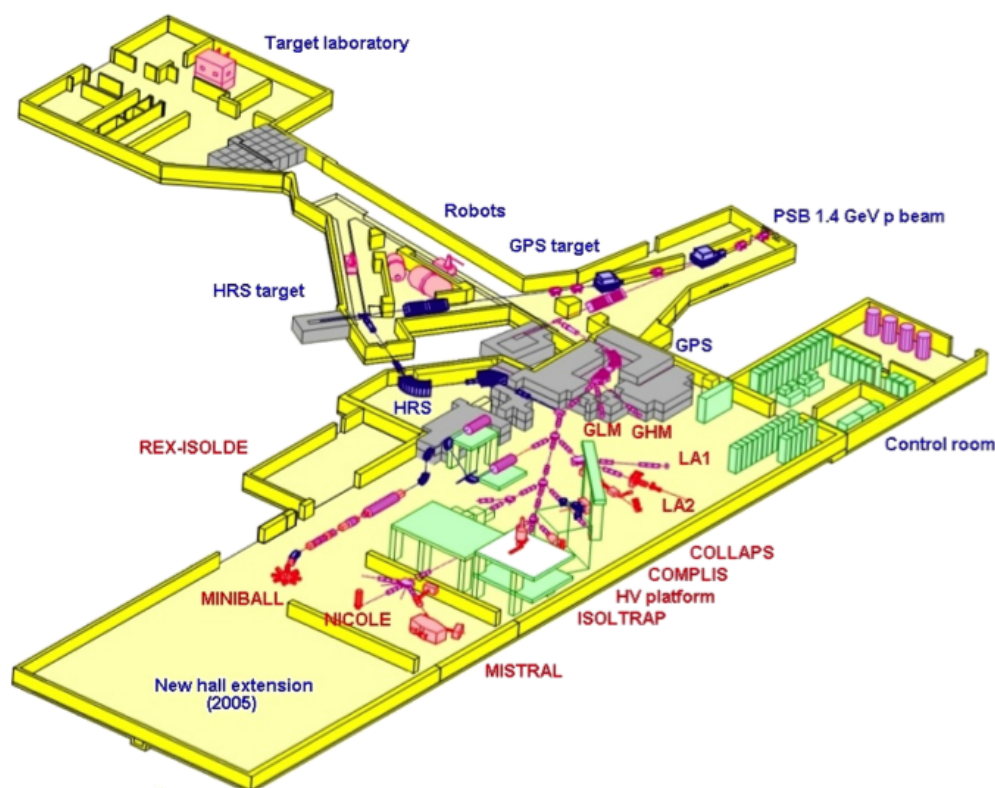


Figure 2.2: Layout of the ISOLDE facility, including the extension to the experimental hall for the HIE-ISOLDE project.

given supercycle,<sup>1</sup> which consists of about a dozen or so PSB cycles and lasts about 15 s. The PSB repetition period is 1.2 s, providing an average proton current of 1.92  $\mu\text{A}$  and an average beam power of a little under 3 kW at the ISOLDE target stations.

After diffusion and effusion out of the target, the mixture of radionuclides is ionised to form singly-charged ions, which are accelerated through an electrostatic potential of either 30 or 60 kV and separated by the GPS ( $\Delta M/M = 1/2400$ ) or HRS ( $\Delta M/M = 1/11000$ ) magnetic mass spectrometers. The development of a laser ion source has been very successful at ISOLDE, which is reflected in its use for about half of the available beam time. The Resonance Ionisation Laser Ion Source (RILIS) [44] can selectively ionise isotopes of radioactive elements efficiently and quickly, even allowing isomeric beams to be isolated. The selected ions are then transported to experiments at either low energy, where they can be trapped at energies as low as  $10^{-6}$  eV, or transported to REX where they can be accelerated up to 3 MeV/ $u$ . The facility has helped to make important contributions to the fields of nuclear structure and astrophysics, as well as atomic physics, solid-state physics, the life sciences and fundamental physics. An overview of the modern experimental programme can be found in the laboratory portrait [45].

## 2.2 REX

The REX experiment [46] was constructed at ISOLDE to test a unique charge breeding concept coupling a Penning trap and an Electron Beam Ion Source (EBIS) to boost the charge-state of radioactive ions before acceleration in a compact normal conducting linac. A three-dimensional realisation of the REX post-accelerator is shown in Figure 2.3 with pictures of the charge breeder and the open accelerating cavities with their drift-tubes exposed. The beta-NMR and Miniball detectors are shown on their respective beam lines after the switchyard magnet. An overview of the design and commissioning of the REX-ISOLDE facility can be found in [47], along with technical details that will also be discussed in more depth in Chapter 4.

---

<sup>1</sup>CERN's heart beats with the PSB every 1.2 s. A periodic sequence of PSB cycles taking protons to each experimental area is termed a supercycle and can last tens of seconds, e.g. protons could be sent to the PS and then the SPS for delivery at CNGS for neutrino production, sent directly to ISOLDE, accelerated in the PS and sent for antiproton production and storage in the AD or sent up the complex to the LHC.

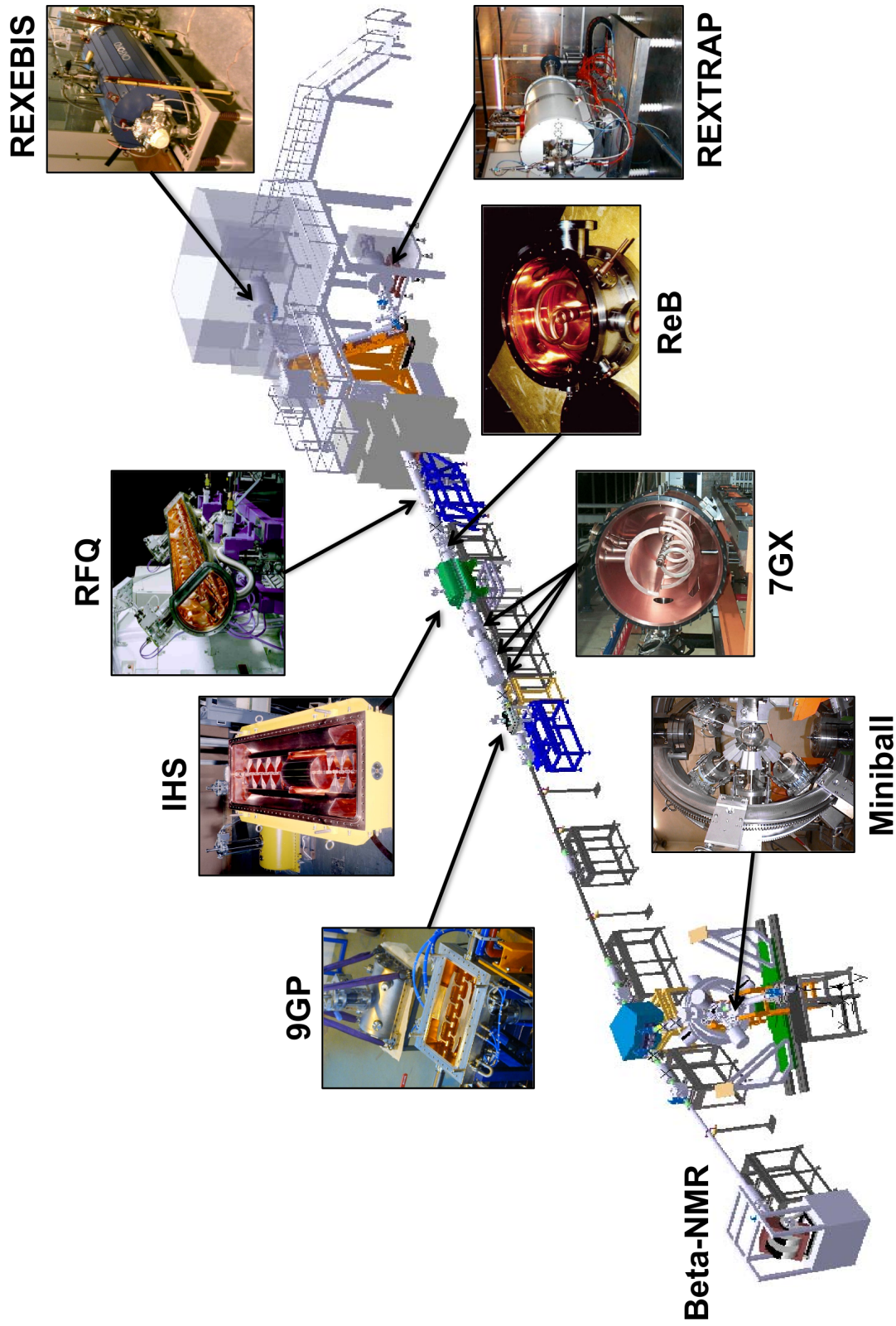


Figure 2.3: The REX post-accelerator, delivering beams up to  $3 \text{ MeV}/u$ .

### 2.2.1 Charge-breeder

The tandem Penning trap and EBIS charge breeding system is shown schematically in Figure 2.4. The Penning trap cools the emittance of the quasi-continuous singly-charged ISOLDE beam, see the time structure in Appendix A, from emittances typically greater than  $30 \pi \text{ mm mrad}$  to below  $10 \pi \text{ mm mrad}$ , so that it can be efficiently trapped and ionised in the narrow acceptance of the electron beam of the EBIS. A mass separator [48] based on the Nier spectrometer [49] ( $\Delta M/M = 1/150$ ) separates the beam extracted from the EBIS, removing ionised residual gas impurities and selecting the mass-to-charge state of the radioactive beam to be accelerated.

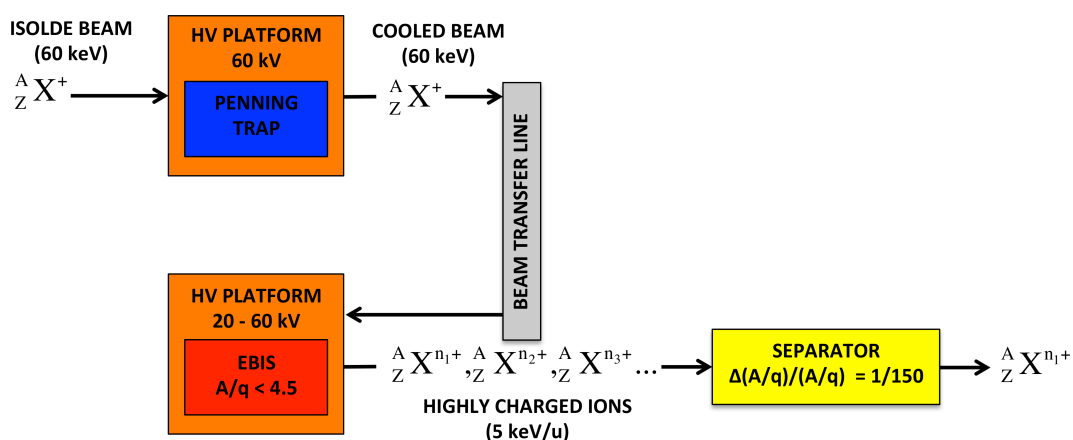


Figure 2.4: Schematic layout of the charge breeding components at REX.

The REXTRAP [51, 52] accumulates, bunches and cools the beam by interacting it with an inert buffer gas of neon or argon whilst it is trapped longitudinally in an electrostatic field applied on drift-tubes and transversely by a magnetic field produced by a superconducting solenoid. In addition, transverse rf electric fields are applied to damp the magnetron motion that becomes radially unstable under buffer gas collisions inside the trap, leading to cooling times of  $\lesssim 20 \text{ ms}$ .

The REXEBIS [53, 54] uses a strongly focused electron beam compressed in the magnetic field of a superconducting solenoid to successively ionise trapped radioactive nuclides to the desired charge-state. The singly-charged radioactive ions are injected and trapped in the electron beam using a longitudinal electrostatic potential created on drift-tubes and transversely by the negative space-charge of the electron beam itself. Once the desired charge-state has been bred the drift-tube voltages are adjusted and the beam ex-

tracted with a voltage that is scaled with the  $A/q$  to match the velocity acceptance of the RFQ. The normalised transverse beam emittance is typically less than  $0.3 \pi$  mm mrad. The system was designed with light ions of  $A < 50$  in mind and is capable of charge-boosting all singly-charged ions in this mass range up to  $A/q < 4.5$  within 20 ms, which corresponds to the mass-to-charge state acceptance of the linac. The ion source has been used as a test bed for different methods of beam purification and breeding schemes. Space-charge effects in the Penning trap limit the ion throughput of the system to a few  $10^8$  ions per pulse at 50 Hz. Although in principle the ion source can deliver over 1 nA of radioactive beam, the intensities are typically much lower; normally the ion source can achieve efficiencies of between 5 - 12 %, breeding ions as heavy as  $^{238}\text{U}^{52+}$  over times extending to as long as 500 ms [55].

### 2.2.2 Linac

The linac was originally built to accelerate beams with  $A/q < 4.5$  up to 2.2 MeV/u, allowing the Coulomb barrier to be reached for isotopes with  $A < 50$ . The addition of a 9-gap IH cavity in 2004 pushed the energy range up to 3.0 MeV/u for  $A/q < 3.5$  and extended the reach of the Coulomb barrier to  $A < 85$  [56]. Today the REX linac consists of the following normal conducting rf structures operating at 101.28 or 202.56 MHz, congruent with Linac2 and Linac3 structures at CERN:

- **Radiofrequency Quadrupole (RFQ)** [57] - a four-rod- $\lambda/2$  design [58], similar to those installed at the GSI HLI [59] and the MPIK HCI [60], optimised for  $A/q < 4.5$  and used to efficiently bunch and accelerate beams from the ion source energy of 5 keV/u to 300 keV/u.
- **Rebuncher (ReB)** [61] - a three-gap split-ring cavity used to longitudinally match the beam from the RFQ into the succeeding IH structure.
- **20-gap IH Structure (IHS)** [62, 63] - a compact and highly efficient  $\text{TE}_{11(0)}$ -type<sup>1</sup> [64] structure employing Combined Zero-Degree Structure (KONUS) [65, 66] beam dynamics that boosts the beam up to 1.2 MeV/u; two KONUS drift-tube

<sup>1</sup>The brackets on the third index imply that the variation of the longitudinal field distribution of the actual  $\text{TE}_{111}$  mode has been significantly flattened to resemble an  $\text{TE}_{110}$ -like mode.

sections with 8 and 9 gaps are separated by a grounded quadrupole triplet magnet and a 3-gap rebunching section housed inside the structure.

- **7-gap Split-ring Resonators (7GX: 7G1, 7G2 and 7G3)** [67] - based on the design of cavities made for the HCI at MPIK [68], three split-ring cavities with constant geometric velocities of 5.4, 6.0 and 6.6 % are used to provide variable beam energy up to 2.2 MeV/ $u$ .
- **9-gap IH Structure (9GP)** [69] - a 7-gap IH structure designed for the MAFF project [70] was converted to a 9-gap structure with a modified drift-tube structure.

The main parameters of the rf structures are summarised in Table 2.1 and defined later in Chapter 3.

Table 2.1: Parameters of the REX linac structures

Parameter <sup>a</sup>	RFQ	ReB	IHS	7GX	9GP
$f$ [MHz]	101.28	101.28	101.28	101.28	202.56
No. of gaps/cells	232	3	20	7	9
$\beta_{\text{in}} \rightarrow \beta_{\text{out}}$ [%]	0.3 $\rightarrow$ 2.5	2.5 $\rightarrow$ 2.5	2.5 $\rightarrow$ 5.1	5.1 $\rightarrow$ 6.9 <sup>b</sup>	6.9 $\rightarrow$ 7.8 <sup>b</sup>
$W_{\text{in}} \rightarrow W_{\text{out}}$ [MeV/ $u$ ]	0.005 $\rightarrow$ 0.3	0.3 $\rightarrow$ 0.3	0.3 $\rightarrow$ 1.2	1.2 $\rightarrow$ 2.2 <sup>b</sup>	2.2 $\rightarrow$ 2.8 <sup>b</sup>
$E_{\text{acc}}$ [MV/m]	0.44	0.36	2.7	$\sim$ 2.5	5.2
$L_a$ [m]	3	0.2	1.5	$\sim$ 0.60	0.52
$Z_{\text{eff}} = Z_0 T^2$ [M $\Omega$ /m] <sup>c</sup>	-	20	225	$\sim$ 55	165
$R_p'$ [k $\Omega$ m] <sup>c</sup>	146	-	-	-	-
$Q$ (unloaded)	4050	3700	13000	$\sim$ 5250	10100
$P$ [kW] <sup>c</sup>	36.3	1.6	50	$\sim$ 75	90
$A/q$ limits	$\lesssim$ 5.5	$\gtrsim$ 2.5	$\lesssim$ 4.5	$\gtrsim$ 2.5	$\gtrsim$ 2.5

<sup>a</sup> Cavity figures of merit are defined in Chapter 3.2.3.

<sup>b</sup> Intermediate energies at entry to 7G2 and 7G3 are 1.55 and 1.88 MeV/ $u$ , respectively.

<sup>c</sup>  $A/q = 4.5$ .

The difficulty in maintaining the rf stability at low fields restricts the  $A/q$  acceptance of the linac to  $\gtrsim$  2.5 and the internal quadrupole triplet of the IHS limits the upper end of the acceptance to  $\lesssim$  4.5. The duty cycle of the linac is variable up to 10 % and was designed to match the time structure of the ion source operating with nuclides in the mass range  $A < 50$ , corresponding to rf pulses no longer than 1 ms at a maximum repetition rate of 100 Hz; the time structure of the REX-ISOLDE beam is shown in Appendix A. Space-charge effects were not a design consideration for the linac because of the low intensity of beams at ISOLDE; the radioactive beams are typically regarded as high intensity if the

average beam current is  $\gtrsim 50$  pA, at which level there are approximately  $10^5 - 10^6$  ions per pulse and the instantaneous current is only of the order of 1 nA. In the rare case of operating at the throughput limit of the ion source one can start to imagine instantaneous beam currents in the order of 1  $\mu$ A, but even in this case space-charge effects can be neglected [71]. The present status and latest developments at REX-ISOLDE can be found in [72].

### 2.2.3 Experiments

The versatile charge breeding system at REX has allowed the post-accelerator access to the entire range of radionuclides available at ISOLDE and this is reflected in the diverse list of experiments that have been approved. After almost 10 years of operation only about 10 % of the available isotopes have actually been post-accelerated for Coulomb excitation, few-nucleon transfer and fusion evaporation reactions at a few MeV/ $u$ , highlighting the large number of experimental possibilities that remain as the facility is upgraded. A very brief overview of the experimental programme is given below.

Some of the first beams accelerated by REX were  $^9\text{Li}$  nuclei, used to induce the neutron transfer reaction  $^9\text{Li}(d,p)^{10}\text{Li}$  on deuterated polyethylene targets at 2.36 MeV/ $u$  from which, amongst other things, information about the halo nucleus  $^{11}\text{Li}$  could be derived [73]. Other beams have tested the nuclear shell model and its evolution away from the ‘valley of stability’, in particular at the ‘island of inversion’ around  $^{32}\text{Mg}$  ( $N = 20$ ), the neutron-rich nickel region ( $Z = 28$ ) and both the neutron-deficient and neutron-rich tin regions ( $Z = 50$ ). After the discovery of three distinct coexisting isomeric states in  $^{70}\text{Cu}$ , which were isolated using RILIS at ISOLDE [74], REX was able to accelerate pure ( $\sim 90$  %) isomeric beams of these nuclei, along with two other known isomeric states of  $^{68}\text{Cu}$ , to probe their structure via Coulomb excitation. Shape coexistence that had previously been discovered at ISOLDE in neutron-deficient mercury isotopes [75] is also being probed through Coulomb excitation, which constitutes the post-acceleration of very heavy ( $A \sim 200$ ) radionuclides [76]. A small number of astrophysics-related experiments have also been performed.

The Coulex experiments rely heavily on the detection of  $\gamma$ -rays in order to identify the

excited states that are populated during the Coulomb interaction between the target and projectile. In addition, the detection of the outgoing energy and direction of the projectile and/or the target nuclei is crucial for reconstructing the kinematics of the interaction. For this purpose the Miniball detector was constructed, consisting of an array of 24 cryogenically cooled germanium  $\gamma$ -ray detectors to cover as much as 60 % of the  $4\pi$  solid angle around the target and detect  $\gamma$ -rays that are emitted in all directions. The Miniball array is shown in position around the vacuum chamber housing the target in Figure 2.5. The velocity of the beam, some 8 % of the speed of light at 3 MeV/ $u$ , demands that the  $\gamma$ -spectra are accurately Doppler-corrected, requiring pulse-shape analysis of the segmented germanium detectors and accurate detection of the forward moving projectile and/or target nuclei using a CD-type Double-Sided Silicon Strip Detector (DSSSD) detector, as shown in Figure 2.6.

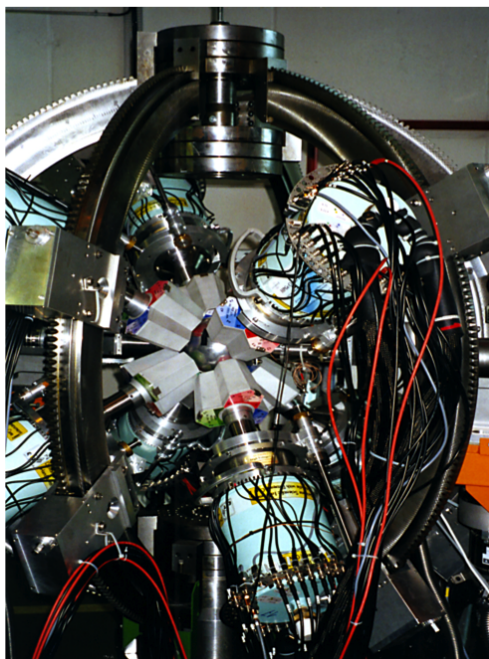


Figure 2.5: The Miniball array closed around the vacuum vessel enclosing the target.

For few-nucleon transfer reactions an extra detection system called T-REX has been used in addition to the Miniball array that can measure  $\gamma$ -rays in coincidence with charged particles, as shown in Figure 2.7. It consists of a small barrel that can fit inside the Miniball array, containing at both ends the above-mentioned CD-type detector and 8 planar DSSSD detectors that cover the sides of the barrel. The detectors work like  $\Delta W - W$  telescopes and have two layers of silicon from which the particle type can be uniquely

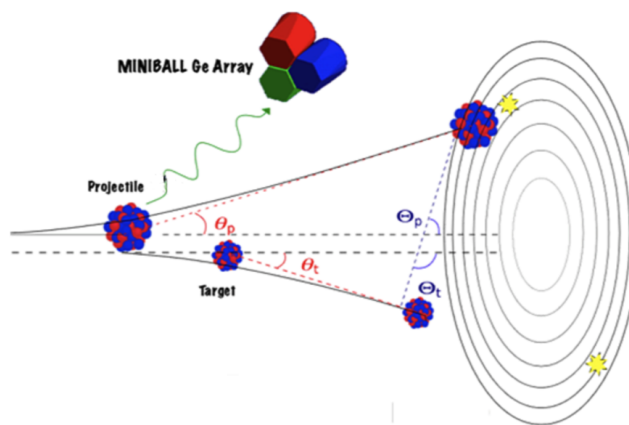


Figure 2.6: Schematic of a Coulomb interaction at REX with the forward moving projectile and target particles shown hitting the CD detector.

identified; the energy deposited on passing through the first thin layer gives a characteristic signal when combined with the total energy deposited in the second thick layer. The T-REX detector played an important role in understanding the ‘island of inversion’ observed near  $^{32}\text{Mg}$ , where an energetically favoured ‘rugby ball’-shaped deformed state coexists with a spherical state that would otherwise be expected to lie in the ground-state. A two-neutron transfer reaction of a  $^{30}\text{Mg}$  beam delivered from ISOLDE on a radioactive tritium target at 1.83 MeV/u enabled the discovery of the excited spherical state by measuring the energies and angular distribution of the emitted protons [77], which differs significantly from theoretical predictions. A comprehensive review of the REX-ISOLDE facility and its experimental programme can be found in [25].

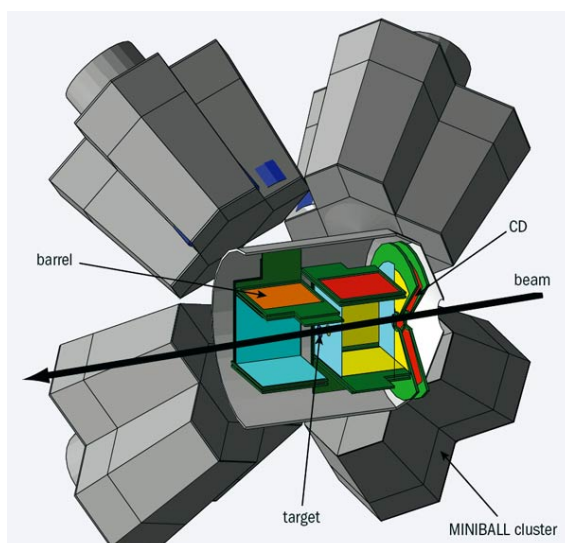


Figure 2.7: Schematic of the T-REX detector inside the Miniball array. Figure courtesy of K. Wimmer.

## 2.3 HIE-ISOLDE

The HIE-ISOLDE project [78] represents a major upgrade of the ISOLDE facility with a mandate to significantly improve the quality and increase the intensity and energy of radioactive nuclear beams. The project will expand the nuclear physics programme at ISOLDE and was approved as an official project by CERN in the autumn of 2009.

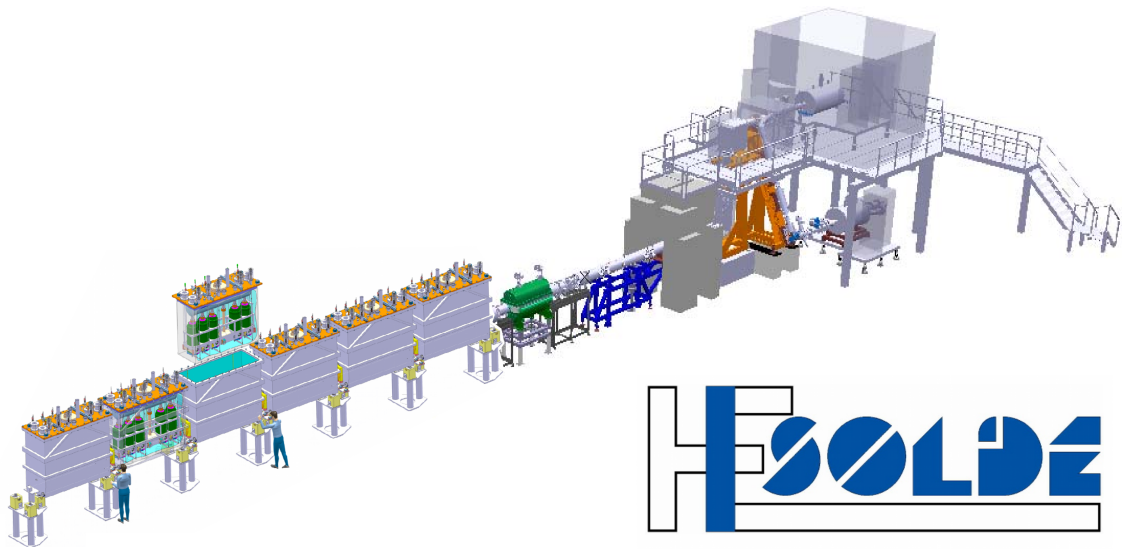


Figure 2.8: The HIE-ISOLDE linac. The installation of six cryomodules will provide almost 40 MV of accelerating potential after the IHS, delivering beams of over 10 MeV/u. The top-loading cryomodule is shown and the superconducting quarter-wave resonators and solenoids are exposed. Figure courtesy of S. Maridor.

Out of the 34 HIE-ISOLDE Letters of Intent that were submitted and accepted, from 284 participants at 76 laboratories in 22 countries, 88 % propose to make use of the increase in energy and intensity, whereas only 12 % propose to exclusively use the increase in intensity [79]; this places the upgrade of the post-accelerator, shown in Figure 2.8, at the forefront of the project. The scientific opportunities offered by the HIE upgrade are outlined at length in [80] and the technological options for the upgrade can be found outlined in [81]. The linac upgrade, which is discussed in more detail below, will replace most of the existing REX post-accelerator and is based on a compact superconducting linac made up of quarter-wave resonators and solenoids housed in six cryomodules.

### 2.3.1 Intensity

Aside from longer term plans to upgrade the PSB [82], the beam intensity of the CERN accelerator complex is to be increased in accordance with the LHC luminosity upgrade and the replacement of Linac2 with Linac4 [83]. The upgrade will increase the injection energy of the PSB from 50 MeV to 160 MeV and reduce the space-charge bottleneck in the PSB so that the beam intensity can be increased by a factor of 2.<sup>1</sup> Along with H<sup>-</sup>

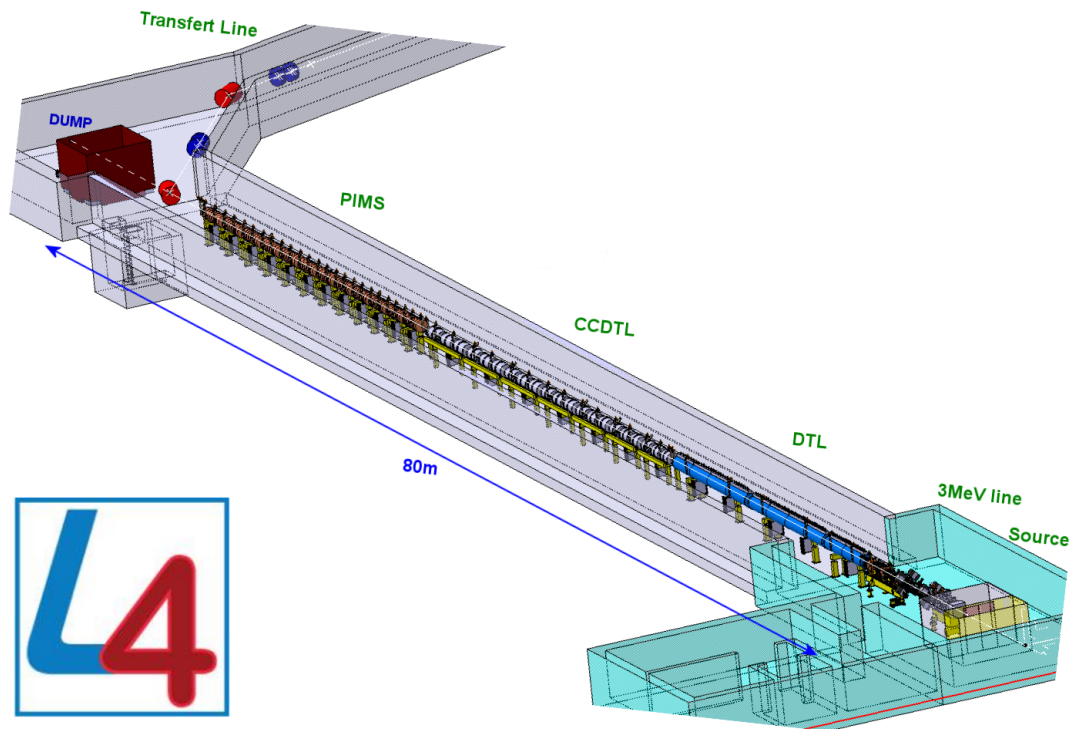


Figure 2.9: The Linac4 injector at CERN and its transfer line to the PSB. Figure courtesy of M. Vretenar.

charge-exchange injection and an increased cycling rate of the PSB, a factor of between 2 - 3 increase in the average driver beam power can be realistically expected at the ISOLDE target stations. Radiation protection studies have been launched to understand the effects of the increase in proton intensity at the target stations.

The radioactive beam intensities will benefit from the increase in the driver beam intensity and planned developments in target technology are being pursued in step with the goals of EURISOL to improve yields. Various upgrades to the charge breeder are being investigated including the test of a new ECR ion source [84], and an RFQ cooler named

<sup>1</sup>The space-charge induced tune spread in a synchrotron scales with the number of protons per bunch and  $1/\beta\gamma^2$ , hence the beam intensity can be doubled without any significant effect if the injection energy of the PSB is increased from 50 to 160 MeV because  $(\beta\gamma^2)_{50 \text{ MeV}}/(\beta\gamma^2)_{160 \text{ MeV}} \approx 1/2$ .

ISCOOL [85, 86] is already on the HRS beam line and capable of injecting cooled beams directly into the EBIS, overcoming the present space-charge bottleneck in the Penning trap.

### 2.3.2 Quality

The HRS will be significantly upgraded and with ISCOOL its mass resolution will be much improved. Other methods of beam purification are being investigated for the low energy section of REX [84] and research and development activities with RILIS are ongoing.

### 2.3.3 Energy

This thesis will focus on the energy upgrade that will come from the installation of 40 MV of accelerating potential in the form of a new superconducting linear post-accelerator. The installation of the upgrade will be staged, as shown in Figure 2.10, which allows for the best handling of the available resources and man-power whilst delivering the ISOLDE users with increased beam energies without delay.

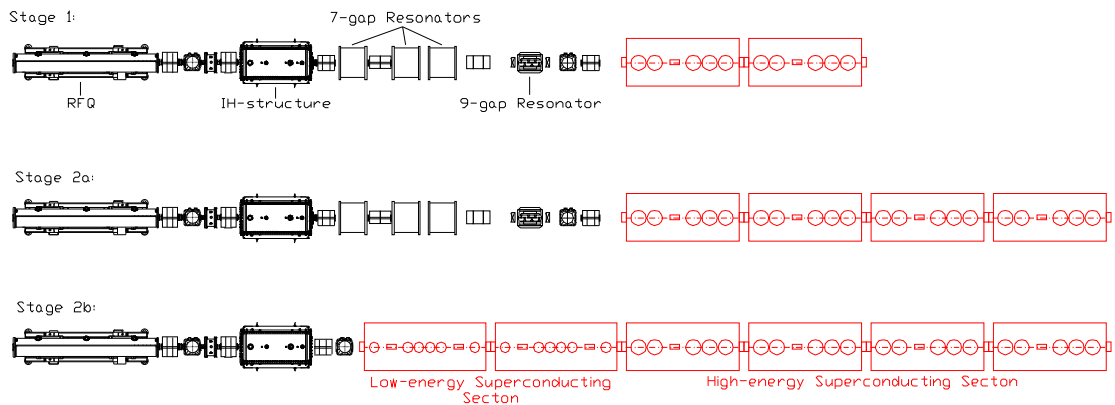


Figure 2.10: Installation stages of the superconducting linac.

In the first stage, cryomodules will simply be added to the existing REX machine to provide energies of up to at least 5.5 MeV/u and allow Coulomb excitation studies to be carried out across the entire range of radionuclides available at ISOLDE. The second stage of the upgrade will continue in this manner until all four high-energy type cryomodules have been added to provide energies of up to at least 9.3 MeV/u, which will make avail-

able a wider range of reactions aside from Coulomb excitation. Finally, all the existing REX accelerating structures after the IHS will be replaced with two low-energy type cryomodules to improve the beam quality and ensure that the energy is continuously variable between 0.45 and 10 MeV/ $u$ .

## 2.4 HIE Linac (SC-REX Linac)

The design objectives of the linac upgrade can be summarised as follows:

- Accelerate all nuclei up to at least 10 MeV/ $u$ .
- Provide full flexibility in the beam energy.
- Preserve beam quality.
- Maintain high transmission for all beams.

The flexibility that is demanded by users wishing to post-accelerate the entire range of radionuclides available at ISOLDE up to and beyond the Coulomb barrier is reflected in the choice of a superconducting linac. The upgrade, based on short and independently tuneable accelerating cavities, is capable of providing continuous flexibility in energy whilst maintaining high beam quality and transmission.

### 2.4.1 Beam Design Parameters

The wide-range of experimental techniques and instrumentation proposed in the accepted Letters of Intent submitted for research at HIE-ISOLDE have resulted in differing beam specifications. Although the priority of each request is still to be finalised, the specification of the beam parameters is broadly summarised in Table 2.2. Apart from the specification of increased energy with variability the user community would like to see a reduction in beam halo and spot size at the experimental targets. A beam diameter of approximately 6 mm ( $\sim$  3 mm FWHM) is currently achievable at the target position in Miniball at an energy of 3 MeV/ $u$  [25]. The beam diameter will reduce on installation of the upgrade because of the adiabatic damping associated with the increasing beam energy, however the

Table 2.2: Requested beam characteristics at HIE-ISOLDE

Beam Parameter	Description or Value
Energy	continuous from $< 0.7$ to at least $10 \text{ MeV}/u$
Beam spot diameter	$< 1 - 3 \text{ mm FWHM}$
Beam divergence	$< 1 - 3 \text{ mrad FWHM}$
Micro-bunch structure <sup>a</sup>	no requirement of micro-bunching to bunched at $< 1 \text{ ns FWHM}$ with $\sim 100 \text{ ns}$ bunch spacing
Macro-bunch structure <sup>a</sup>	longer pulse lengths or cw operation
Energy spread	$< 0.1 \%$
Absolute energy resolution <sup>b</sup>	no specific details given

<sup>a</sup> The time structure of the beam is determined by the charge breeder and the REX front-end, see Appendix A.

<sup>b</sup> No system currently exists to measure the absolute beam energy; time-of-flight systems are being discussed.

ultimate beam size will be limited by the transverse emittance of the ion source and the emittance growth in the REX front-end. The time structure of the beam is also limited by the REX front-end and any modifications made to achieve longer beam pulse lengths, cw beams or even beams with an increased bunch spacing will require significant upgrades of the charge breeder or the installation of additional rf cavities, namely a multi-harmonic buncher upstream of the RFQ and a chopper downstream.

## 2.4.2 Linac Design Parameters

The specification of the basic design parameters for the upgrade are outlined in Table 2.3. As mentioned above, although space-charge effects can occasionally become

Table 2.3: Basic design parameters for the HIE linac

Design Parameter	Description or Value
Particle type	radionuclides with $A \lesssim 250$
Mass-to-charge acceptance ( $A/q$ )	$2.5 \lesssim A/q \lesssim 4.5$
Fundamental beam frequency <sup>a</sup> ( $f$ )	$101.28 \text{ MHz}$
Output beam kinetic energy ( $W$ )	variable up to at least $10 \text{ MeV}/u$
Effective accelerating voltage ( $V_{\text{eff}}$ )	$39.6 \text{ MV}$
Length available for linac	$\sim 20 \text{ m}$
Real-estate gradient	$\sim 2 \text{ MV/m}$
Rf duty cycle	at least $10 \%$
Transmission	$> 95 \%$

<sup>a</sup> A multi-harmonic buncher and beam chopper are being considered for HIE-ISOLDE to reduce the beam frequency by a factor of 10.

a performance-limiting factor at very low energies in the charge breeder [55], the beam intensities are low enough that space-charge effects can be safely neglected in the design of the linac upgrade. The limited space available in the ISOLDE experimental hall presents a real-estate gradient target of 2 MV/m, which would be challenging for a normal conducting machine providing both continuous energy variability and good beam quality.

### 2.4.3 Design Choices

A review of the superconducting and normal conducting upgrade options was undertaken by an International Advisory Board (IAB) following preliminary studies at CERN, with the board unanimously supporting the pursuit of the superconducting option. The main trade-offs between the application of the two technologies highlighted by the IAB are summarised in [87]. The increased cost and demand on resources of the superconducting option was weighed against the superior beam quality it could provide, its ability to tailor the beam energy precisely to the experiment and its future viability with ion source and injector upgrades in terms of potential cw operation. The space available in the experimental hall is also critical and it was concluded that even with further optimisation of the normal conducting designs the superconducting option would be shorter. In addition, the choice to pursue niobium sputter-coated copper cavities was viewed positively in light of the experience at CERN of sputtering accelerating cavities, albeit in a different velocity regime and geometry.

#### 2.4.3.1 Accelerating Structures

Superconducting quarter-wave resonators were identified early on in the design process as a reliable and robust structure able to provide the stable high gradients and the velocity acceptance demanded by the beam specification at HIE-ISOLDE. Superconducting quarter-wave cavities are used in many facilities around the world for applications in heavy ion beam acceleration, e.g. ANL, LNL-INFN and TRIUMF [88].

In order to boost the beam to over 10 MeV/ $u$  a total of 32 cavities are required with two different families of cavity, with geometric velocities ( $\beta_g$ ) of 6.3 and 10.3 %, of which there are 12 and 20 cavities respectively, as shown in Figure 2.12. The total effective

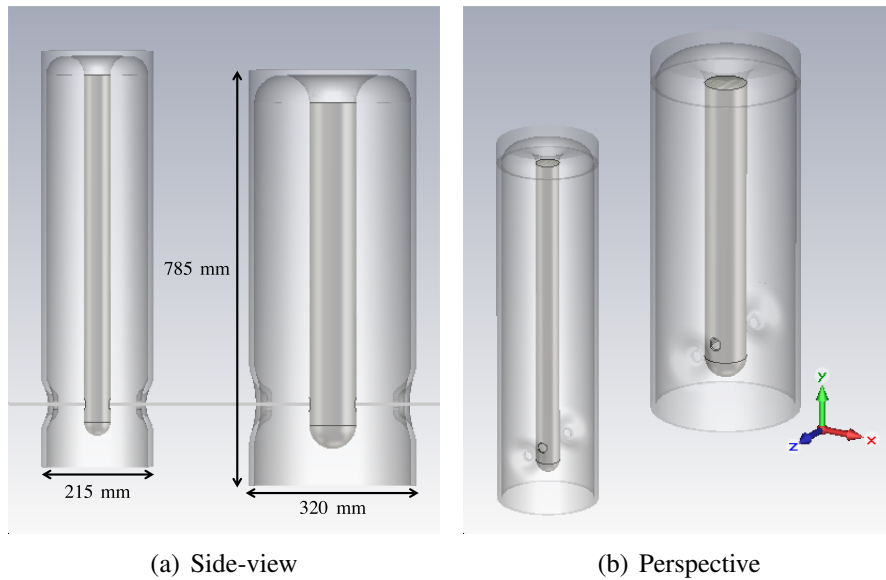


Figure 2.11: The low and high- $\beta$  quarter-wave cavity geometries, realised in CST-MWS [89].

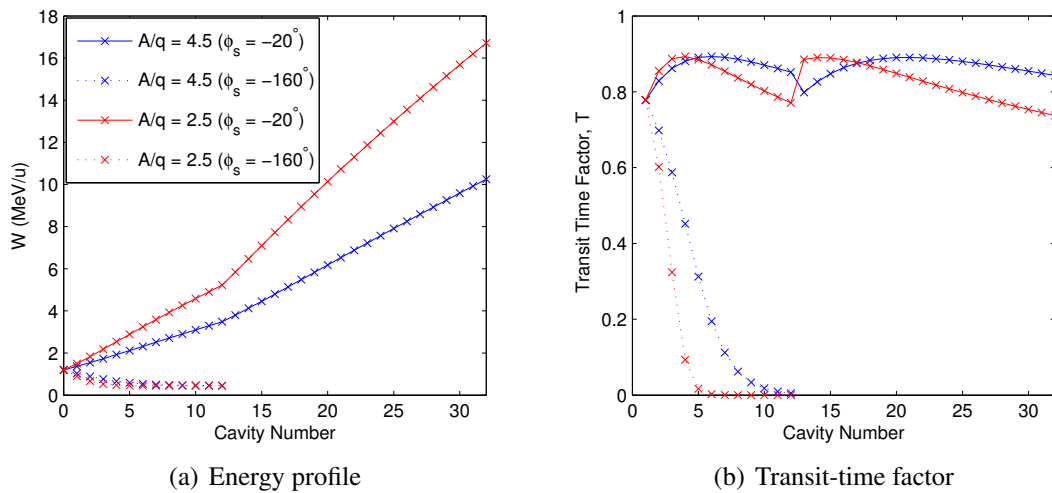
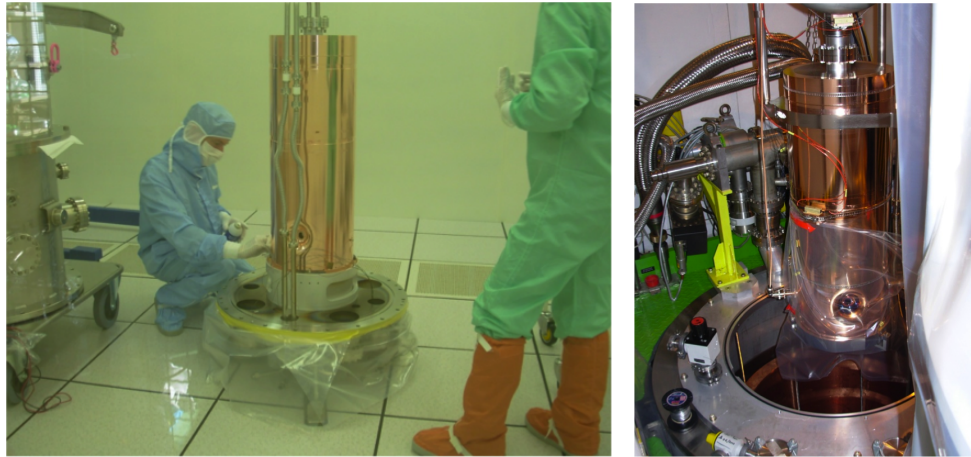


Figure 2.12: The energy profile and transit-time factors along the HIE linac with it phased to accelerate and decelerate.

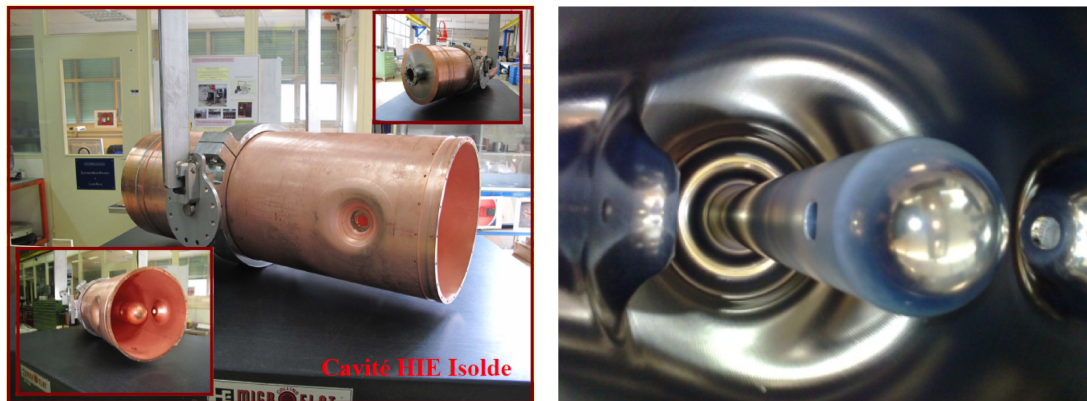
accelerating potential of 39.6 MV can be achieved by assuming a gradient of 6 MV/m and an average synchronous phase of  $-20^\circ$ . The geometric velocities were chosen such that the total number of cavities was minimised and the transition energy between the two types of cavity made as quickly as practically possible to benefit from the increased accelerating potential per cavity in the high- $\beta$  cavity, corresponding to 1.8 MV as opposed to 1.17 MV in the low- $\beta$  cavity. The flexibility of the output beam energy, which can be varied by switching off cavities, is also shown in Figure 2.12 for the upper and lower bounds of the  $A/q$  acceptance. For the low end of the  $A/q$  acceptance beams can be

accelerated to energies as high as 17 MeV/u. The geometric velocity of the low- $\beta$  cavity permits deceleration down to approximately 0.45 MeV/u, limited by the degradation to the beam quality on decelerating through the zero of the first-order transit time factor. The transit-time factor remains greater than 0.8 in all but the first cavities of each section of the linac for beams with the  $A/q = 4.5$ .



(a) Clean room assembly of the cavity in the sputtering chamber. (b) Cavity lowered into the test cryostat at SM18.

Figure 2.13: The preparation of the first prototype high- $\beta$  cavity for rf testing. Figures courtesy of S. Calatroni and M. Therasse.



(a) Undergoing metrology analysis before sputtering. (b) The internal cavity surface after niobium sputtering.

Figure 2.14: The first prototype high- $\beta$  cavity before and after sputtering. Figures courtesy of O. Capatina and S. Calatroni.

An intensive research and development activity has been set in motion at CERN in the last few years, which has culminated in the construction of the necessary infrastructures to manufacture, sputter and test the quarter-wave cavities. The assembly of the cavity before sputtering is shown in Figure 2.13, alongside a cavity being lowered into the test

cryostat located at the CERN SM18 test stand for high power rf measurements. The technical details regarding the design, fabrication and testing of the prototype cavities can be found in [90–94]. The design parameters of the cavities are summarised in Table 2.4. The first high- $\beta$  prototype is shown in Figure 2.14(a) undergoing metrology analysis before sputtering and its surface is shown after niobium sputtering in Figure 2.14(b).

Table 2.4: HIE cavity design parameters

Design Parameter <sup>a</sup>	Low- $\beta$ Cavity	High- $\beta$ Cavity
No. of cavities	12	20
No. of gaps	2	2
$f$ [MHz]	101.28	101.28
$\beta_g$ ( $\beta_{\text{opt}}$ ) [%]	6.3 (7.1)	10.3 (11.3)
$L_g = \beta_g \lambda / 2$ [mm]	93	153
$T_{\text{max}}(\beta_{\text{opt}})$	0.85	0.9
$E_0$ [MV/m]	6	6
$L_a$ [mm]	195	300
Diameter of inner conductor [mm]	50	90
Mechanical length [mm]	215	320
Gap length ( $g$ ) [mm]	50	85
Beam aperture diameter [mm]	20	20
$U/E_0^2$ [mJ/(MV/m) <sup>2</sup> ]	73	207
$E_{\text{pk}}/E_0$	5.4	5.6
$B_{\text{pk}}/E_0$ [Oe/(MV/m)]	80	100.7
$R_{\text{max}}/Q$ [ $\Omega$ ]	564	554
$\Gamma = R_s Q$ [ $\Omega$ ]	23	30
$P$ [W] at $E_0$	7	10
$Q_0$ for $E_{\text{acc}} = 6$ MV/m for $P$ at $E_0$	$3.2 \times 10^8$	$5.0 \times 10^8$
Helium bath temperature [K]	4.5	4.5

<sup>a</sup> Cavity figures of merit are defined in Chapter 3.2.3.

### 2.4.3.2 Focusing Structures

As is common practice with low energy superconducting linacs, a beam focusing system based on superconducting solenoids was chosen and integrated inside the cryomodules alongside the cavities, reducing the overall length and cost of the machine. Less space is lost to the regions between the cryomodules and the longitudinal acceptance is increased as a consequence of the increased packing of the cavities, see Figure 6.7. The single tuning knob makes the linac easier to operate when scaling to accelerate radioactive beams, and solenoids have a higher tolerance to mismatch and acceptance to beams of multiple charge states [95]. The specification of the solenoid, which is based on the beam dynam-

ics studies detailed in this thesis, is summarised in Table 2.5. The design is focused on

Table 2.5: HIE solenoid design parameters

<b>Design Parameter</b>	<b>Description/Value</b>
Inner bore diameter [mm]	$\geq 30$
Mechanical length [mm]	$\leq 400$
Magnetic integral ( $\int B_z^2 dz$ ) [ $T^2m$ ]	16.2
Operating current [A]	$\leq 500$
Stray field (when powered) <sup>a</sup> [G]	$\leq 500$
Magnetic remanence (when unpowered) <sup>a</sup> [G]	$\leq 0.2$
Maximum stored energy [kJ]	$\leq 19$
Helium bath temperature [K]	4.5

<sup>a</sup> Calculated along a vertical line perpendicular to the beam axis at a distance of 230 mm from the centre of the solenoid, representing the cavity wall.

driving down the stray field at the adjacent cavity to below 500 G when the cavity is superconducting. The current direction will be reversible to allow the solenoid to be degaussed when turned off and the cavities are normal conducting to prevent trapping flux in the cavities as they are cooled. The specification is currently met with a design employing Nb<sub>3</sub>Sn coils and short 36 mm prototype bobbins have been produced.

## LINAC BEAM DYNAMICS

In this chapter rf linear accelerators will be introduced before the relevant beam dynamics concepts and formalisms used throughout this thesis are outlined. The chapter is concluded with a summary of the sources of emittance growth characteristic of low velocity ion linacs and a summary of the beam dynamics simulation codes used.

### **3.1 Resonance Linear Accelerators**

Various types of resonance accelerator, e.g. linear accelerators, microtrons, betatrons, cyclotrons and synchrotrons, were conceived in the first half of the last century in a bid to overcome the limitation imposed by electric breakdown in electrostatic accelerators. The concept of applying moderate time-varying electric fields repetitively to do work on a bunched beam was proposed by Ising and demonstrated by Wideröe [96] in 1927 using a single drift-tube placed between grounded electrodes that was excited harmonically by 25 kV at 1 MHz. Indeed, a beam of singly-charged potassium ions was accelerated to 50 keV in the two gaps between the drift-tube and the grounded electrodes and the resonance linear accelerator was born.

The principle design concept behind resonance accelerators is to maintain synchronicity between the beam and the accelerating electric fields to ensure that work is done on the beam. Almost all of the resonance linear accelerators used today derive in one way or another from Wideröe's concept, which is shown schematically in Figure 3.1. A sequence of oppositely polarised drift-tubes is connected to a time-varying voltage source to accel-

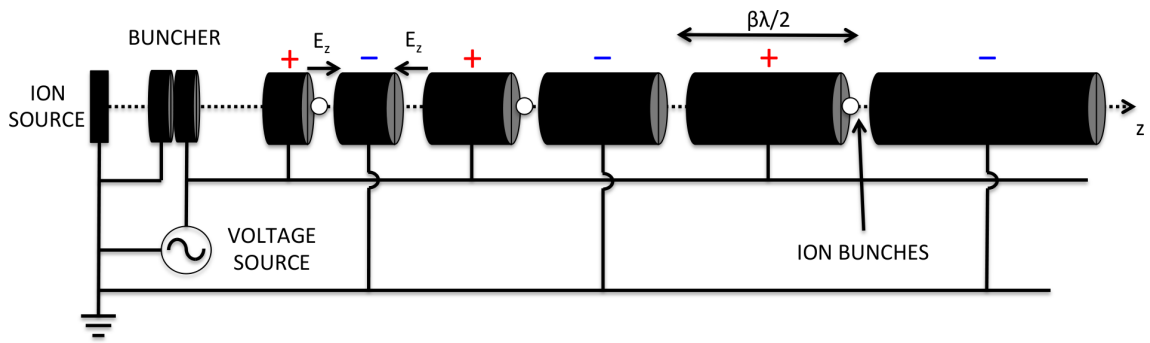


Figure 3.1: Schematic of the Wideröe concept.

erate bunches of charged particles in the electric fields established in the gaps between the drift-tubes. The synchronism between the bunches and the harmonically oscillating electric fields is achieved by correctly profiling the length of the drift-tubes to follow the rapidly changing velocity of the bunched beam as it is accelerated; a particle of reduced velocity  $\beta$  travels a distance  $\beta\lambda$  in one rf period if  $\lambda$  is the wavelength of the oscillating voltage. The rate of acceleration in the Wideröe structure decreases as the velocity increases because the length of the drift-tubes increases accordingly. Any attempt to reduce the length of the linac by increasing the frequency is met with the constraint that the ac circuit that makes up the linac starts to radiate – the wavelength of the voltage source becomes comparable to the length of the drift-tubes and they radiate electromagnetic power like antennas. Therefore, modern linacs are composed of closed structures to prevent radiative power losses and the accelerating electric field is established resonantly inside high quality cavities; a notable example is the Alvarez drift-tube linac (DTL) [97]. Nowadays, there are a vast number of different types of linac in operation at radio frequencies ranging from a few MHz to GHz, which can be broadly grouped into three types:

- **Independent cavity linacs** - made of short and independently powered standing-wave cavities that provide a high degree of operational flexibility. The cavities have a broad velocity acceptance and are independently phased with the beam to maintain synchronicity.
- **Drift-tube or multi-cell linacs** - highly efficient cavities that rely on a fixed energy gain and velocity change between drift-tubes or cells to maintain synchronicity in a standing-wave cavity.

- **Travelling wave linacs** - relativistic beams can be accelerated by the electric field of a travelling wave launched down a waveguide if its phase velocity is synchronous with the beam.

Linacs are versatile machines that are well suited for the acceleration of charged particles in both the low and high energy regimes. Their single-pass nature requires high accelerating gradients but also helps to suppress resonant phenomena that lead to instabilities – strong focusing can be applied and the beam accelerated rapidly to reduce the disruptive space-charge effects of high intensity beams. Linacs are the most common type of injector for synchrotrons or storage rings and the straight-line acceleration makes them attractive for producing ultra-high energy beams of electrons by avoiding the synchrotron radiation losses associated with synchrotrons. Only the accelerating structures relevant to this thesis will be focused on and the reader is referred to [98] for a comprehensive examination of rf linear accelerators.

## 3.2 Accelerating Cavities

The high accelerating voltages demanded in linear accelerators are produced resonantly and efficiently inside cavities with high quality factors. The low level electromagnetic power that is coupled into the cavity builds up as stored energy in the trapped electromagnetic fields; the high quality factor permits large field levels when the cavity is excited on resonance, with only a small fraction of the input power being dissipated as resistive losses on the walls of the cavity. Maxwell's equations in free space,

$$\nabla \cdot \vec{E} = 0, \quad \nabla \cdot \vec{B} = 0, \quad \nabla \times \vec{E} = -\frac{\partial \vec{B}}{\partial t} \quad \text{and} \quad \nabla \times \vec{B} = \mu_0 \epsilon_0 \frac{\partial \vec{E}}{\partial t}, \quad (3.2.1)$$

which govern the nature of electromagnetic radiation with no charge or current sources, reduce to an eigenmode problem when the time-independent wave equations or Helmholtz equations,

$$\nabla^2 \vec{E} + |\vec{k}|^2 \vec{E} = 0 \quad \text{and} \quad \nabla^2 \vec{B} + |\vec{k}|^2 \vec{B} = 0, \quad (3.2.2)$$

are solved in the presence of the physical boundary conditions that define the internal volume of the cavity. These conditions state that for a good conductor parallel electric and perpendicular magnetic fields at the cavity's surface are forbidden, i.e.,

$$\vec{n} \times \vec{E} = 0 \quad \text{and} \quad \vec{n} \cdot \vec{B} = 0, \quad (3.2.3)$$

where  $\vec{n}$  is a unit vector normal to the surface. The boundary conditions 'quantise' the allowed values for the wavenumber  $\vec{k}$  and force the cavity to resonate in specific eigenmodes at associated frequencies. There exists two types of modes:

- **Transverse Electric (TE or H)** - the electric field has only transverse components.
- **Transverse Magnetic (TM or E)** - the magnetic field has only transverse components.

If a conductor is present inside the cavity then a further classification can be made with the electromagnetic fields having only transverse components, known as TEM modes. The above classifications are applicable to cavity geometries with specific symmetries; in general, hybrid modes exist that have both longitudinal and transverse field components. The modes are labelled with indices that refer to the number of maxima or half-waves and correspond to the order of 'quantisation' in the field pattern for each dimensional degree of freedom, e.g.  $x$ ,  $y$  and  $z$  in Cartesian coordinates or  $r$ ,  $\theta$  and  $z$  in cylindrical coordinates.

A multitude of different types of accelerating cavities have been constructed to exploit different electromagnetic modes, usually representing the fundamental mode of the cavity. Most commonly used is the fundamental mode of the cylinder or 'pill-box' known as the  $\text{TM}_{010}$  mode in which the longitudinal electric field is uniform and azimuthally symmetric. Cavity geometries have become highly optimised for different accelerator applications but there remain two main types of geometry on which most structures are based: the 'pill-box' and the 'coaxial resonator'. Although analytic results exist for the electromagnetic eigenmodes in these simple structures, numerical techniques based on finite element calculations using computer codes<sup>1</sup> are required for the optimisation of re-

<sup>1</sup>e.g. CST-MWS [89] or HFSS [99].

alistic cavities used in accelerators. For a comprehensive description and overview of accelerating cavities the reader is referred to [100].

To extend this very brief discussion on accelerating cavities the two cavity geometries most relevant to this thesis will be focused on below: the interdigital H-mode structure and the quarter-wave resonator, before the cavity figures of merit are introduced.

### 3.2.1 Interdigital H-mode Cavity

The IH cavity [64] is operated in either of the fundamental dipole or quadrupole TE modes, otherwise known as H modes, and is a highly efficient DTL offering unrivalled acceleration efficiency for low velocity ions, see e.g. Figure 11 of [64]. The fundamental IH cavity, operating in the  $TE_{111}$  mode, is efficient in the velocity range  $0.015 \lesssim \beta \lesssim 0.25$  and can even compete with superconducting linacs at energies up to about 2 MeV/ $u$ . The analytic components of the electromagnetic fields for the  $TE_{mnp}$  modes in an ideal ‘pill-box’ can be written in cylindrical coordinates as,

$$\begin{aligned}
 E_z &= 0 \\
 E_r &= i \omega \frac{B_0}{k_{r,mn}^2 r} J_m(k_{r,mn} r) \sin m\theta \sin k_{z,p} z e^{i\omega t} \\
 E_\theta &= i \omega \frac{B_0}{k_{r,mn}} J'_m(k_{r,mn} r) \cos m\theta \sin k_{z,p} z e^{i\omega t} \\
 B_z &= B_0 J_m(k_{r,mn} r) \cos m\theta \sin k_{z,p} z e^{i\omega t} \\
 B_r &= \frac{\pi}{L} \frac{B_0}{k_{r,mn}} J'_m(k_{r,mn} r) \cos m\theta \cos k_{z,p} z e^{i\omega t} \\
 B_\theta &= -\frac{\pi}{L} \frac{B_0}{k_{r,mn}^2 r} J_m(k_{r,mn} r) \sin m\theta \cos k_{z,p} z e^{i\omega t},
 \end{aligned}$$

where  $L$  is the length of the ‘pill-box’,  $J_m$  are Bessel functions and  $J'_m$  are their derivatives. The wavenumbers are therefore ‘quantised’ as follows,

$$|\vec{k}| = \sqrt{k_{r,mn}^2 + k_{z,p}^2} = \sqrt{\left(\frac{x'_{mn}}{R}\right)^2 + \left(\frac{p\pi}{L}\right)^2} \quad \text{and} \quad \omega = |\vec{k}|c,$$

where  $R$  is the radius and the zeroes of  $J'_m$  are denoted by  $x'_{mn}$ , i.e.  $J'_m(x'_{mn}) = 0$ . The real parts of the above equations give the field configuration at any given instant in time;

the electric and magnetic fields are out of phase by  $\pi/2$ . For the  $TE_{111}$  mode,

$$|\vec{k}| = \sqrt{k_{r,11}^2 + k_{z,1}^2} = \sqrt{\left(\frac{1.841}{R}\right)^2 + \left(\frac{\pi}{L}\right)^2}.$$

The mode consists of a transverse electric dipole and a longitudinal magnetic field that loops through the electric dipole, as shown schematically in the REX IHS in Figure 3.2. In

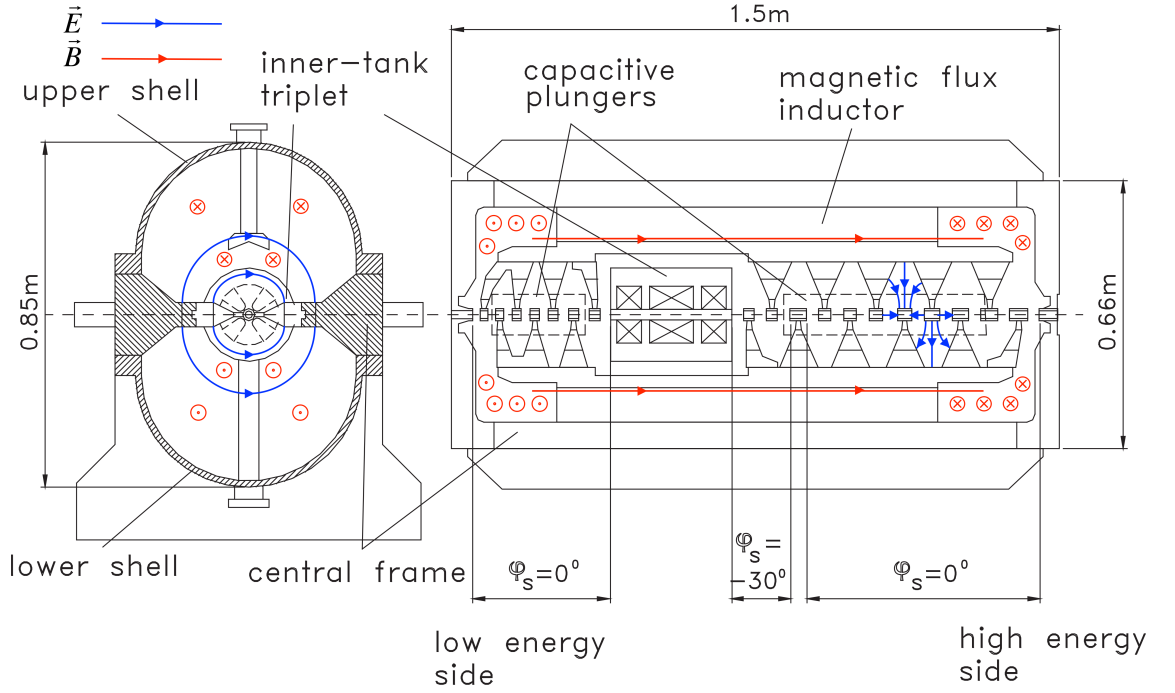


Figure 3.2: Schematic of the  $TE_{11(0)}$  mode in the REX IHS.

order to attain a longitudinal accelerating field the structure is loaded heavily by ‘interdigital’ drift-tubes and the capacitance between the adjacent drift-tubes creates an effective  $\pi$ -mode accelerating structure.<sup>1</sup> The capacitive loading drastically reduces the frequency of the structure – the IHS would have an unloaded resonant frequency of close to 300 MHz if the drift-tubes and their supports were removed. The gap voltage distribution, which is proportional to the longitudinal magnetic flux by Faraday’s law of induction, has a strong  $\sin(\pi z/L)$  dependence in the  $TE_{111}$  mode, which is evident by comparing the above expressions for  $E_r$ ,  $E_\theta$  and  $B_z$ . The distribution is flattened, to resemble a  $TE_{110}$ -like mode by modifying the ends of the drift-tube supports (magnetic flux inductors) and introducing ‘undercuts’ that increase the magnetic field density in the regions at the ends of the

<sup>1</sup>The operating mode of coupled-cell cavities is often described by the phase advance of the fields from cell-to-cell. In the above case the field orientation is opposite from gap-to-gap and therefore out of phase by  $\pi$  or half an oscillation, leading to synchronicity with the beam if the gaps are spaced by  $\beta\lambda/2$ .

cavity, as shown in Figure 3.2. In addition, the gap to drift-tube length ratio is adjusted accordingly. The resulting gap voltage distribution in the IHS can be seen in the bead-pull measurements presented in Figure 4.13. The frequency of the cavity is tuned with capacitive plungers that move vertically over the drift-tube structure and are also used to skew the voltage distribution between the low and high energy sections in order to vary the output energy from 1.2 MeV/u down to 1.1 MeV/u [62, 63]. Although the small drift-tubes make the structure highly efficient, focusing elements cannot be placed inside the drift-tubes and instead KONUS beam dynamics is employed. Described in Chapter 3.3.7, the transverse defocusing forces in the accelerating gaps are relaxed and the focusing elements can be lumped outside of drift-tube sections, and in the case of the REX IHS, inside the structure itself.

### 3.2.2 Quarter-wave Resonator

Many cavities operating at low frequencies ( $\lesssim 200$  MHz) are in fact compact TEM class cavities based on variants of the coaxial transmission line. In the four-rod- $\lambda/2$  RFQ and split-ring cavities capacitively loaded resonant transmission lines are used to generate the accelerating voltages at the electrodes or drift-tubes. In the case of the coaxial resonator, a magnetic field curls around currents flowing on the internal conductor and an electric field is sustained radially between the inner and outer conductors. With both ends of the transmission line closed and shorted the transverse field components can be written,

$$E_r = -2i \sqrt{\frac{\mu_0}{\epsilon_0}} \frac{I_0}{2\pi r} \sin k_{z,p} z e^{i\omega t}$$

$$B_\theta = \frac{\mu_0 I_0}{\pi r} \cos k_{z,p} z e^{i\omega t},$$

where,

$$|\vec{k}| = k_{z,p} = \frac{p\pi}{L} \quad \text{and} \quad \omega = |\vec{k}|c,$$

and the fundamental mode corresponds to the half-wave resonator. The electric field is largest at the cavity mid-plane and zero at the cavity ends where the voltage is shorted; the opposite is the case for the magnetic field. The structure can be made to resonate at an even lower fundamental frequency by turning one of the shorted ends into an open termi-

nation, which is realised in practice by shortening the length of the internal conductor and terminating the cavity with a capacitance to form the quarter-wave resonator, as shown in Figure 3.3. To first-order, the eigenmodes in the quarter-wave resonator are defined by the wavenumber,

$$|\vec{k}| = k_{z,p} = \frac{p\pi}{2L}, \quad (3.2.4)$$

causing the modes to be well separated in frequency.

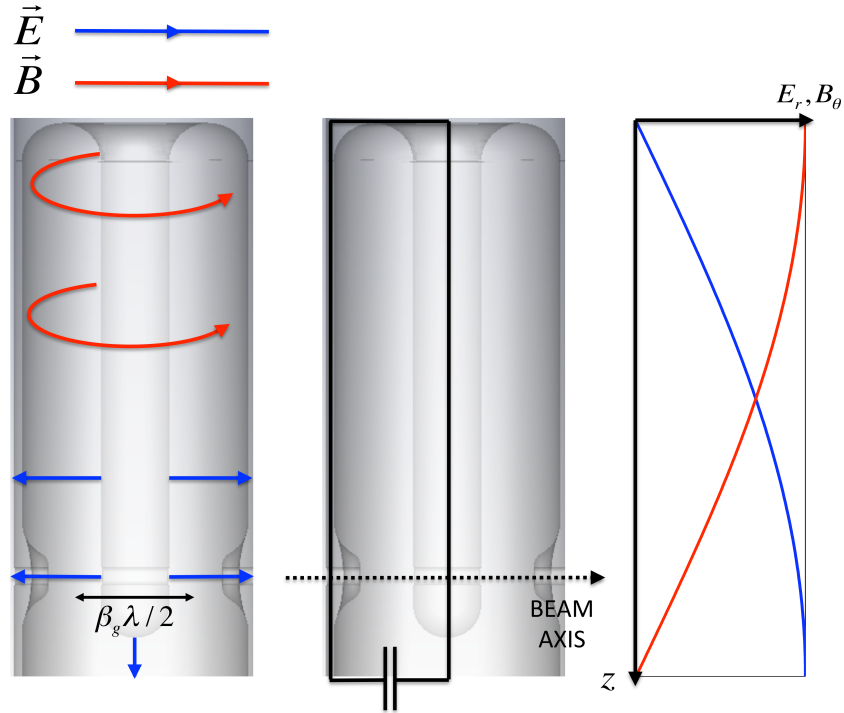


Figure 3.3: Schematic of the TEM mode in the quarter-wave resonator.

Quarter-wave resonators are typically used to accelerate beams in the range  $0.001 \lesssim \beta \lesssim 0.2$  and are usually superconducting to achieve the high gradients needed to make the two-gap structure efficient. The beam axis is positioned to exploit the high voltage in the high impedance region near the open end of the structure and, although the beam could be sent along the axis of the resonator, usually the radial electric field is used in  $\pi$ -mode to accelerate beams efficiently. The asymmetry of the cavity about this choice of beam axis, see Figure 3.3, leads to the presence of significant transverse dipole field components on the beam axis, as shown for the high- $\beta$  cavity using Cartesian coordinates in Figure 3.4. The compensation of the dipole field effects is a key aspect of the studies presented in this thesis. The longitudinal field profiles shown in Figure 3.4(a) are fairly typical of quarter-wave resonators in general. Further details on the design of quarter-wave resonators are

discussed at length in [101, 102].

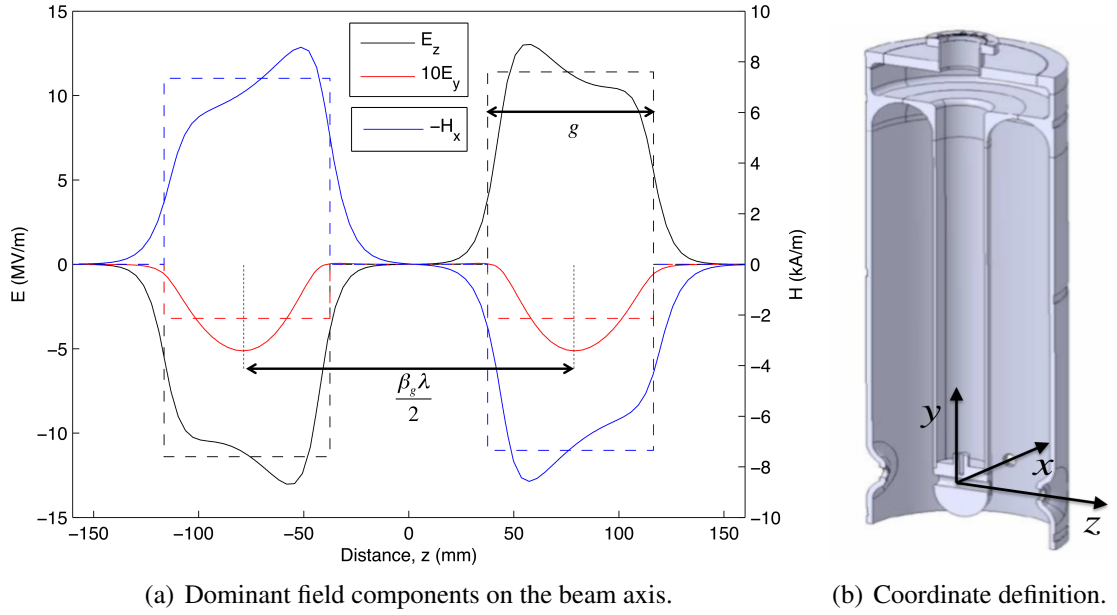


Figure 3.4: Field components on the beam axis of the high- $\beta$  cavity:  $B_x$  leads  $E_y$  and  $E_z$  by  $90^\circ$  in phase, its sign is reversed for ease of presentation and the square-wave approximation is also shown.

### 3.2.3 Figures of Merit

The average accelerating gradient of a cavity is,

$$E_{\text{acc}} = E_0 T = \frac{V_0}{L_a} T, \quad (3.2.5)$$

where  $T$  is the transit-time factor,  $L_a$  is the active length of the average accelerating field amplitude ( $E_0$ ) in the cavity and  $V_0$  is the equivalent electrostatic accelerating voltage on the beam axis,

$$V_0 = \int_{-\infty}^{+\infty} |E_z(z)| dz. \quad (3.2.6)$$

The transit-time factor will be discussed in detail later. The efficiency at which the accelerating voltage can be generated depends on the power ( $P$ ) that is dissipated as resistive losses on the walls of the cavity and is parameterised in terms of the shunt impedance,

$$R_0 = \frac{V_0^2}{P}. \quad (3.2.7)$$

A more useful definition,

$$R_{\text{eff}} = R_0 T^2 = \frac{(V_0 T)^2}{P}, \quad (3.2.8)$$

includes the transit-time factor. As the length of a linac is an important design consideration the shunt impedance is often quoted per unit length and denoted by  $Z_0$  or  $Z_{\text{eff}}$ . For the RFQ it is more conventional to define the specific shunt impedance in terms of the electrode voltage,

$$R'_p = \frac{V_0^2 L_a}{P}. \quad (3.2.9)$$

The unloaded quality factor of a cavity compares the energy lost per cycle in heating the cavity walls to the energy stored in the electromagnetic fields trapped in the cavity,

$$Q = \frac{\omega U}{P}, \quad (3.2.10)$$

where the energy stored in the cavity volume ( $V$ ) is,

$$U = \frac{1}{2} \int_V |\vec{B}|^2 dV, \quad (3.2.11)$$

and the power dissipated over the cavity surface ( $S$ ) with a resistance of  $R_s$  is,

$$P = \frac{R_s}{2\mu_0} \int_S |\vec{B}|^2 dS. \quad (3.2.12)$$

In the above equations  $\vec{B}$  refers to the spatial component of the fields. The geometric shunt impedance  $R/Q$  is a commonly quoted figure of merit, which is independent of the material properties of the cavity surface and is purely geometric in nature. Another geometric parameter that is scale-invariant and often used is,

$$\Gamma = QR_s = \omega\mu_0 \frac{\int_V |\vec{B}|^2 dV}{\int_S |\vec{B}|^2 dS}. \quad (3.2.13)$$

### 3.2.4 Superconductivity vs. Normal Conductivity

The application of superconductivity in accelerators is widespread and has a particularly long and successful history in heavy ion accelerators [103]. This success is largely at-

tributed to the high gradients that can be realised in short and independently phased superconducting cavities that are capable of efficiently accelerating a wide range of velocity whilst maintaining beam quality. The wall heating limitations of normal conducting cavities necessitates a larger number of accelerating gaps to achieve high gradients, which limits their velocity acceptance. The difference between the magnitude and frequency dependence of the rf surface resistance of normal conducting and superconducting cavities leads to different design considerations. Typically,

$$\frac{R_{s,NC}}{R_{s,SC}} \sim 10^5, \quad (3.2.14)$$

and,

$$R_s \propto \begin{cases} f^{1/2} & \text{normal conducting} \\ f^2 & \text{superconducting} \end{cases}, \quad (3.2.15)$$

such that the power dissipated scales as,

$$P \propto \begin{cases} f^{-1/2} & \text{normal conducting} \\ f & \text{superconducting} \end{cases}. \quad (3.2.16)$$

Unfortunately, the dissipation of rf power at liquid helium temperatures reduces the comparative wall-plug efficiency of superconducting linacs from the above-quoted ratio of the surface resistances of  $10^5$ , to something in the order of  $10^2$  or worse because of Carnot's efficiency (0.014 at 4.2 K) and the efficiency of the refrigerator system [104]. As a result, maximising the rf efficiency of superconducting accelerating structures is not always a priority and many designs focus on reducing peak fields or opening up the beam aperture to reduce the disruptive effects of the beam-cavity interaction. The use of superconductivity in low energy heavy ion accelerators is compatible with their frequency, especially when cw operation is a consideration. If the HIE-ISOLDE cavities were normal conducting copper resonators each would demand 0.4 MW of power to achieve their design gradient and the linac would demand 1.4 MW/m of power in cw, disregarding the

fact that the Kilpatrick Limit<sup>1</sup> is far exceeded! This value can be compared to the total electrical power rating of the cryoplant needed for the superconducting HIE linac, which is foreseen at less than 1 MW [105].

### 3.3 Longitudinal Beam Dynamics

#### 3.3.1 Coordinate System Definition

A standard co-moving right-handed coordinate definition is used throughout this thesis, as shown in Figure 3.5. The velocity is denoted by  $\vec{v}$ , such that the reduced or normalised velocity is  $\vec{\beta} = \vec{v}/c$ , the momentum is denoted by  $\vec{p} = \gamma m \vec{\beta} c$  with the relativistic factor  $\gamma = \frac{1}{\sqrt{1-\beta^2}}$  and the kinetic energy is denoted by  $W = (\gamma - 1)mc^2$ . The origin of the co-ordinate system moves with the reference particle at a position  $z_0 = v_0 t = c\beta_0 t$  along the beam axis in the  $z$ -direction. The co-moving system is relevant in a resonance accelerator

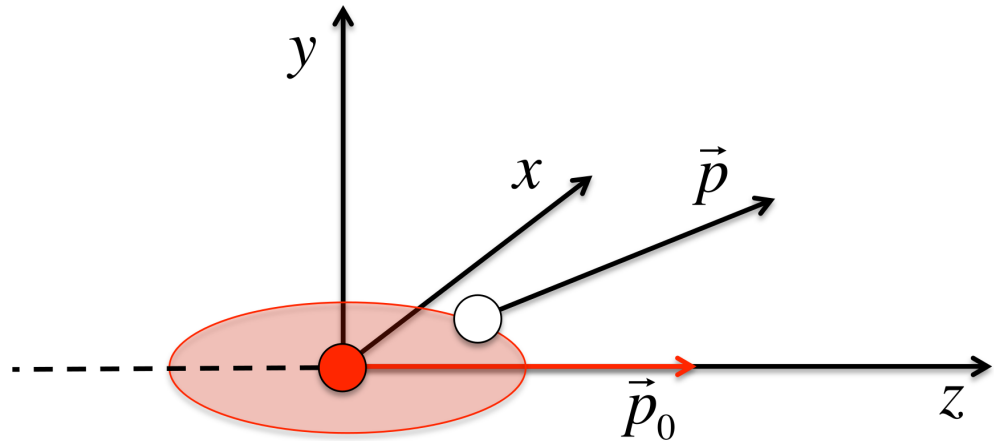


Figure 3.5: The co-moving coordinate system, where a particle is shown in a bunch centred on the reference particle in red.

composed of particle bunches and allows calculations to be carried out sequentially for each element of the linac as a function of  $z$ . In order to illuminate the geometric parameters of the beam it is common to relate derivatives of time to derivatives of the longitudinal spatial coordinate using the relationship,

$$\frac{d}{dt} = \frac{dz}{dt} \frac{d}{dz} = v_z \frac{d}{dz} = c\beta_z \frac{d}{dz}. \quad (3.3.1)$$

<sup>1</sup>The Kilpatrick Limit is an empirical criterion that broadly defines the electric field limit in room-temperature copper cavities as a function of frequency before electric breakdown ensues, see [98].

The divergence of a particle with respect to the  $z$ -axis can be written,

$$x' = \frac{dx}{dt} \frac{dt}{dz} \approx \frac{v_x}{v_z} = \frac{\beta_x}{\beta_z} = \frac{p_x}{p_z}. \quad (3.3.2)$$

The notation,  $' = \frac{d}{dz}$ , is used to denote derivatives with respect to the longitudinal  $z$ -coordinate. The six phase space coordinates are  $\vec{X} = (x, x', y, y', z - z_0, \frac{p-p_0}{p_0})$ , where for small differences, e.g.  $\frac{\Delta p}{p_0} = \frac{p-p_0}{p_0} \ll 1$ , the following relationships can be used to convert between different longitudinal coordinates,

$$\frac{\Delta W}{W_0} = \frac{\gamma + 1}{\gamma} \frac{\Delta p}{p_0} \quad \text{and} \quad \Delta \phi = -\frac{2\pi}{\beta_0 \lambda} \Delta z. \quad (3.3.3)$$

The phase is useful to put the bunch length in comparison with the rf wavelength ( $\lambda$ ).

### 3.3.2 Particle Tracking in Electromagnetic Fields

The equations of motion can be derived from the Lorentz force equation,

$$\frac{d\vec{p}}{dt} = q(\vec{E} + \vec{v} \times \vec{B}), \quad (3.3.4)$$

which describes the force that is imparted on a particle with charge  $q$  that is travelling at a velocity  $\vec{v}$  and corresponding momentum  $\vec{p}$  through an electromagnetic field.

#### 3.3.2.1 Linearised Matrix Tracking

After linearisation, the solutions of the equations of motion for each linac component can be written in matrix form and the particle coordinates tracked through the linac by concatenating matrices representing each component, whether it is a drift, quadrupole, rf gap etc., as,

$$\vec{X}_n = R_n R_{n-1} \dots R_1 \vec{X}_0 = R_{0 \rightarrow n} \vec{X}_0, \quad (3.3.5)$$

where  $R_{0 \rightarrow n}$  is in general a  $6 \times 6$  transfer matrix including all couplings at first-order. The transfer matrices for well-known components can be looked up in e.g. [106] or [107]. It

is usual that the particle coordinate vectors have the form,

$$\vec{X} = \begin{pmatrix} x \text{ [m]} \\ x' \\ y \text{ [m]} \\ y' \\ \Delta z \text{ [m]} \\ \frac{\Delta p}{p_0} \end{pmatrix}. \quad (3.3.6)$$

The transfer matrix can be written as a subset of matrices that describe each 2-dimensional projection or trace space as,

$$R_{0 \rightarrow n} = \begin{pmatrix} R_{xx} & R_{xy} & R_{xz} \\ R_{yx} & R_{yy} & R_{yz} \\ R_{zx} & R_{zy} & R_{zz} \end{pmatrix}, \quad (3.3.7)$$

where in general,

$$R_{0 \rightarrow n} = \begin{pmatrix} R_{11} & R_{12} \text{ [m]} & R_{13} & R_{14} \text{ [m]} & R_{15} & R_{16} \text{ [m]} \\ R_{21} \text{ [m}^{-1}] & R_{22} & R_{23} \text{ [m}^{-1}] & R_{24} & R_{25} \text{ [m}^{-1}] & R_{26} \\ R_{31} & R_{32} \text{ [m]} & R_{33} & R_{34} \text{ [m]} & R_{35} & R_{36} \text{ [m]} \\ R_{41} \text{ [m}^{-1}] & R_{42} & R_{43} \text{ [m}^{-1}] & R_{44} & R_{45} \text{ [m}^{-1}] & R_{46} \\ R_{51} & R_{52} \text{ [m]} & R_{53} & R_{54} \text{ [m]} & R_{55} & R_{56} \text{ [m]} \\ R_{61} \text{ [m}^{-1}] & R_{62} & R_{63} \text{ [m}^{-1}] & R_{64} & R_{65} \text{ [m}^{-1}] & R_{66} \end{pmatrix}.$$

In the horizontal plane, the dispersion function is  $R_{16}$  and when the dynamics is uncoupled, i.e. if  $R_{13} = R_{14} = 0$ , then  $R_{11}$  represents the magnification factor of the beam at the focal point, i.e. when  $R_{12} = 0$ . Although the matrix formalism can be used to track particles, the formalism can be applied to described a beam of particle in terms of the Courant-Snyder or Twiss parameters. The linear formalism is used in the design stages of an accelerator or transfer line and is often used in beam matching routines. The linear formalism can be extended to further include higher-order coupling terms.

### 3.3.2.2 Numerical Tracking

Throughout this thesis electrodynamics calculations are carried out to understand the behaviour of charged particle beams in the realistic field maps of the linac components attained from electromagnetic field solver programs. A numerical integration routine was written to perform these calculations and to benchmark all of the design codes used. In the presence of both an electric field  $\vec{E}(x, y, z)$  and a magnetic field  $\vec{B}(x, y, z)$  the component by component equations of motion as a function of the longitudinal  $z$ -coordinate in Cartesian coordinates are,

$$\begin{aligned}
 p_z(z_f) - p_z(z_i) = & \frac{q}{c} \int_{z_i}^{z_f} E_z(x, y, z) \cos(\psi(z) + \phi) \frac{dz}{\beta_z(z)} \\
 & + q \int_{z_i}^{z_f} \beta_x(z) B_y(x, y, z) \sin(\psi(z) + \phi) \frac{dz}{\beta_z(z)} \\
 & - q \int_{z_i}^{z_f} \beta_y(z) B_x(x, y, z) \sin(\psi(z) + \phi) \frac{dz}{\beta_z(z)}, \quad (3.3.8)
 \end{aligned}$$

$$\begin{aligned}
 p_y(z_f) - p_y(z_i) = & \frac{q}{c} \int_{z_i}^{z_f} E_y(x, y, z) \cos(\psi(z) + \phi) \frac{dz}{\beta_z(z)} \\
 & + q \int_{z_i}^{z_f} \beta_x(z) B_z(x, y, z) \sin(\psi(z) + \phi) \frac{dz}{\beta_z(z)} \\
 & - q \int_{z_i}^{z_f} B_x(x, y, z) \sin(\psi(z) + \phi) dz, \quad (3.3.9)
 \end{aligned}$$

$$\begin{aligned}
 p_x(z_f) - p_x(z_i) = & \frac{q}{c} \int_{z_i}^{z_f} E_x(x, y, z) \cos(\psi(z) + \phi) \frac{dz}{\beta_z(z)} \\
 & + q \int_{z_i}^{z_f} \beta_y(z) B_z(x, y, z) \sin(\psi(z) + \phi) \frac{dz}{\beta_z(z)} \\
 & - q \int_{z_i}^{z_f} B_y(x, y, z) \sin(\psi(z) + \phi) dz, \quad (3.3.10)
 \end{aligned}$$

where  $z_i$  and  $z_f$  are the initial and final longitudinal positions of the particle and  $\psi(z)$  is a phase term defined in Equation 3.3.20. The electromagnetic field values at each integration step are linearly interpolated from the mesh points of the field map. If the above equations of motion are incremented by a small longitudinal distance from a position  $z_i$  to  $z_f = z_i + \Delta z$ , one has expressions for the rate of change of momentum in the form,

$$p'(z) = \frac{p(z + \Delta z) - p(z)}{\Delta z} + O(\Delta z^2). \quad (3.3.11)$$

After expanding the position and velocity as,

$$x(z + \Delta z) = x(z) + x'(z)\Delta z + \frac{x''(z)}{2}\Delta z^2 + O(\Delta z^3), \quad (3.3.12)$$

and,

$$\beta(z + \Delta z) = \beta(z) + \beta'(z)\Delta z + O(\Delta z^2), \quad (3.3.13)$$

and using the following relationships,

$$x'(z) = \frac{1}{c}\beta(z), \quad x''(z) = \frac{1}{c}\beta'(z) \quad \text{and} \quad \beta'(z) = \frac{p'(z)}{\gamma^3 mc}, \quad (3.3.14)$$

the equations of motion can be solved iteratively by employing a simple improved Euler method,<sup>1</sup>

$$\beta_{n+1} = \beta_n + \frac{p'_n}{\gamma_n^3 mc}\Delta z + O(\Delta z^2), \quad (3.3.15)$$

and,

$$x_{n+1} = x_n + \frac{1}{c}\beta_n\Delta z + \frac{p'_n}{\gamma_n^3 mc}\Delta z^2 + O(\Delta z^3). \quad (3.3.16)$$

A benchmarking study with the TRACK code [108], which uses the fourth-order Runge-Kutta integration method and a quadratic interpolation of the fields, showed the discrepancy between the two codes to be less than a factor of  $10^{-3}$ , i.e.,

$$\frac{x_{\text{TRACK}} - x}{x} \lesssim 10^{-3}, \quad (3.3.17)$$

after tracking through the realistic field map of any given HIE-ISOLDE linac element. These integration techniques are non-symplectic and numerical errors do add over long-term integrations, however the above procedure can be reliably applied over the small number of elements in the HIE linac without significant error.

---

<sup>1</sup>Otherwise known as the trapezium rule.

### 3.3.3 Energy Gain in an RF Gap

The work done on a charged particle by a time-dependent electric field is the line integral,

$$\Delta W = qV = q \int_{-\infty}^{+\infty} \vec{E}(\vec{r}, t) \cdot d\vec{l}, \quad (3.3.18)$$

where  $q$  is the charge of the particle and  $V$  is the potential difference seen by the particle as it moves through the field along its trajectory at position  $\vec{r}$ . On the axis of an accelerating cavity this expression becomes,

$$\Delta W = q \int_{-\infty}^{+\infty} E_z(z) \cos(\psi(z) + \phi) dz, \quad (3.3.19)$$

where the field varies harmonically and  $\phi$  is the phase when the particle would cross the origin ( $z = 0$ ) in the absence of acceleration. The phase of the field oscillations seen by the particle can be written in terms of its position along the  $z$ -axis using the following relationship,

$$\psi(z) = \frac{2\pi}{\lambda} \int_{z_i}^z \frac{dz}{\beta(z)} + \psi(z_i), \quad (3.3.20)$$

where the integral starts at an initial position  $z_i$  outside of the influence of the electric field of the cavity, i.e.,

$$\psi(z_i) = \frac{2\pi z_i}{\beta(z_i)\lambda}. \quad (3.3.21)$$

$\phi$  is often referred to as the synchronous phase if the coordinate origin is positioned at the symmetry point in the centre of the accelerating gap or cavity. In many cases the change in velocity is small and the constant velocity assumption is valid; the phase and velocity can be uncoupled in the above integral to give the expression,

$$\Delta W = qV_0 T(\beta) \cos \phi, \quad (3.3.22)$$

where the physics of the interaction between the charged particle and the accelerating field in the cavity is collected into the transit-time factor  $T(\beta)$ . Once the transit-time factor has been calculated it can be used to describe the longitudinal dynamics in a cavity for a wide range of input parameters, provided the constant velocity approximation is valid. In this

approximation,

$$\psi(z) = \frac{2\pi z}{\beta\lambda}, \quad \text{where } \beta = \beta(z_i), \quad (3.3.23)$$

and if the accelerating field profile has an even symmetry then  $T$  can be written,

$$T(\beta) = \frac{1}{V_0} \int_{-\infty}^{+\infty} E_z(z) \cos \frac{2\pi z}{\beta\lambda} dz, \quad (3.3.24)$$

provided that the coordinate system is centred in the cavity. If  $E_z(z)$  is an odd function one should shift the phase of the harmonic term to get an equivalent expression for  $T$  with  $\sin \frac{2\pi z}{\beta\lambda}$  to keep the  $\cos \phi$  linac convention for  $\Delta W$ .

The weighting of the line integral by the cosine term in Equation 3.3.24 results in a drop in efficiency with respect to the dc case, i.e.  $T(\beta) < 1$ . The time variation of the fields reduces the achievable energy gain because (i) the peak rf field is maintained only instantaneously, (ii) the particle has a finite velocity and (iii) the gap cannot be made thin because of concerns of electric breakdown. Noses on the beam axis of cavities are often manufactured to increase  $T$  by compressing the electric field into a narrower gap, which in turn increases  $R/Q$ .

In order to arrive at simple analytic expressions for the transit-time factor the profile of  $E_z(z)$  must be approximated. In the square-wave approximation, see e.g. Figure 3.4, the field is assumed constant over the gap and the transit-time factor for a single gap can be written as,

$$T(\beta) = \frac{\sin \frac{\pi g}{\beta\lambda}}{\frac{\pi g}{\beta\lambda}}, \quad (3.3.25)$$

where  $g$  is the length of the gap. The transit-time factor is useful for parameterising the energy gain in short and independently phased cavities that usually have gaps equally spaced by a distance  $\beta_g \lambda / 2$ , where  $\beta_g$  is the geometric velocity that defines the equivalent phase velocity of the standing-wave fields across the accelerating gaps in the cavity. The above expression can be readily extended to describe the dynamics in multi-gap structures and for a two-gap cavity operating in  $\pi$ -mode one can write,

$$T(\beta) = \frac{\sin \frac{\pi g}{\beta\lambda}}{\frac{\pi g}{\beta\lambda}} \sin \frac{\pi \beta_g}{2\beta}, \quad (3.3.26)$$

where the addition of the synchronisation factor between the two gaps reduces the acceleration efficiency as a function of  $\beta$ . The beam is only truly synchronous if its velocity is equal to  $\beta_g$ , however if the number of gaps per cavity is small and the phase of the rf is stepped from cavity to cavity then the acceleration efficiency can be high over a wide range of velocity. The effect of the number of gaps on the efficiency of the transit-time factor as a function of velocity can be seen e.g. in Figure 2 of [109]. In a symmetric multi-gap structure  $\phi$  not only represents the phase at the cavity centre but also the average synchronous phase in the gaps. The transit-time factor for the HIE-ISOLDE low- $\beta$  cavity is shown in Figure 3.6 using the realistic field and using the analytic square-wave approximation. The optimum velocity ( $\beta_{\text{opt}}$ ) of the transit-time factor occurs at a higher velocity than  $\beta_g$  as a consequence of the finite gap length, see e.g. Figure 4 of [110]; typically for most practically realisable quarter-wave resonators  $\beta_{\text{opt}} \approx 1.1\beta_g$  and  $T$  drops to zero at  $\beta \approx \beta_g/2$ .

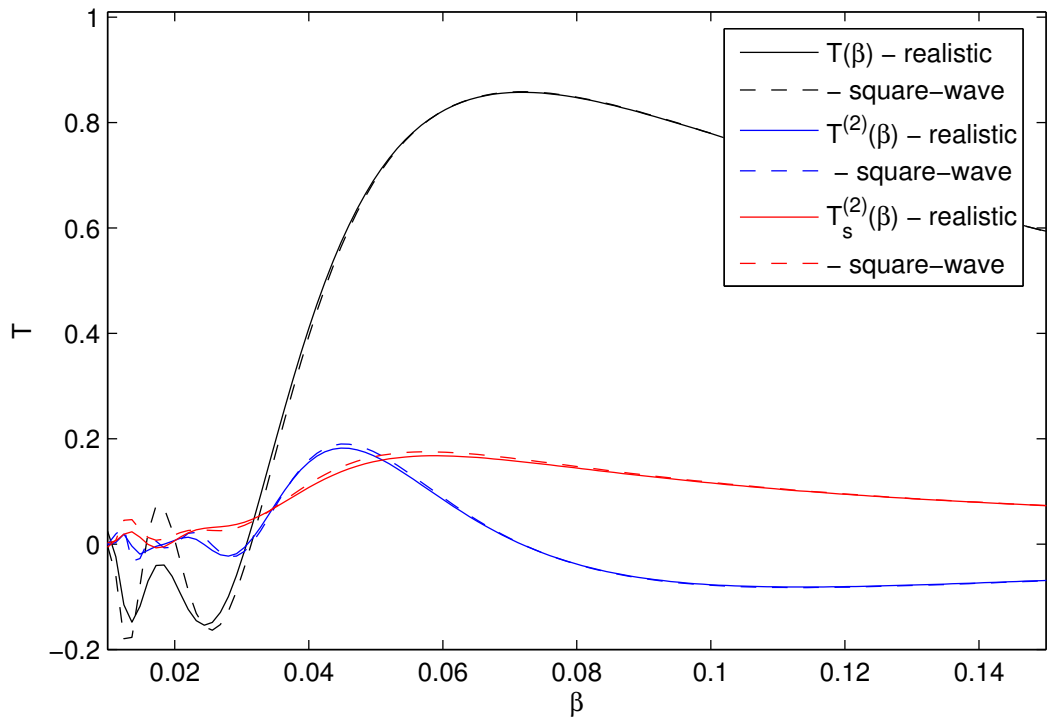


Figure 3.6: Transit-time factors of the HIE-ISOLDE low- $\beta$  cavity.

### 3.3.4 Second-order Calculation of Energy Gain

In certain circumstances, e.g. when the mass or velocity of the particle is small or when the gradient of the cavity is high, the change in velocity inside the cavity can be significant and the energy gain calculation should be carried out numerically by tracking the particle throughout its every interaction with the accelerating field. In general, the transit-time factor is a function of both  $\beta$  and  $\phi$ ,

$$T(\beta, \phi) = \frac{1}{V_0} \int_{-\infty}^{+\infty} E_z(z) \cos \psi(z) dz - \frac{\tan \phi}{V_0} \int_{-\infty}^{+\infty} E_z(z) \sin \psi(z) dz, \quad (3.3.27)$$

and the numerical procedure can become time-consuming and non-intuitive; a better approach is based on a second-order result [110] that takes into account a small change in velocity inside the cavity. The energy gain can be expressed as,

$$\Delta W = qV_0 T(\beta) \cos \phi + \frac{(qV_0)^2}{W} (T^{(2)}(\beta) + T_s^{(2)}(\beta) \sin 2\phi), \quad (3.3.28)$$

where Equation 3.3.27 is expanded about a small perturbation in  $\beta$  and two second-order transit-time factors are introduced in order to uncouple the variables  $\beta$  and  $\phi$ . The second-order transit-time factors, which are derived in [110], can be expressed as,

$$T^{(2)}(\beta) = \frac{1}{V_0^2} \frac{\pi}{\beta\lambda} \int_{-\infty}^{+\infty} E_z(z) \sin \frac{2\pi z}{\beta\lambda} dz \int_{-\infty}^z dz_1 \int_{-\infty}^{z_1} E_z(z_2) \cos \frac{2\pi z_2}{\beta\lambda} dz_2,$$

and,

$$\begin{aligned} T_s^{(2)}(\beta) = & -\frac{1}{2V_0^2} \frac{\pi}{\beta\lambda} \int_{-\infty}^{+\infty} E_z(z) \sin \frac{2\pi z}{\beta\lambda} dz \int_{-\infty}^z dz_1 \int_{-\infty}^{z_1} E_z(z_2) \sin \frac{2\pi z_2}{\beta\lambda} dz_2 \\ & + \frac{1}{2V_0^2} \frac{\pi}{\beta\lambda} \int_{-\infty}^{+\infty} E_z(z) \cos \frac{2\pi z}{\beta\lambda} dz \int_{-\infty}^z dz_1 \int_{-\infty}^{z_1} E_z(z_2) \cos \frac{2\pi z_2}{\beta\lambda} dz_2. \end{aligned}$$

As with the first-order expression given in Equation 3.3.24 the above factors need calculating only once and can be used to accurately calculate the energy gain over a wide-range of parameters:  $\phi$ ,  $\beta$ ,  $A/q$  and  $V_0$ . As will be discussed later, a significant variation in the velocity will impact on the phase at which the energy gain is maximised; the maximum of  $\Delta W$  no longer occurs when  $\phi = 0$  and the longitudinal beam stability can be affected.

In this thesis the second-order formalism is used to calculate the energy range achievable when decelerating in the low energy superconducting section of the HIE linac, which is documented in Chapter 6.8. Analytic expressions for the second-order transit-time factors of a two-gap  $\pi$ -mode cavity were also derived, see Appendix B. Analytical results using the parameters  $\beta_g = 0.063$  and  $g = 5.9$  cm in the square-wave approximation are compared to numerical results that use the realistic field profile in Figure 3.6. The actual shape of the field profile is only important at low velocity where the curves diverge.

### 3.3.5 Phase Focusing

The phase stability of particle bunches is critical in ensuring that a beam current can be accelerated synchronously in a resonance accelerator. The phase focusing of particles about the synchronous particle, which by design remains synchronous with the rf fields, can be achieved by ensuring that the bunch sees the accelerating field increasing in time inside the rf gaps. As a consequence, the slower particles that arrive later than the synchronous particle see a stronger accelerating field and receive a greater boost in velocity than the faster particles that crossed the cavity earlier. The slower particles that are correlated towards the back of the bunch catch up with the faster particles at the front of the bunch and vice versa, as shown schematically in Figure 3.7.

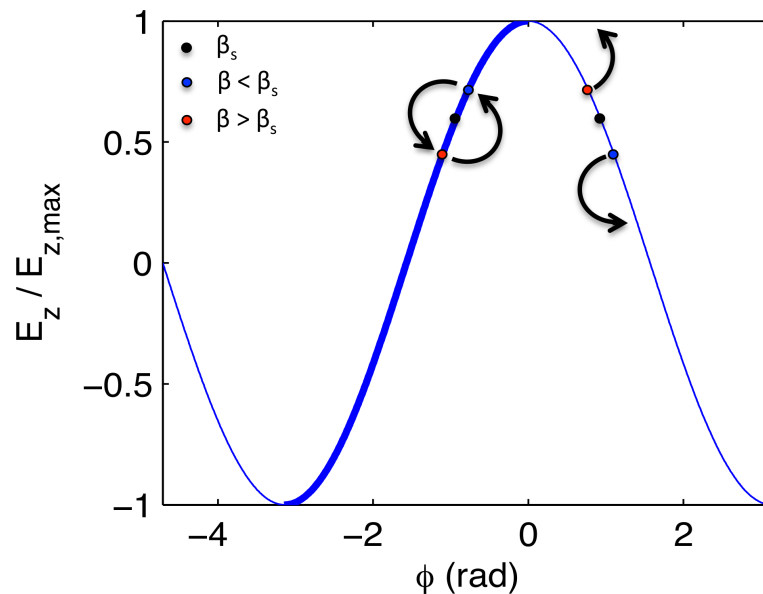


Figure 3.7: Phase focusing keeps bunches stable in heavy ion linacs if an increasing accelerating field is seen by the beam in the cavities, i.e. if  $-\pi < \phi_s < 0$ .

### 3.3.6 Longitudinal Equation of Motion

To understand the limits of stability a longitudinal equation of motion can be developed by considering a long array of discrete rf gaps that are separated by the required drift distances to ensure synchronicity, see e.g. [98]. The synchronous particle then arrives at each rf gap with the designed synchronous phase ( $\phi_s$ ) and velocity ( $\beta_s$ ). The change in energy in each gap relative to the synchronous particle can be written per unit length as,

$$\frac{\Delta(W - W_s)}{L_a} = qE_0T(\cos \phi - \cos \phi_s), \quad (3.3.29)$$

and the relative change in phase across each drift of length  $\beta_s\lambda/2$  can be written per unit length as,

$$\frac{\Delta(\phi - \phi_s)}{\beta_s\lambda/2} = -2\pi \frac{W - W_s}{mc^2\gamma_s^3\beta_s^3\lambda}. \quad (3.3.30)$$

The above equations represent discrete and coupled differential equations that can be combined to form the continuous second-order non-linear longitudinal equation of motion,

$$\frac{1}{\beta_s^3\gamma_s^3} \frac{d}{dz} \left[ \beta_s^3\gamma_s^3 \frac{d(\phi - \phi_s)}{dz} \right] = \frac{k_{l,s}^2}{\sin(-\phi_s)} (\cos \phi - \cos \phi_s), \quad (3.3.31)$$

where the smoothed longitudinal wavenumber is,

$$k_{l,s}^2 = \frac{2\pi qE_0T \sin(-\phi_s)}{mc^2\beta_s^3\gamma_s^3\lambda}. \quad (3.3.32)$$

If the acceleration is slow and  $\beta_s\gamma_s$  is assumed constant then it can be shown that there exists an Hamiltonian<sup>1</sup> invariant of motion and stable motion ensues if,

$$\underbrace{\frac{\pi}{\beta_s^3\gamma_s^3\lambda} \left( \frac{W - W_s}{mc^2} \right)^2}_{\text{kinetic term}} + \underbrace{\frac{qE_0T}{mc^2} (\sin \phi - \phi \cos \phi_s)}_{\text{potential term}} \leq \frac{qE_0T}{mc^2} (\phi_s \cos \phi_s - \sin \phi_s), \quad (3.3.33)$$

Hamiltonian,  $H=T+V$

see e.g. [112]. The above equation defines a ‘fish-shaped’ region of stability in longitudinal phase space called the separatrix, which is shown enclosing the stable particle

<sup>1</sup>The Hamiltonian  $H$  is an invariant of a dynamical system written in terms of the coordinates and conjugate momenta from which the equations of motion can be derived using the well-known Hamilton equations:  $\frac{dx_i}{dt} = \frac{\partial H}{\partial p_i}$  and  $\frac{dp_i}{dt} = -\frac{\partial H}{\partial x_i}$ , see e.g. [111].

trajectories alongside the potential term in the Hamiltonian in Figure 3.8.

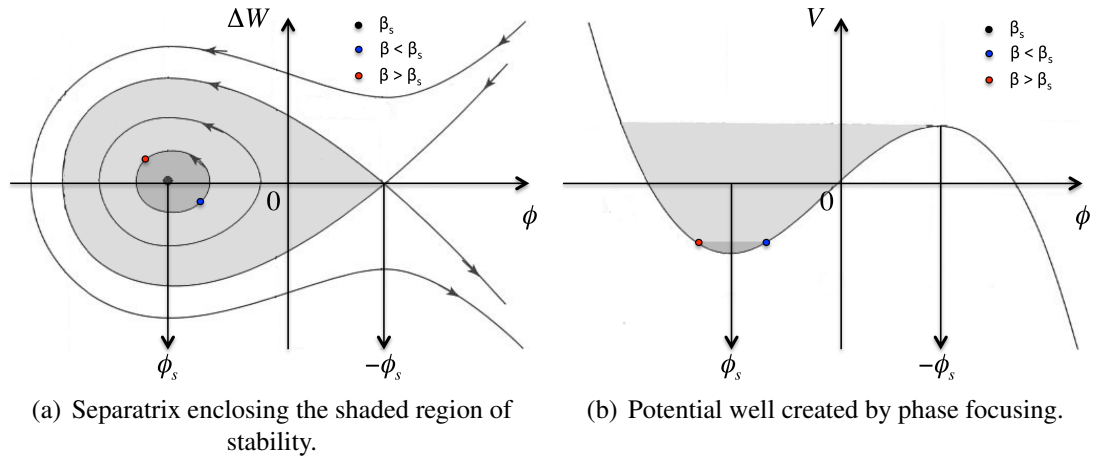


Figure 3.8: Region of stability about the synchronous particle in longitudinal phase space, where the accelerating field is increasing in time:  $-\pi < \phi_s < 0$ .

When the effects of acceleration are properly included and the calculation is carried out numerically the separatrix shape resembles a ‘golf club’ – the shape of the separatrix in the HIE linac can be inferred from the longitudinal acceptance plots in Figures 6.7 and 6.8.

The harmonic variation of the rf fields introduces inherent non-linearity, however for a low rate of acceleration and small oscillations, i.e.  $\Delta\phi = \phi - \phi_s \ll 1$ , the equation of motion in Equation 3.3.31 can be linearised to form the equation for a simple harmonic oscillator,

$$\frac{d^2\Delta\phi}{dz^2} + k_{l,s}^2\Delta\phi = 0. \quad (3.3.34)$$

There exist stable trajectories about the synchronous particle if  $-\pi < \phi_s < 0$  in a region called the ‘bucket’, shown by the shaded area in Figure 3.8. The area of linearity inside the separatrix decreases along with the rate of longitudinal oscillations as the synchronous phase moves higher up the crest of the accelerating field away from  $\phi_s = -\pi/2$  and towards  $\phi_s = 0$ ; the oscillations ‘freeze-out’ rapidly as the beam becomes relativistic. The linear beam dynamics can be parameterised using the Courant-Snyder formalism that will be introduced for the transverse plane.

The longitudinal equation of motion couples to the transverse equation of motion through the radial dependence of the transit-time factor. However, the magnitude of the accelerating field decreases slowly with the transverse displacement and the coupling

effect can be neglected for typical beam sizes. If the rate of acceleration is slow then the longitudinal equation of motion including the leading-order coupling terms can be written [113],

$$\frac{d^2 \Delta\phi}{dz^2} + k_{l,s}^2 \Delta\phi + k_{l,s}^2 \left( \frac{\pi}{\beta_s \gamma_s \lambda} \right)^2 [\cot \phi_s + \Delta\phi] x^2 = 0, \quad (3.3.35)$$

where the transverse coordinate is shown to enter at second-order.

### 3.3.7 KONUS Beam Dynamics

As previously mentioned, Combined Zero-Degree Structure (KONUS) beam dynamics is often employed in H-mode DTLs [65, 66]. As an example the beam dynamics in the first KONUS period of the REX IHS is shown in Figure 3.9, simulated using the LANA code. The geometry of the IHS is shown in Figure 3.2.

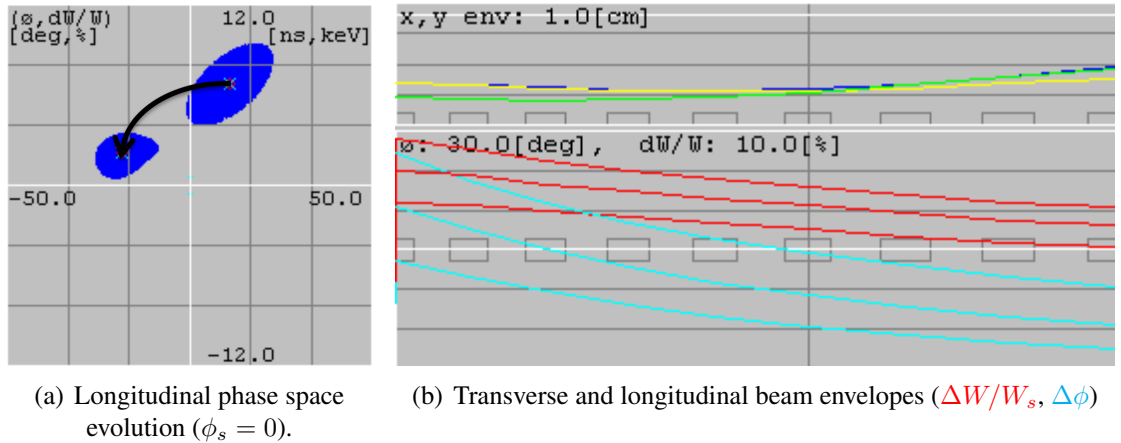


Figure 3.9: KONUS dynamics in the low energy drift-tube section of the REX IHS, simulated using the LANA code.

The KONUS concept facilitates relatively long sections of drift-tubes ( $\sim 10 - 20$  gaps) free of quadrupoles magnets, which are conventionally placed inside the drift-tubes to control the transverse beam size. Thus, unencumbered by quadrupoles, the relatively low capacitance of the small interdigital drift-tubes characteristic of H-mode cavities can be exploited to attain very high acceleration efficiencies compared with other DTLs in the same velocity regime. The effective transverse defocusing force is reduced by accelerating the beam over the crest of the accelerating field shown in Figure 3.7, where both the transverse and longitudinal (de)focusing forces vanish and the quadrupoles can

be grouped outside of the drift-tube sections; see Chapter 3.4.1 for a discussion of the transverse rf (de)focusing effect. The drift-tube section is designed with a fictitious synchronous particle operating at  $\phi_s = 0$  such that when the beam is launched into the drift-tube section faster and delayed with respect to the synchronous particle, i.e.  $\phi_0 > \phi_s$  and  $\beta_0 > \beta_s$ , the elevated velocity of the beam allows it to catch up and overtake the phase velocity of the fictitious particle as it is accelerated over the crest of the accelerating field from  $\phi > \phi_s = 0$  to  $\phi < \phi_s = 0$ . Although the stable area inside the separatrix shrinks to zero at  $\phi_s = 0$ , the beam can be accelerated stably if it enters the KONUS drift-tube section focused longitudinally. The beam is restricted to approximately one quarter of a longitudinal phase space oscillation before needing rebunching and injecting into another KONUS section with a new synchronous particle definition. After the low energy drift-tube section of the REX IHS the beam is focused transversally by an internal quadrupole triplet magnet. The first drift-tubes of the next section are adjusted to provide  $\phi_s = -30^\circ$  to rebunch the beam, as shown in Figure 3.10.

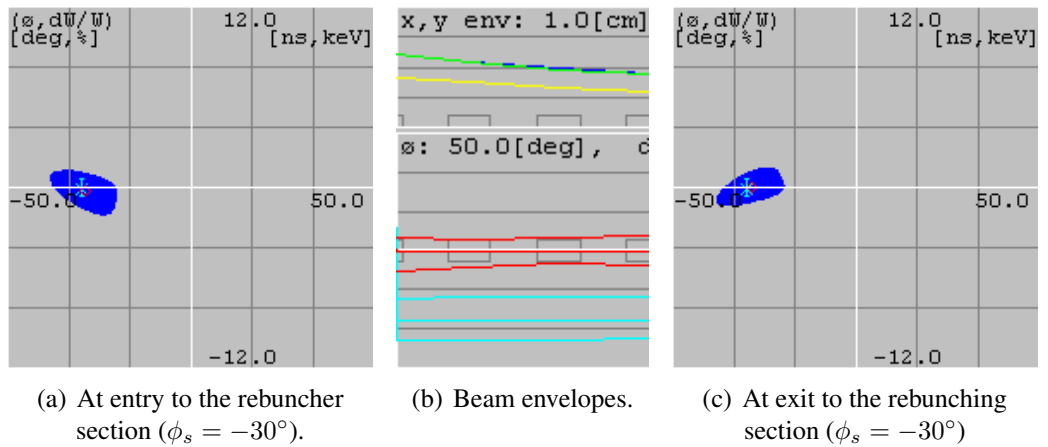
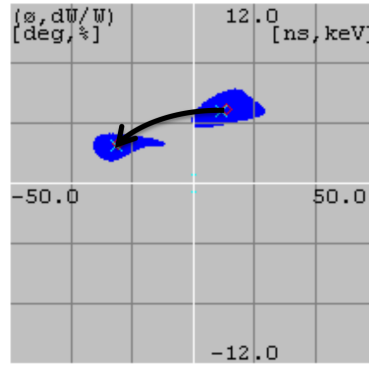
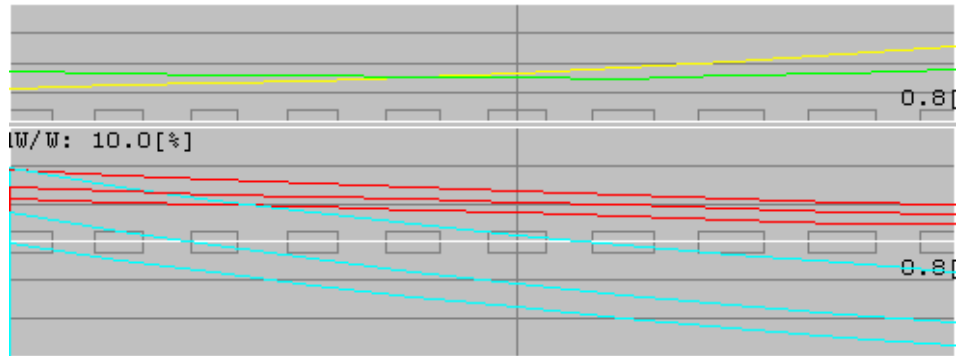


Figure 3.10: Rebuncher section with  $\phi_s = -30^\circ$  after the quadrupole triplet to prepare the beam for the second KONUS drift-tube section, simulated using the LANA code.

After a redefinition of the synchronous particle the beam is accelerated through a second KONUS drift-tube section, which is shown in Figure 3.11.



(a) Longitudinal phase space evolution ( $\phi_s = 0$ ).



(b) Transverse and longitudinal beam envelopes ( $\Delta W/W_s$ ,  $\Delta\phi$ ) with the same scale as Figure 3.9(b)

Figure 3.11: KONUS dynamics in the high energy drift-tube section of the REX IHS, simulated using the LANA code.

### 3.3.8 Beam Dynamics with Stepped RF Phasing

The beam is rarely, if ever, synchronous with the discrete set of phase velocities in the accelerating structures that make up independent cavity linacs. For reasons of economy the fewest number of different cavity families is usually employed, each with its own constant geometric velocity, and the rf phase of the individual cavities is stepped with respect to the beam to give a quasi-synchronicity to the beam dynamics. As a result, the beam is for most of the acceleration outside of the stable region defined by the equivalent stationary separatrix of the synchronous particle that represents the constant geometric velocity, see Figure 3.12. The longitudinal dynamics in independent cavity linacs is comprehensively analysed in [114], where it is shown that the equation of motion about the average stepped synchronous phase  $\bar{\phi}_s$  is in fact equivalent to Equation 3.3.34, which was derived above for synchronous acceleration.

Figure 3.12 demonstrates the phase slippage inside each cavity during acceleration

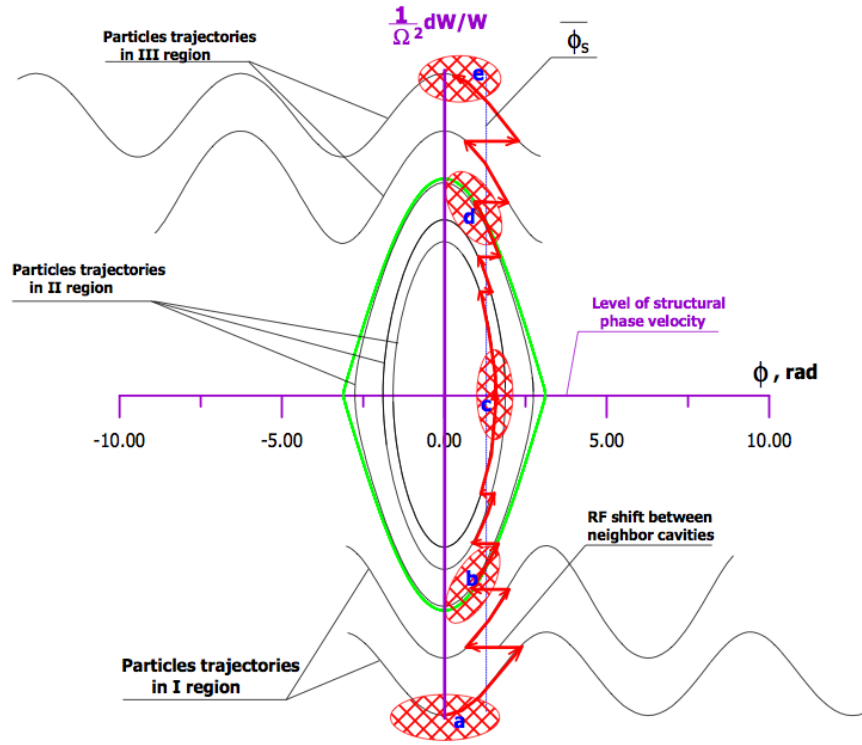


Figure 3.12: Longitudinal dynamics through the stationary separatrix of a fixed  $\beta_g$  independent cavity linac with rf phase stepping. Reprinted with permission from Figure 3 of [114].

and the discrete shifts of phase imposed between neighbouring cavities. The beam rotates about the reference particle much like the bunch rotates about the synchronous particle inside the separatrix of a conventional DTL. For a two-gap resonator where the phase in the first gap is denoted  $\phi_1$  and the phase in the second gap is denoted  $\phi_2$  the phase slips according to the following rules:

- If  $\beta < \beta_g = \beta_s$  then  $\phi_1 < \phi_s < \phi_2$  such that  $\phi_s = \overline{\phi_s} = (\phi_1 + \phi_2)/2$ , i.e. the beam arrives earlier than the synchronous phase in the first gap.
- If  $\beta = \beta_g = \beta_s$  then  $\phi_1 = \phi_2 = \phi_s$ , i.e. the beam arrives synchronously in both gaps.
- If  $\beta > \beta_g = \beta_s$  then  $\phi_1 > \phi_s > \phi_2$  such that  $\phi_s = \overline{\phi_s} = (\phi_1 + \phi_2)/2$ , i.e. the beam arrives later than the synchronous phase in the first gap.

The properties of the reference particle will be denoted, e.g.  $\beta_0$ ,  $\phi_0$  and  $W_0$ , and will be used throughout this thesis to differentiate from the synchronous particle; usually the reference particle is the ‘centre-of-mass’ of the bunch.

## 3.4 Transverse Beam Dynamics

### 3.4.1 RF Defocusing

The cavity must be opened in some way to permit the passage of a beam and as a result the accelerating electric field diverges and leaks into the beam pipe or drift-tubes, see e.g. Figure 7.1 of [98]. The electric field close to the axis of an accelerating cavity or gap with axial symmetry can be written in cylindrical coordinates as an expansion of the accelerating field on axis where,

$$E_z(r, z) = E_z(0, z) - \frac{r^2}{4} \frac{\partial^2 E_z(0, z)}{\partial z^2} + O(r^4), \quad (3.4.1)$$

$$E_r(r, z) = -\frac{r}{2} \frac{\partial E_z(0, z)}{\partial z} + \frac{r^3}{16} \frac{\partial^3 E_z(0, z)}{\partial z^3} + O(r^5), \quad (3.4.2)$$

see e.g. [115]. The divergence of the accelerating field introduces transverse electric field components around the beam axis that act to focus or defocus the beam depending on the rf phase. With the longitudinal electric field directed for acceleration, the transverse field components are naturally focusing on entering the gap or cavity and defocusing on exiting. Although it would be reasonable to expect the two transverse impulses to cancel, the time variation and condition for longitudinal stability results in a net defocusing effect because the field level is larger as the bunch leaves the gap. Other effects caused by the changing particle velocity and the radial field dependence, which is more important in electron linacs, will not be discussed here. In fact, it can be shown [116] that stable acceleration of bunches, i.e. longitudinal stability, is not simultaneously compatible with transverse beam stability and the transverse electric field components act to defocus the beam, thus external focusing elements such as quadrupoles or solenoids are required to maintain beam stability. To leading-order, the (de)focusing impulse imparted on a charged particle in an rf gap is,

$$\Delta r'_{\text{rf}} = \frac{\pi q E_0 T \sin(-\phi) L_a}{m c^2 \gamma^3 \beta^3 \lambda} r, \quad (3.4.3)$$

assuming that both the velocity and coordinate changes across the gap can be neglected, see [98] for the derivation. The transverse force is indeed defocusing for  $\phi = \phi_s < 0$  and is very strong for low velocity beams, becoming vanishingly small in the relativistic limit.

The thin-lens approximation is generally a good one and can be simply extended using the ‘kick-drift-kick’ approximation where the above impulse is split into two kicks that are applied at each end of the gap or cavity, as implemented in the LANA code. The phase dependence of the rf (de)focusing force couples the transverse and longitudinal dynamics in the accelerating cavities. The effect is to modulate the transverse beam envelope, which in certain resonant cases can excite particles into oscillations that are beyond the stability limit provided by external focusing elements.

### 3.4.2 Beam-steering in Quarter-wave Resonators

The dipole electromagnetic field components on the beam axis of the quarter-wave resonator impart phase-dependent beam-steering forces that couple the longitudinal and transverse motions. If not compensated the coupling causes degradation of the transverse beam quality and beam losses on the aperture. The dominant field components include a horizontal component of magnetic field that curls around the internal conductor, and a vertical component of electric field produced by the intrinsic asymmetry of the geometry of the quarter-wave resonator in the vicinity of the beam axis, shown in Figures 3.4(a) and 3.13.

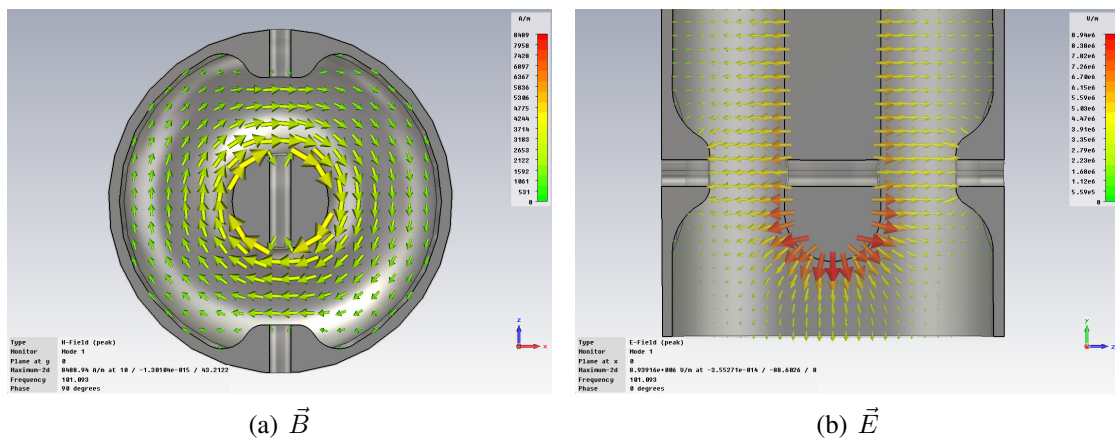


Figure 3.13: The electromagnetic fields in the vicinity of the beam axis of the HIE linac high- $\beta$  cavity.

The steering effect on axis can be written in the square-wave approximation [117,

118] as,

$$\Delta y'_{\text{steering}} = \frac{qE_0(y_0)L_a T(\beta)}{A\gamma uc} \left[ \underbrace{\frac{\kappa_B(y_0)}{\beta}}_{\text{magnetic}} - \underbrace{\frac{\kappa_E(y_0)}{c\beta^2} \cot \frac{\pi\beta_g}{2\beta}}_{\text{electric}} \right] \sin \phi_s, \quad (3.4.4)$$

where the parameters,

$$\kappa_B(y_0) = \frac{1}{2g} \frac{\int_{-\infty}^{+\infty} |B_x(y_0, z)| dz}{\int_{-\infty}^{+\infty} |E_z(y_0, z)| dz} = \frac{1}{2g} \frac{\int_{-\infty}^{+\infty} |B_x(y_0, z)| dz}{E_0(y_0)L_a}, \quad (3.4.5)$$

and,

$$\kappa_E(y_0) = \frac{1}{2g} \frac{\int_{-\infty}^{+\infty} |E_y(y_0, z)| dz}{\int_{-\infty}^{+\infty} |E_z(y_0, z)| dz} = \frac{1}{2g} \frac{\int_{-\infty}^{+\infty} |E_y(y_0, z)| dz}{E_0(y_0)L_a}, \quad (3.4.6)$$

describe the normalised square-wave transverse field component on the beam axis at a height  $y_0$  on the internal conductor –  $y_0$  is defined as the straight part of the internal conductor above the curved end, as shown in Figure 3.14. Note that by definition  $\kappa_B, \kappa_E \geq 0$ . The variation of  $\kappa_B$  and  $\kappa_E$  with  $y_0$  in the HIE-ISOLDE cavities is typical of quarter-wave cavities of this frequency, see e.g. Figure 2 of [117] and the height of the beam axis on the internal conductor is important from the perspective of the beam dynamics and is investigated in Chapter 6.4.

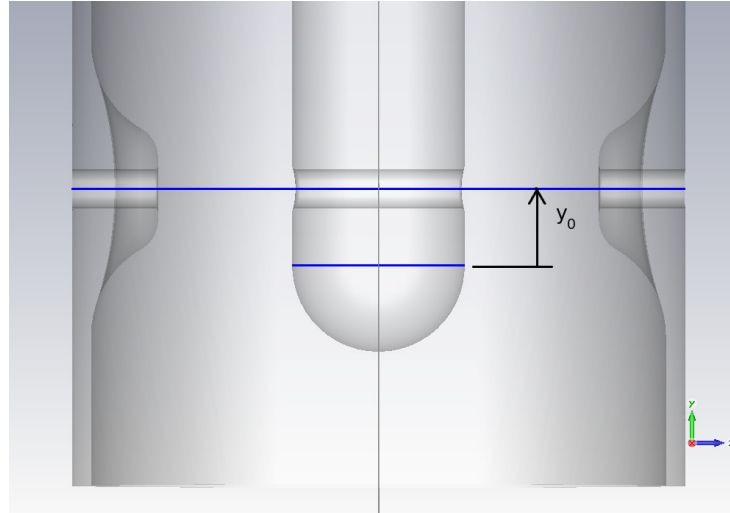


Figure 3.14: The definition of  $y_0$  in the quarter-wave resonator.

The analytic description of the beam-steering in the high- $\beta$  cavity is shown in Figure 3.15 as a function of  $\beta$  for the extremes of the  $A/q$  acceptance with the cavity op-

erating nominally. The steering force acts in the vertical direction and scales with  $q/A$ , making emittance growth control more challenging for lighter or more highly charged beams. It remains invariant whether accelerating or decelerating at stable synchronous phases, i.e. if  $\phi_s = -20^\circ$  or  $\phi_s = -160^\circ$ . At high velocities, typically  $\beta \gtrsim 2\beta_g$ , the difference in the  $\beta$  dependence of the two steering components becomes negligible and the overall steering force is cancelled by the opposite sense of the electric and magnetic contributions. Around the geometric velocity, and close to where the cavity is normally operated, the electric steering contribution in each gap cancels and the dominant effect requiring compensation is the magnetic contribution. The magnitude of the beam-steering is not critical in this region for  $A/q = 4.5$  but particles are lost on the aperture in simulations of the HIE linac without steering correction for  $A/q = 2.5$ . The electric steering contribution is much more important at low velocity because of the  $1/\beta^2$  dependence. In the limit that  $T(\beta) \rightarrow 0$ , i.e. as  $\beta \rightarrow \beta_g/2$ , the electric contribution adds in each gap, which limits the beam quality in the low energy section when decelerating. Although external steering elements are sufficient to return the centroid back to the design orbit, the compensation must take place inside the resonator to reduce the emittance growth caused by the finite phase spread of the bunch coupling with the time variation of the electromagnetic fields inside the cavity.

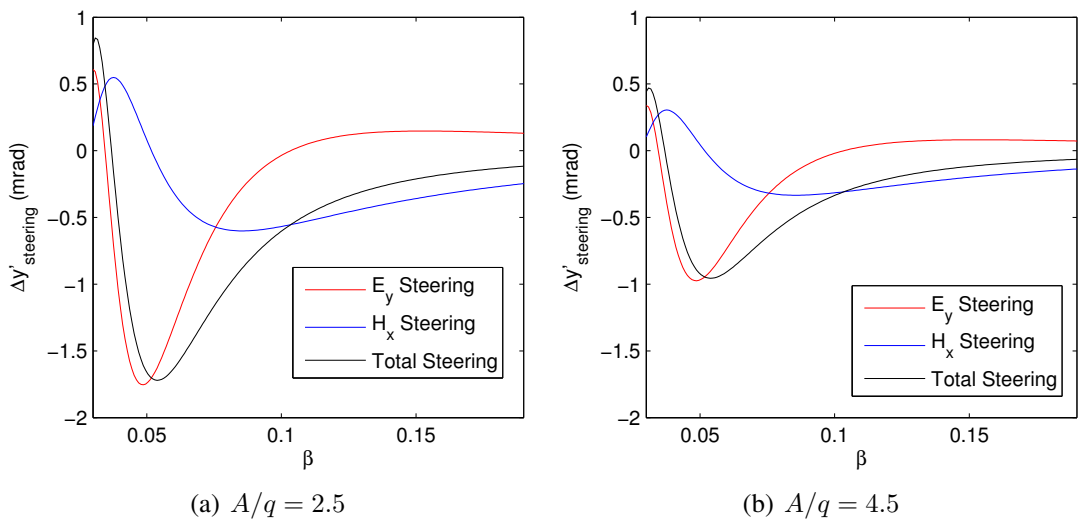


Figure 3.15: An analytic calculation of the beam-steering in the high- $\beta$  cavity ( $\beta_g = 10.3\%$ ,  $E_0 = 6$  MV/m and  $\phi_s = -20^\circ$ ).

### 3.4.3 Quadrupoles as Beam Focusing Elements

To counteract the rf defocusing effect quadrupole magnets are most commonly placed either inside the drift-tubes or outside of the cavity to provide the restoring forces needed to keep the beam stable during acceleration. The quadrupole field pattern provides linear focusing and defocusing forces simultaneously in orthogonal planes such that an overall focusing effect can be attained with a series of quadrupoles of alternating polarity, according to the principle of strong focusing [119]. Common configurations of quadrupoles include the FODO, doublet (FDO) and triplet (FDFO) lattices where F refers to focusing and D to defocusing quadrupoles in a given plane, which are discussed at length in [49].

The Lorentz equation can be used to show how a quadrupole field provides linear attractive or repulsive forces in the two orthogonal transverse planes,

$$F_x(x, z) = -qc\beta_z G_x(z)x \quad \text{and} \quad F_y(y, z) = +qc\beta_z G_y(z)y, \quad (3.4.7)$$

where the quadrupole gradients are,

$$G_x(z) = \frac{\partial B_y(z)}{\partial x} \quad \text{and} \quad G_y(z) = \frac{\partial B_x(z)}{\partial y}, \quad (3.4.8)$$

respectively, specified by the ratio of the field at the pole-tip with its radius, i.e.  $G = B_0/R$ . Once developed, the transverse equations of motion can be written [120],

$$x'' + k_{\text{quad}}^2(z)x = 0, \quad \text{and} \quad y'' - k_{\text{quad}}^2(z)y = 0, \quad (3.4.9)$$

where,

$$k_{\text{quad}}(z) = \frac{|qG(z)|}{mc\gamma_z\beta_z} = \frac{|qG(z)|}{p_z}. \quad (3.4.10)$$

The equation of motion in the  $x$ -plane resembles that of a simple harmonic oscillator and describes stable oscillations about the axis of the quadrupole, whereas the equation of motion in the  $y$ -plane describes unstable and divergent trajectories. The force terms driving the above equations enter at the locations of the quadrupoles, thus  $k_{\text{quad}}$  is in general a function of  $z$ , i.e.  $k_{\text{quad}} = k_{\text{quad}}(z)$ , and for a periodic system the equations represent Hill's equation, in which the restoring force is modulated periodically along

the linac. The Hill's equation is used to develop the Courant-Snyder formalism that is commonly used to represent charged particle beams.

### 3.4.4 Solenoids as Beam Focusing Elements

For the various reasons discussed in Chapter 2.4.3.2, solenoids are often preferred to quadrupoles and incorporated inside the cryomodules of superconducting linacs to control the transverse size of ion beams below about 40 MeV/u. The equations of motion of a charged particle in a solenoid field can be written in the linear approximation [106] as,

$$x'' - \frac{q}{p_z} \left[ B_z(z)y' + \frac{y}{2}B'_z(z) \right] = 0, \quad (3.4.11)$$

$$y'' + \frac{q}{p_z} \left[ B_z(z)x' + \frac{x}{2}B'_z(z) \right] = 0, \quad (3.4.12)$$

where the leading-order field components are,

$$B_z(x, y, z) = B_z(z) + O(x^2, y^2), \quad (3.4.13)$$

$$B_x(x, 0, z) = -\frac{x}{2}B'_z(z) + O(x^3), \quad \text{and} \quad B_y(0, y, z) = -\frac{y}{2}B'_z(z) + O(y^3). \quad (3.4.14)$$

The dynamics is coupled in the transverse plane and the beam rotates inside the solenoid. As a direct consequence, the equations of motion are intrinsically non-linear,<sup>1</sup> even in an ideal solenoid with a linear fringe-field, i.e.  $\partial B'_z/\partial z = 0$ , and the above linearisation is only strictly valid in the paraxial approximation, i.e.  $x', y' \ll 1$ . The coupled equations can be uncoupled [106, 122] in a reference frame that rotates with the Larmor frequency  $\omega_L = qB_z/2\gamma_z m$  about the axis of the solenoid and, in that reference frame, the equations of motion reduce to the first form presented in Equation 3.4.9 for the focusing plane of a quadrupole. The solenoid focuses identically in both orthogonal planes of the Larmor frame and the transverse equations of motion can be expressed in cylindrical coordinates as,

$$r'' + k_{\text{sol}}^2(z) = 0 \quad \text{and} \quad \theta = - \int k_{\text{sol}}(z) dz, \quad (3.4.15)$$

<sup>1</sup>Additional coupling terms are generated by the angular momentum of the beam about the solenoid's axis, i.e.  $L_z = xp_y - yp_x$ , and enter at third-order as  $B'_z x'(x'y - y'x)/2$  and  $B'_z y'(x'y - y'x)/2$  in Equations 3.4.11 and 3.4.12, respectively, see [121].

where,

$$k_{\text{sol}}^2(z) = \left( \frac{q}{2mc\gamma_z\beta_z} \right)^2 \int B_z^2(z) dz = \left( \frac{q}{2p_z} \right)^2 \int B_z^2(z) dz. \quad (3.4.16)$$

The beam is rotated about the axis of the solenoid at a rate of  $\omega_L$ , which is proportional to the normalised focusing strength  $k_{\text{sol}}$ . The solenoid magnet is conventionally used to focus lower velocity beams because the focusing term goes with  $1/p_z^2$  instead of  $1/p_z$  for the quadrupole.

The physical origin of the focusing effect is not immediately obvious in the equations presented above. Its source is illuminated somewhat by considering paraxial rays entering the solenoid off-axis and realising that all rays must be rotated at the same rate for a linear focusing effect to occur, i.e. there must be a linear increase in azimuthal velocity with radius, see e.g. Figure 1 of [123]. A paraxial ray or ‘cold’ beam would remain unrotated in the longitudinal magnetic field because  $v_z \times B_z = 0$ , however due to the diverging fields at the ends of the solenoid some angular momentum is imparted on the beam such that a coupling with the longitudinal magnetic field can arise. If the field on-axis at the entrance to the solenoid is represented by a step function then the fringe-field at  $z = z_0$  can be represented by the Dirac delta function,<sup>1</sup>

$$B_r(r, z) = -\frac{r}{2} B_z(z_0) \delta(z - z_0) + O(r^3). \quad (3.4.17)$$

It follows that the fringe-field imparts a linear transverse impulse such that a paraxial ray will develop an azimuthal velocity in direct proportion to its radius  $r_0$  as follows,

$$\beta_\theta = -r_0 \frac{qB_z(z_0)}{2mc\gamma_z} \int_{z_0-\epsilon}^{z_0+\epsilon} \delta(z - z_0) dz = -r_0 \frac{qB_z(z_0)}{2mc\gamma_z} = -\frac{r_0}{2} \frac{\omega_c}{c}, \quad (3.4.18)$$

where  $\epsilon$  is a small quantity.<sup>2</sup> Importantly, the ray now performs cyclotron oscillations with a radius  $r_0/2$  about an axis parallel to the solenoid, which forces the helical orbit in the longitudinal field to pass through the solenoid axis after half an oscillation. This is true for all paraxial rays, independent of their initial position, and because all paraxial rays

<sup>1</sup>  $\frac{d}{dx} [H(x)] = \delta(x)$  where  $H(x)$  is the Heaviside step function and  $\delta(x)$  is the Dirac delta function.

<sup>2</sup>  $\int_{x_0-\epsilon}^{x_0+\epsilon} \delta(x - x_0) dx = 1$ , where  $\epsilon$  is non-zero.

perform cyclotron oscillations at the same frequency,

$$\omega_c = \frac{qB_z}{m\gamma_z}, \quad (3.4.19)$$

they pass through the axis of the solenoid at the same instant. The beam will continue to make coherent oscillations inside the solenoid every succeeding cyclotron oscillation, see [123] for more details, whilst rotating at a rate of  $\omega_c/2$  about the axis of the solenoid. Although the angular momentum developed in the fringe field on entry to the solenoid is largely cancelled on exit, the overall radial velocity about the solenoid's axis is reduced and the beam is focused by tuning  $k_{\text{sol}}$ .

### 3.4.5 Transverse Equation of Motion

When the rate of acceleration is slow, i.e.  $d(\beta_s\gamma_s)/dz \approx 0$ , the transverse equation of motion can be written,

$$\frac{d^2x}{dz^2} + \left[ k_{\text{sol}}^2(z) - \frac{k_{l,s}^2}{2} \right] x = 0, \quad (3.4.20)$$

where  $k_{l,s}$  is the smoothed longitudinal wavenumber, which assumes that the effect of the rf (de)focusing in the cavities is equivalent to a continuous travelling wave. The appropriate balance between the external focusing applied to the beam, in this case solenoid focusing, and the defocusing effect of the cavities must be found to ensure the beam is stably accelerated. The analysis of transverse stability is commonly done at first-order with the matrix formalism, which has been extensively studied, see e.g. the Smith and Gluckstern stability charts of [124], and for focusing with solenoids see [125]. The condition for transverse stability on the trace of the transfer matrix ( $R$ ) that describes the dynamics in a given uncoupled plane is [98],

$$|\text{Tr}(R)| \leq 2. \quad (3.4.21)$$

In the smooth approximation, i.e. if the phase advance of the oscillations is slow with respect to the magnet period of the accelerator lattice, the transverse oscillations can be described by the smoothed wavenumber  $k_{l,s}$ , which includes the rf (de)focusing effect for

the synchronous particle, and the equation of motion can be written simply as,

$$\frac{d^2x}{dz^2} + k_{t,s}^2 x = 0. \quad (3.4.22)$$

For particles that are non-synchronous, i.e.  $\phi = \phi_s + \Delta\phi$ , the transverse equation of motion is coupled at first-order to the longitudinal equation of motion and can be written including leading-order coupling terms as [126],

$$\frac{d^2x}{dz^2} + \left[ k_{t,s}^2 - k_{l,s}^2 \cot \phi_s \frac{\Delta\phi}{2} \right] x = 0. \quad (3.4.23)$$

Assuming that the longitudinal motion is equivalent to harmonic oscillations about the synchronous particle with amplitude  $\Phi_0$ , the motion in the linear region of the separatrix shown in Figure 3.8(a) can be expressed,

$$\Delta\phi = \Phi_0 \sin(k_{l,s}z), \quad (3.4.24)$$

and one arrives at the Mathieu-Hill equation,

$$\frac{d^2x}{dz^2} + F(z)x = 0, \quad \text{where} \quad F(z) = k_{t,s}^2 - k_{l,s}^2 \frac{\Phi_0}{2} \cot \phi_s \sin(k_{l,s}z), \quad (3.4.25)$$

where the transverse restoring force is modulated periodically. By normalising the longitudinal coordinate and introducing a dimensionless variable,

$$\tau = \frac{k_{l,s}}{2\pi} z, \quad (3.4.26)$$

which describes the number of longitudinal oscillations performed, the transverse equation of motion can be expressed in the form of the Mathieu equation [127],

$$\frac{d^2x}{d\tau^2} + \pi^2 [a + 2q \sin 2\pi\tau] x = 0, \quad (3.4.27)$$

where,

$$a = \left( \frac{2k_{t,s}}{k_{l,s}} \right)^2 \quad \text{and} \quad q = \Phi_0 \cot(-\phi_s). \quad (3.4.28)$$

The regions of stability for the Mathieu equation are shown in Figure 3.16 after numerical calculation, where the stable regions are shaded. This type of instability is often described as a parametric resonance because the equation describing the simple harmonic motion is parametrically excited by the periodic variation of a parameter describing the motion, namely the resonant frequency, e.g. a child parametrically excites a swing by periodically changing its moment of inertia, or a pendulum can be parametrically excited by a periodic variation in its length. The transverse equation of motion becomes resonantly unstable if the smoothed transverse and longitudinal phase advances satisfy the condition,

$$k_{t,s} = \frac{j}{2} k_{l,s} \quad j = 1, 2, 3, \dots, \quad (3.4.29)$$

where the index  $j$  denotes the order of the instability. The regions of stability are probed in the HIE linac in Chapter 6.2.

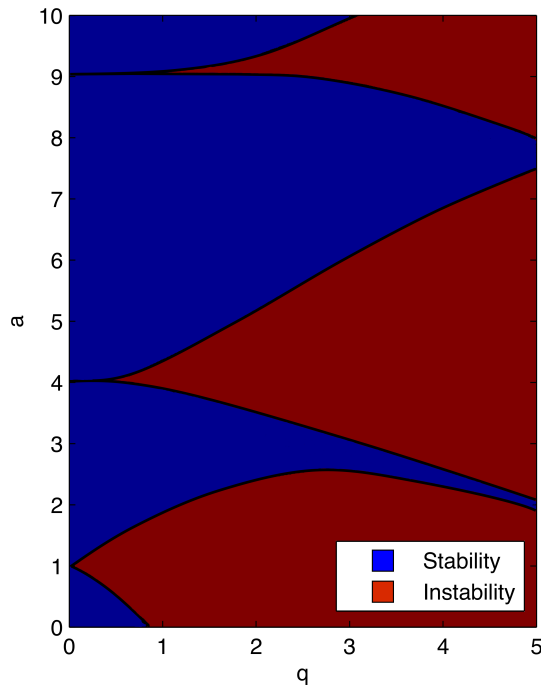


Figure 3.16: Stability regions of the Mathieu-Hill equation calculated numerically.

With the application of periodic boundary conditions it can be shown that there exists solutions to the Mathieu-Hill equation of the form [127],

$$x(z) = \sqrt{\epsilon \tilde{\beta}(z)} \cos(\tilde{\psi}(z) + \psi_0), \quad (3.4.30)$$

where  $\epsilon$  and  $\psi_0$  are constants of motion. The envelope function  $\tilde{\beta}(z)$  and phase function

$\tilde{\psi}(z)$  are commonly used to parameterise beams and are related by,

$$\tilde{\psi}(z) = \int \frac{dz}{\tilde{\beta}(z)}. \quad (3.4.31)$$

In principle, the above solution and its associated functions only exist in the presence of strict periodic boundary conditions, which can be imposed in circular resonance accelerators such as synchrotrons but not in linear systems. Nonetheless, the  $\tilde{\beta}$ -function can still be used to parameterise beams in the quasi-periodic structures of transfer lines and linear accelerators. In a circular machine the periodicity of the lattice itself uniquely defines closed solutions for  $\tilde{\beta}(z)$ , however in a linac such solutions do not exist and equivalent  $\tilde{\beta}$ -functions at input are relied on, defined by the beam itself, and are propagated through the linac. The beam must therefore be matched into the quasi-periodic structure of the linear accelerator.

A particle viewed in phase space at positions separated periodically in the accelerator lattice, i.e. at the locations  $z = z_0 + nL$ , will follow elliptical orbits according to the equation,

$$\epsilon = \tilde{\gamma}(z)x^2 + 2\tilde{\alpha}(z)xx' + \tilde{\beta}(z)x'^2, \quad (3.4.32)$$

where the Courant-Snyder or Twiss parameters  $\tilde{\alpha}(z)$ ,  $\tilde{\beta}(z)$  and  $\tilde{\gamma}(z)$  are related by,

$$\tilde{\alpha}(z) = -\frac{1}{2} \frac{d\tilde{\beta}(z)}{dz} \quad \text{and} \quad \tilde{\gamma}(z) = \frac{1 + \tilde{\alpha}(z)^2}{\tilde{\beta}(z)}. \quad (3.4.33)$$

The phase space ellipse is shown in Figure 3.17 enclosing an area of phase space equal to  $\pi\epsilon$ , which is an invariant of the motion. The period-to-period advance around the ellipse can be parameterised by the phase advance,

$$\mu = \Delta\tilde{\Psi} = \int_{z_0}^{z_0+L} \frac{dz}{\tilde{\beta}(z)}. \quad (3.4.34)$$

The smooth approximation can be applied when the phase advance across the period

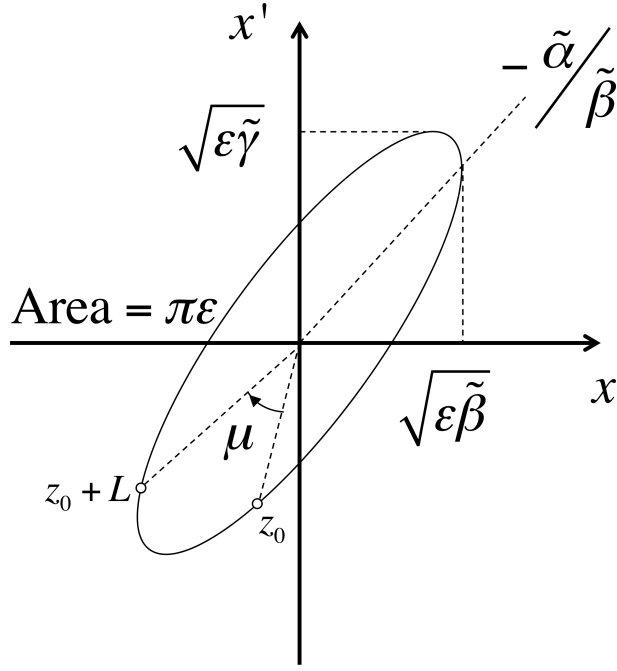


Figure 3.17: Transverse phase space ellipse of a particle at  $z_0$  and  $z_0 + L$  with an emittance  $\epsilon$ , and the associated Twiss parameter definitions.

defining the accelerator magnet period ( $L$ ) is small, i.e.,

$$\frac{\Delta\tilde{\Psi}}{2\pi} = \frac{\tilde{\Psi}(z_0 + L) - \tilde{\Psi}(z_0)}{2\pi} \ll 1, \quad (3.4.35)$$

and particles undergo harmonic-like oscillations inside the envelope defined by  $\tilde{\beta}(z)$ . The phase space ellipse equation can be written in  $\sigma$ -matrix form as [128],

$$1 = \vec{X}^T \sigma^{-1} \vec{X}, \quad (3.4.36)$$

where,

$$\sigma = \epsilon \begin{pmatrix} \tilde{\beta} & -\tilde{\alpha} \\ -\tilde{\alpha} & \tilde{\gamma} \end{pmatrix}, \quad \vec{X} = \begin{pmatrix} x \\ x' \end{pmatrix}, \quad \vec{X}^T = \begin{pmatrix} x & x' \end{pmatrix}, \quad (3.4.37)$$

and  $\vec{X}^T$  is the transpose of vector  $\vec{X}$ . The transformation of the phase space ellipse through a series of linear beam line elements can then be described in terms of the transfer matrix ( $R$ ) and written as,

$$\sigma_1 = R\sigma_0 R^T. \quad (3.4.38)$$

From this equation one can show that the Twiss parameters in any given uncoupled plane are propagated through a transfer matrix according to,

$$\begin{pmatrix} \tilde{\beta} \\ \tilde{\alpha} \\ \tilde{\gamma} \end{pmatrix}_1 = \begin{pmatrix} R_{11}^2 & -2R_{11}R_{12} & R_{12}^2 \\ -R_{11}R_{21} & 1 + 2R_{12}R_{21} & -R_{12}R_{22} \\ R_{21}^2 & -2R_{21}R_{22} & R_{22}^2 \end{pmatrix} \begin{pmatrix} \tilde{\beta} \\ \tilde{\alpha} \\ \tilde{\gamma} \end{pmatrix}_0, \quad (3.4.39)$$

and  $\epsilon$  is a constant. The Twiss parameters can be matched by adjusting the appropriate transfer matrix elements using numerical matching routines included in design codes such as TRACE 3-D [107].

### 3.4.6 Beam Representation and Emittance

As a direct consequence of Liouville's theorem [129] it is possible to choose a single set of Twiss parameters that are representative of an entire beam of particles. Liouville's theorem states that the density of non-interacting particles in phase space remains constant under the action of conservative forces, even if the forces are non-linear. The contour lines of constant particle density in phase space will propagate such that, although their shape and projection onto any given phase space plane might change, their total volume in phase space will not change [130]. In other words, the beam emittance is conserved.

Twiss parameters calculated from the second moments of the beam intensity distribution are commonly used to characterise beams. The rms emittance is used as a figure of merit to describe the beam quality because it is sensitive to the distortions caused by non-linear forces, which can produce an effective increase in the emittance by diluting the particle density in phase space through filamentation, see e.g. Figure 1 of [131]. In addition, beams with matched rms properties can be thought of as equivalent if they are composed of the same particle species and have the same kinetic energy. In the absence of space-charge the propagation of the rms emittance in a linear system is independent of the distribution of particles if the rms emittance is matched, see e.g. [132].

In general, the  $\sigma$ -matrix formalism can be extended to include all  $n$  components of  $\vec{X}$  and the  $n$ -dimensional invariant of motion or emittance for the fully coupled motion is

attained from the determinant of  $\sigma_{n \times n}$ , i.e.,

$$\epsilon_n = \sqrt{\det(\sigma_{n \times n})}. \quad (3.4.40)$$

The  $\sigma$ -matrix including all 6 phase space coordinates is related to the second moments of the particle distribution according to,

$$\sigma_{6 \times 6} = \begin{pmatrix} \langle x^2 \rangle & \langle xx' \rangle & \langle xy \rangle & \langle xy' \rangle & \langle x\Delta z \rangle & \langle x\frac{\Delta p}{p} \rangle \\ \langle x'x \rangle & \langle x'^2 \rangle & \langle x'y \rangle & \langle x'y' \rangle & \langle x'\Delta z \rangle & \langle x'\frac{\Delta p}{p} \rangle \\ \langle yx \rangle & \langle yx' \rangle & \langle y^2 \rangle & \langle yy' \rangle & \langle y\Delta z \rangle & \langle y\frac{\Delta p}{p} \rangle \\ \langle y'x \rangle & \langle y'x' \rangle & \langle y'y \rangle & \langle y'^2 \rangle & \langle y'\Delta z \rangle & \langle y'\frac{\Delta p}{p} \rangle \\ \langle \Delta zx \rangle & \langle \Delta zx' \rangle & \langle \Delta zy \rangle & \langle \Delta zy' \rangle & \langle \Delta z^2 \rangle & \langle \Delta z\frac{\Delta p}{p} \rangle \\ \langle \frac{\Delta p}{p}x \rangle & \langle \frac{\Delta p}{p}x' \rangle & \langle \frac{\Delta p}{p}y \rangle & \langle \frac{\Delta p}{p}y' \rangle & \langle \frac{\Delta p}{p}\Delta z \rangle & \langle \frac{\Delta p}{p}^2 \rangle \end{pmatrix}. \quad (3.4.41)$$

For a given phase space particle density distribution, e.g.  $\rho(x, x', y, y', \Delta z, \frac{\Delta p}{p})$ , the second moments can be written in the form,

$$\langle xy \rangle = \frac{\int_{-\infty}^{+\infty} (x - \langle x \rangle)(y - \langle y \rangle) \rho(x, x', y, y', \Delta z, \frac{\Delta p}{p}) dV}{\int_{-\infty}^{+\infty} \rho(x, x', y, y', \Delta z, \frac{\Delta p}{p}) dV} \quad (3.4.42)$$

where the first moments have the form,

$$\langle x \rangle = \frac{\int_{-\infty}^{+\infty} x \rho(x, x', y, y', \Delta z, \frac{\Delta p}{p}) dV}{\int_{-\infty}^{+\infty} \rho(x, x', y, y', \Delta z, \frac{\Delta p}{p}) dV}, \quad (3.4.43)$$

and  $dV = dx dx' dy dy' d\Delta z d\frac{\Delta p}{p}$ . The complete  $\sigma_{6 \times 6}$  matrix can be written as a subset of matrices that describe each 2-dimensional projection or trace space as,

$$\sigma_{6 \times 6} = \begin{pmatrix} \sigma_{xx} & \sigma_{xy} & \sigma_{xz} \\ \sigma_{yx} & \sigma_{yy} & \sigma_{yz} \\ \sigma_{zx} & \sigma_{zy} & \sigma_{zz} \end{pmatrix}, \quad (3.4.44)$$

and after comparing  $\sigma_{xx}$  with Equation 3.4.36 the rms emittance in trace space can be written written,

$$\epsilon_x = \sqrt{\det(\sigma_{xx})} = \sqrt{\langle x^2 \rangle \langle x'^2 \rangle - \langle xx' \rangle^2}. \quad (3.4.45)$$

When tracking a distribution of  $N$  particles in beam dynamics simulation codes the rms Twiss parameters in any given phase space projection can be extracted statistically from the output particle distribution using the relationships,

$$\tilde{\alpha}_x = -\frac{\langle xx' \rangle}{\epsilon_x}, \quad \tilde{\beta}_x = \frac{\langle x^2 \rangle}{\epsilon_x} \quad \text{and} \quad \tilde{\gamma}_x = \frac{\langle x'^2 \rangle}{\epsilon_x}, \quad (3.4.46)$$

where,

$$\langle x \rangle = \frac{1}{N} \sum_{i=1}^N x_i, \quad \langle x' \rangle = \frac{1}{N} \sum_{i=1}^N x'_i, \quad \langle x^2 \rangle = \frac{1}{N} \sum_{i=1}^N (x_i - \langle x \rangle)^2,$$

$$\langle x'^2 \rangle = \frac{1}{N} \sum_{i=1}^N (x'_i - \langle x' \rangle)^2 \quad \text{and} \quad \langle xx' \rangle = \frac{1}{N} \sum_{i=1}^N (x_i - \langle x \rangle)(x'_i - \langle x' \rangle),$$

see e.g. [133]. The emittance containing a given fraction of the beam is calculated by scaling the emittance of the rms ellipse until the given fraction of  $N$  particles is contained within the scaled ellipse.

Various distributions are used to simulate particle beams [134]; the Gaussian and Waterbag distributions were used throughout this thesis in the design studies before the realistic distribution output from the RFQ beam dynamics simulations was used. The properties of these two distributions are summarised in Table 3.1. The Waterbag uniformly popu-

Table 3.1: Properties of the 4-dimensional Gaussian and Waterbag distributions

Distribution	Phase Space Density <sup>a</sup> $\rho(r, r')$	Real Space Density <sup>b</sup> $n(r)$	Emittance Ratio <sup>c</sup> $\epsilon_{\text{total}}/\epsilon_{\text{rms}}$
Waterbag	$\frac{2N}{\pi^2 R_0^4}$	$\frac{2N}{\pi R_0^2} \left(1 - \frac{r^2}{R_0^2}\right)$	6
Gaussian	$\frac{N}{4\pi^2 \sigma^2} \exp\left(-\frac{r^2 + r'^2}{2\sigma^2}\right)$	$\frac{N}{2\pi \sigma^2} \exp\left(-\frac{r^2}{2\sigma^2}\right)$	$\infty$

<sup>a</sup>  $r^2 = x^2 + y^2$ ,  $r'^2 = x'^2 + y'^2$  and  $r^2 + r'^2 \leq R_0^2$ .

<sup>b</sup>  $r \leq R_0$ .

<sup>c</sup> For an  $n$ -dimensional Waterbag distribution  $\epsilon_{\text{total}}/\epsilon_{\text{rms}} = n + 2$ . The Gaussian distribution is usually truncated at  $m\sigma$  such that  $r \leq R_0 = m\sigma$  and  $\epsilon_{\text{total}}/\epsilon_{\text{rms}} = m^2$ .

lates an  $n$ -dimensional hyper-ellipsoid in phase space with  $N$  particles. The distributions can also be extended to take into account the longitudinal distribution of bunched beams.

The phase space volume or emittance of a particle beam is a constant of motion only under the influence of conservative forces and not in the case of acceleration or dissipative

forces that act to damp the motion, such as synchrotron radiation. In the case of acceleration, the choice of the divergence ( $x'$ ) for the momentum coordinate results in adiabatic damping proportional to  $1/\beta_z\gamma_z$  during acceleration because  $x' \approx p_x/p_z$ . In this case it is useful to define a normalised transverse emittance that is invariant under acceleration, i.e.,

$$\epsilon_{\text{norm}} = \epsilon_{\text{geom}} (\beta_z \gamma_z), \quad (3.4.47)$$

where the emittance defined previously is referred to as the geometric emittance. The main definition of the longitudinal emittance used throughout this thesis is normalised, i.e. in units of  $\Delta t$  and  $\Delta W$ , however when units of  $\Delta\phi$  and  $\frac{\Delta W}{W_0}$  are used one should take care of the beam energy and rf frequency.

### 3.4.7 Acceptance

The acceptance corresponds to the largest phase space ellipse that the physical aperture will accept along the accelerator, i.e.,

$$A = \frac{R_{\text{ap}}(z)}{\tilde{\beta}(z)} \Big|_{\text{min}}, \quad (3.4.48)$$

where  $R_{\text{ap}}$  is the half-aperture shown in the schematic of Figure 3.18(a).

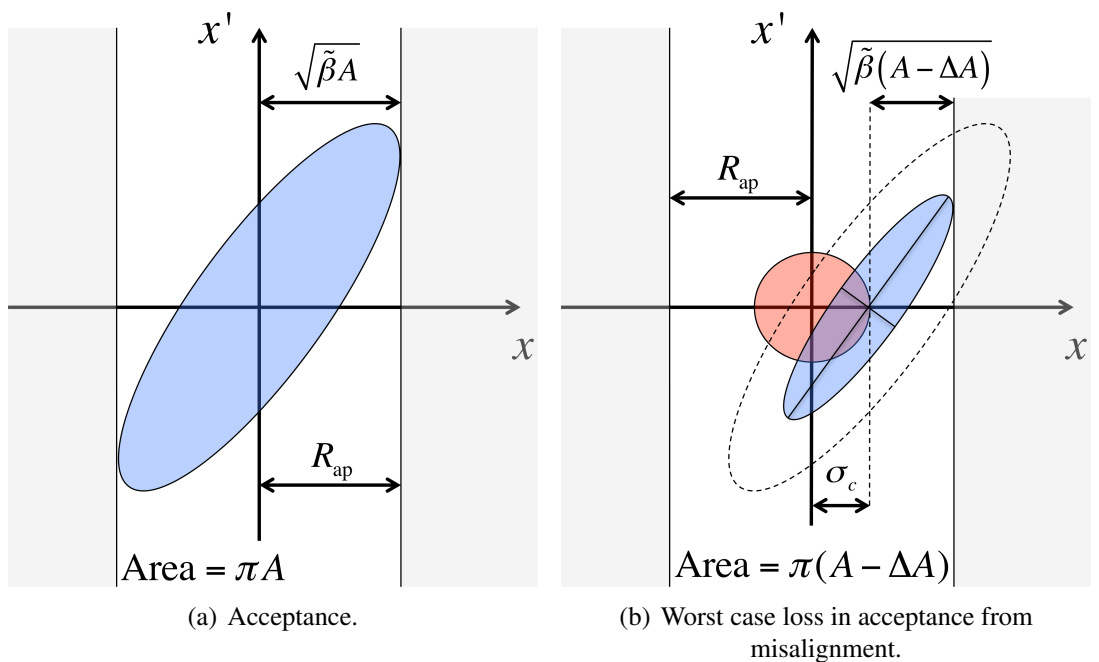


Figure 3.18: The definition of the acceptance and loss of acceptance with misalignment.

In the presence of misalignment the centroid will be kicked away from the origin in phase space. Using statistical error analysis one can understand the trajectories that the beam centroid could take under given misalignment tolerances and parameterise the result of a large number of error seeds with a phase space ellipse, shown shaded in red in Figure 3.18(b), see also Chapter 6.7. The worst case is shown in Figure 3.18(b), and by writing the maximum possible beam size in the remaining aperture as,

$$R_{\text{ap}} - \sigma_c = \sqrt{\tilde{\beta}(A - \Delta A)}, \quad (3.4.49)$$

the loss in acceptance can be written,

$$\frac{\Delta A}{A} = \frac{\sigma_c(z)}{R_{\text{ap}}(z)} \left( 2 - \frac{\sigma_c(z)}{R_{\text{ap}}(z)} \right) \Big|_{\text{min}}, \quad (3.4.50)$$

where  $\sigma_c$  parameterises the maximum spatial excursion of the centroid.

### 3.5 Sources of Emittance Growth

The effects of space-charge in driving emittance growth will not be discussed here and can be found summarised elsewhere, see e.g. [135]. Emittance growth can be broadly grouped as coming from four main sources:

- **Couplings** – the transfer of emittance between coupled phase space planes can cause the emittance in a given trace space plane to increase, even though the overall 6-dimensional phase space volume remains invariant.
- **Imperfections** – e.g. misalignment, jitter and manufacturing errors.
- **Non-linearities** – phase space is distorted such that the effective emittance is increased.
- **Parametric resonances** – single-particle resonances.

The instability mechanisms characteristic of ion linacs can be found summarised in [131]. The most important sources of emittance growth in the HIE linac are briefly discussed below.

### 3.5.1 Couplings

If the beam is asymmetric in the transverse and vertical planes the projected emittance will oscillate as it is rotated inside a solenoid focusing channel, see e.g. [136]. Similarly, if beam line elements that break the axial symmetry are placed in the solenoid focusing channel the projected emittance will also oscillate. In this case, the effective emittance growth is not easily reversed.

The phase spread of a bunched beam causes transverse emittance growth in an rf cavity because of the phase dependence of the rf (de)focusing force; particles at the front and back of the bunch receive different transverse kicks on traversing the cavity. To leading-order, the emittance growth depends on the square of the transverse and longitudinal beam dimensions [137] and decreases rapidly with the beam energy. The beam phase spread also induces transverse emittance growth due to the phase dependence of the beam-steering force in the quarter-wave resonators. Other effects that cause emittance growth in trace space include the radial dependence of the transit-time factor, chromaticity and dispersion.

### 3.5.2 Imperfections

Static errors such as misalignment can increase the emittance of the beam as it is forced to sample non-linear fields that are enhanced further from the axis. In particular, the emittance growth in an rf cavity is increased if the beam is displaced away from the axis. Dynamic errors such as rf jitter in the cavities can have a strong effect on the time-averaged or effective emittance of the bunch train because each bunch is mismatched differently at the output of the linac.

### 3.5.3 Non-linearities

Non-linear forces distort phase space such that filamentation ensues and the emittance is effectively diluted. Operating the cavities with a low synchronous phase and close to the crest of the rf waveform introduces strong non-linearities in the longitudinal dynamics that can cause strong changes in the emittance. The intrinsic aberration of optical elements

introduces non-linearities that increase the effective beam emittance. For a solenoid, the emittance growth is proportional to the fourth power of the beam size and the aberration depends on the aperture size, see e.g. [138].

### 3.5.4 Parametric Resonances

The parametric single-particle resonance described above for the rf (de)focusing force can cause effective emittance growth. Other examples include space-charge driven transverse parametric resonances and drift-space driven longitudinal parametric resonances, see e.g. [139].

## 3.6 Beam Dynamics Simulation Codes

The codes used throughout the beam dynamics studies presented in this thesis are outlined in Table 3.2 and references are given for further information.

Table 3.2: Summary of beam dynamics codes

Simulation Code	Developers	Comments
PARMTEQM	LANL [140]	RFQ design code with multi-particle beam dynamics
TRACE 3-D	LANL [140]	first-order beam dynamics design and matching code
LANA	INR [133]	first-order beam dynamics code with multi-particle tracking
LORASR	IAP [141]	KONUS multi-particle beam dynamics design code
TRAVEL (PATH Manager)	CERN [142]	numerical tracking of multi-particle beams in field maps <sup>a</sup>
TRACK	ANL [108]	numerical tracking of multi-particle beams in field maps <sup>a</sup>

<sup>a</sup> Hard-edge elements also can be implemented.

The next chapter will discuss the investigation and recommissioning of the REX-ISOLDE linac.

## INVESTIGATION OF THE REX LINAC

The Radioactive ion beam EXperiment (REX) was, as its name suggests, integrated at CERN as an experiment, which was designed and built by a range of collaborators under the auspices of the REX-ISOLDE Collaboration [46]. The linac was installed and commissioned at ISOLDE independently of CERN, escaping the standard protocols governing machine integration, before being handed over to support infrastructures at CERN. Consequently, although there existed a wealth of scattered documentation, a lot was either missing or misunderstood and there lacked any tool other than an unbenchmarked TRACE 3-D model that could be used to describe the beam dynamics of the linac and to tune it.

The REX linac will be a critical component of the upgrade as it will inject the beam into the superconducting linac during the first stages of the upgrade, which could involve between 2 - 4 years of operation. Even after the upgrade is complete a substantial part of the REX front-end will remain to boost the beam up to 1.2 MeV/ $u$ , thus it was made a priority to better understand the existing machine and its performance. An investigation of the REX linac was undertaken to review the available literature [46–48, 50, 56, 57, 61–63, 67, 69, 143–151] and the working points of the machine, with the objective of creating benchmarked beam dynamics simulations tested with beam measurements. A schematic layout of the REX linac is shown next to the proposed HIE upgrade in Figure 4.1 and included are the acronyms used throughout for each accelerating structure. The results of the investigation were important for providing reliable input to simulations of the HIE linac. The RFQ beam dynamics simulations were benchmarked and bead-pull

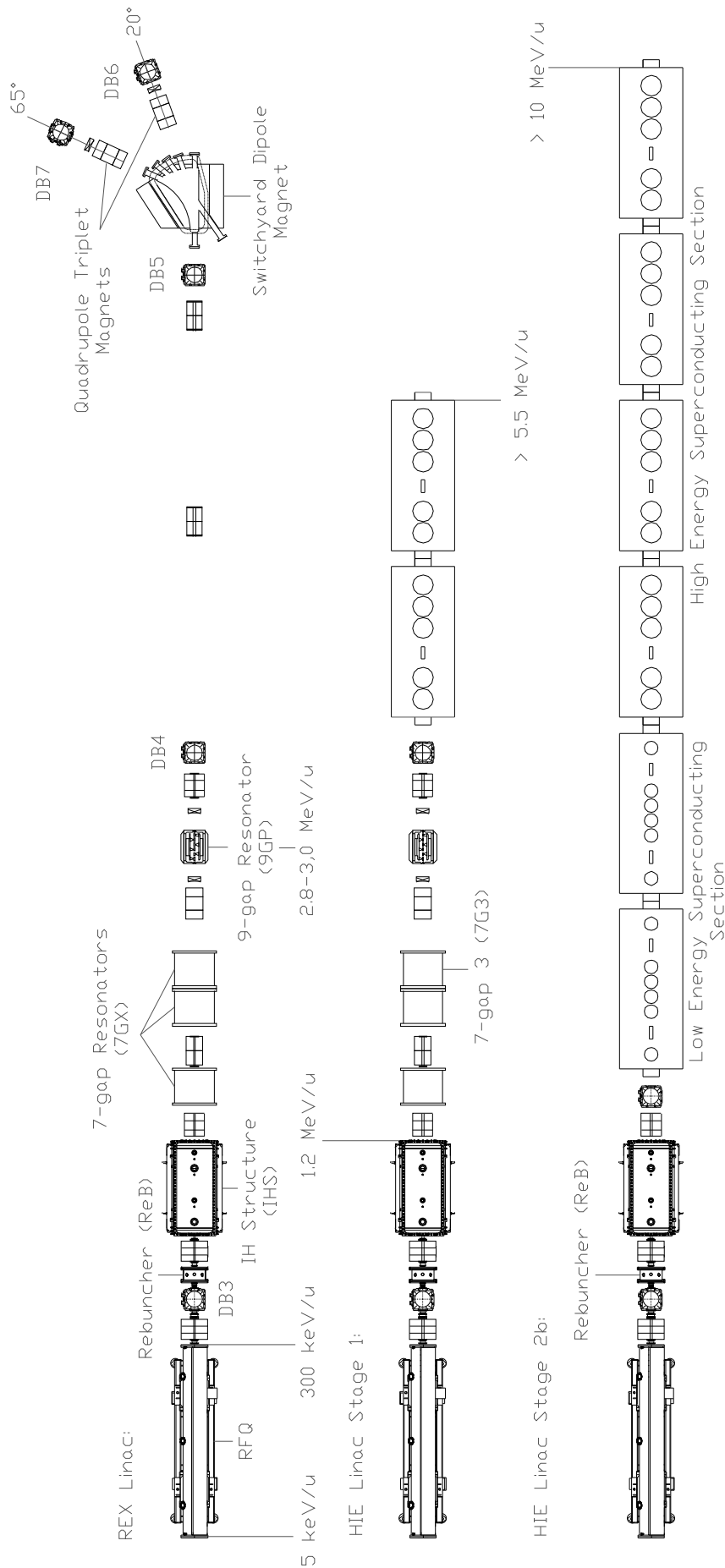


Figure 4.1: The REX linac juxtaposed with the HIE linac to illustrate the emittance measurement campaign: measurements were made before and after the IHS using the ReB and 7G3 cavities to assess its performance and to understand the longitudinal beam parameters at injection to the upgrade.

measurements of the IHS were undertaken in order to benchmark the different codes used to simulate it. Models of the 7GX cavities and the 9GP cavity were also implemented into a single end-to-end LANA simulation that was benchmarked with measurement. The longitudinal beam parameters were measured both after the RFQ and before the 7G3, and will be described in detail in the next chapter.

## 4.1 Radio Frequency Quadrupole (RFQ)

### 4.1.1 Code Benchmarking

The design of the RFQ was done by the Institute of Applied Physics (IAP) at Goethe University, Frankfurt, using an adapted version of PARMTEQM, which was delivered to CERN along with the RFQ. The IAP code was benchmarked with PARMTEQM v3.07 and the electrode geometry, used to create the fields for the beam dynamics calculations, was shown to agree to better than 0.3 % in each cell, as well as with the geometry published in [57]. It was not known what assumptions were made in the IAP code for the type of longitudinal modulation of the electrodes, however the results as a function of modulation type were not found to vary significantly. The beam dynamics calculations in both codes were consistent and further details can be found in [152]. The rms and 95 % longitudinal emittances are consistent across all the simulations at 0.26 and 1.80  $\pi$  ns keV/ $u$ , respectively, with minimal transverse emittance growth.

### 4.1.2 Beam Dynamics Simulations

PARMTEQM v3.07 was used to generate a realistic particle distribution. The RFQ electrodes were simulated as vanes to model the ‘mini-vane’ shape that was employed to permit the electrodes to be water-cooled using internal piping. It was not possible to expand the electromagnetic fields in the vicinity of the beam axis using the actual radial curvature of the electrodes of 0.38 cm. Nonetheless, the effect on the beam dynamics of increasing the radius was shown to be negligible and 0.40 cm was used instead. The output particle distribution is shown in Figure 4.2 and the beam parameters, which are collected at the end of the chapter in Tables 4.1, 4.2 and 4.3, are consistent with those used to design the

RFQ-IHS matching section [63]. The beam dynamics is summarised by the screenshot of the PARMTEQM v3.07 simulation in Figure 4.3.

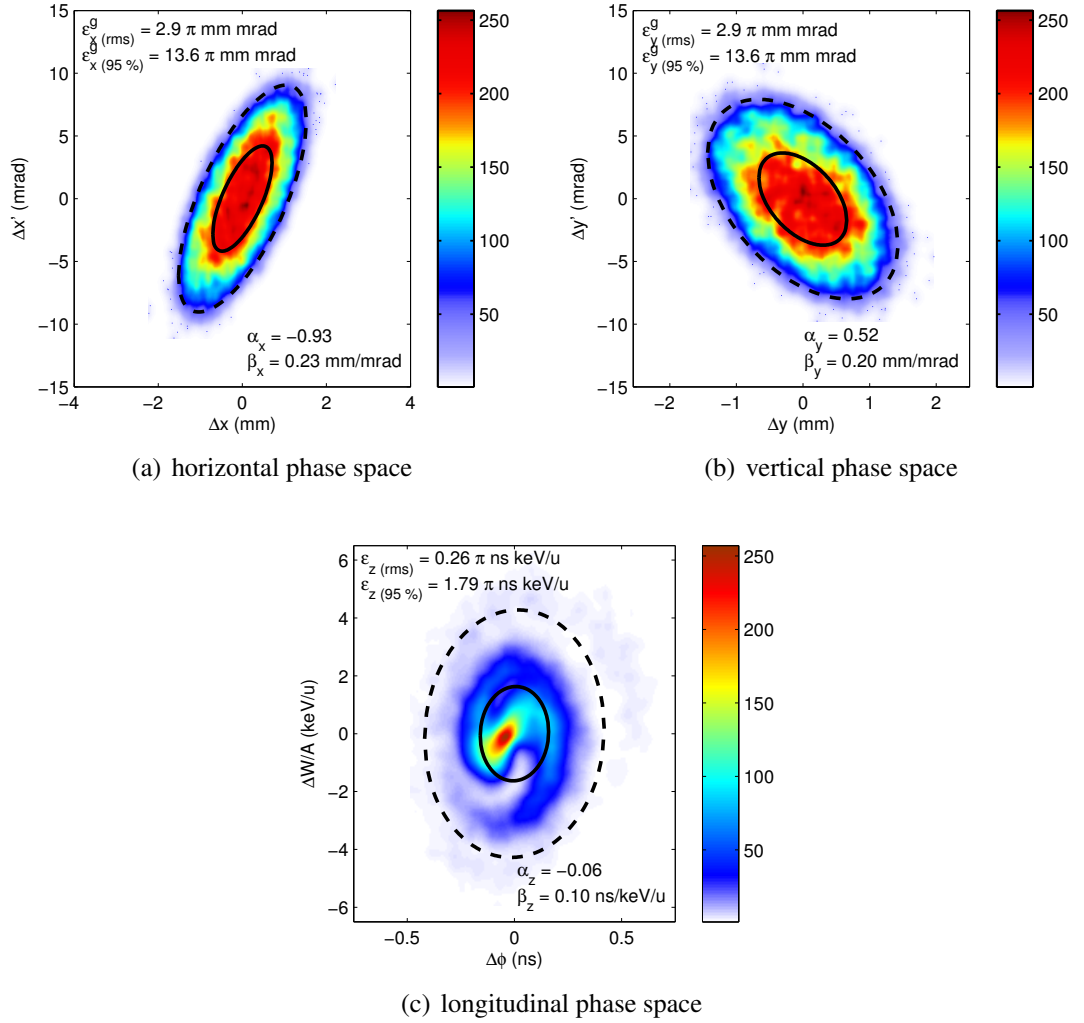


Figure 4.2: Beam phase space distribution after the RFQ, simulated with PARMTEQM v3.07,  $W_0 = 0.3 \text{ MeV/u}$  (colour bars: particle density).

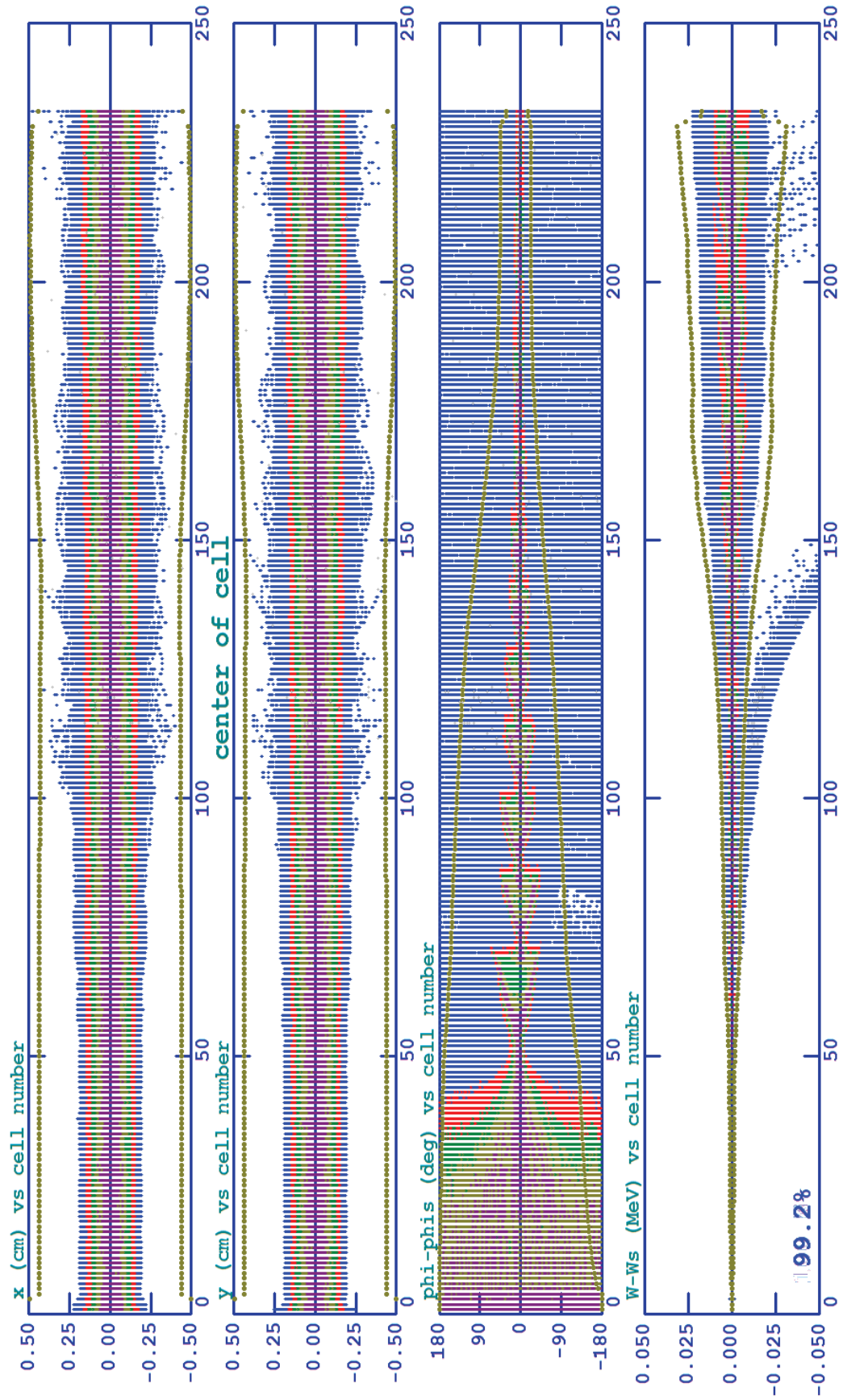


Figure 4.3: Summary of the beam dynamics of the REX RFQ, simulated with PARMTEQM v3.07.

### 4.1.3 Beam Measurements

To check the working point of the RFQ the energy spread at its output was measured using the REX switchyard magnet. The beam was moved across a slit larger than its width in front of a Faraday cup, such that the derivative of the intensity measured on the cup gave a profile of the beam as it traversed both edges of the slit. The energy spread was found to be very sensitive to the voltage of the RFQ. A comparison between the measured energy spread and simulation is shown in Figure 4.4. As the voltage is lowered the energy spread increases rapidly as particles are lost out of the bucket; discrepancies between measurement and simulation at lower voltages can be explained by the exclusion of the low energy particles in the rms measurement as a result of poor transmission. Otherwise, the simulations are in good agreement with measurement. The nominal beam parameters were found close to the minimum in the energy spread at a pick-up voltage of 1980 mV, which on comparison with simulation, see Figure 4.4, corresponds to an electrode voltage of 36.6 kV at  $A/q = 4$ , or 98 % of the design voltage.

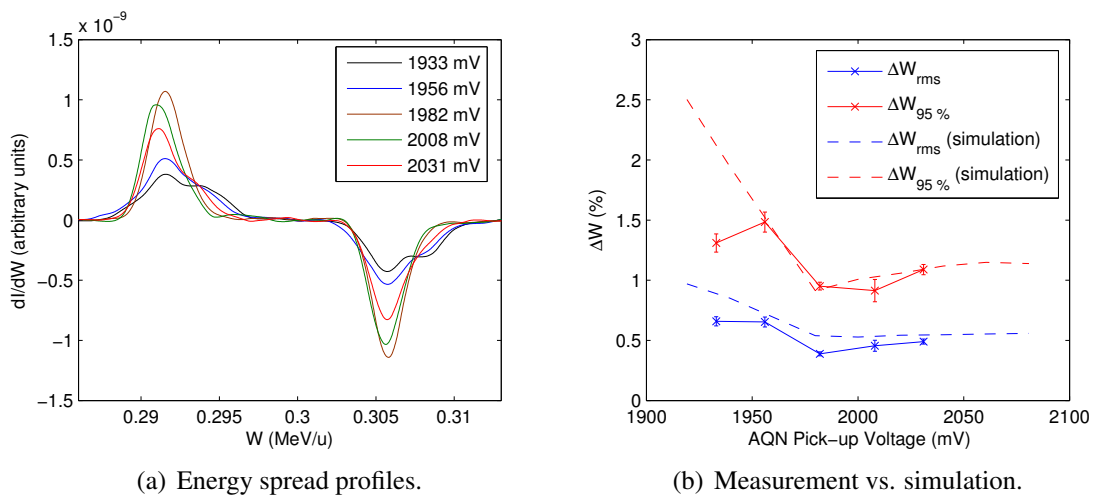


Figure 4.4: Energy spread measurements after the RFQ as a function of voltage versus simulation.

Using this pick-up calibration the working point of the RFQ was checked again by comparing the measured transmission as a function of voltage with simulation, as is shown in Figure 4.5. The correlation between simulation and measurement is impressive, where the transmission was measured at diagnostic box 3 (DB3) after the beam had passed through the first quadrupole triplet magnet.

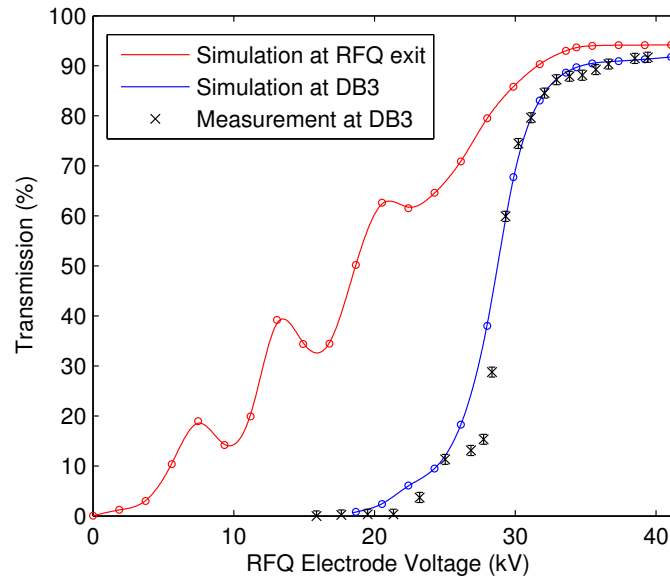


Figure 4.5: RFQ transmission measurements at DB3 versus simulation,  $A/q = 4$ .

## 4.2 Rebuncher (ReB)

The RFQ-IHS matching section, which comprises of two quadrupole triplet magnets and a 3-gap split-ring rebuncher cavity ensures the beam is convergent in all phase space planes on entering the IHS, see [63] for more details. The spacings of the three gaps inside the rebuncher were made approximately 1.5 mm smaller than  $\beta\lambda/2$  at 300 keV/u due to problems incurred during manufacturing [63]. As a result, the gap spacing is 36 mm instead of 37.5 mm and the beam sees accelerating and decelerating fields at phases of  $\pm 7.5^\circ$  in the external gaps.

To procure the realistic electromagnetic fields in the vicinity of the beam axis of the ReB an rf simulation was carried out using CST-MWS. The simulation was validated with a comparison to the measured longitudinal electric field published in [61] and the simulated results at different radii presented in [63].

The emittance growth introduced by the ReB was assessed by tracking the particle distribution at output from the RFQ through the matching section to the entrance of the IHS using the realistic fields of the ReB. The transit-time factor on axis for the structure is 0.78 at 300 keV/u, where  $\beta = 0.0254$ . In the study, non-linear effects caused by the large phase spread after the drift from the RFQ and the radial dependence of the transit-time factor were of particular interest. As shown in Figure 4.6, at the design voltage the growth

of the rms longitudinal emittance was calculated as just 3.7 %; the transverse emittance growth is negligible. The rebuncher is therefore not a cause of significant longitudinal emittance dilution in the linac and can be used to measure the longitudinal emittance without significantly affecting the measurement.

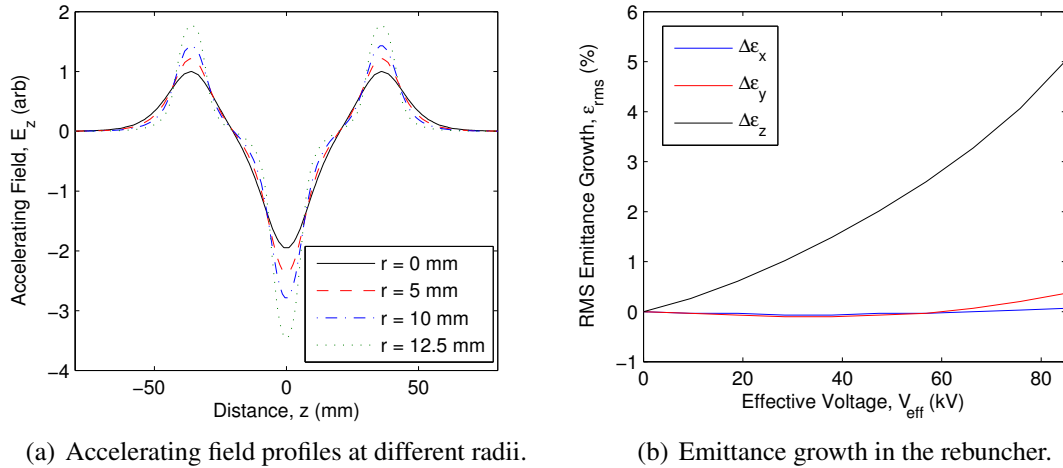


Figure 4.6: Simulated accelerating field of the ReB at different radii inside the 15 mm radial aperture using CST-MWS and the emittance growth.

### 4.3 20-gap IH Structure (IHS)

A bead-pull measurement campaign was undertaken in order to allay uncertainties in the profile of the accelerating field in the IHS. The main objective was to obtain the longitudinal electric field profile on axis, for known positions of the capacitive plungers referenced with a fixed external fiducial, which could then be used to study the beam dynamics in the structure. The results of the measurement campaign were used to validate new rf simulations of the cavity that provided 3-dimensional field maps with all 6 components of the electromagnetic fields in the vicinity of the beam axis. The realistic field maps provided a means to benchmark various beam dynamics codes and to calculate the longitudinal acceptance of the structure, which was used to determine the optimum phase at which to operate the structure. The phase dependence of the energy gain, which was derived from the simulations, proved a useful tool for quickly setting the correct working point of the cavity.

### 4.3.1 Cavity Geometry

The copper coating to the drift-tubes of the IHS was erroneously applied ten times too thick (500  $\mu\text{m}$  thickness instead of 50  $\mu\text{m}$ ) during manufacturing [145]. As a consequence the resonance frequency of the cavity was 1 MHz too low and the capacitive plungers could not be used to attain the correct voltage distribution across the gaps at 101.28 MHz. The extra copper was filed off the drift-tubes to ensure the correct gap size but nothing was done to modify the extra copper deposited on the curved external surfaces of the drift-tubes. Instead, the lengths of the undercuts were modified by introducing copper plates to increase the frequency of the cavity and to adjust the voltage profile [62]. Although acceleration to 1.2 MeV/u was achievable after adjusting the undercut lengths, the voltage distribution across the gaps could not be tilted to achieve a flexible output energy down to 1.1 MeV/u. A new set of drift-tubes was manufactured but they were never fitted and are still available at CERN for installation.

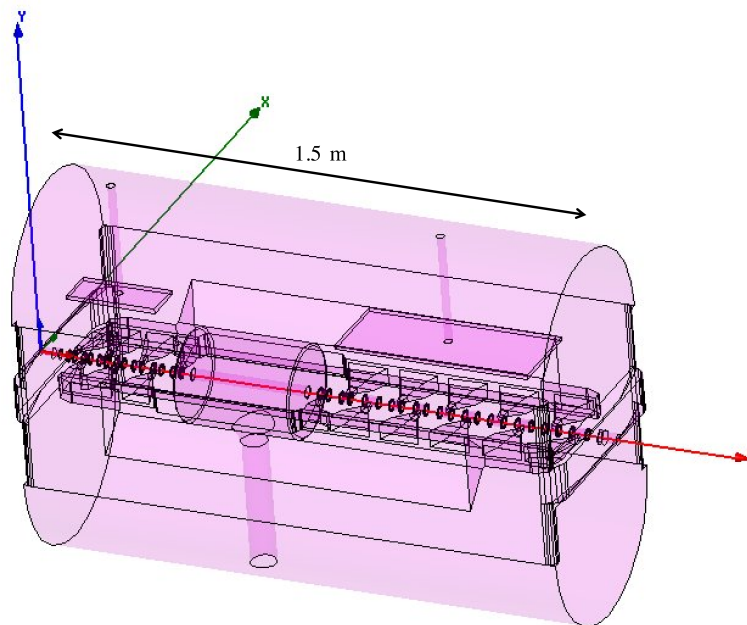


Figure 4.7: IHS geometry implemented in HFSS [99].

The geometry of the IHS, including the adjusted undercut lengths and capacitive plungers, was implemented in the rf electromagnetic field solver code HFSS [99] with the capacitive plungers at their nominal height, see Figure 4.7. The drift-tube dimensions could be corroborated with measurements of the spare drift-tubes without needing to open the IH tank. The complexity of the geometry required a significant amount of comput-

ing power in order to resolve the axial fields. The computing resources needed for the simulation were attained through internal collaboration at CERN [153].

### 4.3.2 Bead-pull Measurements

Rf bead-pull measurements of the IHS were undertaken. The electric field on the axis of the IHS was measured by perturbing the cavity with a small body moved through it on a wire. In the adiabatic limit, i.e. when the perturbation to an oscillating system is much slower than its time period, the frequency response of the cavity is linear with respect to the perturbation in the stored energy, which is summarised by Slater's cavity perturbation theorem [154],

$$\frac{\Delta f}{f} = \frac{\Delta U}{U} = \frac{1}{4U} \int_{\Delta V} \frac{1}{\mu_0} |\vec{B}|^2 - \epsilon_0 |\vec{E}|^2 dV. \quad (4.3.1)$$

The cavity is perturbed by the removal of a small volume  $\Delta V$  from inside the cavity and the unperturbed stored energy is,

$$U = \frac{1}{4} \int_V \frac{1}{\mu_0} |\vec{B}|^2 + \epsilon_0 |\vec{E}|^2 dV. \quad (4.3.2)$$

The perturbation is introduced by the displacement of the cavity's electromagnetic fields from inside the volume of the small body as it becomes polarised; a phenomenon that transfers the cavity's field energy into the potential energy of the polarised body. The frequency perturbation of a spherical metal bead with radius  $R$  can be written in the absence of magnetic field as,

$$\frac{\Delta f}{f} = -\frac{\pi R^3}{U} \epsilon_0 |\vec{E}|^2, \quad (4.3.3)$$

where the electric field is assumed constant over the entire sphere [155, 156]. To avoid the effects of image charges on the cavity walls the above expression is also only strictly valid if the bead is further than a diameter from the nearest wall or drift-tube. The bead's diameter was therefore restricted to less than 6 mm in the drift-tubes of the IHS. The accelerating field is proportional to the square root of the frequency perturbation where the longitudinal component of the electric field is dominant in comparison to the radial components,

$$E_{\text{acc}} \propto \sqrt{\frac{\Delta f}{f}}, \quad (4.3.4)$$

because of the proximity to the beam axis.

#### 4.3.2.1 Experimental Overview

An experimental apparatus designed for measuring the field flatness of Linac4 structures at CERN was adapted to facilitate a measurement of the IHS on the REX beam line [157]. The impending schedule of the nuclear physics programme and other practical constraints ruled out the removal of the IHS from the accelerator hall. The modification took the motor and pulleys off the Linac4 bead-pull test bench and clamped them securely to the side of the IHS, see Figure 4.8(a).



(a) Motor and pulleys secured to the IHS.



(b) Alignment with crosshairs.

Figure 4.8: Photos documenting the bead-pull measurement.

A standard technique was employed using a Vector Network Analyser (VNA) to measure the phase difference between the rf signal exciting the cavity by the main coupler and the response signal of the cavity measured at the pick-up, as shown by the schematic of Figure 4.9. The phase difference ( $\Delta\phi$ ) between the signal driving the cavity at the unperturbed resonance frequency and the signal measured at the pick-up are related to the change in resonance frequency by the expression [158],

$$\frac{\Delta f}{f} = \frac{1}{2Q_L} \tan \Delta\phi, \quad (4.3.5)$$

where  $Q_L$  is the loaded quality factor.<sup>1</sup>

The set-up included software to control the bead velocity and to sample the data acquired by the VNA. The alignment of the setup was done with crosshairs made over the beam ports on each end of the cavity, as shown in Figure 4.8(b), with an estimated accuracy of 0.5 mm. The bead was moved through the cavity suspended on a nylon wire with a cross-sectional diameter of 0.4 mm, which was chosen thicker than normal to relax concerns of the wire breaking and the bead being dropped inside the cavity. In fact, the bead was directly fixed to the wire.

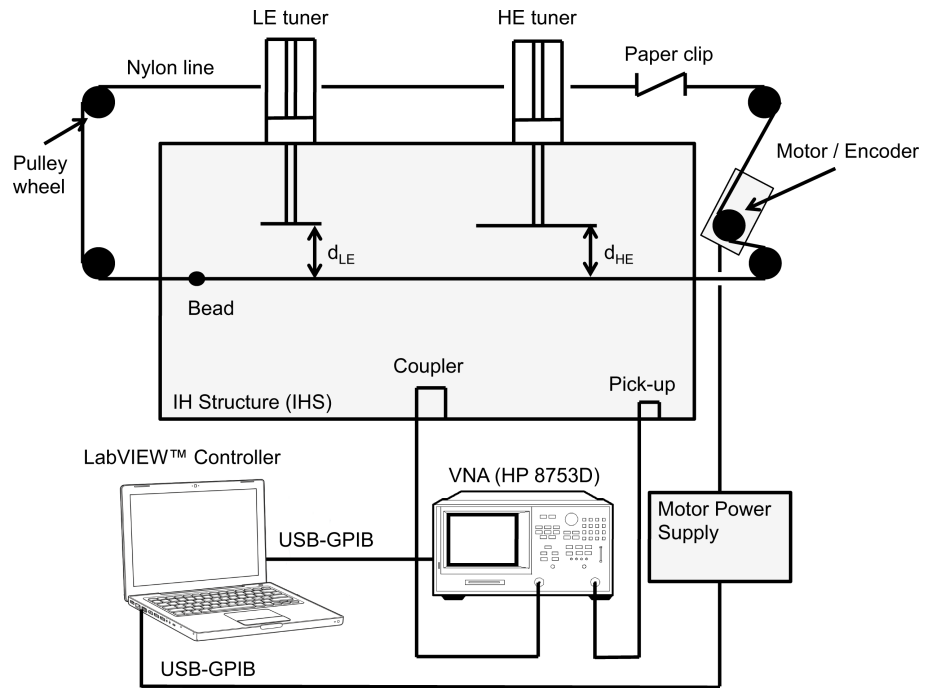


Figure 4.9: Schematic of the bead-pull measurement apparatus.

The calibration of the encoders on the motors actuating the tuners was made using the known minimum and maximum heights of the tuners above the beam axis ( $d_{LE/HE}$ ) at the range of their movement controlled by limit switches,

$$d_{LE}[\text{mm}] = \left( 84.6 + \frac{z_{LE}-500}{11.2} \right) \quad \text{and} \quad d_{HE}[\text{mm}] = \left( 80.3 + \frac{z_{HE}-500}{11.2} \right), \quad (4.3.6)$$

where  $z_{LE}$  and  $z_{HE}$  are the encoder values of the low and high energy tuners, respectively. A physical reference ( $D$ ) defined in Figure 4.10 was also taken to define the tuner position

<sup>1</sup>As well as resistive losses on the cavity walls, the stored energy can be lost from the cavity through the coupler port that connects it to the rf generator. This loss mechanism can be parameterised by the external quality factor ( $Q_e$ ) and included in a loaded quality factor seen by the rf generator:  $\frac{1}{Q_L} = \frac{1}{Q_e} + \frac{1}{Q}$ .

independently of the encoder.

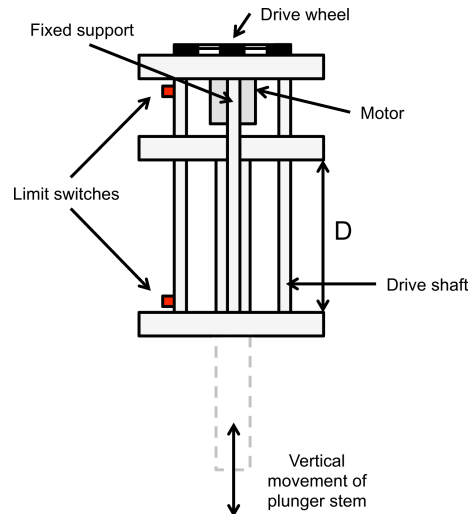


Figure 4.10: Schematic of the REX IHS tuner actuator.

To reduce the noise on the phase signal the intermediate frequency (IF) bandwidth of the VNA was narrowed until its sampling speed limited the spatial resolution of the measurements caused by the velocity of the bead. An IF bandwidth of 100 Hz allowed measurements to be sampled every 80 ms, corresponding to every 0.3 mm, at a bead velocity of approximately  $4 \text{ mm s}^{-1}$ , taking 6 minutes per measurement. The motor could not be slowed further without the motion of the bead becoming unstable. With a 4 mm bead a signal-to-noise ratio of less than 1 % could be achieved in the centre of the gaps. To assess the effect of the nylon wire itself the bead was removed and the wire moved alone through the cavity with different values of the IF bandwidth, see Figure 4.11. The

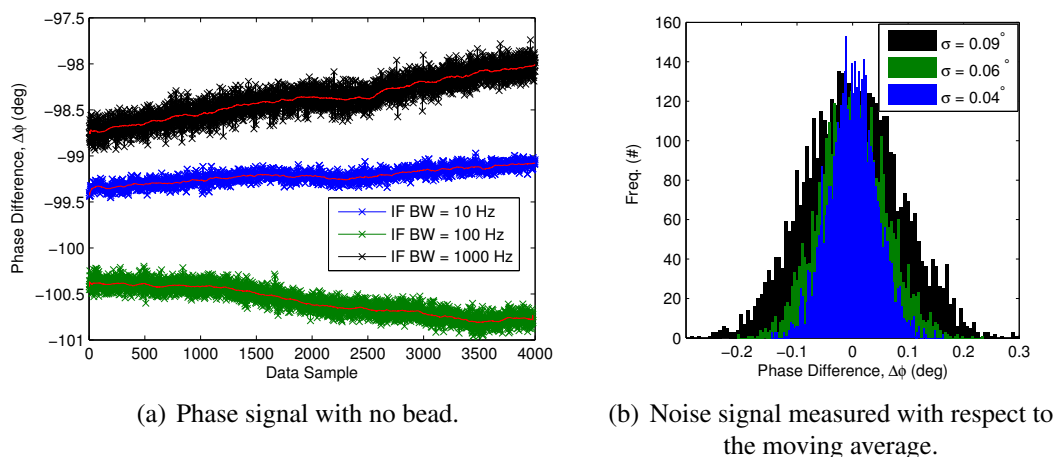


Figure 4.11: Analysis of the phase noise in the bead-pull measurement.

phase was observed to drift by up to  $1^\circ$  over any single measurement run, corresponding

to a frequency drift of 60 Hz. No correlation was observed with the motion of the wire itself and the drift in the resonant frequency was attributed to temperature, humidity or pressure fluctuations in the accelerator hall.

The spatial resolution of the measurement was probed using a range of spherical metal beads from 3 to 6 mm in diameter. Although larger beads give a stronger frequency perturbation and an enhanced signal-to-noise ratio, their effect on the spatial resolution can limit the measurement. The changing gap size associated with the velocity profiling of the drift-tubes inside the IHS was exploited to determine whether the measurement resolution was satisfactory. If the size of the bead is not a significant contribution to the resolution then the relative field levels in the two main drift-tube sections of the IHS is independent of the bead size. A bead of 6 mm in diameter was observed to tilt the measured field profile and so a 4 mm diameter bead had to be used for the measurements.

Even with feedback control of the motor's speed using an encoder fixed to the drive wheel, large numbers of measurements needed to be taken and averaged in order to achieve the precision required to reconstruct the axial accelerating field. The largest variation in the data was attributed to the nylon wire slipping over the pulleys. The problem was mitigated by increasing the tension in the wire, however the wire deformed plastically and the tension decreased with time so that the wire required re-tensioning regularly. The noisy environment of the ISOLDE hall was handled with a careful post-processing of the data.

#### **4.3.2.2 Post-processing of Data**

The desired precision was attained through repeating the measurements; typically 15 repeats were needed for any given tuner configuration. To cope with the large amounts of data a program was written to treat the data automatically. The main post-processing steps involved locating the average position of each gap, tracking the drifting resonance frequency throughout a measurement, smoothing noise, combining the datasets into an averaged field profile or gap voltage distribution and scaling the longitudinal axis.

The variation of the resonance frequency of the cavity was tracked in each drift-tube, where the cavity was assumed to be unperturbed, and subtracted by assuming a linear

variation from gap to gap. An example of the baseline tracking algorithm is shown in Figure 4.12. A peak-search algorithm was used to calculate the average position of the

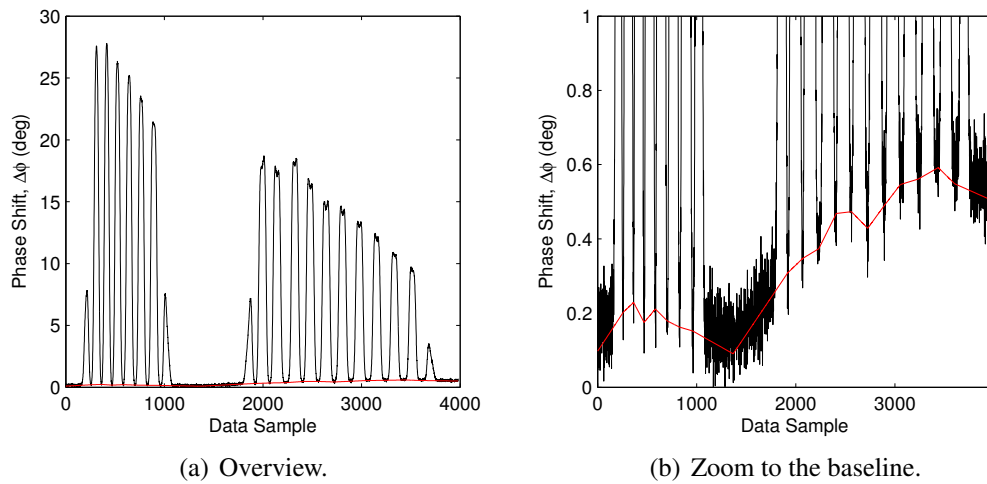


Figure 4.12: Baseline tracking algorithm implemented in the bead-pull measurement software to remove the effect of changes in the resonance frequency.

peak field in each gap relative to the first gap. The noise was smoothed by fitting a spline to the data and inside the drift-tubes a threshold was set below which the data was forced to the baseline. The average accelerating field was reconstructed by cutting up each measurement gap by gap and re-aligning the fields with their average position. After the adjustment to the longitudinal position of each gap the entire data set was averaged. The longitudinal axis did not need calibrating to calculate the voltage distribution, however it was necessary to scale the distance accurately for the accelerating field. As the motor was not stepped and there were no reference markers in the data, e.g. known physical ‘start/stop’ positions, a scaling factor had to be imposed externally from the measurement. It was achieved most accurately by scaling according to the distance between the peak fields in the external gaps, which was taken from simulation and prior knowledge of the drift-tube geometry. For particle tracking studies the correct drift-tube polarity was applied and the direction of the field orientated properly. The measured and simulated fields are compared in Figure 4.14. The post-processing code was also used to assess the field-flatness measured in the PIMS and DTL structures of Linac4 [157].

### 4.3.2.3 Reconstruction of Gap Voltage Distribution

The gap voltage distribution was reconstructed from the measured profile of the phase difference using the relationship,

$$V \propto \int \sqrt{\tan \Delta\phi} dz, \quad (4.3.7)$$

and normalised to a total voltage of 5.04 MV, sufficient to boost a beam with  $A/q = 4.5$  to 1.2 MeV/u. The voltage distribution measured with the tuners in the nominal position for acceleration to 1.2 MeV/u is compared to the results of the latest rf simulation of the structure using HFSS and the design voltages in Figure 4.13.

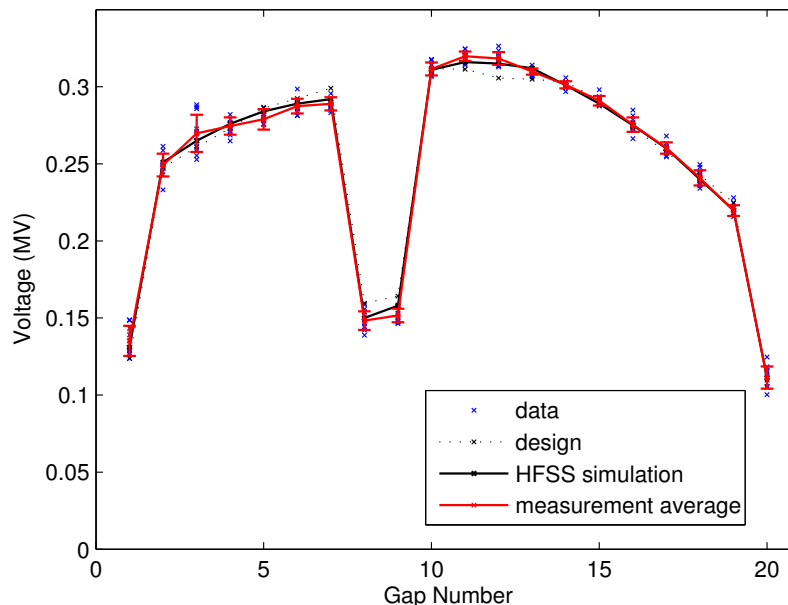


Figure 4.13: IHS gap voltage distribution with nominal plunger positions:  $z_{LE} = 1572$  ( $D_{LE} = 304.4$  mm) and  $z_{HE} = 1633$  ( $D_{HE} = 296.4$  mm).

The measurements and simulations are in good agreement, and with exception to the external gaps, the measurements also compare well to bead-pull measurements made before the IHS was installed on the beam line [62]. The voltage distribution was found to be only weakly dependent on the tuner position when moved within the few percent needed to maintain the resonance frequency of the cavity during operation.

#### 4.3.2.4 Reconstruction of Accelerating Field Profile

The electric field was reconstructed using the relation,

$$E_{\text{acc}} \propto \sqrt{\tan \Delta\phi}, \quad (4.3.8)$$

which was scaled accordingly. The agreement between the reconstructed accelerating field and simulation shown in Figure 4.14 is compelling. Also included is the simulated horizontal dipole electric field component on axis. The validation of the simulation

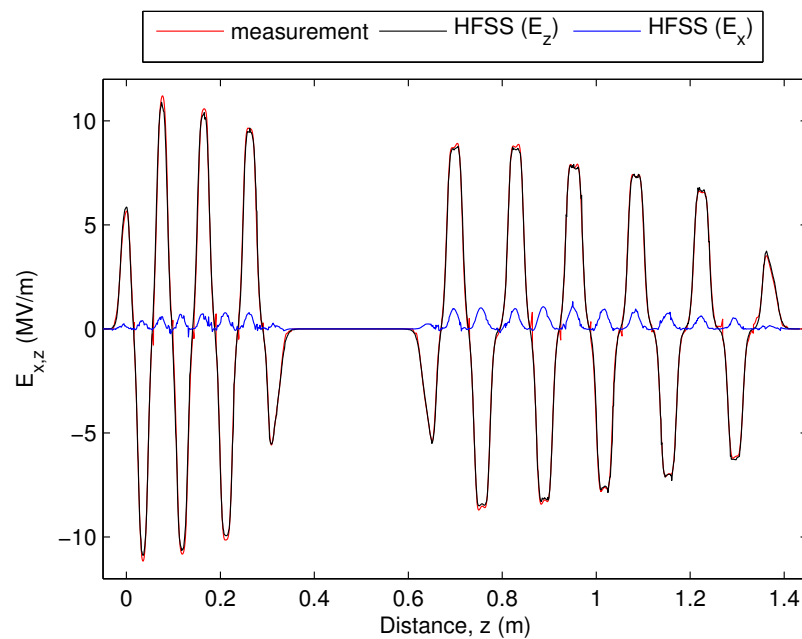


Figure 4.14: IHS accelerating field with nominal plunger positions:  $z_{\text{LE}} = 1572$  ( $D_{\text{LE}} = 304.4$  mm) and  $z_{\text{HE}} = 1633$  ( $D_{\text{HE}} = 296.4$  mm).

through measurement allowed for the first beam dynamics simulations of the IHS using the measured electromagnetic fields. All 6 electromagnetic field components in the vicinity of the beam axis were extracted from simulation and used in a numerical particle tracking code.

### 4.3.3 Energy Gain vs Phase

The energy gain as a function of phase was calculated numerically by tracking a particle with  $A/q = 4.5$  through the measured and simulated field maps. The sensitivity of the beam dynamics to the field profile is illustrated by comparing the results using the mea-

sured and simulated fields (HFSS) in Figure 4.15. Also plotted is the same calculation carried out with LORASR, which was used to design the IHS, across the range of phases permitted by the code.

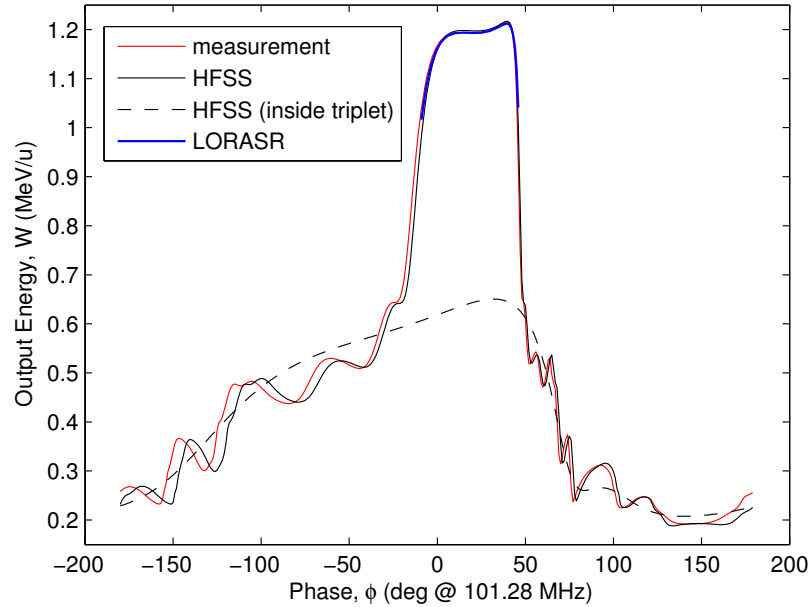


Figure 4.15: The output energy of the IHS as a function of phase.

The phase dependence of the energy gain is also shown as if observed from inside the internal triplet magnet, which has a shape more typical of IH structures operating a single KONUS period without internal focusing elements, see e.g. [159]. The drift-space of the internal triplet magnet, in which the beam travels for 3 rf periods, narrows the phase acceptance of the cavity because any significant mismatch of the design velocity after the first drift-tube section, caused by injecting at the wrong phase, results in a large phase error at entry to the second section and a loss of synchronism.

The sensitivity of the output energy in Figure 4.15 was used to study the working point of the IHS. The phase of the cavity was rotated and the beam energy measured whilst over and under-powering the cavity by 10 %. As shown in Figure 4.16(a), the measurements are well correlated to simulation, allowing the amplitude and phase to be confidently set. The absolute values of phase used in Figure 4.16 are arbitrary. A similar exercise was attempted by using the rebuncher to change the beam energy at injection, see Figure 4.16(b), however because the longitudinal beam parameters were mismatched at injection to the IHS the transmission was poor and less correlation can be seen with

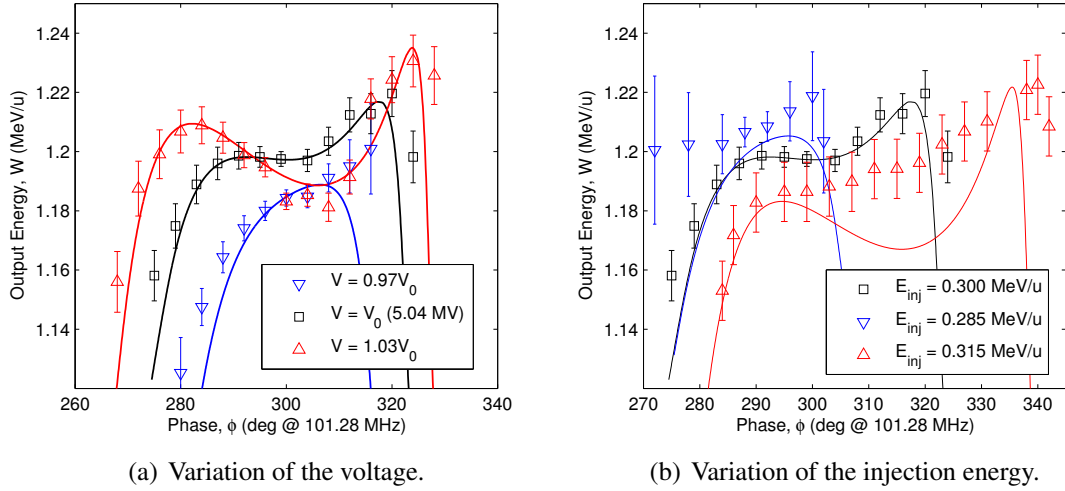


Figure 4.16: Measured IHS output energy as a function of phase with variation of voltage and input beam energy versus simulation.

simulation. Nonetheless, the phase acceptance is well correlated to simulation; as the velocity is increased the beam can be injected at later phases.

### 4.3.4 Dipole Steering

A detailed description of the compensation technique used to reduce the electric dipole component on the axis of this type of linac structure can be found in [64]. The effectiveness of the compensation of the dipole steering in the IHS was evaluated using the new rf simulations of the cavity, which included the bulges on the drift-tubes.

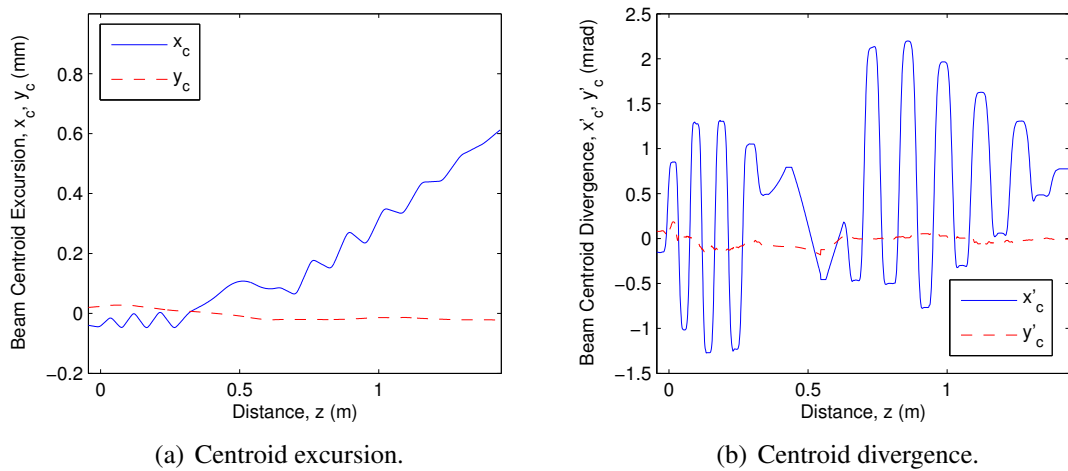


Figure 4.17: Simulations of the dipole steering in the IHS.

Although the dipole kicks are largely cancelled by the alternating phase of the fields

from gap to gap, the long drift-space of the internal triplet significantly decreases the effectiveness of the compensation. As is shown by tracking the beam centroid in Figure 4.17, even for a well aligned beam, a kick of approximately 1 mrad of divergence is imparted to the beam overall in the horizontal plane. This finding supports the installation of an orbit corrector magnet between the IHS and the superconducting linac.

### 4.3.5 Code Benchmarking

The benchmarking presented previously with LORASR was extended to multi-particle simulations and a tracking code was developed with the aim of making an end-to-end realistic field simulation of the HIE linac and its injector. The results of the tracking are compared to simulations of the IHS using three other codes: LORASR, LANA and TRACE 3-D in Figure 4.18.

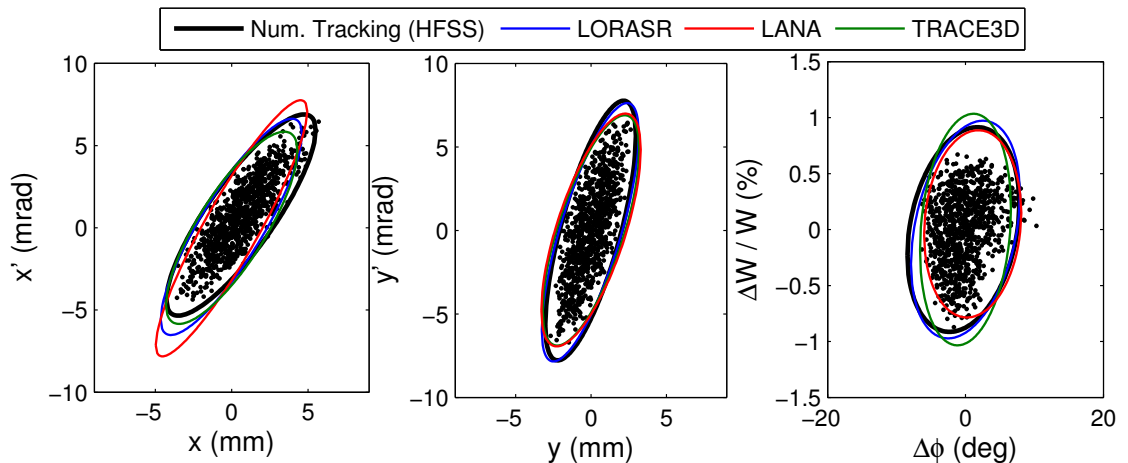


Figure 4.18: Benchmarking of beam dynamics codes simulating the IHS.

The particle distribution from the numerical tracking routine is shown against scaled rms ellipses taken from the output distributions of the other codes at the exit of the IHS. A 6-dimensional Waterbag distribution was simulated and ellipses representing the total emittance are plotted. In the case of LANA a 4-dimensional Waterbag distribution was used for the transverse phase space and a 2-dimensional Waterbag distribution for the longitudinal phase space. The different distributions were matched with their rms parameters. The design gap voltages defining the drift-tube geometry could not be adjusted to the measured voltages in LANA. Nonetheless, the difference between LANA

and the other codes is small. The TRACE 3-D model of the IHS was constructed from the phase and effective voltage information calculated using the realistic fields and used as a matching tool.

### 4.3.6 Longitudinal Acceptance Calculations

The longitudinal acceptance of the IHS is maximised at phases close to  $20^\circ$  on the plateau of the curve shown in Figure 4.15. The longitudinal acceptance is plotted in Figure 4.19 at a phase of  $20^\circ$ . The acceptance of the IHS is  $6.6 \pi \text{ ns keV/u}$ , however the motion is highly non-linear towards the edge of the acceptance ellipse and for the beam to be accelerated with a reasonable emittance growth of less than a factor of 2 the acceptance is closer to  $3 \pi \text{ ns keV/u}$ .

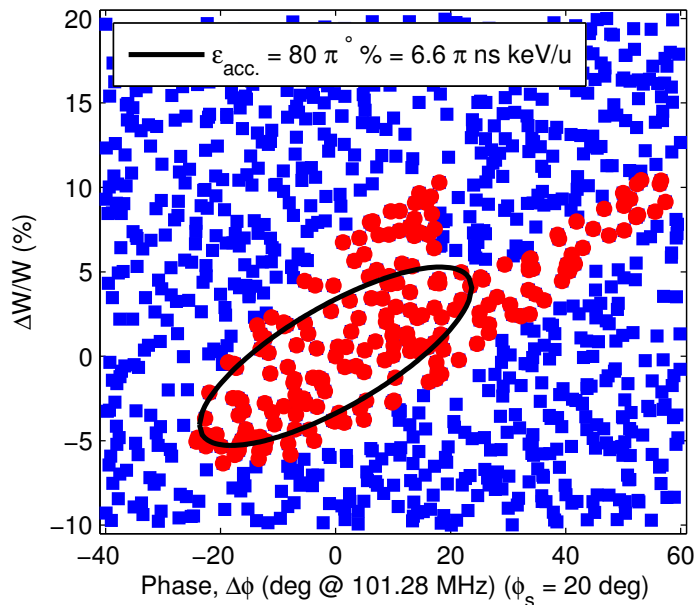


Figure 4.19: Longitudinal acceptance of the IHS accelerating to  $1.2 \text{ MeV/u}$  (red particles are transmitted and blue particles are lost).

### 4.3.7 Optimum Input Parameters

The tracking routine was used to find the optimum longitudinal Twiss parameters to inject into the IHS, which would prove useful if the matching section was redesigned to incorporate a chopper line. The rms longitudinal emittance growth in the IHS was surveyed as a function of the input longitudinal Twiss parameters for a beam with a total emittance of

$2\pi$  ns keV/u accelerated to 1.2 MeV/u. The survey is summarised in Figure 4.20, where the emittance growth factor is plotted as a contour map on a logarithmic scale where,

$$\epsilon_{\text{out}}/\epsilon_{\text{in}} = 10^{f_{\text{rms}}}. \quad (4.3.9)$$

As specified in the literature, the beam should be focused just inside the first drift-tube section of the IHS. The range of Twiss parameters that can be achieved at the entrance to the IHS by varying the voltage of the rebuncher are shown with the matching section in its present configuration and if the IHS was moved back closer toward the rebuncher. The working point of the ReB is marked in Figure 4.20 at an effective rebuncher voltage of 68 kV at  $A/q = 4.5$ , which is very close to the optimum input Twiss parameters:  $\alpha_{\text{in}} = -0.8$  and  $\beta_{\text{in}} = 4^\circ/\%$  or 0.0019 ns/(keV/u).

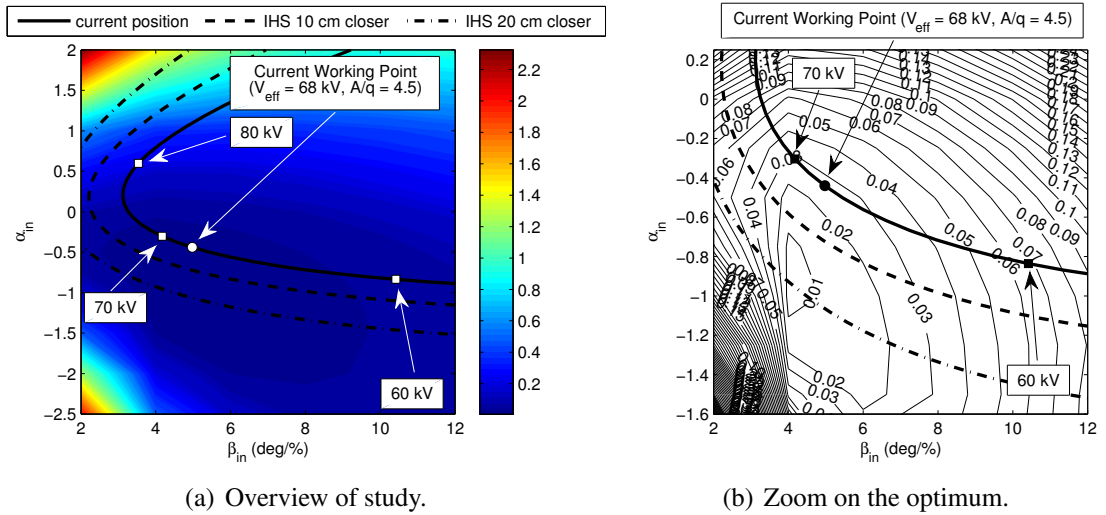


Figure 4.20: Logarithmic contour plots of the emittance growth factor ( $f_{\text{rms}}$ ) in the IHS as a function of input Twiss parameters.

From the study one can conclude that the matching section is permitting the IHS to perform close to its optimum, however if the IHS was moved closer to the rebuncher the emittance growth would be reduced and the transmission would be less sensitive to the voltage of the rebuncher.

### 4.3.8 RF Error Study

The sensitivity of the longitudinal beam quality to rf jitter was studied. The phase and voltage of the cavity was jittered with a Gaussian distribution characterised by the rms

values  $\sigma_{\Delta\phi}$  and  $\sigma_{\Delta V}$ , respectively. The rf was assumed stable during the 12 rf periods that a bunch takes to traverse the cavity and the time-averaged longitudinal emittance growth was studied for 250 bunches each containing 2000 particles subjected to different error seeds. The result of the study is shown in Figure 4.21 for independent phase or voltage errors. The stability of the low-level rf system is quoted as better than  $0.3^\circ$  and 1 % [47], which would increase the time averaged longitudinal emittance by less than 10 %.

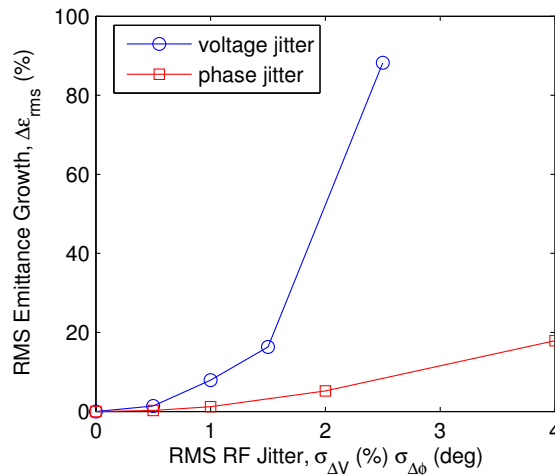


Figure 4.21: Time-average longitudinal emittance growth in the IHS as a function of the rf phase and voltage stability.

## 4.4 7-gap Split-ring Cavities (7GX)

The geometry of each 7-gap split-ring cavity was validated by comparing the accelerating field profile attained from rf simulations with field profiles that were measured by bead-pull and published in [67]. The three 7-gap split-ring cavities were simulated with LANA using the measured gap voltages and geometric parameters. The LANA models were benchmarked with numerical tracking in the realistic fields and compared to beam measurements. The energy dependence on phase for the 7G3 is shown in Figure 7.11 for measurements made with a silicon detector versus simulation. The longitudinal beam parameters before the 7G3 were measured and compared to simulation, see Chapter 5.

## 4.5 9-gap IH Cavity (9GP)

The 9-gap IH cavity will play an important role injecting the beam into the high energy section of the superconducting linac during the intermediate stages of the upgrade. The longitudinal beam matching in this scenario is critical. The gap voltage distribution and geometry published in [149] were used to create a model of the cavity, which was benchmarked with beam measurements and used to study the matching section.

### 4.5.1 Cavity Geometry

The cavity was originally designed to have a constant gap spacing, however after beam tests showed that the shunt impedance of the cavity was not sufficient to attain the desired energy gain, the gap lengths were adjusted from 19 to 27 mm, incrementing by 1 mm in each gap. The drift-tube structure gained some characteristics of a velocity-profiled structure, the transit-time factor was boosted and the desired energy gain was attained, however the flexibility of the structure was considerably reduced [149].

### 4.5.2 Energy Gain vs Phase

The energy gain as a function of phase for a particle with  $A/q = 4$  was first calculated using the measured gap voltages and applying thin lens kicks according to,

$$\Delta W = \sum_{i=1}^N qV_i T(g_i, \beta_i) \cos \phi_i, \quad (4.5.1)$$

where a hard-edge field shape was assumed in the analytic result for the single-gap transit-time factor. Figure 4.22 shows how the simple calculation was used to benchmark simulations using LANA and LORASR. The calculation is also compared to the average beam energy measured using the spectrometer.

The transmission to the spectrometer dropped quickly as the phase was adjusted away from close to the crest of the curve in Figure 4.22(b), which increased experimental uncertainties on the average beam energy. Nonetheless, the agreement with simulation is good in the narrow range of phase that could be probed.

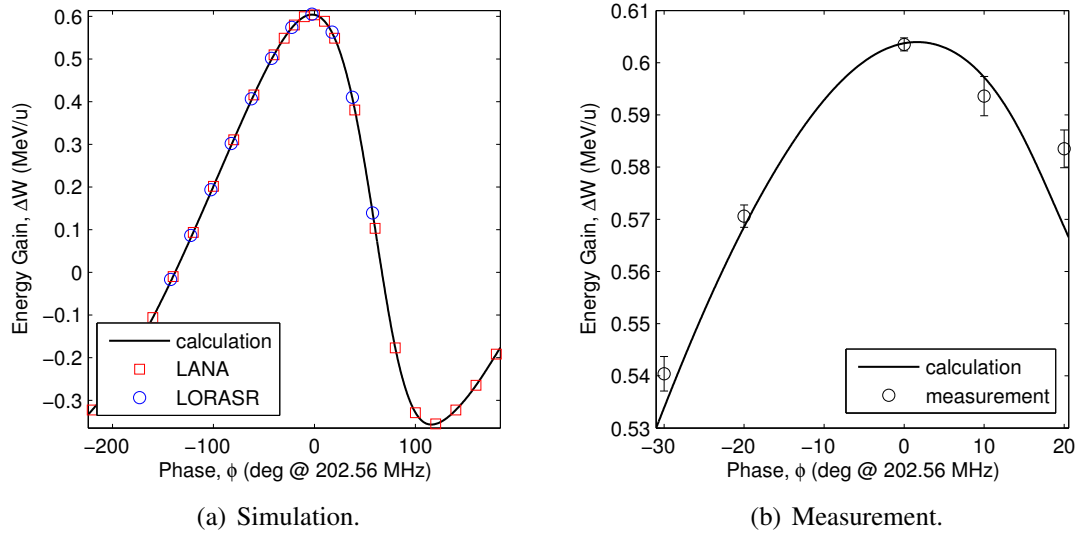


Figure 4.22: Benchmarking of LANA and LORASR simulations with a simple calculation and beam measurements of the energy gain in the 9GP,  $A/q = 4$ .

### 4.5.3 Energy Spread

The energy spread was measured using both the energy spectrometer and a silicon detector as a function of the 9GP phase and compared to simulation to validate the models. The simulated rms energy spread was calculated after tracking the realistic particle distribution through the 9GP and truncating the distribution at 95 %; this was done to permit a reasonable comparison with measurement in which extended distributions or tails are largely hidden by noise. The comparison is shown in Figure 4.23. The phase at which the energy

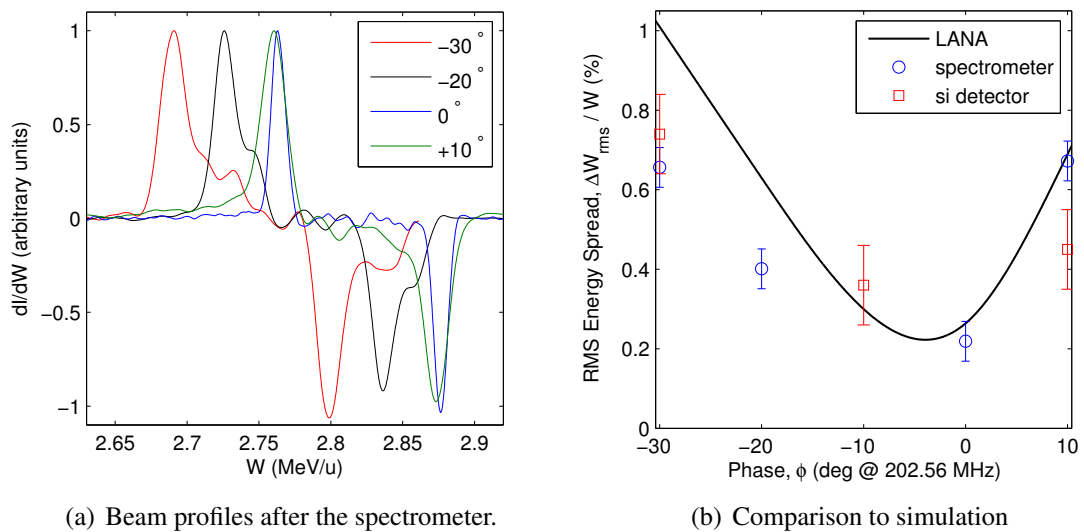


Figure 4.23: Energy spread measurements after the 9GP versus simulation.

spread is minimised is consistent with simulation, however the measured data is generally

smaller than simulation, especially where the transmission was low.

#### 4.5.4 Bunch Length

The silicon detector was exploited to measure the bunch length as a function of the 9GP phase at its position 9.5 m downstream in DB5. The arrival time of particles measured with respect to the rf master clock oscillating at 101.28 MHz is shown in Figure 4.24 for data acquired at five different phases. It was concerning to observe an apparent bunch splitting after the 9GP with a frequency twice that of the beam frequency, which is equal to the resonant frequency of the 9GP cavity. In the limited time available for the measurement it was not possible to diagnose the source of the discrepancy, however the splitting was not observed using the 7G3 with the 9GP switched off, see Figure 5.14.

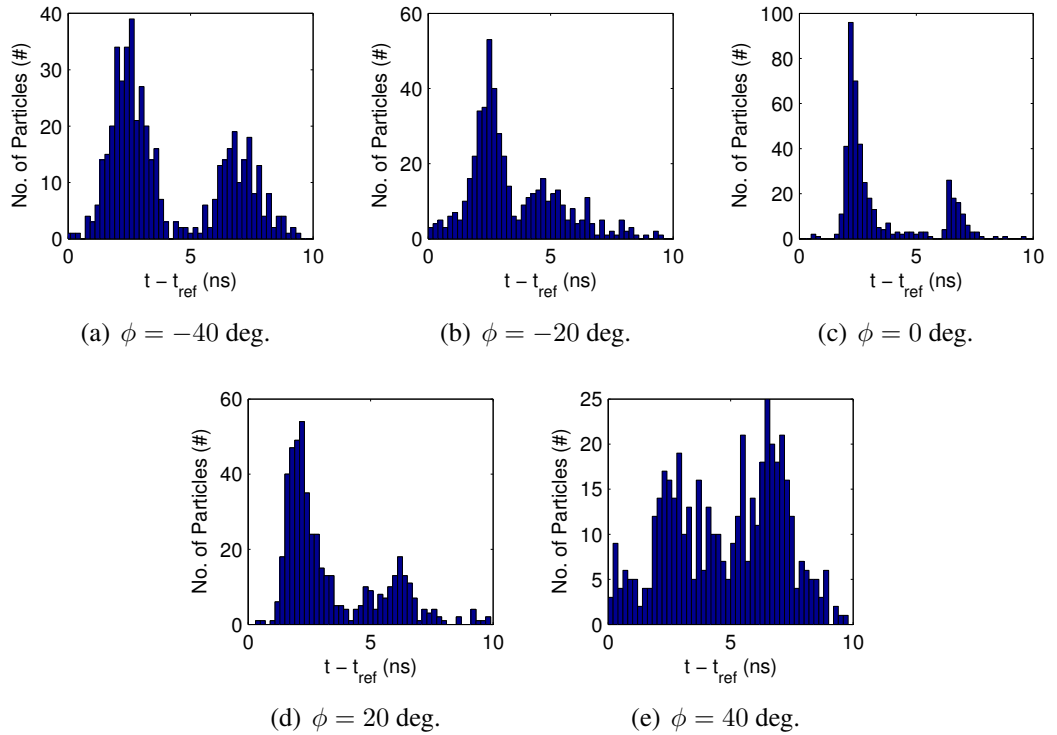


Figure 4.24: Bunch length profiles as a function of 9GP phase using the silicon detector.

By adjusting the phase of the 9GP to focus the bunch length at the detector's position in DB5 simulation predicts an rms bunch length of 0.7 ns at a phase of  $-5^\circ$ . The measured rms bunch length of the main peak in Figure 4.24(c) at  $0^\circ$  is in close agreement with simulation. Assuming that the longitudinal beam ellipse was upright at DB5 with the 9GP operating at  $0^\circ$ , the rms emittance can be estimated by combining the corresponding

bunch length and energy spread measurements to give  $3.8 \pi$  ns keV/u, roughly a factor of 5 larger than expected.

## 4.6 Beam Emittance

The transverse emittance measurements were already made before the investigations that are detailed in this thesis were carried out. Energy spread measurements taken during the commissioning of REX are briefly re-analysed here.

### 4.6.1 Transverse Emittance

During shutdown periods in 2006 and 2008 the transverse emittance was measured at various energies behind the RFQ, IHS, 7G3 and 9GP structures using a dedicated emittance rig positioned after the switchyard magnet on the  $0^\circ$  beam line. The measurement campaign is discussed in [160]. The results are summarised and compared to other measurements made during commissioning [47, 150] in Figure 4.25. The emittance was measured

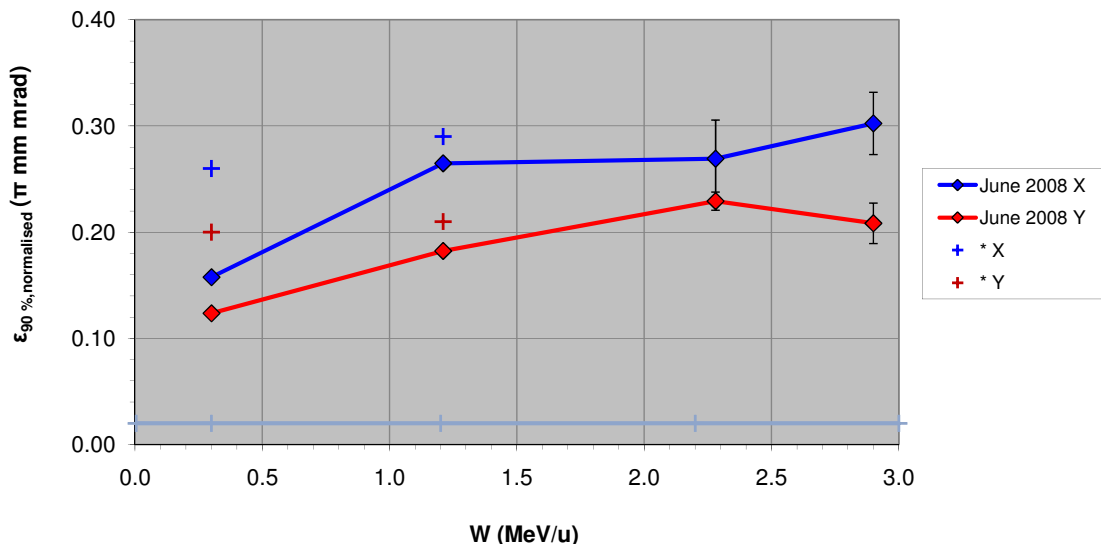


Figure 4.25: Summary of the transverse emittance measurements at REX (\*Data from [47, 150]). Reproduced from Figure 4 of [160].

larger in the horizontal projection, which was most likely because of the horizontal slit used after the  $A/q$ -separator that bends the beam vertically down from the EBIS to the REX beam line [48]. The IHS appears to be the dominant source of emittance growth,

increasing the emittance by approximately 50 %. This observation supports a recommissioning of the IHS accompanying the upgrade of the linac. The measured 90 % normalised emittance of  $0.3 \pi$  mm mrad was used as input for the end-to-end beam dynamics studies.

#### 4.6.2 Longitudinal Emittance from Analysis of Commissioning Data

Longitudinal beam measurements were made at the test stand at the Maier-Leibnitz Laboratory during the initial testing period of the REX front-end before commissioning at CERN [57, 143, 144]. The measured energy spread and bunch length were consistent with beam dynamics simulations of the RFQ, however the signal from the fast Faraday cup placed downstream of the RFQ suffered from a strong rf background that contributed to a significant uncertainty in the measurement, see Figure 3.5.3.8 of [57].

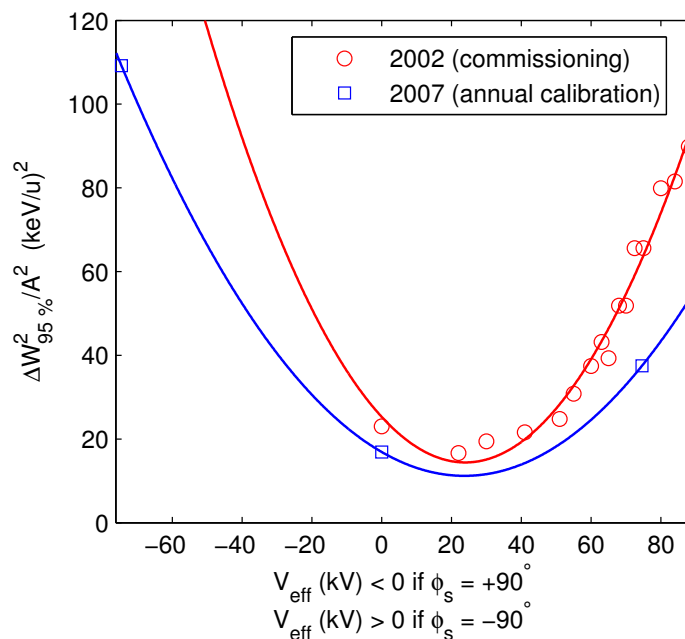


Figure 4.26: Summary of energy spread data as a function of the ReB voltage taken during commissioning [63] and during the calibration of the switchyard magnet in 2007 that permitted estimates of the longitudinal emittance.

Energy spread measurements were also made after each structure on installation and commissioning at ISOLDE [147]. The energy spread was measured in 2002 as a function of the ReB voltage using a spectrometer magnet located close to the RFQ but a detailed analysis of the longitudinal beam parameters was not carried out [63, 148]. The dataset is analysed here, along with another measured during an annual calibration of the ReB

in 2007, both of which are shown in Figure 4.26. A more detailed discussion of this investigation can be found in [161]. The datasets were fitted with parabolae from which the longitudinal beam parameters at the ReB were extracted; the three-gradient technique used to extract the beam parameters will be discussed in Chapter 5. Although the details of the measurements are not well known, it is understood that they were resolution limited and that the energy spread including 95 % of the beam current was measured [162]. The measurement errors are not plotted but assumed to be equally weighted across the data set at 0.5 keV/ $u$  or 0.2 % and the errors on the fitted beam parameters parameters were taken from a weighted least-squares fit. The 86 % emittance is estimated as  $3.3 \pm 0.4 \pi$  ns keV/ $u$  and  $1.9 \pm 0.4 \pi$  ns keV/ $u$  for the 2002 and 2007 measurements, respectively. The beam parameters are collected in Table 5.4 of the summary in Chapter 5.

## 4.7 Summary of End-to-end Beam Dynamics Simulations

The investigation of REX was concluded with end-to-end beam dynamics simulations of the linac using the realistic particle distribution from the RFQ simulations to provide the beam parameters at the exit of the IHS and 9GP cavities, which were required to design the matching sections for the upgrade. The RFQ simulations were also validated with measurements that will be described in detail in the next chapter. Due to a lack of reliable data it was not deemed worthwhile to create a realistic field simulation of the entire REX linac, however a LANA model provided a good insight. The beam envelopes were matched using the TRACE 3-D model that is presented in Figure 4.27. The end-to-end LANA simulations are summarised in Figure 4.28 and the relevant simulated beam parameters are collected in Tables 4.1, 4.2 and 4.3. The simulations identified three main regions of emittance growth:

- the internal re-bunching section of the IHS introduces emittance growth in all three phase space planes.
- matching from a triplet focusing channel to a doublet across the 7G1 introduces emittance growth in the vertical phase space projection.
- operating the 9GP close to the crest of the rf introduces significant longitudinal emittance growth.

The transverse emittance is increased in the internal re-bunching section of the IHS where the synchronous phase is lowered and the transverse beam size is large due to its proximity to the internal quadrupole triplet magnet. The large phase spread of the beam in the 7G1 combined with the vertical beam size, which has to be increased to match the beam through the quadrupole doublet magnet, causes emittance growth in predominantly the vertical projection. The 9GP is operated at a synchronous phase of  $0^\circ$  to attain the maximum possible energy gain requested by the experiments at ISOLDE, which introduces strong non-linearity in the longitudinal dynamics. The emittance growth is made worse by the long drift preceding it after the 7G3 and the doubling of the rf frequency.

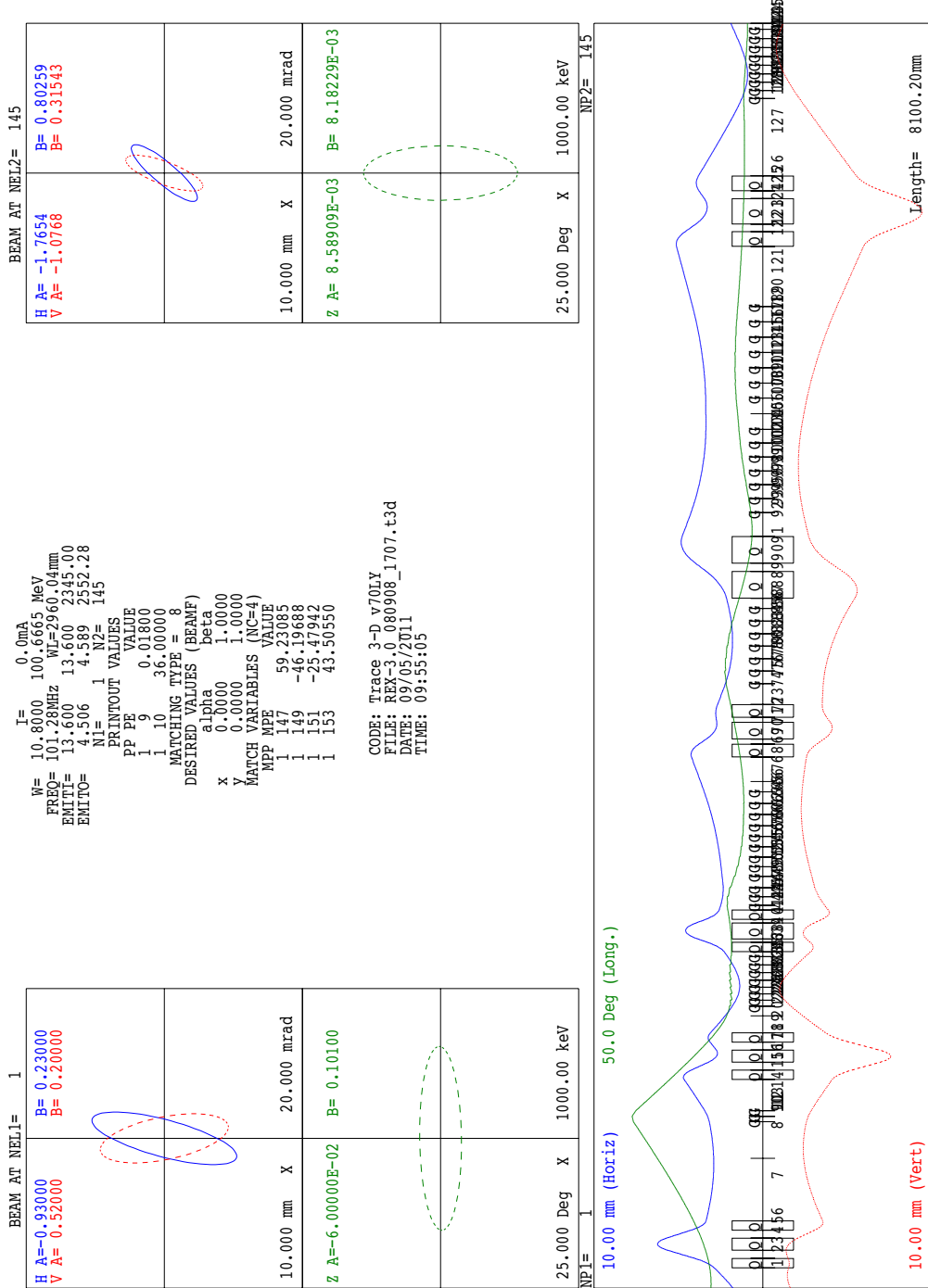


Figure 4.27: TRACE 3-D model of the REX linac.

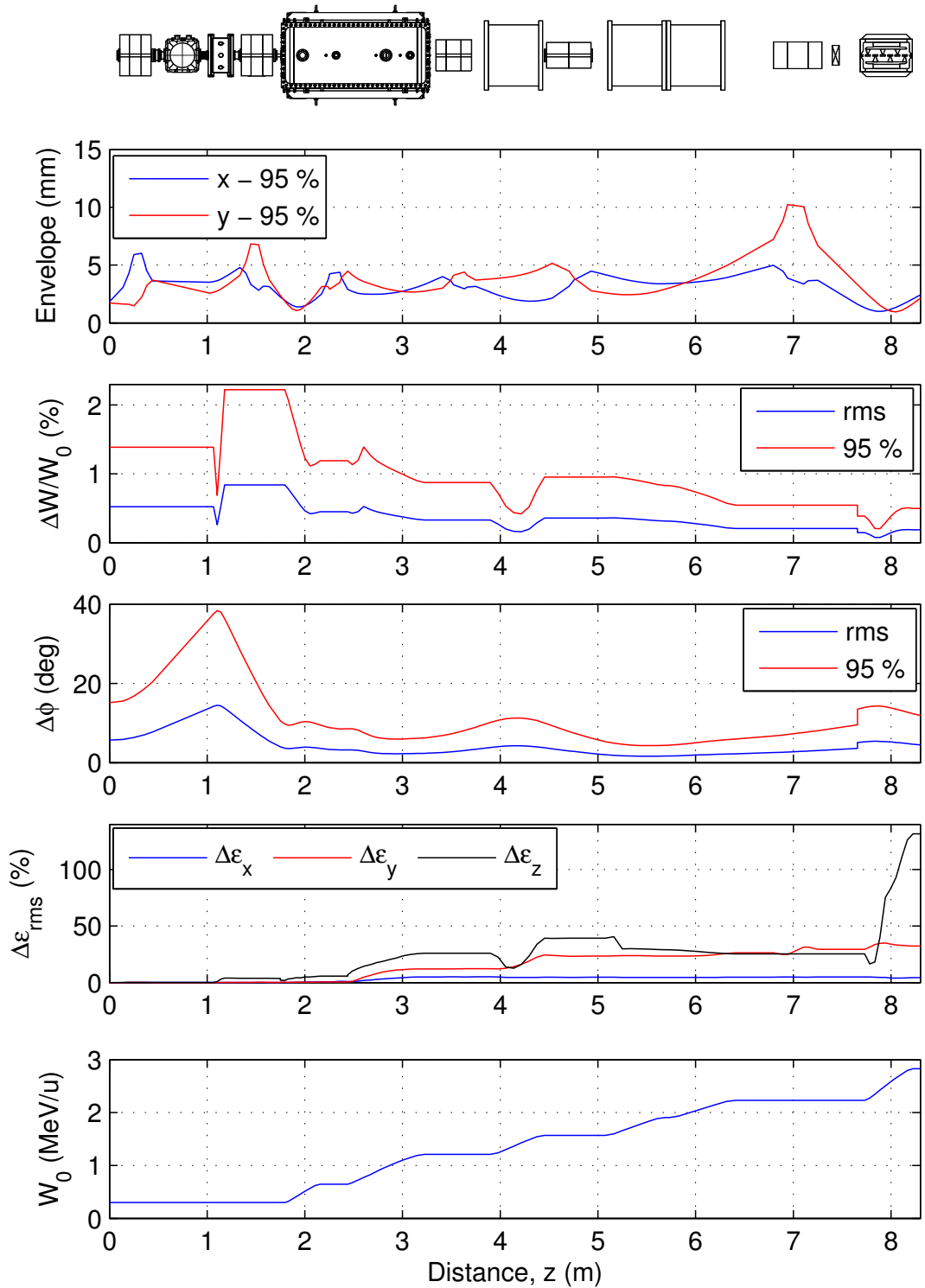


Figure 4.28: Summary of end-to-end multi-particle LANA simulations of REX,  $A/q = 4.5$ .

Table 4.1: Summary of the simulated horizontal REX beam parameters<sup>a</sup>

Position	Simulation Code	Energy [MeV/ $u$ ]	$\tilde{\alpha}_x$	$\tilde{\beta}_x$ [mm/mrad]	$\epsilon_{x \text{ rms}}^{\text{geom}}$ [ $\pi$ mm mrad]	$\epsilon_{x \text{ 95\%}}^{\text{geom}}$ [ $\pi$ mm mrad]	$\epsilon_{x \text{ rms}}^{\text{norm}}$ [ $\pi$ mm mrad]	$\epsilon_{x \text{ 95\%}}^{\text{norm}}$ [ $\pi$ mm mrad]
RFQ exit	PARMTEQM	0.30	-0.93	0.23	2.92	13.6	0.07	0.35
IHS exit	Tracking code	1.20	-1.72	2.06	1.66	8.47	0.08	0.43
9GP exit	LANA	2.82	-2.44	1.25	0.99	4.78	0.08	0.37

Table 4.2: Summary of the simulated vertical REX beam parameters<sup>a</sup>

Position	Simulation Code	Energy [MeV/ $u$ ]	$\tilde{\alpha}_y$	$\tilde{\beta}_y$ [mm/mrad]	$\epsilon_{y \text{ rms}}^{\text{geom}}$ [ $\pi$ mm mrad]	$\epsilon_{y \text{ 95\%}}^{\text{geom}}$ [ $\pi$ mm mrad]	$\epsilon_{y \text{ rms}}^{\text{norm}}$ [ $\pi$ mm mrad]	$\epsilon_{y \text{ 95\%}}^{\text{norm}}$ [ $\pi$ mm mrad]
RFQ exit	PARMTEQM	0.30	0.52	0.20	2.90	13.6	0.07	0.35
IHS exit	Tracking code	1.20	-0.83	1.30	1.64	8.45	0.08	0.43
9GP exit	LANA	2.82	-2.23	0.74	1.25	7.37	0.10	0.58

Table 4.3: Summary of the simulated longitudinal REX beam parameters<sup>a</sup>

Position	Simulation Code	Energy [MeV/u]	$\tilde{\alpha}_z$	$\tilde{\beta}_z$ [ns/(keV/u)]	$\epsilon_{z, \text{rms}}$ [ $\pi$ ns keV/u]	$\epsilon_{z, 95\%}$ [ $\pi$ ns keV/u]	$\epsilon_{z, \text{rms}}$ [ $\pi^\circ$ %] <sup>b</sup>	$\epsilon_{z, 95\%}$ [ $\pi^\circ$ %] <sup>b</sup>
RFQ exit	PARMTEQM	0.30	-0.06	0.10	0.26	1.79	3.12	21.8
IHS exit	Tracking code	1.20	0.32	0.03	0.32	2.11	0.96	6.41
9GP entry	LANA	2.23	1.26	0.07	0.32	1.96	0.52	3.20
9GP exit	LANA	2.82	-0.59	0.03	0.64	4.18	0.82	5.4

<sup>a</sup> The input files to all the simulation codes can be found on the CERN Engineering and Equipment Data Management Service (EDMS) under the HIE-ISOLDE project.

<sup>b</sup> At 101.28 MHz.

### 4.7.1 Beam Parameters for Stage 1 and 2a

The realistic phase space distribution at the output of REX is shown in Figure 4.29, using LANA. The 7GX resonators were set at a synchronous phase of  $-20^\circ$  and the 9GP at  $-10^\circ$ . The non-linearity in the dynamics of the longitudinal and vertical planes is clearly observed in the phase space distributions. In particular, the longitudinal phase space is shown both before and after the 9GP to show the non-linearity developed inside the structure. This non-linearity could be reduced by moving the 9GP closer to the 7G3 before the superconducting linac is installed and the transverse emittance growth in the 7GX cavities could be reduced by replacing the quadrupole doublet magnet with a triplet.

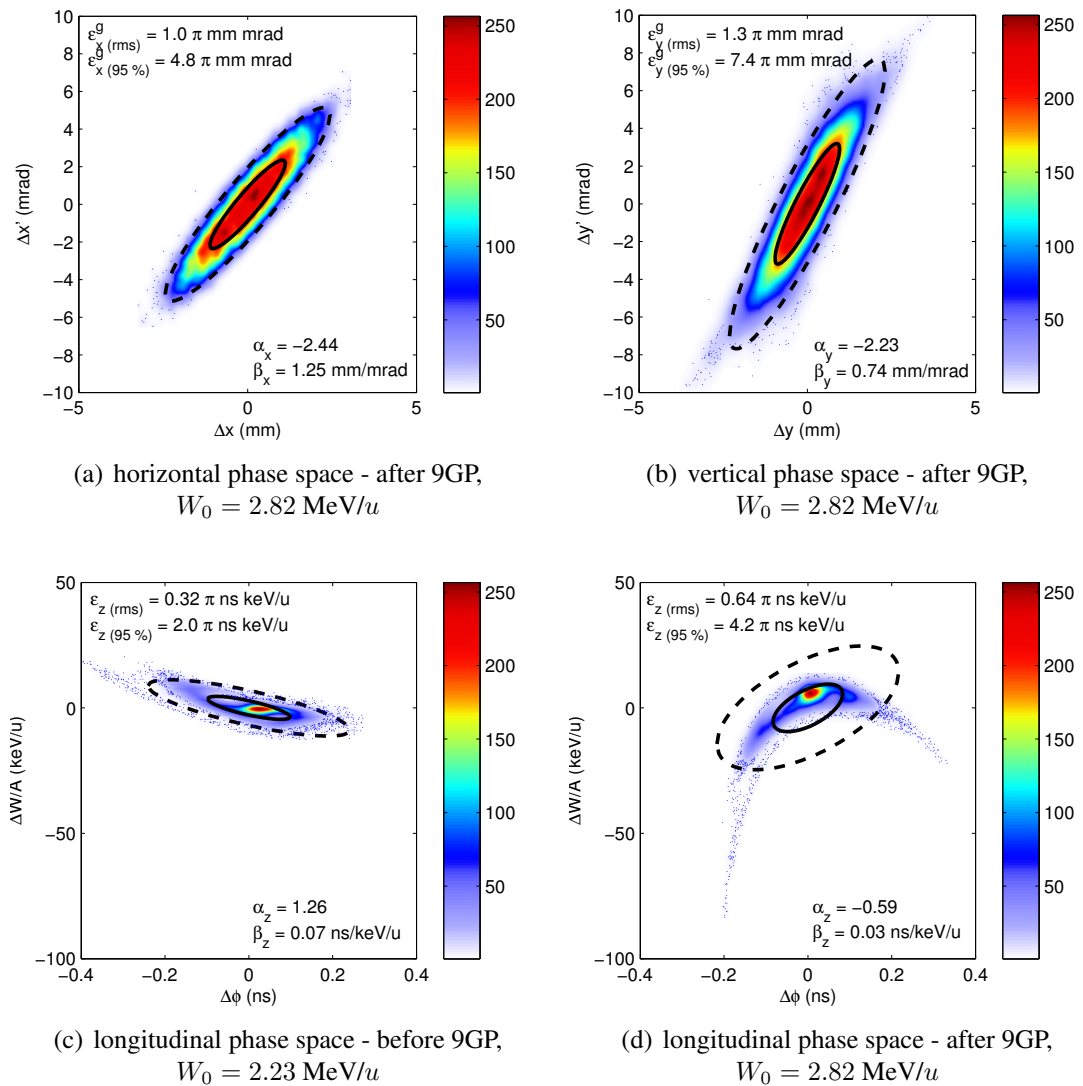


Figure 4.29: Beam phase space distribution at exit to REX, simulated with LANA.

### 4.7.2 Beam Parameters for Stage 2b

The beam parameters at output from the IHS were calculated by tracking through the realistic fields of the ReB and IHS. The phase space distribution of the beam at exit from the IHS is shown in Figure 4.30 where a horizontal displacement caused by the dipole kick in the IHS is noticeable. The beam parameters are also summarised in Tables 4.1, 4.2 and 4.3.

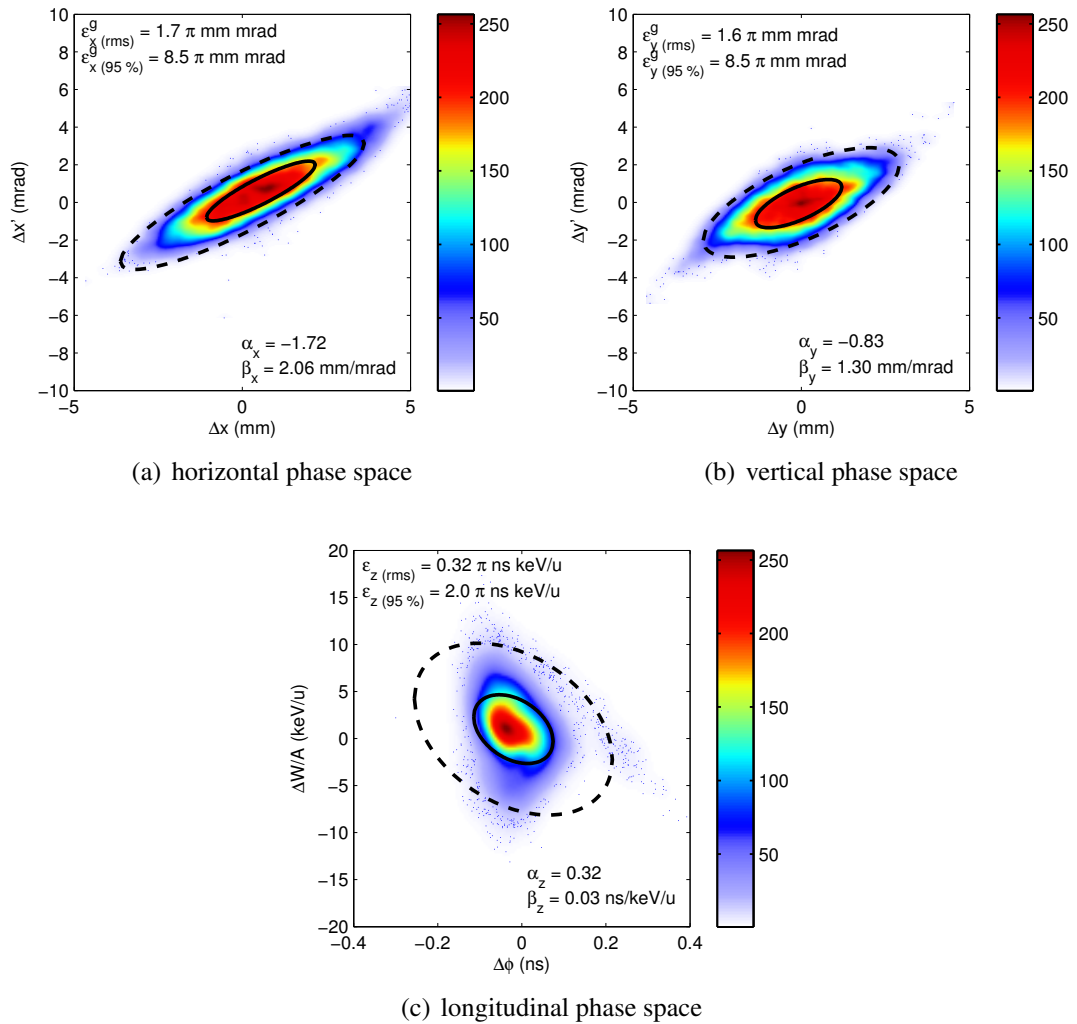


Figure 4.30: Beam phase space distribution at the exit to the IHS, simulated by tracking in the realistic fields of both the ReB and IHS.

The next chapter will describe the campaign of emittance measurements that was undertaken to ensure the compatibility of REX with the HIE upgrade.

## LONGITUDINAL EMITTANCE MEASUREMENTS

The longitudinal emittance was measured at REX to ensure its compatibility with the acceptance of the superconducting linac. The linac was shown next to the proposed upgrade in Figure 4.1 where one can find the locations of the cavities and diagnostic boxes discussed in this chapter. The upgrade will be staged with the high energy section arriving before the low energy section, thus it was important to investigate the beam properties at both low and high energies. In 2010 and 2011 the longitudinal emittance was measured at REX for the first time at opportune moments during pauses in the nuclear physics programme. The experimental procedure and formalism used for reconstructing the longitudinal beam parameters will be described before the results are presented and compared with simulation. The results are summarised and put in context with the longitudinal acceptance of the superconducting upgrade.

### **5.1 Experimental Overview**

Aside from a few dedicated techniques for emittance measurement in which simultaneous measurements of all phase space variables enable the direct measurement of emittance, e.g. pepperpots for the transverse emittance [163] and solid-state detectors for the longitudinal emittance [164, 165], the emittance can be reconstructed indirectly by manipulating the beam in a controlled way and measuring the response of just one of the phase space variables, usually the transverse beam size [106] or the energy spread of the beam [166–168]. With an understanding of the applied manipulation the beam ellipse can be reconstructed in two-dimensional phase space from a minimum of three independent

measurements. As a result, such techniques are generally termed three-gradient or three-profile measurements of emittance and there exist a wide number of techniques that apply the same general procedure [169, 170].

The longitudinal emittance was measured using the three-gradient technique before and after the IHS at 0.3 MeV/ $u$  and 1.92 MeV/ $u$ . The three-gradient technique uses an rf device operating at non-accelerating phases to vary the energy spread of the beam as a function of the rf voltage. The response of the energy spread to the rf voltage can then be measured and the emittance extracted by fitting the data using the Courant-Snyder formalism if the transfer matrix of the rf device is known [171].

The bulk of the measurements used the switchyard magnet to measure the energy spread of the beam as a function of the voltage of the ReB and 7G3 cavities operating in a non-accelerating mode. The emittance could not be measured using the 9GP because of the velocity profiling of its drift-tubes and the resulting variation of the rf phase seen by the beam in each gap. The 7G3 cavity was selected instead of the 7G1 and 7G2 cavities because its geometric velocity is the closer to the beam velocity in normal operation. The energy spread was inferred from measurements of the horizontal beam size in the dispersive region after the switchyard magnet. A silicon detector under development for the longitudinal diagnostic systems of the HIE linac was also exploited for both energy and timing measurements. The silicon detector was placed in DB5.

In the absence of a dedicated offline ion source for machine development a beam consisting of residual gas from the REXEBIS was used for the measurements and a mass-to-charge state  $A/q = 4$  was chosen to deliver beams composed predominantly of neon buffer gas ( $^{20}\text{Ne}^{5+}$ ) leaked from the adjacent Penning trap (REXTRAP). Intensities from the ion source of over 100 pA were achieved by increasing the repetition rate of the ion source close to 50 Hz and increasing the pressure in the EBIS to a few  $10^{-10}$  mbar. As a result of leaking gas into the EBIS, which is usually done to produce high beam intensities for machine development (a few nA for all charge states), the source emittance increases because the radial potential of the electron beam trapping the ions is somewhat compensated. Nevertheless, the effect of the ion source transverse emittance on the longitudinal emittance at output from the RFQ was shown by simulation to be weak, as shown

in Figure 5.1.

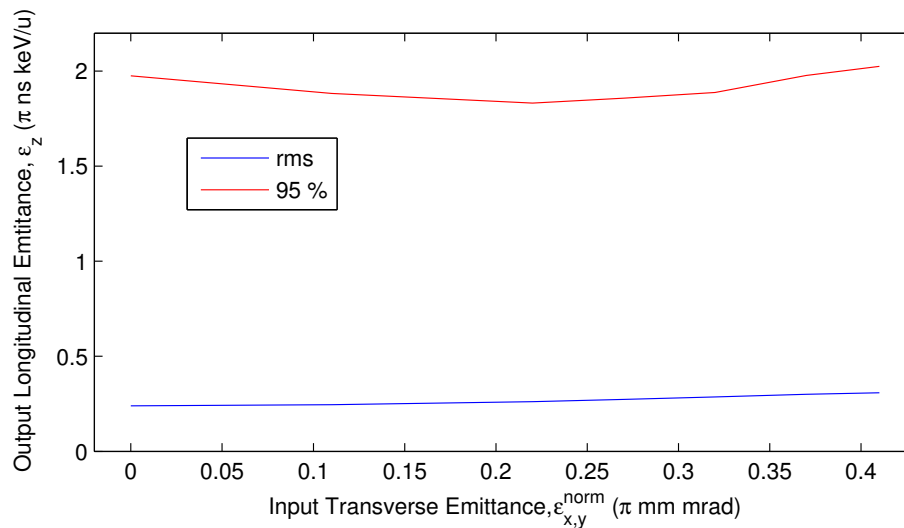
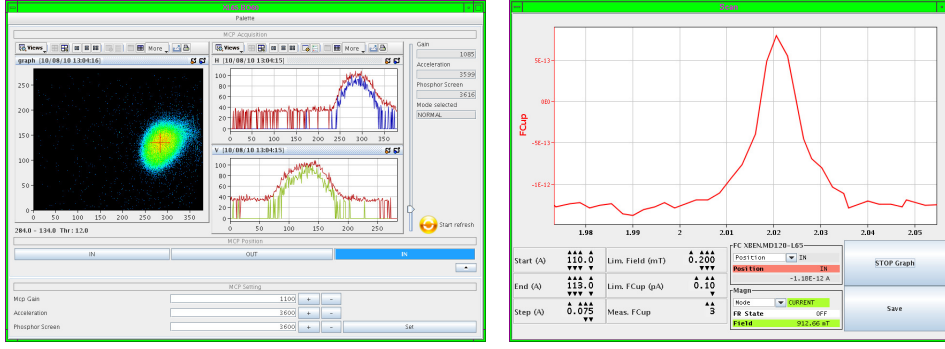


Figure 5.1: The longitudinal emittance created by the RFQ as a function of the input transverse emittance simulated by PARMTEQM.

As discussed in Chapter 4.6.1, the 90 % normalised transverse emittance was measured with the EBIS operating under similar conditions at approximately  $0.3 \pi$  mm mrad. The energy spread of the beam coming from the source is estimated as 0.1 %, which was also shown by simulation to have a negligible effect on the longitudinal emittance developed in the RFQ [152, 172]. The transmission through the linac at 300 keV/u was typically as low as 50 % because of the large beam size, misalignment of the linac [173] and lack of steerers. As experience was gained with tuning low energy beams, transmissions of up to 80 % were possible towards the end of the measurement campaign.

The diagnostic system normally used to profile the low intensity beams is based on the amplification of secondary electrons created from the beam impinging on an aluminium foil and provides a good qualitative representation of the beam profile, which is useful during beam tuning but is not well calibrated [174]. It was deemed more accurate to measure the energy spread by varying the dipole field of the switchyard magnet and scanning the beam across a slit in front of a Faraday cup located in the diagnostic boxes DB6 and DB7. A control software was custom-built for the measurement campaign in order that the beam current on the Faraday cup could be acquired as a function of the dipole field measured on a Hall probe inside the switchyard magnet [175]. The online software controlling the low intensity diagnostic system is shown next to the software displaying

Faraday cup signal in Figure 5.2.



(a) The low intensity beam profiler.

(b) The energy scan application.

Figure 5.2: Beam diagnostics at REX displaying the beam at DB7 at 1.92 MeV/u.

## 5.2 Theory of Three-gradient Emittance Measurement

The discussion below focuses on the measurement of the longitudinal emittance with an rf cavity upstream of a diagnostics system. Assuming that the cavity can be approximated as a thin element, its transfer matrix when operating at the non-accelerating synchronous phases can be expressed as,

$$R_{\text{buncher}} = \begin{pmatrix} 1 & 0 \\ -qV_{\text{eff}} \sin \phi_s & 1 \end{pmatrix}, \quad \text{where } \phi_s = \pm 90^\circ, \quad (5.2.1)$$

as is derived in Appendix C.1. A drift of length  $L$  is described by,

$$R_{\text{drift}} = \begin{pmatrix} 1 & -\frac{2\pi L}{\gamma(\gamma+1)\beta\lambda W_0} \\ 0 & 1 \end{pmatrix}, \quad (5.2.2)$$

where the ion has  $q$  units of elementary charge,  $\beta$  and  $\gamma$  are the usual relativistic factors,  $V_{\text{eff}}$  is the rf voltage including transit-time factor and  $L$  is the drift length to the diagnostics system located downstream of the cavity. The longitudinal phase space variables of energy and phase spread about the reference particle are used, i.e.  $\Delta W$  and  $\Delta\phi$ , respectively. The linearised mapping of the longitudinal coordinates through the cavity to the

diagnostics system can then be written in the non-relativistic limit as,

$$X_1 = R_{\text{drift}} R_{\text{buncher}} X_0, \quad (5.2.3)$$

or,

$$\begin{pmatrix} \Delta\phi_1 \\ \Delta W_1 \end{pmatrix} = \begin{pmatrix} 1 + \frac{\pi q V_{\text{eff}} L}{\beta \lambda W_0} \sin \phi_s & -\frac{\pi L}{\beta \lambda W_0} \\ -q V_{\text{eff}} \sin \phi_s & 1 \end{pmatrix} \begin{pmatrix} \Delta\phi_0 \\ \Delta W_0 \end{pmatrix}, \quad \text{where } \phi_s = \pm 90^\circ. \quad (5.2.4)$$

Using the  $\sigma$ -matrix formalism the Twiss parameters can be propagated through the buncher and succeeding drift by calculating,

$$\sigma_1 = R_{\text{drift}} R_{\text{buncher}} \sigma_0 (R_{\text{drift}} R_{\text{buncher}})^T. \quad (5.2.5)$$

### 5.2.1 Energy Spread Measurements in the Thin Lens Approximation

Using Equation 5.2.5, the square of the energy spread measured after the buncher cavity ( $\Delta W_1^2$ ) can be written as a quadratic function of  $V_{\text{eff}}$  and the Twiss parameters immediately before the cavity ( $\tilde{\alpha}_0, \tilde{\beta}_0, \tilde{\gamma}_0$  and  $\epsilon_0$ ) as,

$$\frac{\Delta W_1^2}{A^2} = \epsilon_0 \left[ \left( \frac{q}{A} \right)^2 \tilde{\beta}_0 \sin^2 \phi_s V_{\text{eff}}^2 + 2 \left( \frac{q}{A} \right) \tilde{\alpha}_0 \sin \phi_s V_{\text{eff}} + \tilde{\gamma}_0 \right], \quad (5.2.6)$$

where  $\phi_s = \pm 90^\circ$  and the mass number ( $A$ ) of the ion is shown explicitly to demonstrate the effect of the mass-to-charge state on the measurement. Experimentally the emittance can be determined from a quadratic fit of the form  $y = a_2 x^2 + a_1 x + a_0$ , where  $x = V_{\text{eff}} \sin \phi_s$  and  $y = \frac{\Delta W_1^2}{A^2}$ . Therefore,

$$\epsilon_0 = \left( \frac{A}{q} \right) \sqrt{a_0 a_2 - \frac{a_1^2}{4}}, \quad (5.2.7)$$

and the other Twiss parameters can be written,

$$\tilde{\alpha}_0 = \frac{1}{2} \left( \frac{A}{q} \right) \frac{a_1}{\epsilon_0}, \quad \tilde{\beta}_0 = \left( \frac{A}{q} \right)^2 \frac{a_2}{\epsilon_0} \quad \text{and} \quad \tilde{\gamma}_0 = \frac{a_0}{\epsilon_0}. \quad (5.2.8)$$

### 5.2.2 Bunch Length Measurements in the Thin Lens Approximation

The square of the bunch length ( $\Delta t^2$ ) measured at a distance ( $L$ ) downstream of the buncher cavity is also a quadratic function of  $V_{\text{eff}}$  and can be written,

$$\Delta t^2 = a_2 \sin^2 \phi_s V_{\text{eff}}^2 + a_1 \sin \phi_s V_{\text{eff}} + a_0, \quad (5.2.9)$$

where  $\phi_s = \pm 90^\circ$ . The fit parameters  $a_0$ ,  $a_1$  and  $a_2$  can be expressed in terms of the Twiss parameters before the buncher and the reduced velocity ( $\beta$ ),

$$\frac{a_2}{\epsilon_0} = \left(\frac{q}{A}\right)^2 \left(\frac{\pi L}{\beta \lambda \frac{W_0}{A}}\right)^2 \tilde{\beta}_0, \quad (5.2.10)$$

$$\frac{a_1}{\epsilon_0} = 2 \left(\frac{q}{A}\right) \frac{\pi L}{\beta \lambda \frac{W_0}{A}} \left[ \frac{\pi L}{\beta \lambda \frac{W_0}{A}} \tilde{\alpha}_0 + \tilde{\beta}_0 \right], \quad (5.2.11)$$

and,

$$\frac{a_0}{\epsilon_0} = \tilde{\beta}_0 + 2 \frac{\pi L}{\beta \lambda \frac{W_0}{A}} \tilde{\alpha}_0 + \left(\frac{\pi L}{\beta \lambda \frac{W_0}{A}}\right)^2 \tilde{\gamma}_0. \quad (5.2.12)$$

The expression for the bunch length is somewhat more complicated than that for the energy spread because it depends on the distance of the measurement downstream of the cavity. The emittance is given in terms of the fit parameters as,

$$\epsilon_0 = \left(\frac{A}{q}\right) \left(\frac{\beta \lambda \frac{W_0}{A}}{\pi L}\right)^2 \sqrt{a_2 a_0 - \frac{a_1^2}{4}}, \quad (5.2.13)$$

and Equations 5.2.10, 5.2.11 and 5.2.12 can be rearranged to calculate the other Twiss parameters from the experimental fit.

### 5.2.3 Energy Spread Measurements with a Multi-gap Buncher

The ReB and 7G3 cavities have 3 and 7 accelerating gaps respectively, which limits the application of the thin lens approximation in the three-gradient emittance measurement. The extent of the limitation was investigated and a formalism developed to extend the approximation to make accurate emittance measurements with multi-gap cavities. The longitudinal transfer matrix ( $R_{\text{buncher}}^{N_{\text{gaps}}}$ ) describing the dynamics between the first and last

gaps of an  $N$ -gap buncher cavity with a constant geometric velocity operating in  $\pi$ -mode can be calculated by concatenating the matrices,

$$R_{\text{buncher}}^{N\text{gaps}} = R_{1,\text{buncher}} R_{1,\text{drift}} R_{2,\text{buncher}} R_{2,\text{drift}} \cdots R_{N-1,\text{buncher}} R_{N-1,\text{drift}} R_{N,\text{buncher}}, \quad (5.2.14)$$

where the  $i^{\text{th}}$  gap is approximated by a thin element. The drift-spaces in a  $\pi$ -mode structure with constant gap spacing can be mapped as,

$$R_{i+1,\text{drift}} = R_{i,\text{drift}} = \begin{pmatrix} 1 & -\frac{\pi}{2W_0} \\ 0 & 1 \end{pmatrix}, \quad (5.2.15)$$

where the average beam energy ( $W_0$ ) is assumed as matched to the geometric velocity. The total effective voltage is defined by the sum of the voltages in each gap ( $V_{i,\text{eff}}$ ) such that,

$$V_{\text{eff}} = \sum_{i=1}^N V_{i,\text{eff}}. \quad (5.2.16)$$

By assuming that the beam energy is matched to the geometric velocity of the cavity the beam velocity remains constant between the gaps at the non-accelerating phases and the synchronous phase is the same in each gap. Therefore, after expanding out Equation 5.2.14 one can write,

$$R_{\text{buncher}}^{N\text{gaps}} = \sum_{i=1}^N \begin{pmatrix} f_{i,11}(N) \left(\frac{\pi}{2} \sin \phi_s\right)^{i-1} \left(\frac{qV_{\text{eff}}}{W_0}\right)^{i-1} & -\frac{\pi}{2W_0} f_{i,12}(N) \left(\frac{\pi}{2} \sin \phi_s\right)^{i-2} \left(\frac{qV_{\text{eff}}}{W_0}\right)^{i-2} \\ -qV_{\text{eff}} \sin \phi_s f_{i,21}(N) \left(\frac{\pi}{2} \sin \phi_s\right)^{i-1} \left(\frac{qV_{\text{eff}}}{W_0}\right)^{i-1} & f_{i,22}(N) \left(\frac{\pi}{2} \sin \phi_s\right)^{i-1} \left(\frac{qV_{\text{eff}}}{W_0}\right)^{i-1} \end{pmatrix}.$$

The matrix elements of  $R_{\text{buncher}}^{N\text{gaps}}$  are finite polynomial expansions in  $\frac{qV_{\text{eff}}}{W_0}$  with an order less than  $N$  and with coefficients  $f_{i,jk}$  that are simple functions of  $N$ . Each term in the expansion can be written in matrix form,

$$R_{\text{buncher}}^{N\text{gaps}} = \sum_{i=1}^N R_i. \quad (5.2.17)$$

In this form one can truncate the polynomials and write approximate expressions for the transfer matrix of an  $N$ -gap buncher when  $qV_{\text{eff}} \ll W_0$ . The transfer matrix for an  $N$ -gap

buncher cavity can be approximated as,

$$R_{\text{buncher}}^{N \text{ gaps}} \approx R_1 + R_2 + R_3, \quad (5.2.18)$$

where  $R_1$  represents the thin lens approximation. The next two matrices act as corrections, sufficient to calculate the beam parameters downstream to second-order in  $\frac{qV_{\text{eff}}}{W_0}$ . The coefficients  $f_{i,jk}$  depend on the voltage distribution across the gaps inside the cavity and were derived up to  $i = 3$  for a flat voltage distribution and a flat distribution with the external drift-tubes grounded, see Appendix C.2. By truncating the expansion at  $i = 2$ , such that  $R_{\text{buncher}}^{N \text{ gaps}} = \sum_{i=1}^2 R_i = R_1 + R_2$ , the energy spread downstream of a multi-gap buncher can be approximated to orders linear in  $\frac{qV_{\text{eff}}}{W_0}$  as a cubic function of  $V_{\text{eff}}$ , where expressions for the polynomial coefficients can be found derived in Appendix C.2. By truncating the expansion at  $i = 3$  the energy spread downstream of a multi-gap buncher can be written as a quartic function of  $V_{\text{eff}}$ , also see Appendix C.2.

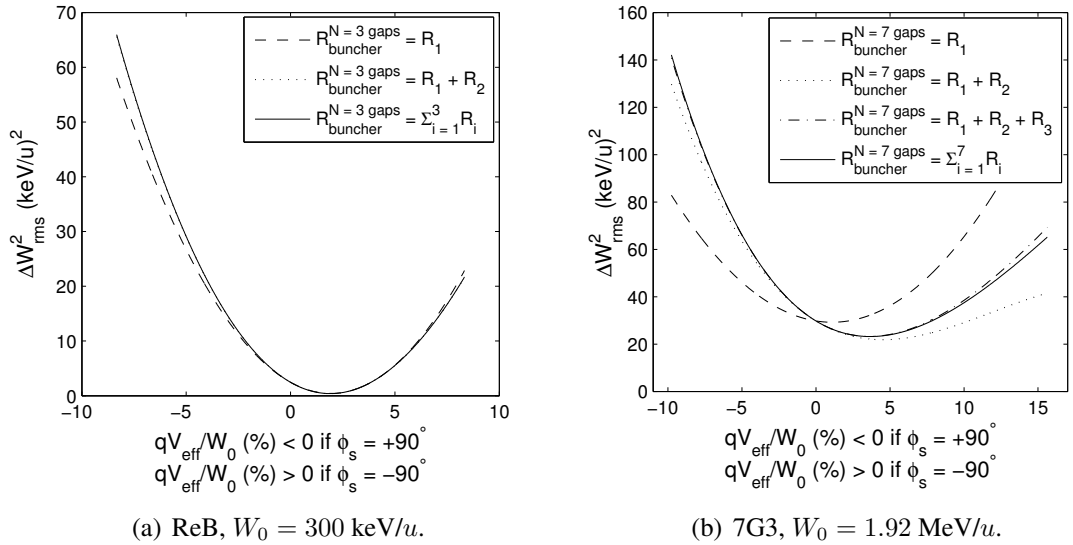


Figure 5.3: Energy spread calculated downstream of the ReB and 7G3 compared to the approximations discussed.

The coefficients of the polynomials in these extensions of the thin lens approximation characterise more simultaneous equations than independent and unknown Twiss parameters. The problem is over-constrained and a unique expression for the emittance does not exist as it does for the quadratic case. Nonetheless, one can implement the above relationships into a least-square fitting routine to solve the beam parameters from experimental

data. The energy spread of the beam calculated downstream of the ReB and 7G3 cavities is plotted using nominal beam parameters taken from simulation as a function of typical values of  $\frac{qV_{\text{eff}}}{W_0}$  in Figure 5.3. The  $V_{\text{eff}}$  dependence of the complete transfer matrix ( $R_{\text{buncher}}^{N_{\text{gaps}}}$ ) is compared with the simple thin lens approximation and the extensions described above. Although the thin lens approximation is reasonable for the ReB, it is imperative that the thin lens approximation is extended in the case of the 7G3.

### 5.3 Spectrometer

The switchyard magnet was incorporated into a spectrometer system comprising the diagnostic boxes and quadrupole triplet magnets located behind it on two beam lines at  $20^\circ$  and  $65^\circ$ . The basic geometric parameters used to model the switchyard magnet are collected in Table 5.1 [176]. The system was made point-to-point between the entry slit of the system in DB5 and the exit slits in front of the Faraday cups in DB6 and DB7 by tuning the quadrupole gradients of the triplet magnets and setting the transfer matrix elements  $R_{12}$  and/or  $R_{34}$  to zero,

$$x_{\text{DB6/7}} = R_{11}x_{\text{DB5}} + R_{12}x'_{\text{DB5}} + R_{16}\frac{\Delta p}{p_0}. \quad (5.3.1)$$

The quadrupoles were tuned with a TRACE 3-D model shown in Figure 5.4.

Table 5.1: Parameters of the REX switchyard magnet

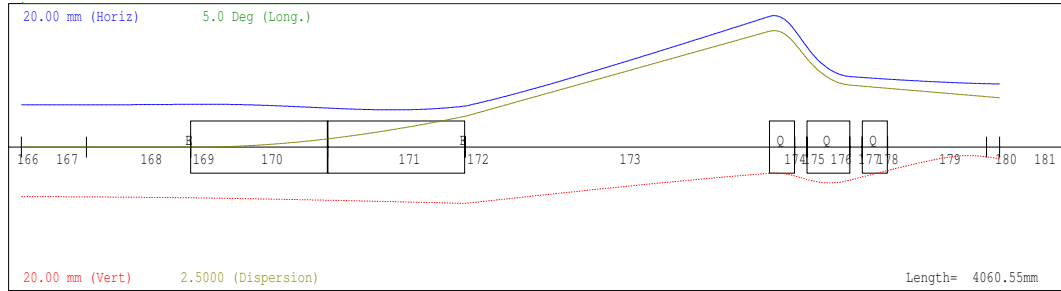
Beam Line [deg]	Edge Angle* [deg]	Bend Radius [m]	Max. Rigidity [Tm] [ $B_{\text{max}} = 1.14 \text{ T}$ ]	Gap Height [mm]
20	10	2.878	3.3	50
65	32	0.930	1.1	50

\* No edge angle on entry.

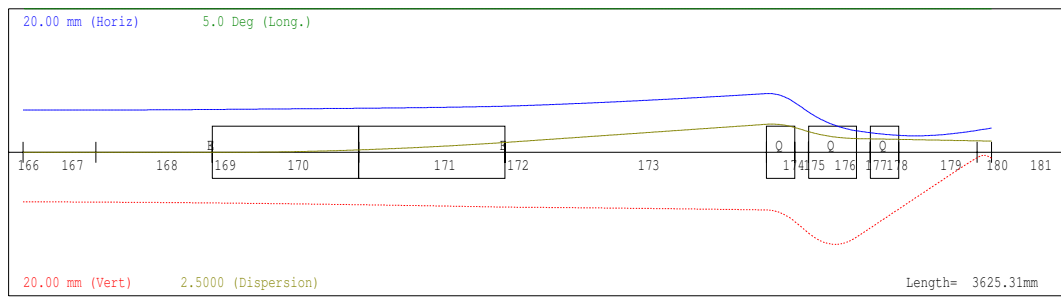
Profiling the beam by varying the dipole field of the switchyard magnet has its drawbacks because the optics of the spectrometer system is perturbed, affecting the measurement through the various listed mechanisms:

- The dispersion function ( $R_{16}$ ) changes as the radius of the beam trajectory changes.
- The edge angle seen by the beam as it leaves the switchyard magnet varies.

- The point-to-point optics solution is mismatched because the quadrupole gradients were not varied with the dipole field.
- Some of the beam may be lost on the aperture of the quadrupole as the beam is moved.



(a) 65° beam line.



(b) 20° beam line.

Figure 5.4: The spectrometer simulated with TRACE 3-D, giving a stigmatic focus ( $R_{12} = R_{34} = 0$ ) at RFQ energy with the first two quadrupole magnets powered.

Although the 65° beam line provides a resolution of almost three times that possible on the 20° beam line, the large edge angle on the 65° beam line strongly defocuses the beam in the dispersive plane and brings the beam envelope close to the aperture of the first quadrupole at 20 mm, as is evident in Figure 5.4. Assuming that the beam size after the switchyard magnet is dominated by dispersion, the momentum acceptance through the spectrometer is 1.0 % and 4.1 % on the 65° and 20° beam lines, respectively; the range of beam energy spread measurable on the most dispersive beam line is restricted.

Attempts were made to directly profile the beam over a slit with a size smaller than the beam in front of the Faraday cup, however in order to attain a satisfactory signal-to-noise ratio the size of the entrance slit had to be increased and the resolution of the spectrometer was compromised. This was most problematic on the more dispersive beam line where the beam size is larger and the intensity is spread over a wider area at the Faraday cup.

The beam current was very low and typically less than 10 pA after a 1 mm vertical slit was placed in DB5 at the entrance to the spectrometer. Instead, the beam was profiled using a slit wider than the horizontal beam size in front of the Faraday cups in DB6 and DB7. The beam profile was reconstructed from the derivative of the beam current measured on the Faraday cup as the beam was swept over each edge of the aperture, described in [49]. An example profile measurement at 1.92 MeV/ $u$  is shown in Figure 5.5 alongside the reconstruction of the beam profile on each side of the slit, which involved smoothing, fitting and differentiating the data. The dipole field of the switchyard magnet was calibrated by assuming that the beam energy after the RFQ was 300 keV/ $u$ , which is a reasonable assumption to within the  $\pm 1.5\%$  energy spread of the beam [177].

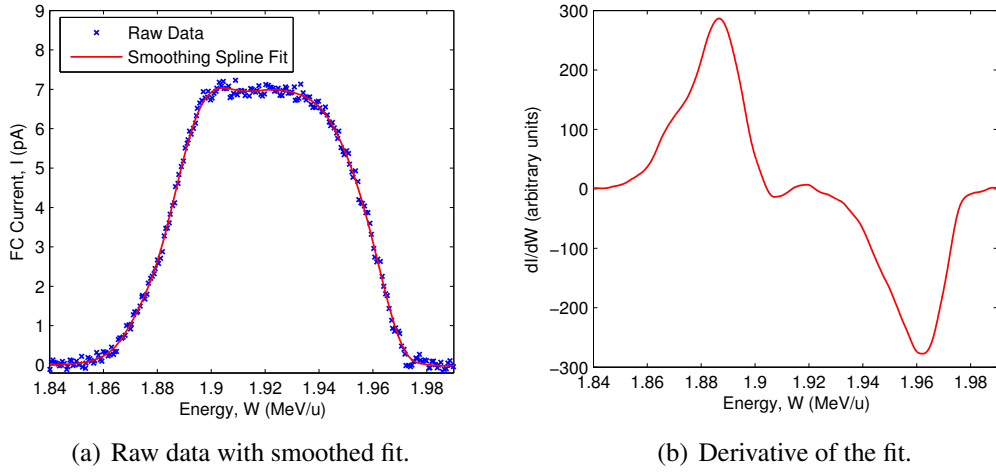


Figure 5.5: An example profile measurement made on the  $65^\circ$  beam line using a 1 mm vertical slit on entry to the spectrometer and a 15 mm circular aperture in front of the Faraday cup.

The beam current measured on the Faraday cup was analysed to determine the rms energy spread. From the derivative with respect to energy of the current ( $I$ ) measured on the cup one can write,

$$\sigma_{\Delta W}^2 = \frac{\int_{-\infty}^{\infty} (W - W_0)^2 \frac{dI(W)}{dW} dW}{\int_{-\infty}^{\infty} \frac{dI(W)}{dW} dW}, \quad (5.3.2)$$

where  $W_0$  is defined by the position of the centre of the slit after the switchyard magnet,

$$W_0 = \frac{\int_{-\infty}^{\infty} W \frac{dI(W)}{dW} dW}{\int_{-\infty}^{\infty} \frac{dI(W)}{dW} dW}. \quad (5.3.3)$$

The spectrometer was tuned to maximise the dispersion function at either DB6 or DB7 whilst keeping the system point-to-point, which reduces the perturbation required to move the beam across the slit at the Faraday cup and reduces the probability of beam loss on the aperture of the quadrupole. The spectrometer settings are collected in Table 5.2 for a low energy measurement. The dispersion function at the Faraday cup is increased when operating the system with a stigmatic focus. The optimum situation was found with the two external quadrupoles of the triplet powered with opposite polarity providing a stigmatic focus at the Faraday cup. As the polarity of the current leads did not facilitate this configuration the first two quadrupoles were powered instead. The quadrupole triplet magnets behind the switchyard magnet were removed from the beam line, calibrated and realigned when replaced [178].

Table 5.2: Spectrometer settings for  $A/q = 4$  and  $W_0 = 300$  keV/ $u$ 

Beam Line [deg]	Quadrupole Polarities	$kL_{\text{eff}}$ [T]	$R_{16}^{\text{FC}}$ [m]	$\frac{R_{11}}{R_{16}}$	$R_{12}$ [m]	$R_{34}$ [m]
65	+, 0, 0	0.49, 0, 0	-0.53	0.89	0	3.80
65	+, -, 0	0.77, 1.85, 0	-0.86	0.89	0	0
65	+, 0, -	0.72, 0, 1.12	-0.94	0.89	0	0
20	+, 0, 0	0.57, 0, 0	-0.12	2.52	0	6.60
20	+, -, 0	1.22, 1.55, 0	-0.20	2.52	0	0
20	+, 0, -	0.80, 0, 1.41	-0.21	2.52	0	0

One drawback of maximising the dispersion function is that the beam size at the Faraday cup is large, which limits the range of beam dispersion that can be measured with this technique; for a given slit size and dispersion function the range of energy spread measurable is limited by the requirement that the beam fits inside the slit. As machine interventions had to be kept to a minimum the collimator wheels in front of the Faraday cups were not modified and in order to measure large beam sizes on the most dispersive beam line a circular aperture had to be used.

## 5.4 Simulations of the Measurement

The TRAVEL code [142] was used to validate the technique employed to measure the energy spread, including higher-order effects. Losses inside the quadrupole and the shape

of the aperture in front of the Faraday cup can have a strong impact on the measurement and for this reason the consequences and their mitigation were rigorously simulated.

#### 5.4.1 Effect of a Circular Aperture

A simulation is shown in Figure 5.6 where the realistic particle distribution is tracked through the spectrometer on the  $65^\circ$  beam line as the dipole field is scanned and the beam is moved across the Faraday cup. A 1 mm vertical slit was placed at entry to the spectrometer and a 15 mm vertical slit compared to a circular aperture with a diameter of 15 mm at the Faraday cup in the stigmatic and astigmatic cases. In the astigmatic case only the first quadrupole is powered and as a result of the circular aperture the reconstructed energy spread is considerably larger. The circular aperture in front of the Faraday cup was shown to have a negligible effect on the measurement if a stigmatic focus was used and the vertical beam size made much smaller than the radius of the aperture.

#### 5.4.2 Effect of Perturbing the Switchyard Magnet

The variation in the  $R_{11}$  and  $R_{12}$  transfer matrix elements through the spectrometer was studied as a function of the perturbation of the dipole field. Eigenvectors made of 11 particles evenly spaced within the limits of  $\pm 10$  mm and  $\pm 10$  mrad in transverse phase space were launched into the spectrometer as its dipole field was perturbed. The beam dispersion was set to zero to negate the effect of the dispersion function. The transfer matrix elements are represented by the gradients of the linear fits in Figures 5.7(b) and 5.7(c) for a variation of  $\pm 1.5\%$  in the dipole field of the switchyard magnet, sufficient to move the beam across a 15 mm aperture in the astigmatic case on the  $65^\circ$  beam line. The dynamics is closely linear over the range of phase space probed by the eigenvectors, which is consistent with the expected beam parameters. The  $R_{11}$  term changes by no more than  $\pm 6\%$ , which accounts for a very small change in the resolution if the entry position is restricted to  $\pm 0.5$  mm with a 1 mm vertical slit. The  $R_{12}$  term does vary from zero under the perturbation but at a level that does not compromise the resolution attained from using a 1 mm vertical entrance slit and even for strongly divergent beams of 10 mrad. Finally, the dispersion function  $R_{16} = -0.53$  m changes linearly with  $\frac{\Delta B}{B_0}$ , therefore the energy

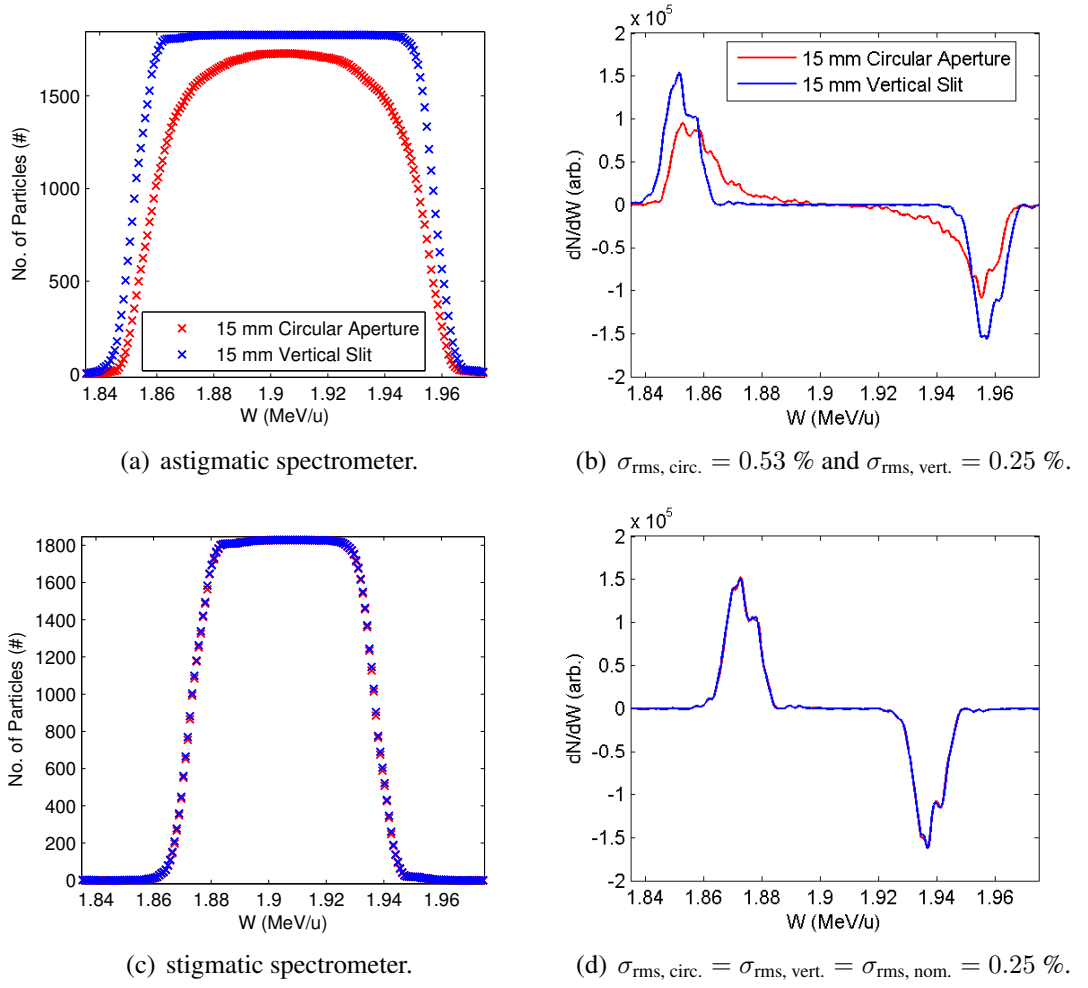


Figure 5.6: TRAVEL simulations of the measurement on the  $65^\circ$  line with the 7G3 turned off. The rms energy spread of the simulated beam was  $\sigma_{\text{rms, nom.}} = 0.25\%$ .

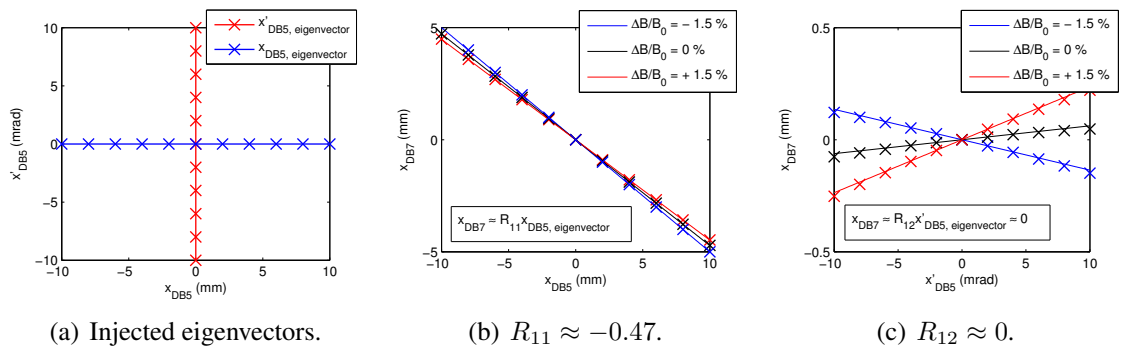


Figure 5.7: TRAVEL calculations to assess the effect of perturbing the switchyard magnet.

spread can be reconstructed to within a few percent with this method.

### 5.4.3 Effect of Losses

Beam losses in the dispersive region after the switchyard magnet are the biggest limitation of the procedure employed. To mitigate the effect of losses the transmission was optimised at well above 95 % through the spectrometer between variations in the cavity voltage and before the dipole field was scanned each time. At higher beam energies transmission is increased through the spectrometer because the beam dispersion represents a lower fraction of the beam energy and the beam is less divergent due to the effect of the adiabatic damping of the transverse betatron oscillations.

### 5.4.4 Complete Measurement Simulations

Simulations are presented in Figure 5.8 of the ReB and 7G3 measurements on each beam line with a 5 mm vertical slit and a 15 mm circular aperture in front of the Faraday cups on the 20° and 65° beam lines, respectively. A 1 mm vertical slit was placed at the entrance to the spectrometer. The 65° beam line is suited for the 7G3 measurement because of its increased resolution, which is required to measure the small relative beam dispersion at 1.92 MeV/u. Losses are observed in the spectrometer on the 65° beam line for the ReB measurement at high voltages, where the simulated data points fall below the nominal energy spread. Therefore, the 20° beam line was chosen for the ReB measurement.

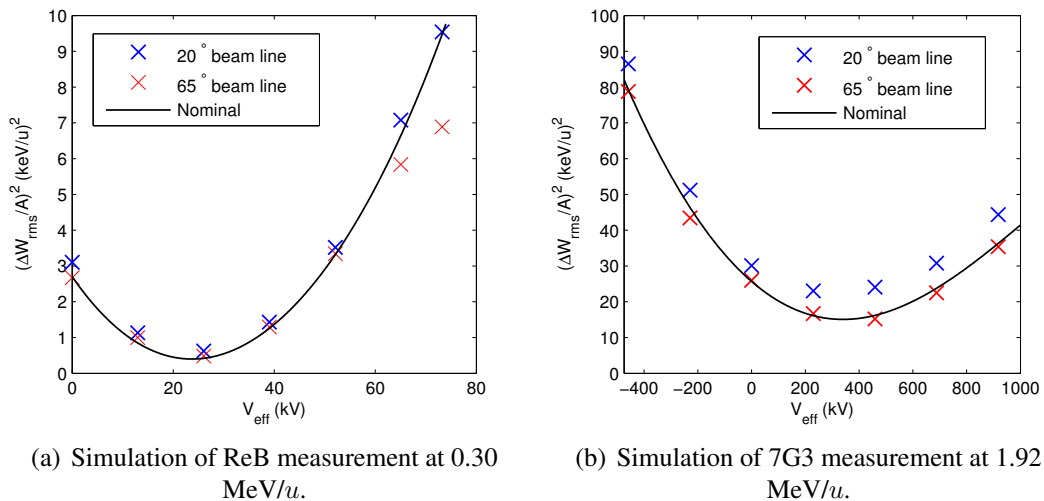


Figure 5.8: TRAVEL simulations of the measurement.

## 5.5 Effect of Resolution

The resolution of the measurement adds in quadrature such that the measured value of the energy spread is enlarged with respect to the actual value,

$$\left(\frac{\Delta W_1}{A}\right)_{\text{measured}}^2 = \left(\frac{\Delta W_1}{A}\right)_{\text{actual}}^2 + \left(\frac{\Delta W_1}{A}\right)_{\text{resolution}}^2. \quad (5.5.1)$$

The resolution is therefore absorbed into the value of the fit parameter  $a_0$ , whilst the other fit parameters remain unchanged. In principle the resolution can be subtracted in quadrature if it remains constant throughout the measurement.

A finite resolution increases the energy spread measured in front of the buncher cavity, as shown for energy resolutions corresponding to 0.4 and 0.7 % in Figure 5.9(a) for the ReB measurement. The measured emittance is always over-estimated due to a finite resolution. When the measured ellipse is tracked back along the accelerator, e.g. to the exit of the RFQ, the systematic error caused by the resolution is scaled by the drift distance and the reconstructed beam ellipse can appear very different to the actual ellipse, as shown by Figure 5.9(b). Even though the resolution can be subtracted if it remains

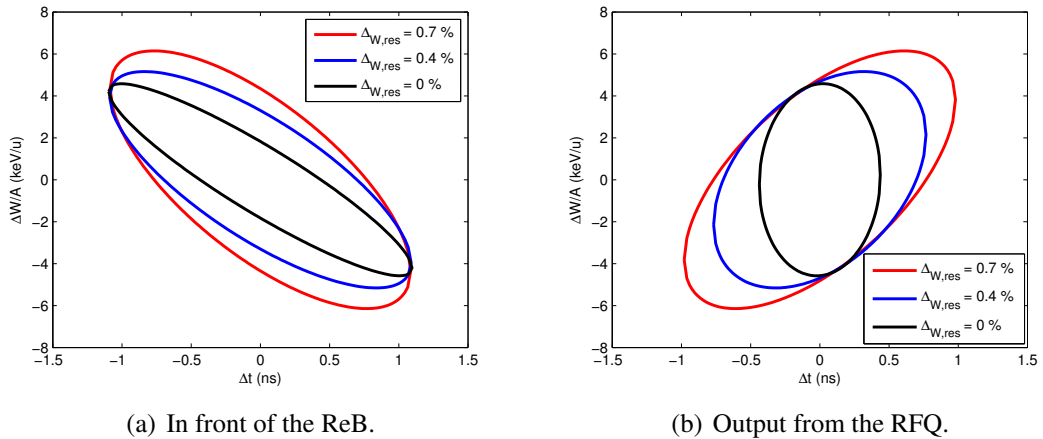


Figure 5.9: The effect of a finite energy resolution on the reconstruction of the beam ellipses at the buncher cavity and at a position upstream, e.g., at the exit to the RFQ.

constant throughout the measurement, the details of any structure or filamentation in the distribution remain masked.

The expression for the energy spread given in Equation 5.2.6 can be differentiated and rearranged to give the effective voltage required to minimise the energy spread of the

beam,

$$V_{\Delta W_{\min}} = \left| \frac{-1}{\sin \phi_s} \left( \frac{A}{q} \right) \frac{\tilde{\alpha}_0}{\tilde{\beta}_0} \right|, \quad \text{where } \phi_s = \pm 90^\circ. \quad (5.5.2)$$

It is reasonable to expect that the resolution is constant and independent of  $V_{\text{eff}}$ , which leads to the conclusion that the voltage required to minimise the energy spread is independent of the resolution, i.e. the ratio  $\tilde{\alpha}_0/\tilde{\beta}_0$  remains constant. Therefore, the measurement of  $V_{\Delta W_{\min}}$  serves as a useful diagnostic parameter no matter what resolution is available, within reasonable bounds, and allows the beam parameters to be checked independent of a truly accurate emittance measurement.

The effect on the measured Twiss parameters at the buncher are summarised in Table 5.3 and can be generalised to other types of three-gradient emittance measurements, e.g. the quadrupole scan measurement.

Table 5.3: Qualitative effect of the energy resolution on the Twiss parameters reconstructed through a three-gradient emittance measurement

Twiss Parameter	Qualitative Effect on the Reconstruction at the Buncher
$\tilde{\alpha}_0$	decreases
$\tilde{\beta}_0$	decreases
$\epsilon_0$	increases
$\frac{\tilde{\alpha}_0}{\tilde{\beta}_0}$	constant

## 5.6 ReB Measurements

Three-gradient emittance measurements were made at various RFQ voltages and the nominal beam parameters at the output to the RFQ were found close to a signature minimum in the energy spread, as was shown in Figure 4.4. The ReB was not stable when operated below an amplitude corresponding to an effective voltage of 35 kV because of multipacting<sup>1</sup> and the energy spread was too large to take measurements at the debunching synchronous phase of  $+90^\circ$ . The difference of  $\pm 7.5^\circ$  in the synchronous phase seen by the beam in

<sup>1</sup>Multipacting is a resonant phenomenon by which electrons are repeatedly accelerated and collided with the cavity walls in phase with the rf fields such that at each subsequent collision more electrons are produced. The avalanche effect prevents the rf power that is coupled into the cavity from building up high field levels because the energy is absorbed by the dynamics of the electrons.

the external gaps caused by problems in the manufacturing of the ReB was shown to have a negligible effect on the measurement. Although initial measurements were made on the  $65^\circ$  beam line of the spectrometer, it was challenging to ensure transmission through the spectrometer as the dipole field was perturbed and the  $20^\circ$  beam line was preferred instead. The calibration of the ReB is shown in Appendix D.

### 5.6.1 Spectrometer Measurements

The emittance was inferred from a quadratic fit to the data plotted in Figure 5.10 using Equation. 5.2.6. The least-squares fit, which was weighted with the random errors shown

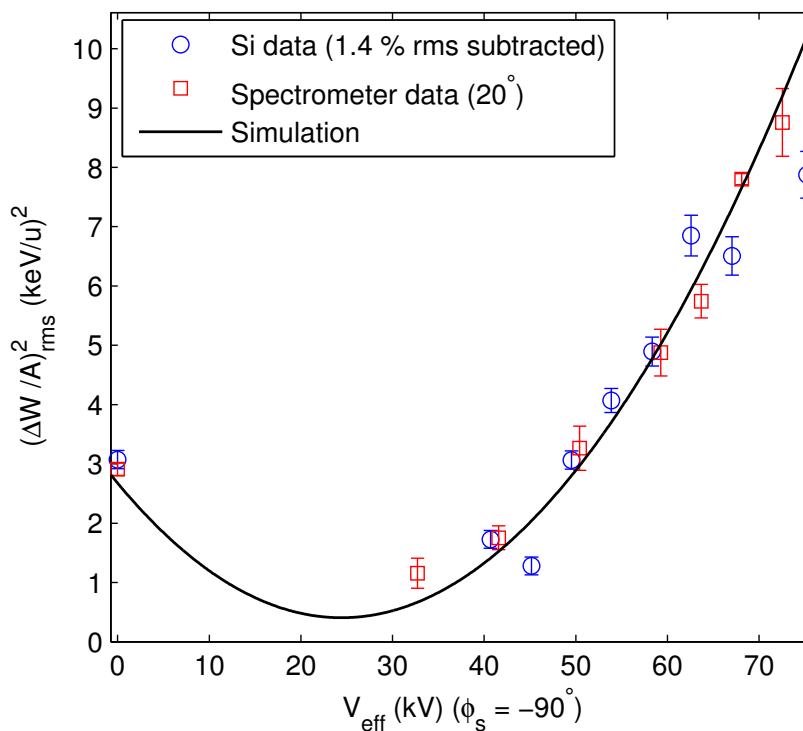


Figure 5.10: Energy spread measured as a function of the ReB voltage using the spectrometer and the silicon (Si) detector, where the silicon detector results are plotted with the estimated resolution subtracted.

by the error bars in Figure 5.10, gave an rms emittance of  $0.34 \pm 0.08 \pi \text{ ns keV}/u$  with a 1 mm entry slit. The raw data and the energy spread profiles are shown in Figure 5.11 for a range of effective buncher voltages with a 5 mm vertical slit placed in front of the Faraday cup. An estimate of the systematic error arising from the contribution to the resolution from the finite width of the entry slit was made by comparing the measured beam profiles with different slit sizes, as is shown explicitly in Figure 5.12 for the 7G3

measurement. By assuming that the beam distribution is uniform across the slit one can write the resolution contribution per mm of entry slit at a given effective voltage as,

$$\sigma_{\text{res/mm}} = \frac{1}{4} \sqrt{\Delta_{5\text{ mm}}^2 - \Delta_{3\text{ mm}}^2}, \quad (5.6.1)$$

where  $\Delta_{3\text{ mm}}$  and  $\Delta_{5\text{ mm}}$  are the measured energy spreads with 3 and 5 mm slits, respectively. The resolution from the 1 mm slit was estimated at  $0.4 \pm 0.1$  keV/u, which corresponds to a resolution of 0.13 % and is considerably lower than the estimated resolution of 0.50 %. After the subtraction of the resolution the emittance can be estimated as  $0.29 \pm 0.07 \pi$  ns keV/u, a factor of 1.12 larger than simulation, see Table 5.4.

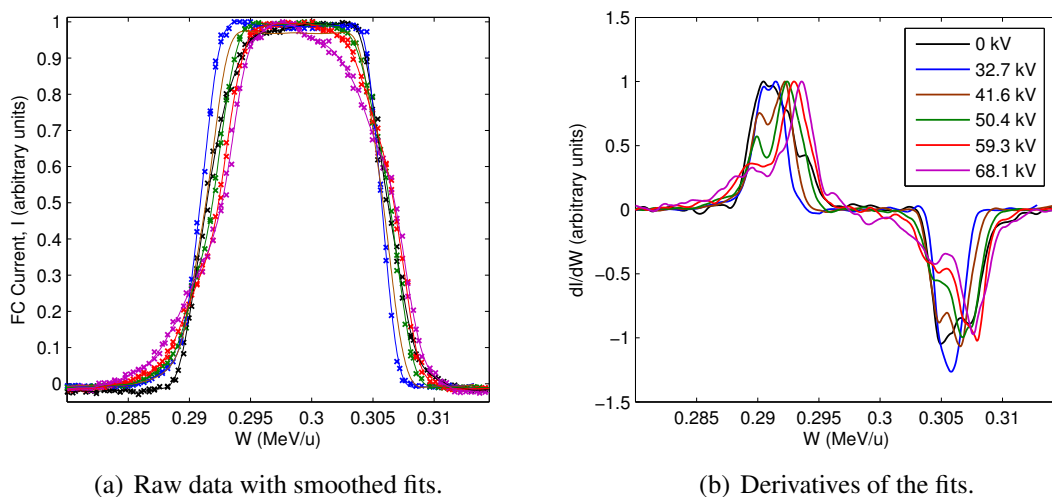


Figure 5.11: The raw data and energy spread profiles for a range of effective buncher voltages measured at 300 keV/u on the 20° beam line of the spectrometer.

## 5.6.2 Silicon Detector Measurements

In accordance with an investigation of the energy resolution of a solid-state diagnostic system, which is detailed in Chapter 7, the longitudinal emittance was measured. The rms emittance measured with the silicon detector is a factor of 4.6 times larger than the measurement with the spectrometer on the 20° beam line and a factor of 6 times larger than simulation. The system performs well in comparison to other solid-state systems used to measure the longitudinal emittance. During the commissioning of the new injector at LNL-INFN direct emittance measurements using correlated energy and time signals from a silicon detector led to a measurement a factor of 18 times larger than simulation [165].

Time-of-flight (ToF) measurements at LNL-INFN using the three-gradient method gave a factor of 2.5 times the expected value. At GSI, a solid-state system was used in a direct measurement that attained an rms emittance some 7.5 times larger than simulation [164].

Nonetheless, the estimated resolution of 1.4 % rms still severely impaired the measurements at REX. The value of 3.9 (keV/u)/ns for the ratio of  $\tilde{\alpha}_0/\tilde{\beta}_0$ , which defines the minimum of the parabola in Figure 5.10, agrees closely with simulation. After subtraction of the resolution in quadrature, the energy spread agrees closely with both measurements using the spectrometer and simulation, as shown in Figure 5.10.

## 5.7 7G3 Measurements

In nominal operation the beam has an energy of 1.9 MeV/u at the 7G3 and a reduced velocity of 6.4 %, which is smaller than the geometric velocity of the 7G3 cavity of 6.6 % [67]. Consequently, the phase deviates from the non-accelerating phases of  $\pm 90^\circ$  in each gap. The variation was shown to be at most  $\pm 20^\circ$  in the first and last gaps, where the voltage is lower than in the other gaps because the external drift-tubes are grounded. The effect of the mismatched velocity was simulated using a LANA model of the 7G3 and the emittance could be reliably reconstructed to within 12 % using a quartic fit. The calibration of the 7G3 can be found in Appendix D.

### 5.7.1 Spectrometer Measurements

The energy spread was measured on the  $65^\circ$  beam line as a function of the effective voltage of the 7G3 and is presented in Figure 5.12 with three different vertical slits placed at entry to the spectrometer system to illustrate the effect of the entry slit on the resolution of the measurement. The energy spread was reconstructed from scans across a 15 mm circular aperture in front of the Faraday cup. The error bars on each data point reflect the standard deviation of three scans made at each voltage, corresponding to an ensemble of six measurements of the energy spread. The non-quadratic behaviour of the 7G3 is evident through the asymmetry of the data about the minimum; quartic fits were fitted to the data, giving emittances of  $0.36 \pm 0.05$ ,  $0.42 \pm 0.04$  and  $0.51 \pm 0.02 \pi$  ns keV/u

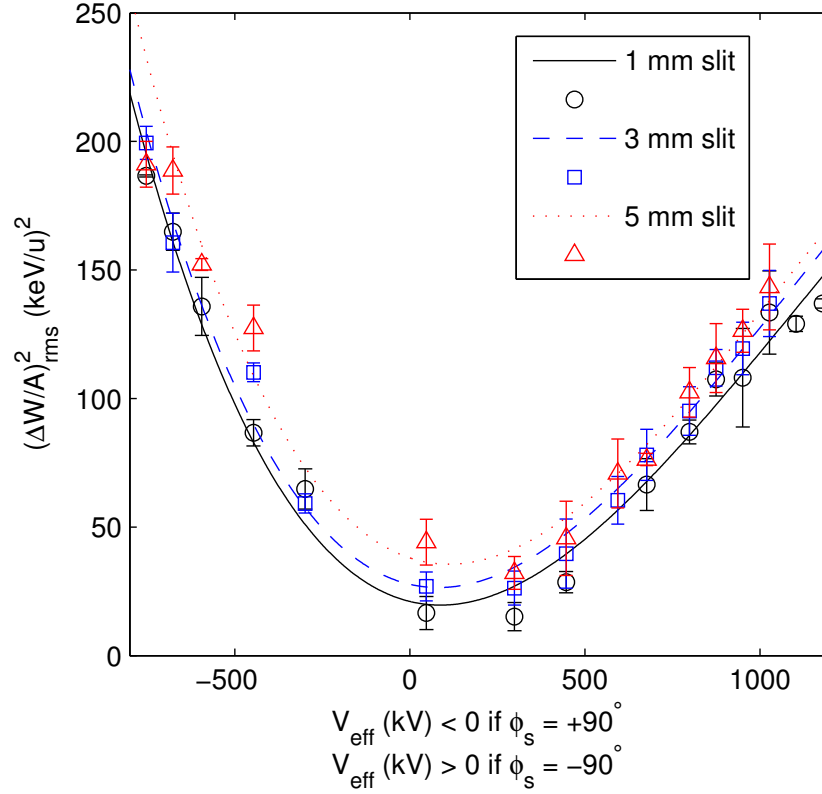


Figure 5.12: Energy spread measured as a function of the 7G3 voltage using the spectrometer with different entry slits.

for 1, 3 and 5 mm entry slits, respectively. At low voltages the resolution contribution from a 1 mm slit is estimated as  $1.0 \pm 0.2 \text{ keV/u}$ , which is negligible when compared to the random error involved in the measurement. This corresponds to a resolution of 0.05 %, considerably lower than the estimated resolution of 0.17 % but a similar factor lower than was estimated for the ReB measurement on the  $20^\circ$  beam line. The measured rms emittance is a factor of 1.13 larger than simulation, see Table 5.4.

### 5.7.2 Silicon Detector Measurements

The bunch length was measured by a Time of Flight (ToF) technique using the silicon detector in DB5 located 11.4 m downstream of the 7G3. The data, plotted in Figure 5.13, was fitted with a quadratic polynomial and the beam parameters calculated using Equation 5.2.9. The position of the detector in DB5 was selected primarily to favour ease of access and development of the solid-state diagnostic system away from possible sources of noise in the linac and not specifically for an emittance measurement. Nonetheless, after

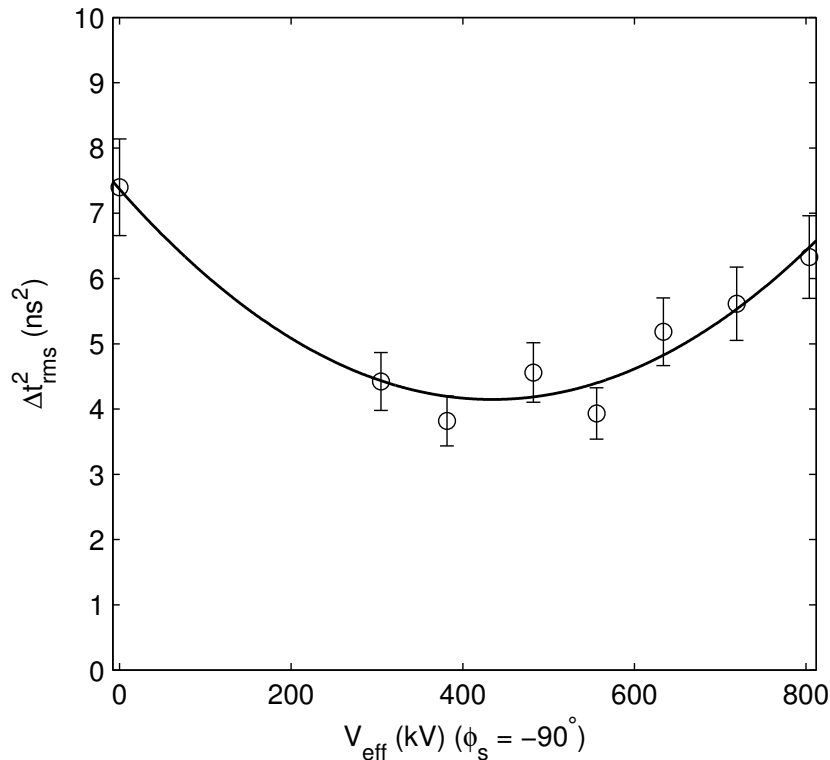


Figure 5.13: Bunch length measured downstream of the 7G3 using the silicon detector.

a drift of over 11 m to the focal plane at the detector in DB5, the bunches were resolvable at 101.28 MHz. Unfortunately, as a result of the flight distance, the voltage required to focus the bunch in time was small and the low-level rf feedback control of the cavity's amplitude and phase was not always possible, which would have increased the time-averaged emittance. More importantly, the bunches started to coalesce at DB5 making the analysis of the rms bunch length difficult, as shown in Figure 5.14. The data was divided into 9.87 ns windows and the rms of each peak calculated inside these windows. The tails of the adjacent bunches inevitably biased the measurements and the rms emittance was measured a factor of 5.8 times larger than the spectrometer measurement and a factor of 6.6 times larger than simulation at  $2.1 \pi \text{ ns keV}/u$ . The reconstructed beam parameters are still qualitatively consistent with simulation and the spectrometer measurements, as shown in Table 5.4. The time resolution of the solid-state diagnostic system is estimated as  $< 0.1 \text{ ns rms}$  and the system could provide a useful tool for bunch length and emittance measurements if the time structure of the beam is modified, as is in discussion for the HIE-ISOLDE upgrade.

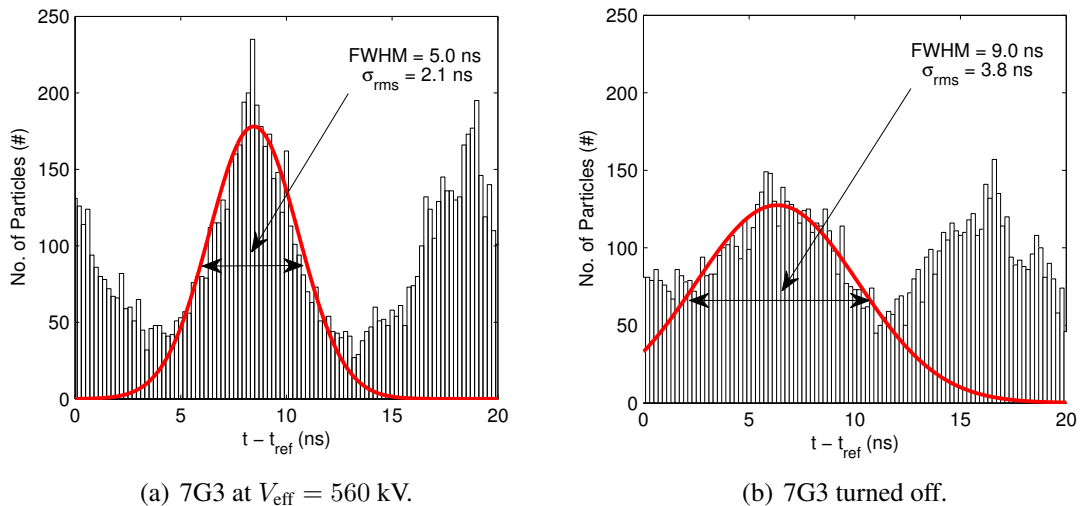


Figure 5.14: Bunch length distributions measured at DB5 during the ToF emittance measurement.

## 5.8 Longitudinal Phase Space Distribution

### 5.8.1 Three-gradient Phase Space Reconstruction

The distribution of each energy spread scan was analysed and longitudinal phase space ellipses containing different fractions of the beam were calculated by applying the three-gradient method, as was described in the case of the rms emittance. This indirect measurement of the distribution of the beam in longitudinal phase space is compared to simulation in Figure 5.15, where the signal-to-noise ratio allowed the distribution to be probed up to an emittance containing 86 % of the beam. The core of the beam is closely Gaussian but particles further from the core populate more extreme regions of phase space than is described by the Gaussian distribution; tails were observed in Figure 5.11(b). The ellipses were interpolated in the longitudinal phase plane and compared to the simulated particle distributions, as shown in Figures 5.16 and 5.17 for the ReB and 7G3 measurements, respectively. In the case of the ReB measurement the reconstructed phase space was tracked back 1.026 m to the exit of the RFQ. The beam parameters appear more convergent than simulation at exit from the RFQ because of the effect of the energy resolution of the measurement, which was discussed previously in Chapter 5.5.

This reconstruction technique assumes that the distribution is symmetric and, through the application of the Courant-Snyder formalism, can be described by elliptical iso-contours.

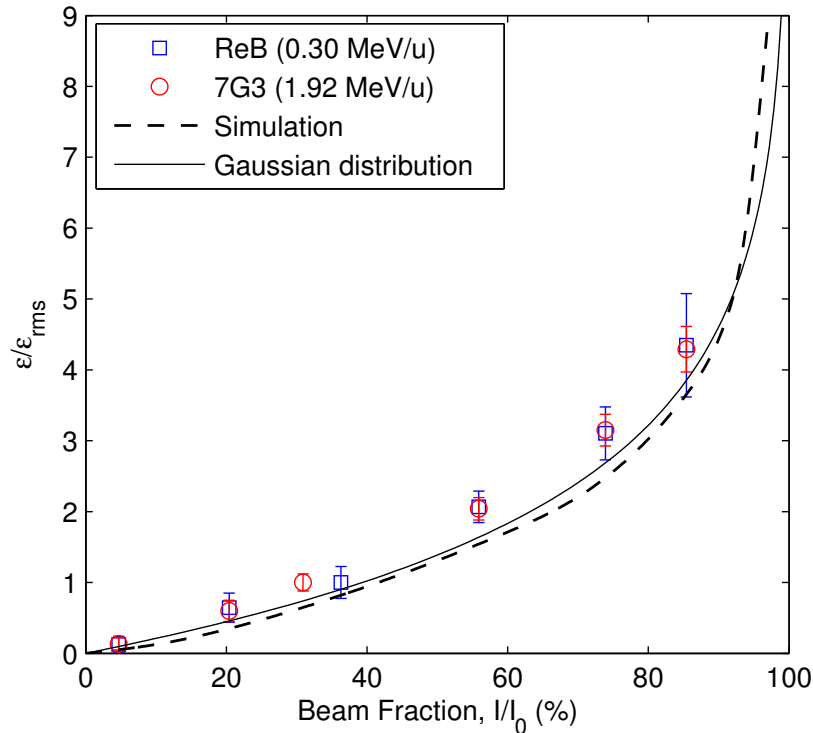


Figure 5.15: An indirect measurement of the distribution of the beam in longitudinal phase space.

Judging from the measured distributions presented in Figure 5.11(b), this was not the case. Consequently, there are some irregularities in the interpolation because the interior ellipses representing the core of the beam are rotated with respect to those on the exterior, see Figure 5.17(b).

## 5.8.2 Tomographic Phase Space Reconstruction

As discussed, Figures 5.16 and 5.17 do not provide much further insight into the details of the phase space distribution. To this end, the distribution was reconstructed by tomography using a computer program developed at PSI, which is based on the MENT (Maximum ENTropy) algorithm from LANL, see [179] and [180] for more details. The program takes the energy projections of the beam measured at different orientations after a linear manipulation in the cavity, which must be specified in the program with a transfer matrix, and reconstructs the two-dimensional phase space distribution based on an algorithm that maximises the entropy of the resulting distribution [181]. The output of the program for the ReB measurement is shown in Figures 5.18 and 5.19; the 7G3 measurements are

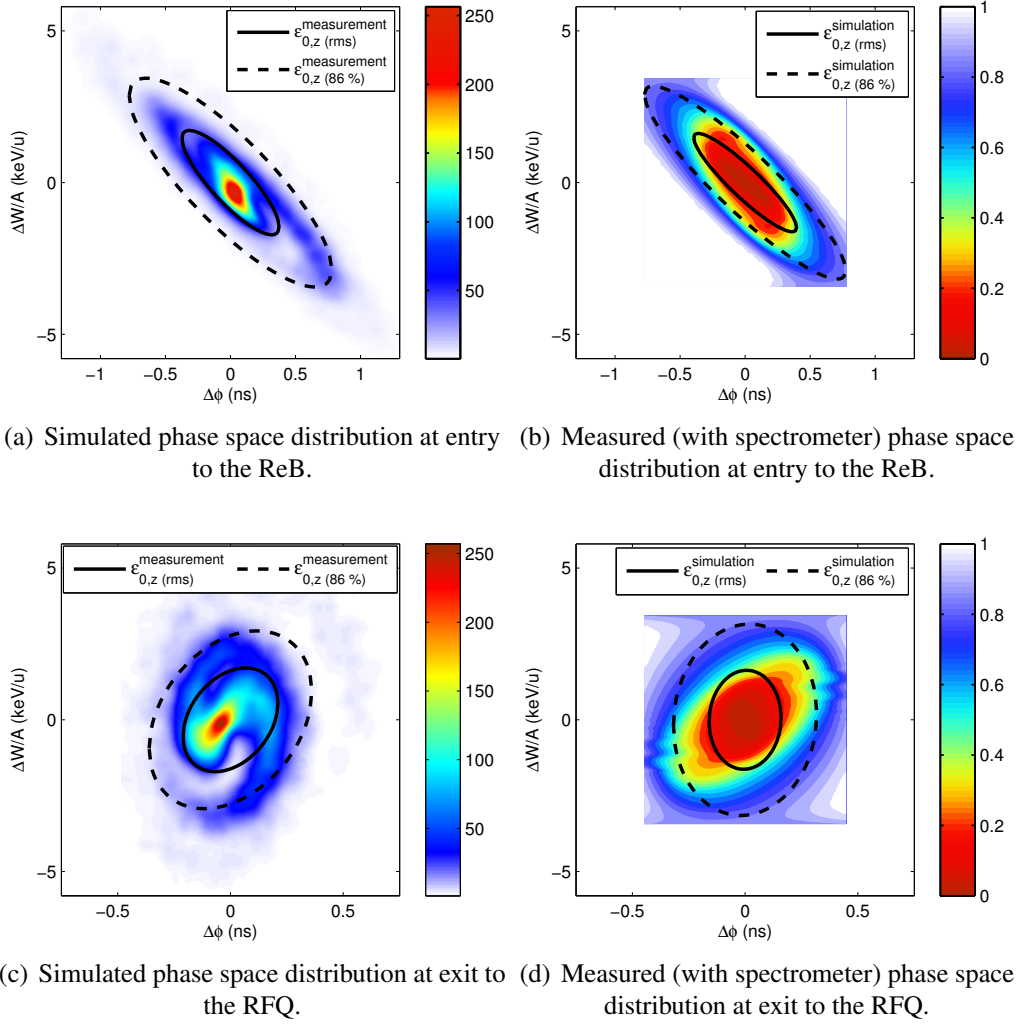


Figure 5.16: A comparison between the simulated particle distribution and the measured phase space distribution using the ReB at 0.3 MeV/u (colour bars: (a) and (c) particle density, (b) and (d) beam fraction).

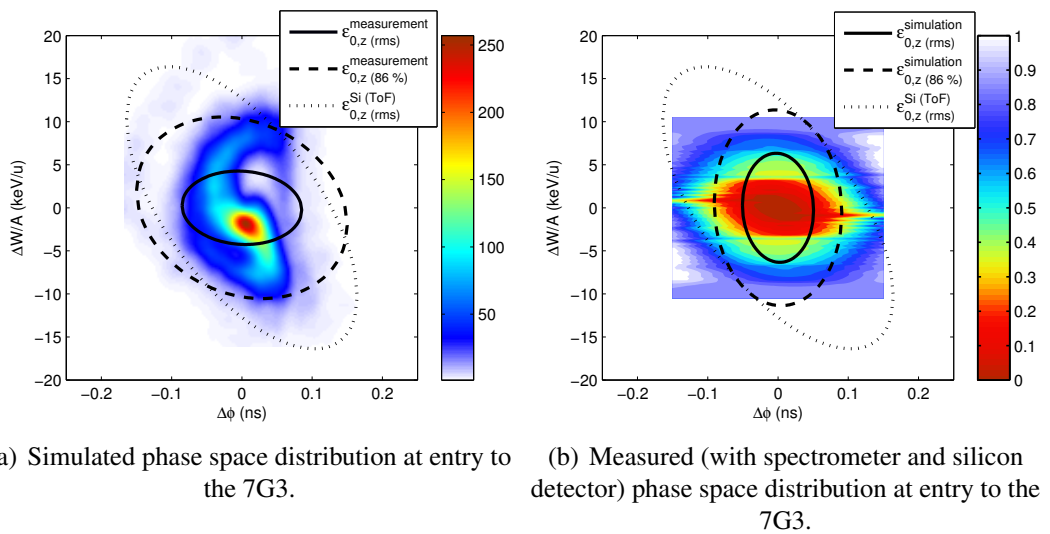


Figure 5.17: A comparison between the simulated particle distribution and measured phase space distribution (with spectrometer and silicon detector) using the 7G3 at 1.92 MeV/u (colour bars: (a) particle density and (b) beam fraction).

collected in the figures of Appendix E. In both cases the results confirm that the core is closely Gaussian, see the logarithmic dependence of the beam fraction in e.g. Figure 5.18, and that the 86 % emittance is approximately  $1.5 \pi$  ns keV/u, which in agreement with the results presented in Table 5.4. The reconstructed distribution is projected back onto the measured profiles with good agreement and a filamented arm of the distribution predicted by simulation is clearly visible.

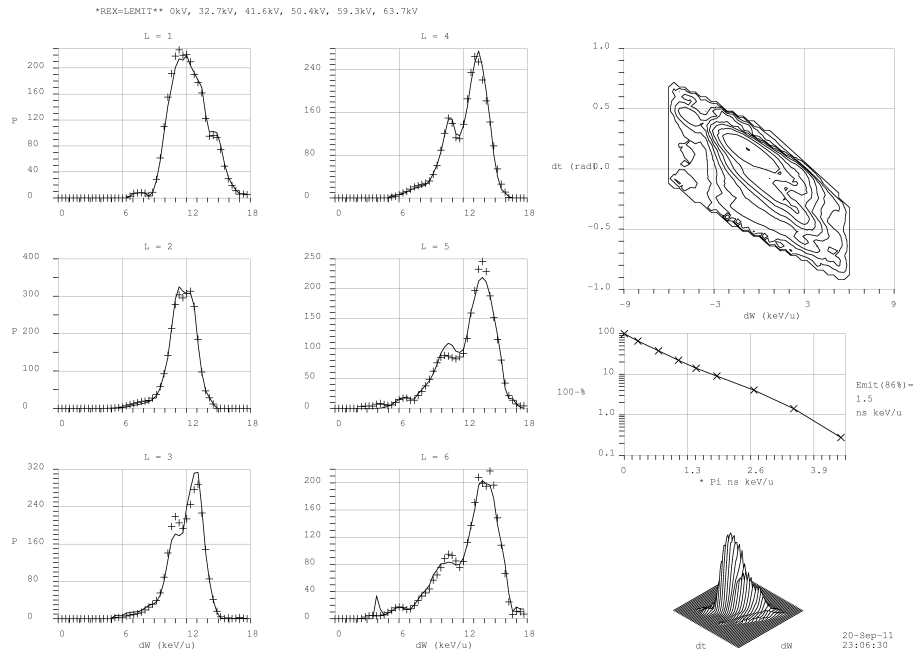


Figure 5.18: MENT Beam Tomography Program [179] analysis for the ReB measurement.

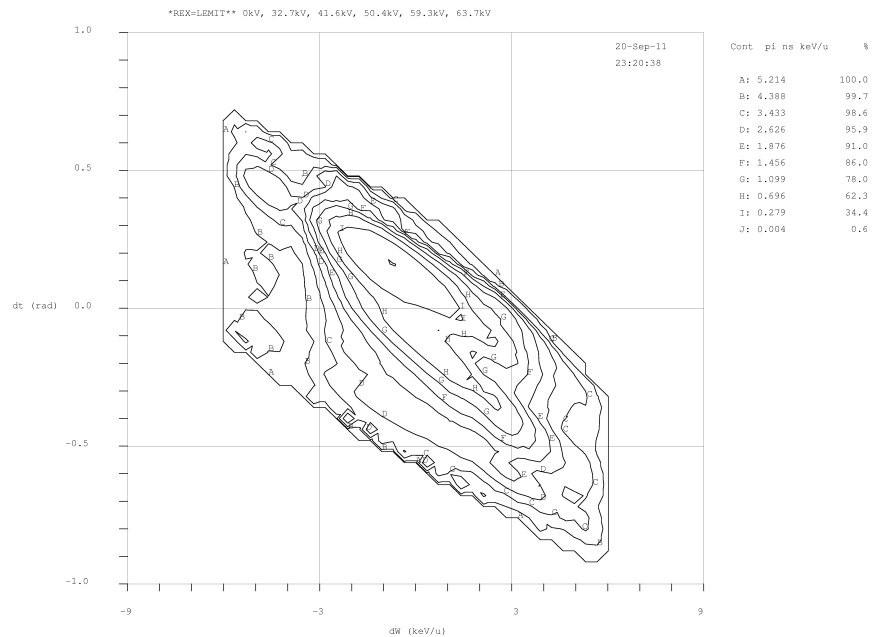


Figure 5.19: Contour plot from MENT Beam Tomography Program [179] for the ReB measurement.

## 5.9 Summary

The rms longitudinal emittance at output from the RFQ was measured as  $0.34 \pm 0.08 \pi \text{ ns keV}/u$  and at entry to the 7G3 as  $0.36 \pm 0.04 \pi \text{ ns keV}/u$ , indicating a small growth of emittance in the IHS. After the subtraction of the estimated resolution from the 1 mm slit in front of the spectrometer the rms emittance measured before the IHS is  $0.29 \pm 0.07 \pi \text{ ns keV}/u$ , which gives an emittance growth in the IHS, 7G1 and 7G2 cavities of approximately 20 %, consistent with simulation. The 86 % emittance was measured a factor of approximately 4.4 times larger than the rms emittance at  $1.48 \pm 0.2$  and  $1.55 \pm 0.12 \pi \text{ ns keV}/u$  at the RFQ and 7G3, respectively. Systematic errors arising from the resolution of the spectrometer and the mismatch of the beam velocity with the bunching cavity's geometric velocity were estimated at approximately 10 %. A silicon detector in its development phase was also exploited to measure the longitudinal beam properties but the measurements were resolution limited. The results of the measurement campaign are summarised in Table 5.4 along with the analysis of data taken during the commissioning of the REX front-end in 2002 and during an annual calibration in 2007 [63, 161].

An emittance after the RFQ of  $2 \pi \text{ ns keV}/u$  is consistent with simulation and the recent measurement campaign. The realistic particle distribution was tracked through the REX linac up to the first cavity of the HIE linac in Stages 1 and 2b of the upgrade, without and with the low energy section, respectively. The emittance can be accepted into the longitudinal acceptance of the superconducting HIE-ISOLDE linac, as shown in Figure 6.7(b) for Stage 2b at injection after the IHS and in Figure 6.8(b) for Stage 1 at injection after the 9GP. The simulations indicate that at injection to Stage 1 the longitudinal emittance is approximately a factor of 2 larger due to non-linear effects in the 9GP cavity.

The next chapter will discuss the design studies carried out for the linac upgrade; work that was underpinned by the results of the beam dynamics simulations and measurement presented so far.

Table 5.4: Summary of the longitudinal emittance measurements with the ReB (0.3 MeV/u) and the 7G3 (1.92 MeV/u)<sup>a</sup>

Buncher	Measurement	$\tilde{\alpha}$	$\tilde{\beta}$ [ns/(keV/u)]	$\tilde{\alpha}/\tilde{\beta}$ [(keV/u)/ns]	$\epsilon_{\text{rms}}$ [ $\pi$ ns keV/u]	$\epsilon_{86\%}$ [ $\pi$ ns keV/u]	Transmission <sup>c</sup> [%]
ReB	Spectrometer (20°)	1.58	0.41	3.85	0.34±0.08	1.48±0.2	60
ReB	Silicon Detector ( $\Delta W$ )	0.29	0.074	3.92	1.56±0.17	5.44±0.7	60
ReB	Commissioning (2002) <sup>b</sup>	0.87	0.23	3.78	n/a	3.3±0.4	95
ReB	Calibration (2007) <sup>b</sup>	0.72	0.17	4.4	n/a	1.9	75
ReB	Simulation	2.25	0.60	3.75	0.26	0.96	99.9
7G3	Spectrometer (65°)	0.06	0.02	3.0	0.36±0.05	1.55±0.12	80
7G3	Silicon Detector (ToF)	0.81	0.013	62.3	2.09	n/a	80
7G3	Simulation	0.05	0.008	6.3	0.32	1.03	99.8

<sup>a</sup> Beam parameters given in front of the respective buncher without any correction for the resolution.

<sup>b</sup> Assuming the energy spread profiles represented a 95 % beam fraction [63, 161].

<sup>c</sup> Beam losses were predominantly on the physical aperture of the linac and therefore only weakly correlated to the longitudinal phase space plane.

## BEAM DYNAMICS DESIGN STUDIES OF THE HIE-ISOLDE LINAC

Standard design procedures were employed to ensure a cost-effective but high performance superconducting accelerator design, see e.g. [182]. The low intensity of the beams at ISOLDE permit the use of long focusing periods with a densely packed lattice of superconducting cavities operating at high gradient, which helps to minimise the length and cost of the accelerator. As a result the design pushes the limit of zero-current stability at the first-order transverse parametric resonance and the acceleration is non-adiabatic in nature. In this chapter the first-order design of the HIE linac is summarised along with the design of the matching sections using the results of the last two chapters. The beam-steering and the asymmetry of the rf (de)focusing fields in the quarter-wave cavities is investigated, the extent to which the linac can be used as a decelerator is presented and the beam parameters at the experiments are given using a preliminary HEBT design. In addition, the stability of the design to errors and misalignment is rigorously studied and tolerances specified, all of which had an impact on the design of the low-level rf control system, cryomodels and orbit correction system.

### **6.1 Lattice Design**

The lattice was designed to be as compact as possible to maximise the acceptance of the linac and optimise the beam quality, but also to allow adequate space in the experimental hall for physics instrumentation. The linac was divided by grouping the two cavity families together in different cryomodels. The low energy section contains two cryomodels,

each housing six low- $\beta$  cavities and two solenoids, and the high energy section contains four cryomodules, each housing five high- $\beta$  cavities and one solenoid. For reasons of economy the designs of the cryomodules were standardised and the sizes of the low and high energy cryomodules were kept similar. The lattice is shown schematically in Figure 6.1 and the important properties and dimensions of the lattice are summarised in Table 6.1.

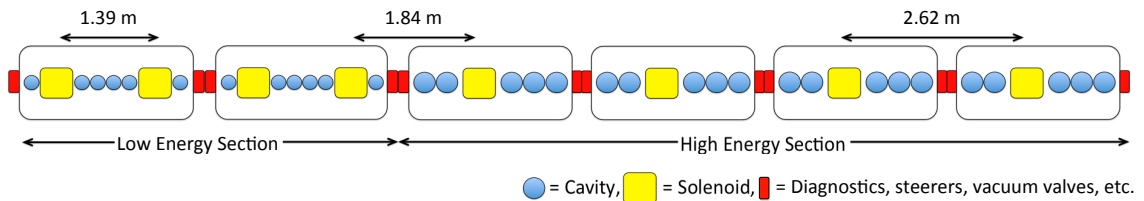


Figure 6.1: Schematic of the lattice of the HIE linac.

The lattice of the low energy section is somewhat irregular to facilitate the longitudinal matching of the beam after the IHS by separating the first cavity from the others and using it as a rebuncher with the succeeding drift region containing a solenoid. This removes the need for a dedicated rebuncher outside the cryomodule and as a consequence reduces the length of the machine. A synchronous phase of just  $-40^\circ$  in the first cavity is adequate to capture the beam after the IHS, by minimising the phase spread in the second cavity. The last cavity in the low energy cryomodule is also separated by a solenoid, making itself and the fifth cavity useful for completing the longitudinal phase space gymnastics early in the acceleration.

The cavities are placed asymmetrically about the solenoid in the high energy section with only two cavities before and three after the solenoid. The ‘missing’ first cavity is replaced by the drift-space between the cryomodules, compensating for the inter-cryomodule distance and permitting smooth and period beam envelopes to be matched. The ‘missing’ cavity reduces the beam divergence across the transition region between the low and high energy section and allows the beam to be matched into the high energy section without a dedicated matching section. The transverse phase advance is lowered in the second low energy cryomodule to facilitate a match into a focusing channel with a transverse phase advance of  $90^\circ$  per period in the high energy section [39]. The length of the focusing period changes across the transition region between the two sections of the

Table 6.1: HIE linac lattice parameters

Design Parameter	Low Energy Section	High Energy Section
No. of cryomodules	2	4
No. of cavities	12	20
Cavity geometric velocity ( $\beta_g$ ) [%]	6.3	10.3
No. of solenoids	4	4
No. of focusing periods	4	4
Length of focusing period [m]	1.39	2.62
Transverse phase advance per period ( $\mu_T$ ) [deg]	60 - 90	90
Solenoid strength ( $\int B_z^2 dz$ ) [T <sup>2</sup> m]	$\leq 8.8$	$\leq 15.0$
Long phase advance per period ( $\mu_L$ ) [deg]	$\sim 100$	$\sim 100$
Inter-cryomodule distance <sup>a</sup> [m]	0.50	0.50
Inter-cavity distance [m]	0.02	0.02
Inter-cavity distance with solenoid [m]	0.46	0.46
Length of cryomodule [m]	2.77	2.62
Total length [m]	5.54	10.48
Packing factor ( $F$ ) [%]	47	61

<sup>a</sup> Distance between the closest cavities in adjacent cryomodules.

linac, from 1.39 m in the low energy section to 2.62 m in the high energy section, with an intermediate transition period length of 1.84 m. No adjustment of the synchronous phases is needed to match the beam longitudinally into the high energy section once the upgrade is complete and the low energy section is in place.

The longitudinal beam dynamics is fixed by the energy gain specification and the lattice, which was chosen to be economical with long focusing periods and tightly packed cavities; the packing factor is maximised to 56 %. The packing factor is affected mainly by the spacing between cryomodules and the space required for the solenoids. A low synchronous phase of  $-20^\circ$  keeps the lattice compact and relaxes the transverse stability limits by reducing the longitudinal phase advance. The calculations detailed below show that the longitudinal-transverse coupling and the transverse emittance growth is minimised to just a few percent at a transverse phase advance of  $90^\circ$  per focusing period, well away from the first-order parametric resonance at  $\sim 50^\circ$  per focusing period. No strong parametric resonance of the longitudinal motion was observed in the lattice, see e.g. [139]. The beam dynamics in the superconducting linac is summarised in the TRACE 3-D model shown in Figure 6.2. A comprehensive set of matched beam parameters and solenoid field values are collected in Appendix H.

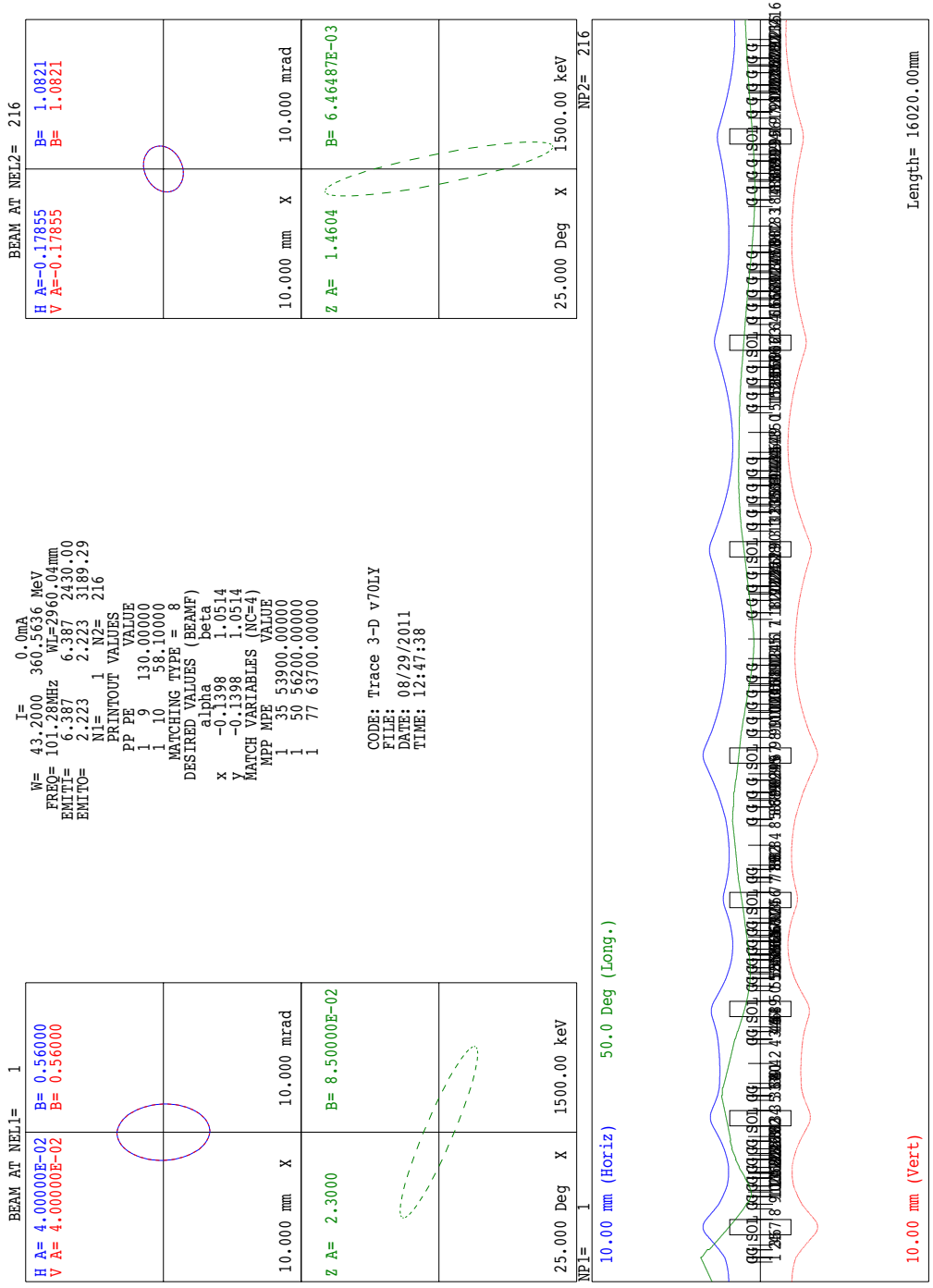


Figure 6.2: TRACE 3-D model of the HIE linac ( $A/q = 4.5$ ).

## 6.2 Suppression of Longitudinal-Transverse Coupling

The coupling of the transverse and longitudinal dynamics through the phase dependence of the transverse (de)focusing force in the accelerating cavities is a strong source of transverse emittance growth in the HIE linac. The perturbation of the beam envelope is driven by the phase spread of the beam in the cavities and the moderately large longitudinal emittance of  $2 - 4 \pi \text{ ns keV}/u$  delivered by the REX linac contributes to the production of a strong resonance. Although the acceleration is non-adiabatic and the phase advances in the linac are on the edge of the smooth approximation one can make some approximate analytic calculations to determine the limits of stability in the linac. As discussed in Chapter 3.4.5, the transverse equation of motion becomes resonantly unstable if the smoothed transverse and longitudinal phase advances satisfy the condition,

$$\mu_T = \frac{j}{2} \mu_L \quad j = 1, 2, 3, \dots, \quad (6.2.1)$$

where the index  $j$  denotes the order of the instability. The form of the Mathieu equation presented in Chapter 3.4.5 is consistent with the notation used in the analysis of its stability in [183] from which one can express the instability bounds of the transverse phase advance with knowledge of the magnitude of the parameter  $q$  using Figure 3.16. Therefore, the instability limits of an  $n^{\text{th}}$ -order resonance can be written in terms of the variable  $a$  as,

$$a_{n,\min} \lesssim a_n \lesssim a_{n,\max}, \quad (6.2.2)$$

or in terms of the longitudinal phase advance per period as,

$$\frac{\sqrt{a_{n,\min}}}{2} \mu_L \lesssim \mu_T \lesssim \frac{\sqrt{a_{n,\max}}}{2} \mu_L, \quad (6.2.3)$$

which is consistent with other analyses of zero-current resonances, see e.g. [127, 184].

If one assumes that the small longitudinal oscillations have an amplitude  $\Phi_0$  equal to the amplitude of the synchronous phase then  $q \approx 1.0$  for  $\phi_s = -20^\circ$  and the upper and lower bounds of the first-order instability are found to be  $0 \lesssim a_1 \lesssim 1.8$ . Therefore the instability bounds of the first-order parametric resonance in the HIE linac can be estimated

as,

$$0^\circ \lesssim \mu_T \lesssim 70^\circ, \quad (6.2.4)$$

where  $\mu_L \sim 100^\circ$ . The time constant describing the exponential build up of the oscillation amplitude of the first-order resonance is estimated to be equivalent to the transit-time through two focusing periods, or approximately half the longitudinal oscillation period, which demonstrates the strength of the coupling. The width of the second-order instability is much narrower ( $3.9 \lesssim a_2 \lesssim 4.3$ ) and the corresponding second-order instability bounds are,

$$99^\circ \lesssim \mu_T \lesssim 104^\circ, \quad (6.2.5)$$

and the oscillations take many times longer to build up.

The effects of zero-current coupling in low energy ion linear accelerators (below about 10 MeV/ $u$ ) are summarised in [112] where the emittance growth in a long channel under adiabatic conditions is derived at first-order as,

$$\Delta \epsilon_{T(z \rightarrow \infty)}^{1st \text{ order}} \approx \frac{\mu_L^2}{4\mu_T |2\mu_T - \mu_L|} \cot(-\phi_s) \Delta \phi_0. \quad (6.2.6)$$

The analysis of the HIE linac was simplified by splitting the linac into the low and high energy sections and the instability limits of each was studied separately. The analytic result for the emittance growth given in Equation 6.2.6 is compared to LANA simulations of each section of the linac in Figure 6.3. The growth of the rms and 99 % normalised transverse emittances was simulated with 50000 particles as a function of the strength of the solenoid focusing channel, which was parameterised by  $\mu_T$ . The longitudinal beam parameters were fixed in both sections of the linac equivalent to those used for acceleration to the design energy with  $A/q = 4.5$ .

The effect of the longitudinal emittance driving the transverse emittance growth is clearly demonstrated by the simulations with 2 and 4  $\pi$  ns keV/ $u$ . The coupling is suppressed with stronger focusing channels and at higher phase advances the transverse emittance growth depends only very weakly on the longitudinal emittance. At phase advances close to  $90^\circ$  per focusing period the emittance growth is minimised. The emittance growth compares well with the numerical simulation at higher phase advances but the resonance

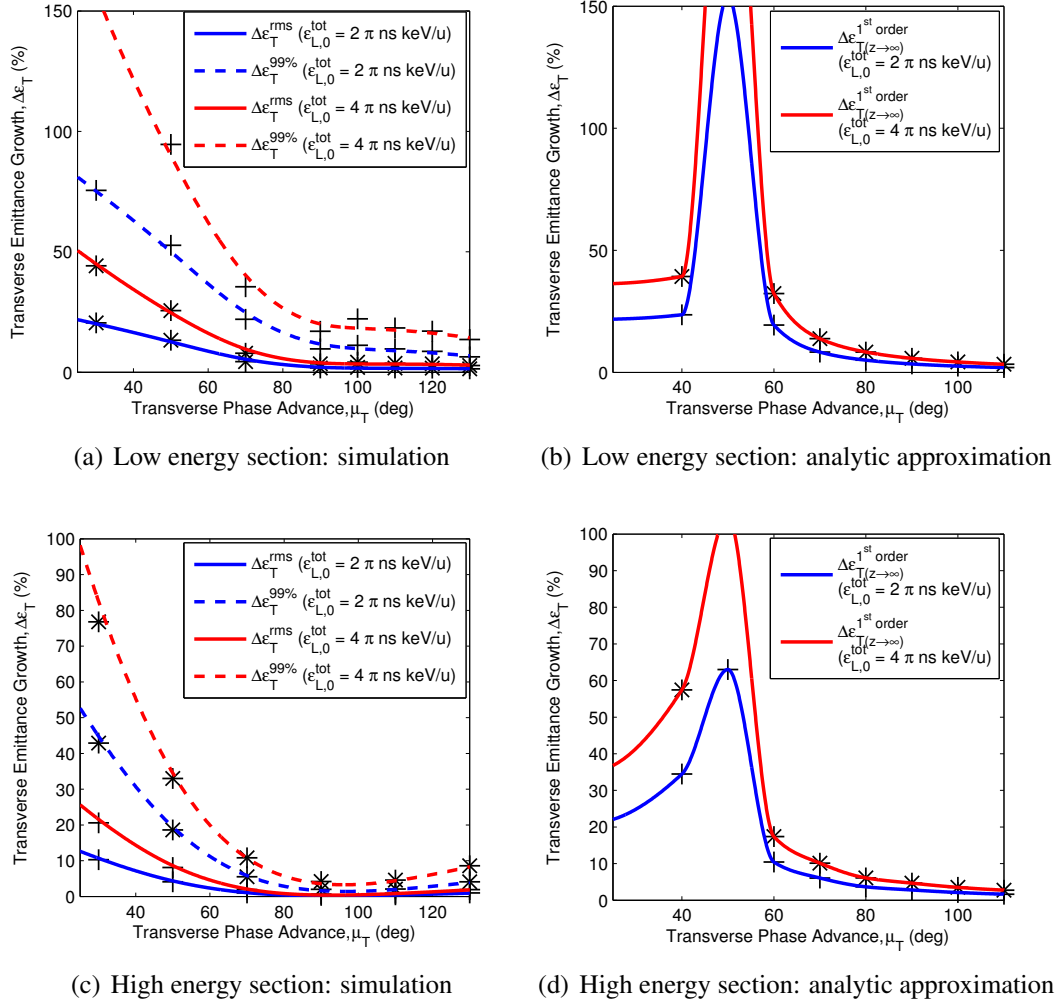


Figure 6.3: Survey of the parametric resonance driving transverse emittance growth; simulation is compared to analytic calculations for  $A/q = 4.5$ .

peak itself is not resolved numerically. The likely cause of the discrepancy is that at low phase advance with only four periods the beam has not relaxed to the limit made in the analytic estimate. In addition, the longitudinal phase advance varies with acceleration, which introduces a range of unstable oscillation frequencies and a broadening of the resonance. There is evidence in Figure 6.3 of the second-order resonance being excited.

The LANA simulations above were validated with realistic field simulations of the high energy section in Stage 2a of the upgrade using TRACK, as shown in Figure 6.4. After the beam-steering in the cavities is compensated, the parametric excitation of the transverse motion by the cavities is the dominant source of emittance growth remaining and the LANA model for the rf (de)focusing well approximates the realistic fields.

The sensitivity of the transverse emittance growth to the beam parameters at low energy is shown in Figure 6.5 as presented in [185]. The study includes both sections of

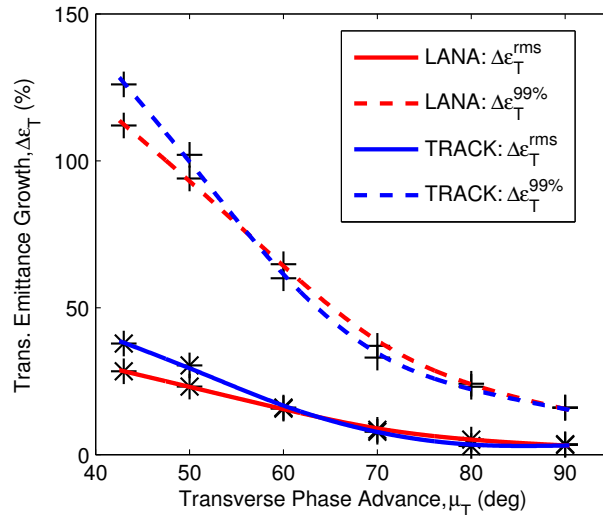


Figure 6.4: Transverse emittance growth calculated with LANA and TRACK as a function of focusing strength in Stage 2a of the HIE linac ( $\epsilon_{L,0}^{\text{tot}} = 2 \pi \text{ ns keV}/u$ ).

the linac as would be present in the complete upgrade but with a larger inter-cryomodule distance of 80 cm. The strength of the focusing system in the low energy section was varied and matched into a focusing channel of  $60^\circ$  per period in the high energy section. A region of instability is crossed that causes a resonant response in the transverse emittance growth. In contrast to the simulations of the separate sections of the linac the extra length allows a resonance peak to be resolved.

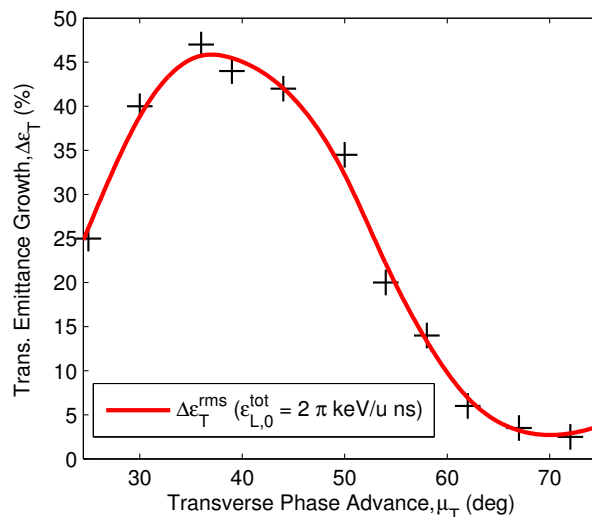


Figure 6.5: Excitation of the parametric resonance in the HIE linac as a function of the focusing strength in the low energy section.

Although the resonant conditions lie at higher phase advances for lower  $A/q$  beams it was shown that as a result of the increased energy gain of the lighter beams the focusing

channel does not require significant retuning [186]. An increase of just a few percent in the output emittance was observed for beams with  $A/q = 2.5$  at  $90^\circ$  phase advance per focusing period with respect to  $A/q = 4.5$ .

The focusing system was specified at a phase advance of  $90^\circ$  per period to largely decouple the effect of the longitudinal emittance on the transverse beam quality. In Stages 1 and 2a of the upgrade the 9GP will increase the longitudinal emittance injected into the superconducting linac by a factor of 2 at close to  $4 \pi \text{ ns keV}/u$ , which will affect the transverse beam quality. An integrated solenoid field of up to  $15.0 \text{ T}^2\text{m}$  is required, specified with some margin at  $16.2 \text{ T}^2\text{m}$ , for the heaviest ions at  $10 \text{ MeV}/u$ .

The first-order beam dynamics studies for Stage 2b of the superconducting linac are summarised with a beam of  $A/q = 4.5$  in Figure 6.6. The study was carried out by tracking 50000 particles in the LANA model without imperfections and no particles were lost. A small growth of the transverse emittance arises in the first cavity, which acts as a rebuncher, because of the increased phase spread of the beam after the drift from the IHS. The focusing strength is sufficient that the parametric resonance of the transverse motion is suppressed, even though the phase advance in the second low energy cryomodule is relaxed to match the beam into a focusing strength of  $90^\circ$  per period in the high energy section. The growth of the normalised rms emittances is at the level of just a few percent and the adiabatic damping of the transverse beam size is observable. The longitudinal emittance growth arises from the non-linear nature of the phase space gymnastics in the low energy section and across the transition region into the high energy section. However, the non-linear effects do not grow and are largely cancelled out. The absence of a dedicated matching section between the two sections of the the linac does not have a significant effect on the beam quality.

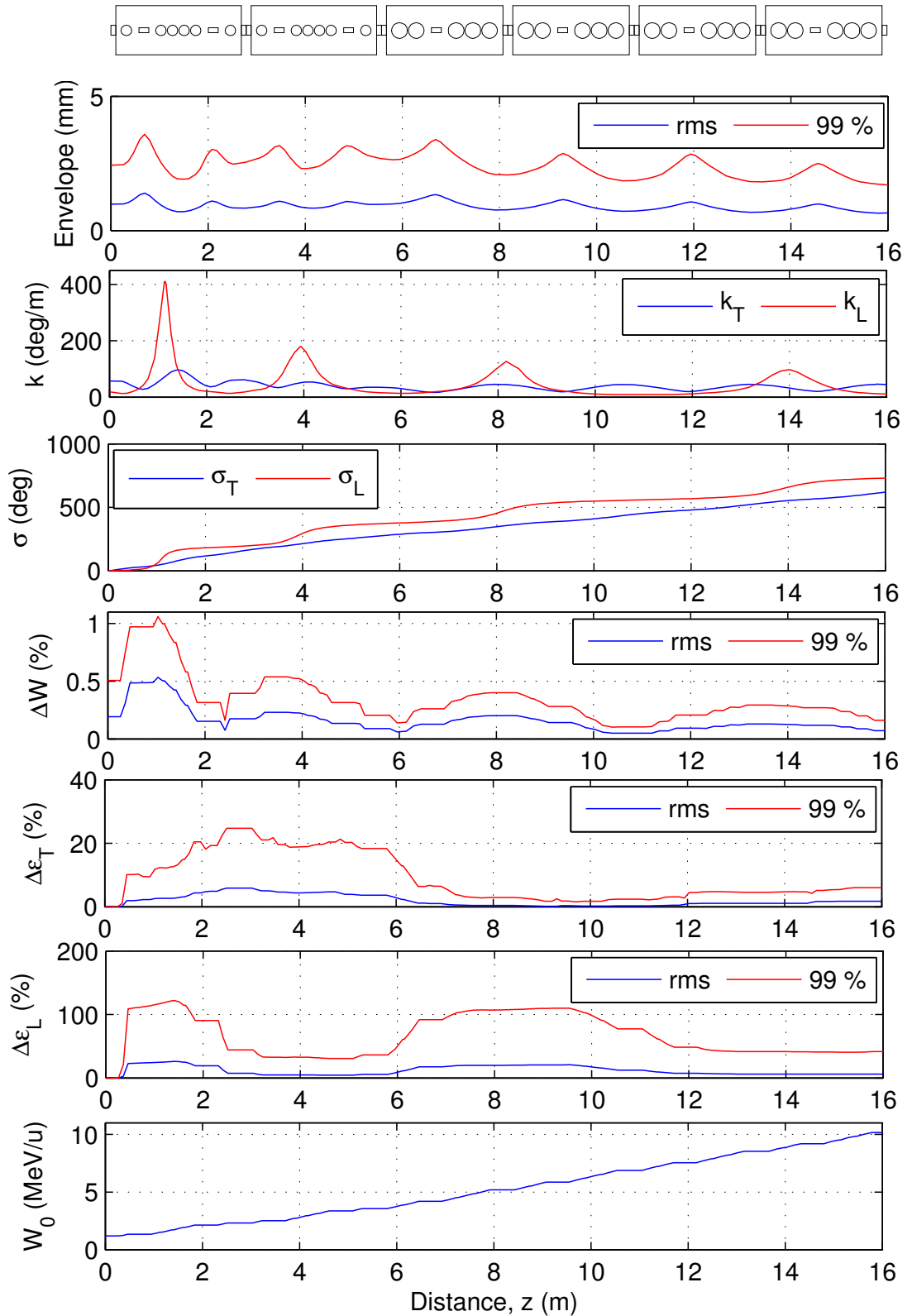


Figure 6.6: Summary of multi-particle LANA simulations of the HIE linac,  $\mu_T = 90^\circ$  and  $A/q = 4.5$ .

## 6.3 Matching Sections

The results of Chapters 4 and 5 were used to design the matching sections from REX to the HIE linac in both stages of the upgrade.

### 6.3.1 Acceptance

The normalised transverse acceptance of the HIE linac is  $2.8 \pi$  mm mrad with a circular aperture of radius 10 mm in the cavities and 15 mm in the solenoids, which is a factor of 10 larger than the measured 90 % beam emittance of  $0.3 \pi$  mm mrad

The longitudinal acceptance for Stage 2b of the superconducting linac is shown in Figure 6.7 at the entrance to the low energy section with the distance between the cryomodels doubled and halved. The strength of the transverse-longitudinal coupling is reduced as the packing factor and the longitudinal acceptance are increased because the bunch can be constrained tighter in its phase extent. Only a small increase in acceptance is achieved by reducing the spacing between cryomodels below 50 cm because of the longitudinal space already taken up by the solenoids inside the cryomodels. The longitudinal acceptance is close to a factor of 5 times larger than the nominal emittance of  $2 \pi$  ns keV/ $u$ , where the matched beam ellipse is enlarged to coincide with the shape of the acceptance region.

### 6.3.2 Stage 1 and 2a

The first high energy cryomodel will be installed at a position 1.59 m downstream of the 9GP, which is compatible with its position in Stage 2b and prevents it having to be moved when the low energy superconducting section is installed.<sup>1</sup> The REX beam is shown against the longitudinal acceptance of Stage 1 at entry to the first superconducting cavity in Figure 6.8, with the 9GP operating at three different synchronous phases. The longitudinal matching is optimised with the 9GP operating at  $-10^\circ$ ; the emittance grows by over a factor of 2 in the 9GP but no more growth occurs in the superconducting machine.

<sup>1</sup>If a chopper line is installed with Stage 2b the REX front-end could be extended by the length of one high energy cryomodel such that only the first high energy cryomodel will require moving to the end of the linac, leaving the other three cryomodels and the cryogenic distribution line undisturbed. A possible configuration is shown in Figure 6.46.

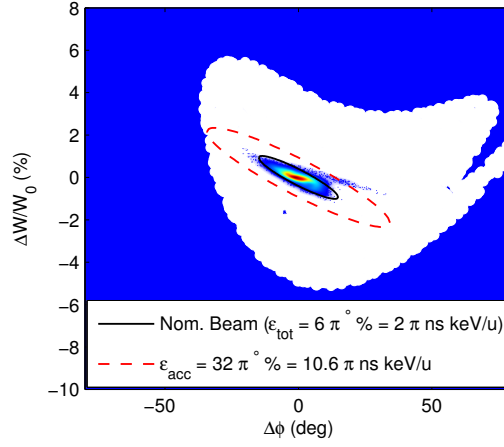
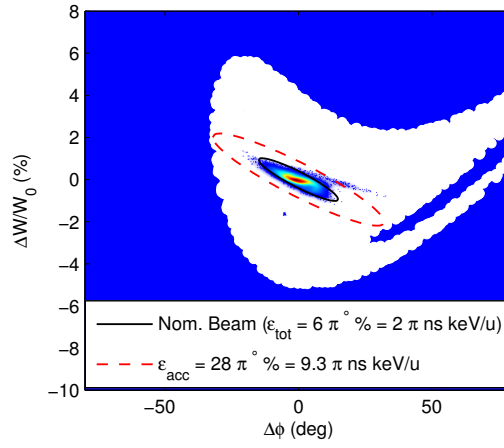
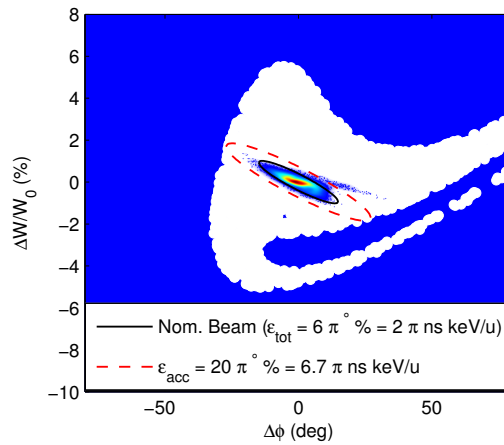
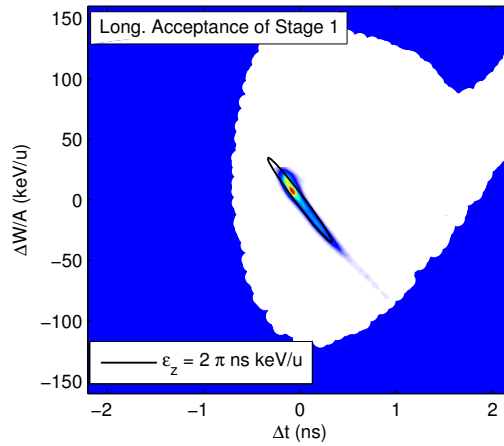
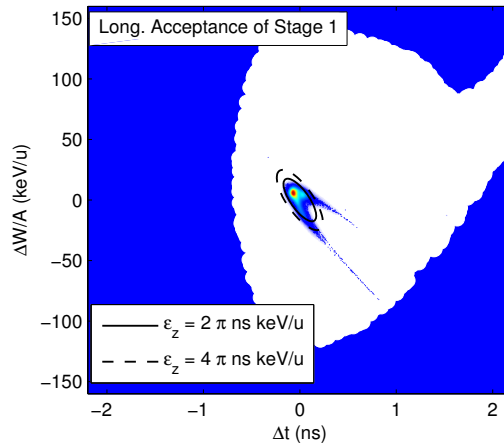
(a)  $F = 62 \%$ : inter-cryomodule dist. = 25 cm.(b)  $F = 56 \%$ : inter-cryomodule dist. = 50 cm.(c)  $F = 47 \%$ : inter-cryomodule dist. = 100 cm.

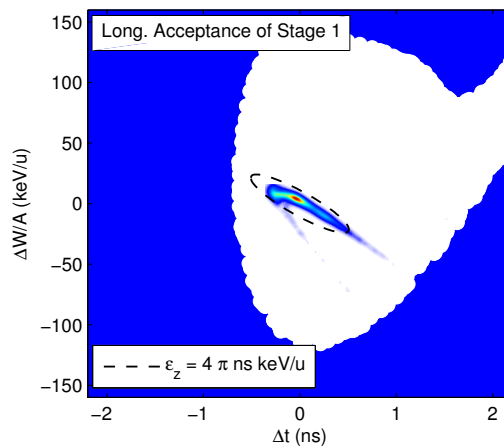
Figure 6.7: The longitudinal acceptance of Stage 2b for different inter-cryomodule distances and corresponding packing factors ( $F$ ) shown with the beam delivered by REX at the entrance to the low energy section,  $W_0 = 1.2 \text{ MeV/u}$ .



(a)  $\phi_s = -20^\circ$ : large energy spread causes filamentation.



(b)  $\phi_s = -10^\circ$ : optimum solution, no further emittance growth.



(c)  $\phi_s = 0^\circ$ : large phase spread causes filamentation.

Figure 6.8: Longitudinal acceptance of Stage 1 of the HIE linac and the beam at its entrance for different 9GP synchronous phases.

The  $4 \pi \text{ ns keV}/u$  emittance is best accepted when the synchronous phases of the first two high- $\beta$  cavities are lowered to  $-30^\circ$ . When the 9GP is operated at higher synchronous phases the phase spread of the beam is too large, and at lower phases the energy spread is too large, to be efficiently captured by the superconducting linac and filamentation ensues. The transverse matching to the solenoid channel can be achieved with four quadrupoles characterised by gradients below 50 T/m, each with an effective length of 200 mm and a radial aperture of at least 15 mm, which was specified at a little over twice the 95 % beam size, see Figure 6.9.

### 6.3.3 Stage 2b

The matching section was made as compact as possible with only 1 m between the output of the IHS and the first low- $\beta$  cavity. To this end, a triplet was chosen because the beam is closely round on exit from the IHS and only small additional adjustments to the last quadrupole of the triplet internal to the IHS are needed to provide the four matching parameters for the solenoid channel. As described in [177], a pole tip radius of 15 mm is adequate to keep 95 % of the beam within half the aperture and demanding up to 0.9 T on the pole tip, see Figure 6.10.

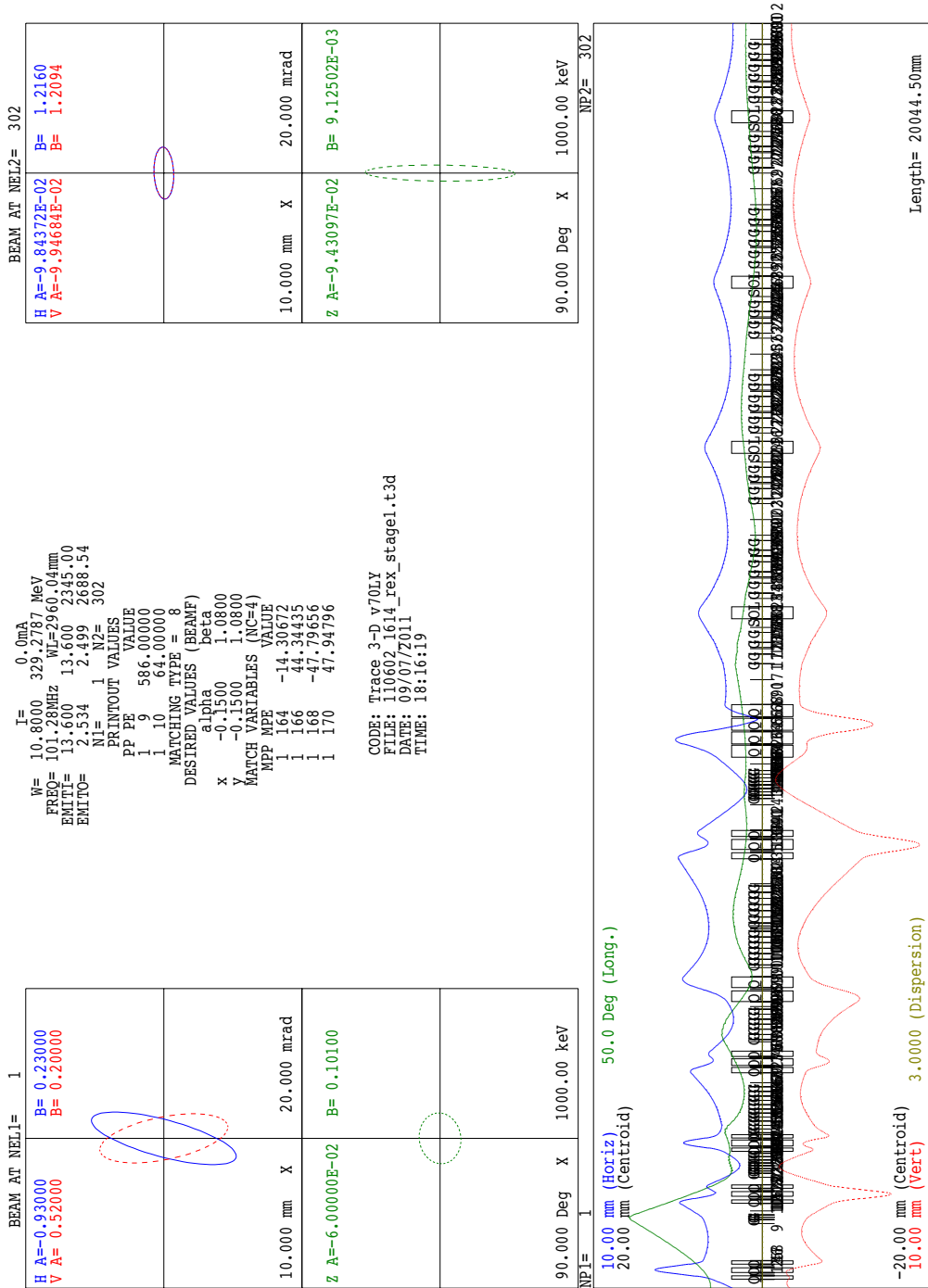


Figure 6.9: TRACE 3-D model for matching REX to Stage 1 and 2a of the HIE linac ( $A/q = 4.5$ ).

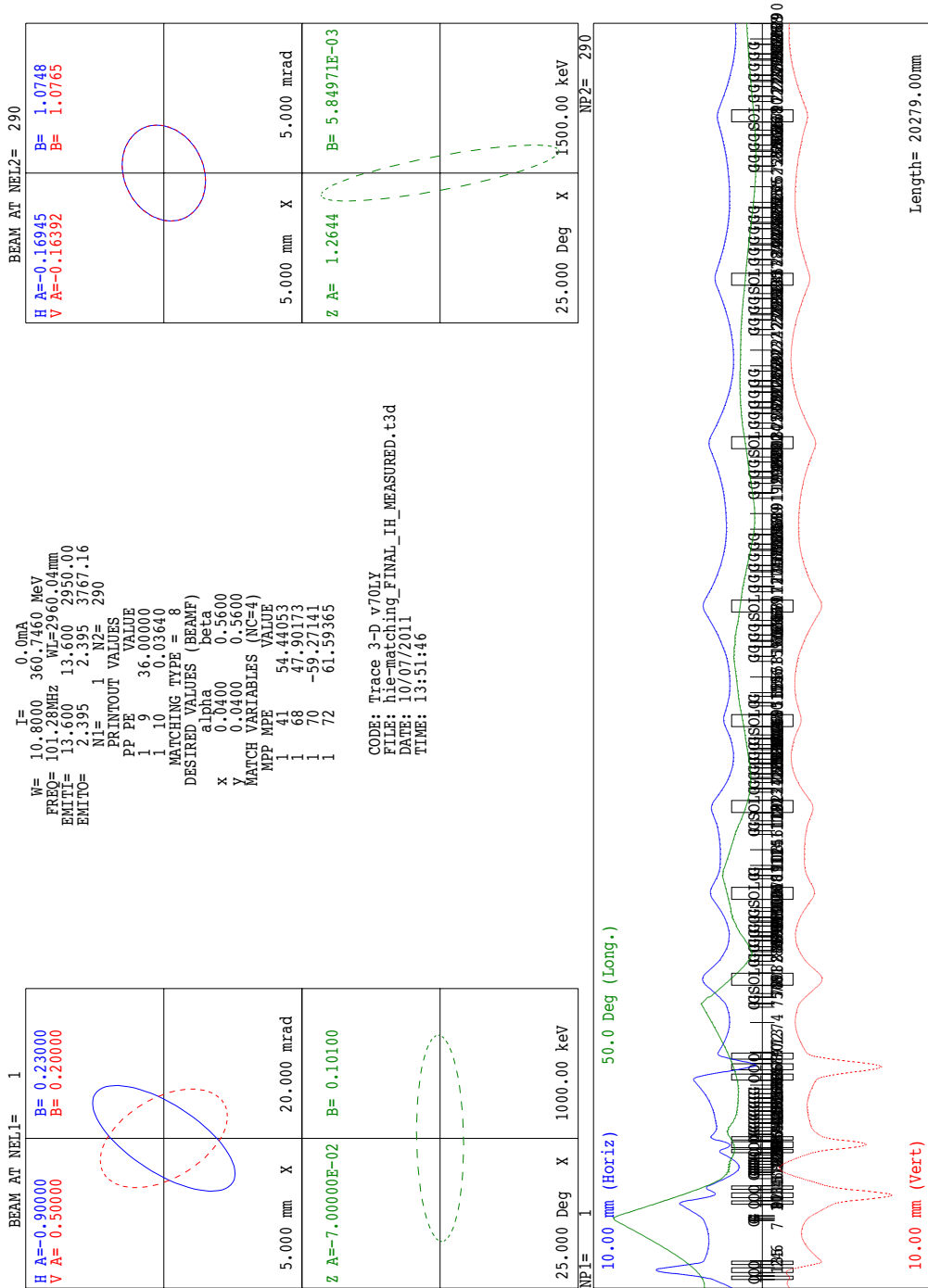


Figure 6.10: TRACE 3-D model for matching REX to Stage 2b of the HIE linac ( $A/q = 4.5$ ).

## 6.4 Compensation of Beam-steering

Two commonly applied techniques for compensating the steering inside quarter-wave resonators involve:

- Making local modifications to the cavity geometry near the beam axis in order to modify the longitudinal profile of the transverse electric field or to reduce the magnetic field in the gap.
- Using the rf (de)focusing force by offsetting the beam inside the aperture.

A detailed discussion of the above listed techniques can be found in [118, 187]. With cavities at 101.28 MHz the steering forces are moderate and can be compensated using the rf (de)focusing force by deliberately offsetting the beam inside the aperture. The beam-steering due to rf (de)focusing can be written in the same form as Equation 3.4.4,

$$\Delta y'_{\text{steering}} = - \frac{qE_0(y_0)L_a T(\beta)}{A\gamma uc} \underbrace{\delta \frac{\pi}{\lambda c\gamma^2\beta^3}}_{\text{rf (de)focusing}} \sin \phi_s, \quad (6.4.1)$$

where  $\delta$  is the offset of the beam centroid with respect to the centre of the aperture. The beam-steering can be compensated by adjusting  $\delta$  as a function of  $\beta$  such that,

$$\delta_{\text{comp}} = \frac{\lambda c}{\pi} \left[ \beta^2 \kappa_B(y_0) - \frac{\beta \kappa_E(y_0)}{c} \cot \frac{\pi \beta_g}{2\beta} \right]. \quad (6.4.2)$$

The  $1/\beta^3$  dependence of the rf (de)focusing force makes the compensation very effective at low velocity and requires only small offsets of the beam inside the aperture. At higher velocity, the offset becomes larger and limits the application of the technique. The offset allows for an effective compensation over a wide range of velocities, as is shown in Figure 6.11 for the high- $\beta$  cavity in normal operating conditions with  $\delta_{\text{comp}} = 2.5$  mm. The compensation ability of the rf (de)focusing force is only effective for  $\beta \gtrsim \beta_g/2$  because the rf (de)focusing force in each gap cancels in the limit that  $\beta \rightarrow \beta_g/2$ . Below  $\beta \approx \beta_g/2$  the  $1/\beta^3$  dependence of the rf defocusing force causes the compensation offset to become inhibitive, as is shown by the comparison with and without an offset in Figure 6.11.

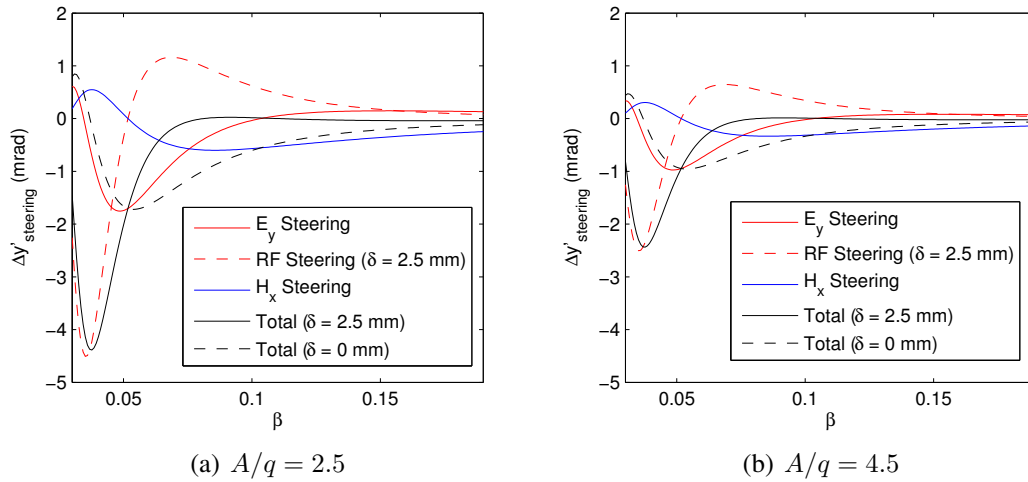


Figure 6.11: An analytic calculation showing the compensation of beam-steering using the rf (de)focusing force in the high- $\beta$  cavity ( $\beta_g = 10.3\%$ ).

$\delta_{\text{comp}}$  of approximately 0.5 mm is required in the low- $\beta$  cavity whereas in the high- $\beta$  cavity the offset necessary is 5 times larger at closer to 2.5 mm, which represents a quarter of the radial aperture. The compensation of the beam-steering by modifying the cavity geometry in the vicinity of the beam axis was ruled out to avoid complications in sputtering the copper substrate with niobium. Instead, an elongated aperture in the direction of the offset was used to reduce the loss in aperture arising from the offset, see Figure 6.12.

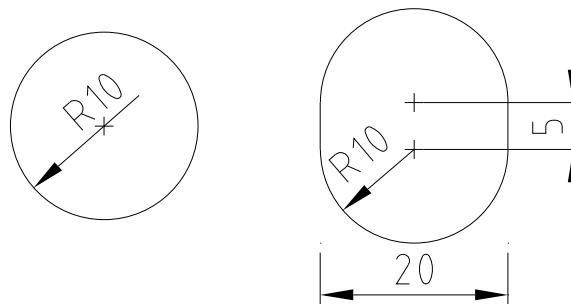


Figure 6.12: Schematic of the circular and racetrack apertures. Dimensions in mm.

The steering effect was calculated numerically by integrating the equation of motion of a single particle representing the centroid in the electromagnetic field maps exported from CST-MWS simulations of the cavity. A grid size of 1 mm was used and the field values interpolated linearly between the mesh at each integration step. The synchronous

phase of the cavity was adjusted relative to the maximum of the energy gain to maintain longitudinal phase stability, even at low velocity. The numerical calculations of the steering with  $A/q = 4.5$  and acceleration at a synchronous phase of  $-20^\circ$  in the two cavities is shown in Figure 6.13, with and without compensation. The steering can be well com-

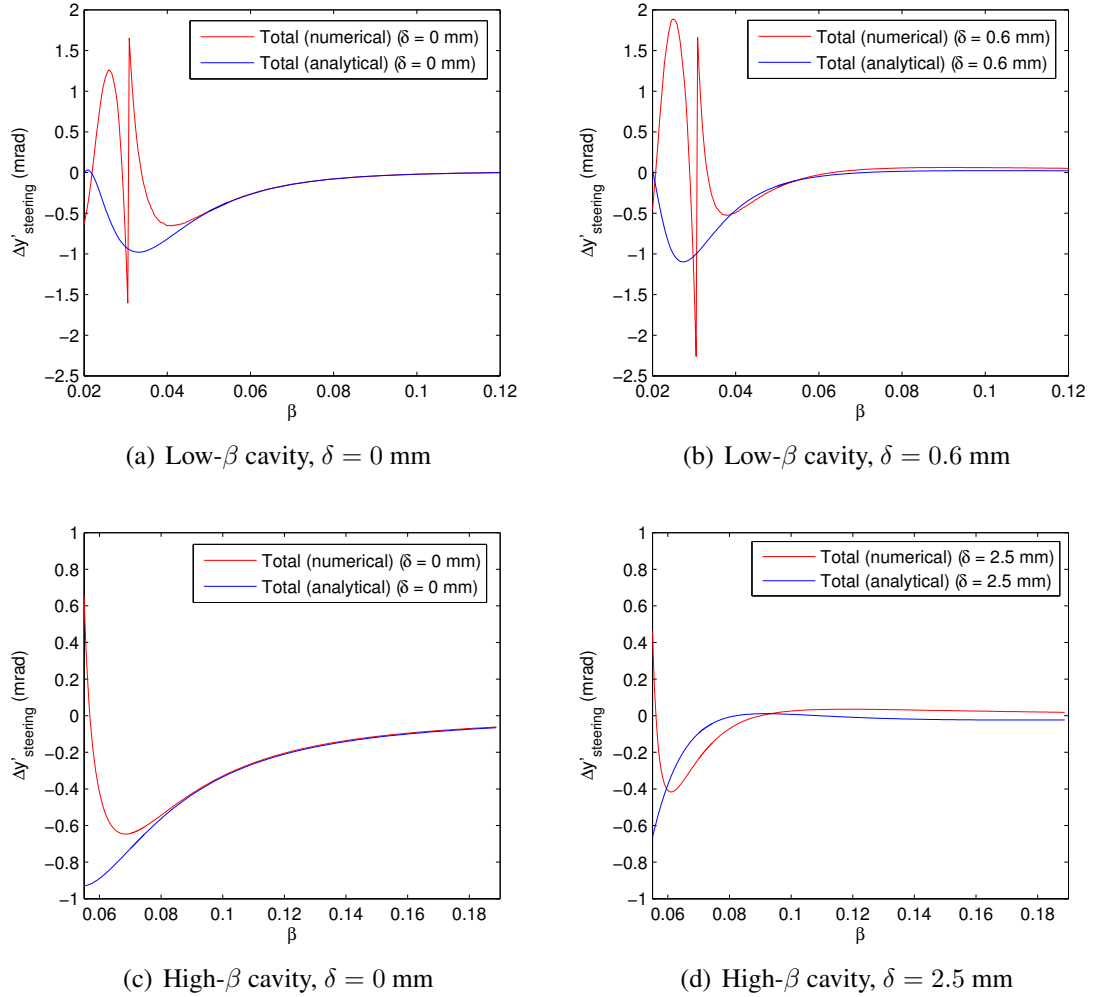


Figure 6.13: Beam-steering in the HIE cavities: analytical vs. numerical calculations ( $\phi_s = -20^\circ$  and  $A/q = 4.5$ ).

pensated above the injection velocities of  $0.051c$  and  $0.088c$  in the low and high energy sections, respectively. The calculation is extended to very low velocity in the case of the low- $\beta$  cavity. The analytic approximation is excellent above the geometric velocity in the uncompensated case but breaks down at low velocities; the adjustment of the synchronous phase in the numerical case causes most of the discrepancy with the analytic calculation, which assumes a constant velocity. The cavity geometry is not cylindrically symmetric about the beam axis, as is assumed in the analytic approximation, therefore the agreement is not so good where the cavity is offset and the rf (de)focusing force is invoked. The

analytic calculation close to  $\beta \rightarrow \beta_g/2$  is conservative compared to the numerical result. The discontinuity in the numerical calculation arises from the shift in phase of  $\pi$  required to continue accelerating as the zero of  $T(\beta)$  is traversed and its sign reverses, as will be discussed in Chapter 6.8.

### 6.4.1 Optimisation of Cavity Geometry

To keep the design of the cryomodules as simple as possible it was decided to apply the same compensation offset ( $\delta_{\text{comp}}$ ) to all cavities of a given family. The cavity geometry was optimised using the single-particle tracking routine to calculate the beam-steering kicks in each cavity along the linac. The rms deviation from zero of the ensemble of kicks in  $N$  cavities,

$$\sigma_{\Delta y'} = \frac{\sqrt{\sum_{i=1}^N \Delta y_{i,\text{steering}}'^2}}{N}, \quad (6.4.3)$$

was evaluated and used as a figure of merit to assess the quality of the compensation of the beam-steering as a function of the height of the beam axis  $y_0$  and  $\delta$ , where the parameter  $y_0$  was defined in Figure 3.14. The velocity dependence of the steering force and the variable velocity profiles developed by different beams along the linac makes the optimum cavity offset dependent on  $A/q$ . The optimum offset ( $\delta_{\text{opt}}$ ) was determined by minimising the sum of the squares of the steering kicks in each cavity along the linac, across the mass-to-charge state acceptance. A survey of  $\sigma_{\Delta y'}$  as a function of  $y_0$  and  $\delta$  in the high energy section of Stage 2a is shown in Figure 6.14 and summarised in Table 6.2, where the circular beam ports had a radial aperture of 10 mm.

Table 6.2: Summary of the optimisation of  $y_0$  and  $\delta$  in the high energy section.

$y_0$ [mm]	$R_{\text{max}}/Q$ [ $\Omega$ ]	$\delta_{\text{opt}}$ [mm] ( $A/q = 4.5/2.5$ )	Loss of Vertical Acceptance [%] ( $A/q = 4.5/2.5$ )
20	569	2.2 / 1.6	39.2 / 29.4
30	564	2.3 / 2.0	40.7 / 36.0
40	559	2.4 / 2.3	42.2 / 40.7
50	553	2.6 / 2.5	45.2 / 43.8
60	545	2.6 / 2.8	45.2 / 48.2
70	539	2.8 / 3.0	48.2 / 51.0
80	531	3.0 / 3.2	51.0 / 53.8

The beam-steering is minimised when the height of the centre of the beam port is

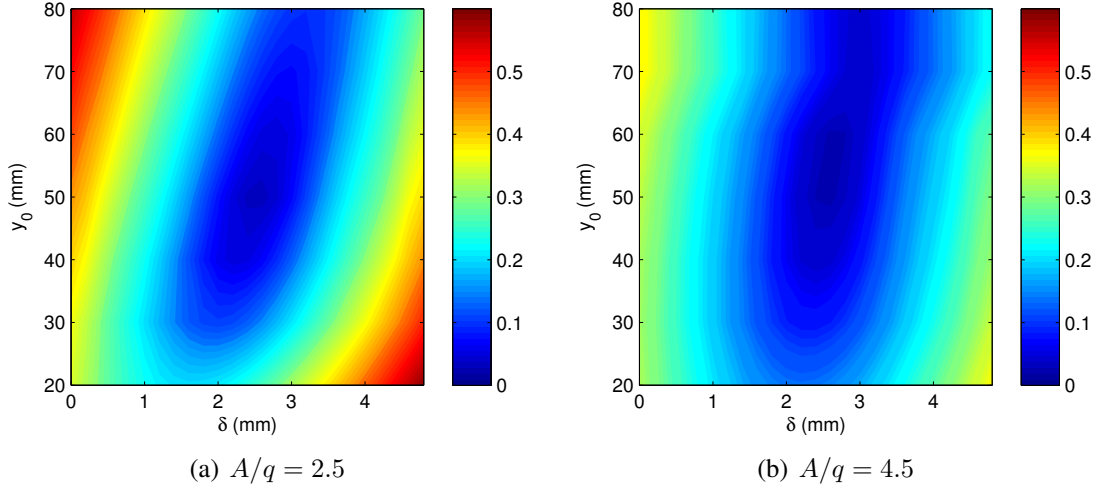


Figure 6.14: Contours of  $\sigma_{\Delta y'}$  (mrad) in the high energy section for Stage 2a ( $\phi_s = -20^\circ$ ).

located approximately 50 mm above the end of the straight part of the internal conductor with  $\delta \approx 2.5$  mm; the steering becomes rapidly difficult to compensate close to the end of the internal resonator because the  $\kappa_E$  term rises significantly in this region. The  $\kappa$  terms change much less rapidly with height moving up the resonator as  $y_0$  increases. The correlation between  $\delta_{\text{opt}}$  and  $y_0$  arises because of the variation in the shunt impedance and the rf (de)focusing force with the height of the beam port in the resonator, and is best observed in Figure 6.14(a) by the tilt of the contour lines.

The applicability of such an optimisation routine for setting the beam port height and compensation offset is highlighted by comparing  $\sigma_{\Delta y'}$  with the emittance growth calculated using TRACK. The correlation between  $\sigma_{\Delta y'}$  and the transverse emittance growth in

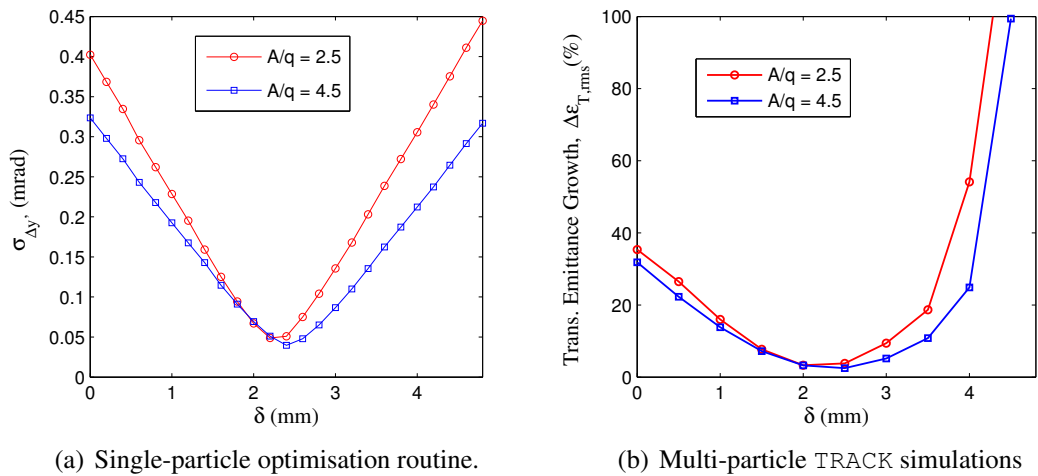


Figure 6.15: Comparison of the single-particle optimisation routine with TRACK in the high energy section of Stage 2a ( $\phi_s = -20^\circ$  and  $y_0 = 40$  mm).

the high energy section of Stage 2a is shown in Figure 6.15. The focusing strength was set to  $\pi/2$  per focusing period to suppress the parametric coupling discussed previously.

An offset of 2.5 mm inside the 10 mm aperture significantly reduces the vertical acceptance. Although larger circular apertures were considered, the loss of acceptance was countered by extending the beam port aperture vertically by 5 mm to form the racetrack geometry shown in Figure 6.12. The racetrack geometry keeps the shunt impedance high with respect to a circular beam port with a radius equivalent to the major radius of the racetrack. For the racetrack aperture, the offset has to increase to 2.8 mm to optimise the compensation of the beam-steering.

### 6.4.2 Offset of the Beam Port Noses

The magnitude of  $\delta_{\text{opt}}$  was reduced by placing the beam port asymmetrically on the nose of the cavity by a distance  $\Delta$ , as is demonstrated in Figure 6.16. The asymmetry introduces a

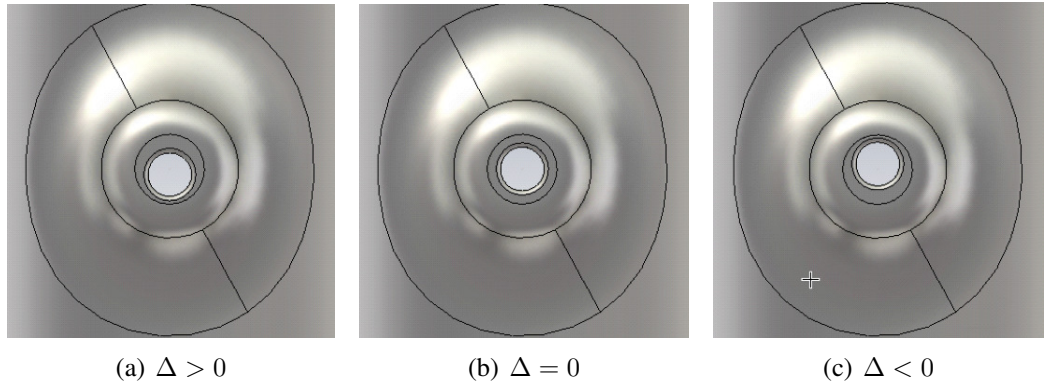


Figure 6.16: The position of the centre of the noses relative to the centre of the beam port, parameterised by  $\Delta$ .

small additional vertical dipole component of electric field on the beam axis that modifies the intrinsic electric dipole. The modification introduces higher harmonic terms in the Fourier expansion for  $E_y(z)$  that results in a force with the correct phase to compensate the magnetic steering, as is discussed in [187]. The dipole component that is introduced on to the beam axis in the presence of a racetrack shaped aperture by shifting the position of the noses upwards by 2 mm ( $\Delta = +2$  mm) is shown in Figure 6.17 alongside a survey of  $\sigma_{\Delta y'}$  for  $\Delta = \pm 2$  mm at  $y_0 = 40$  mm. If the offset is made in the correct direction, not only is  $\delta_{\text{opt}}$  reduced but so is the magnitude of  $\sigma_{\Delta y'}$  at the optimum.

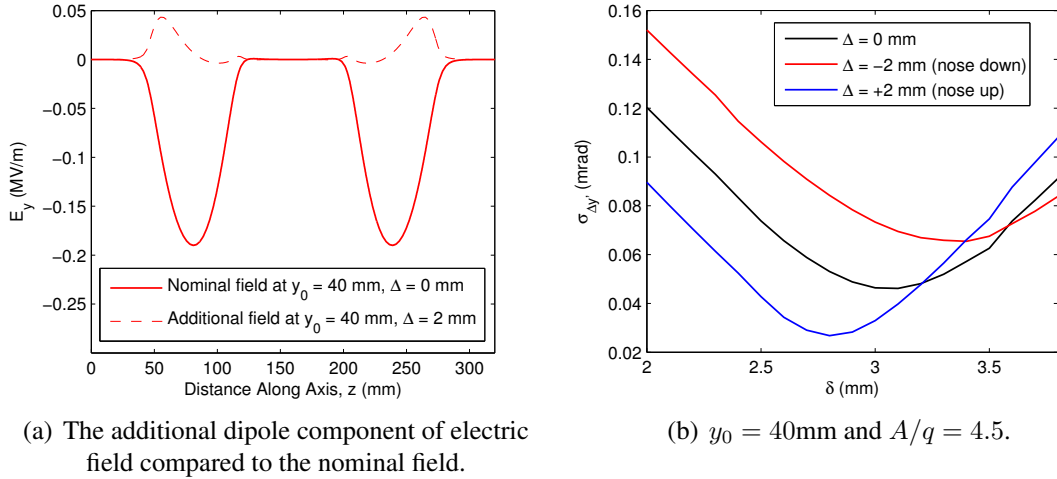


Figure 6.17: The consequence of positioning a racetrack shaped beam port 2 mm above and below the centre of the noses ( $\Delta = \pm 2$  mm).

$\delta_{\text{opt}}$  is reduced by 10 % by shifting the noses 2.5 mm upwards with respect to the beam ports, without any significant effect on the vertical symmetry of the rf (de)focusing. Therefore, the beam axis is positioned in the centre of the nose so that the beam passes 2.5 mm above the centre of the racetrack aperture and the beam-steering is compensated in the high- $\beta$  cavity. The results of the beam-steering study are summarised in Table 6.3. The optimisation routine was also carried out in the low energy section for the linac accelerating with  $\phi_s = -20^\circ$ .

Table 6.3: Summary of the results of the beam-steering optimisation study.

Cavity Family	Beam Port Geometry	$\Delta$ [mm]	$\delta_{\text{opt}}$ [mm]	$y_0$ [mm]
Low- $\beta$	circular	0	+0.6	35
High- $\beta$	racetrack	+2.5	+2.5	40

## 6.5 Compensation of Transverse Asymmetry

The cylindrical geometry of the quarter-wave resonator introduces a quadrupole component to the transverse electric fields in the vicinity of the beam axis, which breaks the radial symmetry of the electromagnetic fields in the linac. The asymmetry is evident by comparing the way the cavity walls bend away from the beam port in the vertical and horizontal planes, as shown for the high- $\beta$  cavity in Figure 6.18. The asymmetry splits the horizontal and vertical phase advances, mismatching the focusing channel and causing

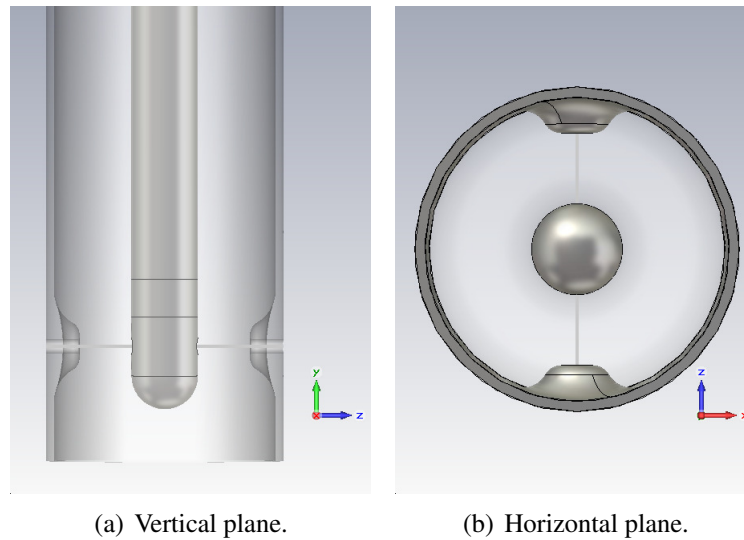


Figure 6.18: Cross-section of the high- $\beta$  cavity at the beam axis.

the horizontal and vertical emittance projections to oscillate as the beam is rotated in the solenoids [188].

The effect of the asymmetry was investigated by tracking a single particle in the field maps and quantified by comparing the rf deflection in the horizontal and vertical planes at a distance of 1 mm from the beam axis. The horizontal and vertical planes represent the two orthogonal axes of the quadrupole. The asymmetry is summarised in Figure 6.19, which also includes a cavity in which the field symmetry was much improved by modifying the geometry of the end of the internal conductor. This cavity is described in more

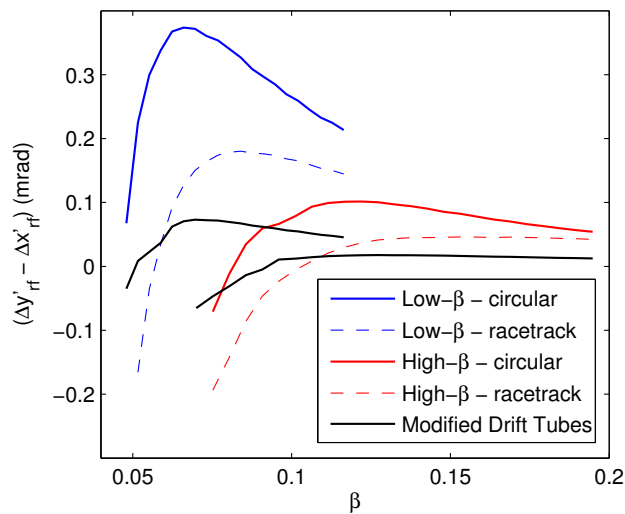


Figure 6.19: Asymmetry of the rf (de)focusing in the cavities at  $\pm 1$  mm from the beam axis ( $A/q = 2.5$  and  $\phi_s = -20^\circ$ ).

detail in Appendix F.1. The racetrack aperture reduces the asymmetry of the (de)focusing

fields considerably over a wide velocity range, which includes the range of beam velocities in each section after the completion of the upgrade:  $\beta > 0.051$  and  $> 0.088$  in the low and high energy sections, respectively.

The effect on the projected emittance caused by the rotation in the solenoids could be isolated from most other sources of emittance growth by setting the longitudinal emittance to zero in the multi-particle simulations. The simulations were carried out with TRACK and an emittance equal to the acceptance of the RFQ. The asymmetry was shown to cause small discrete jumps no more severe than 4 % in the projected emittance after each solenoid rotation. The change in the projected emittance after each solenoid can be modified by changing the sense of the rotation by reversing the longitudinal field direction. Of more concern is the mismatch from the splitting of the transverse phase advances and the single tuning parameter of the solenoid focusing channel. The mismatch that develops in each section is shown in Figure 6.20 with a comparison of the 95 % beam envelopes.

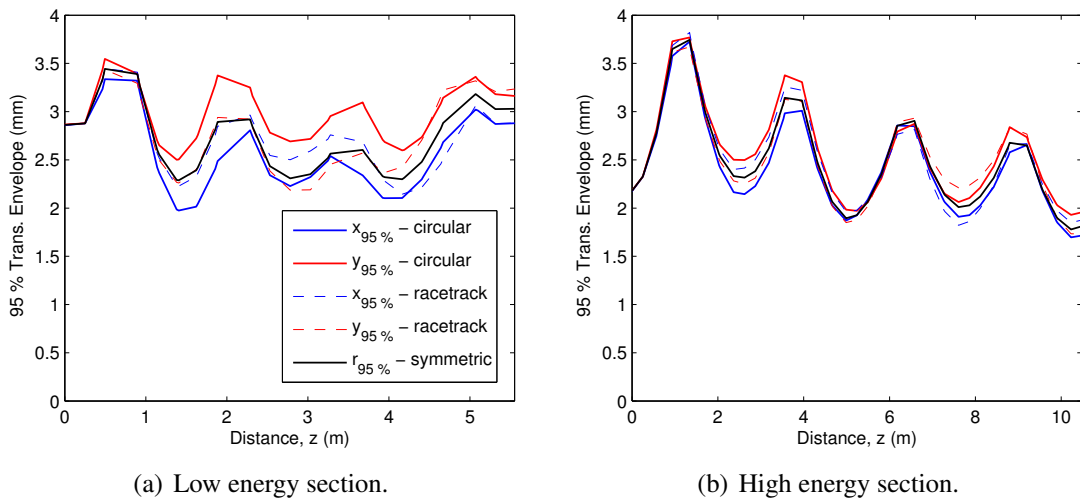


Figure 6.20: The horizontal and vertical beam envelopes in each section of the HIE linac with different modifications to the cavity geometry in the vicinity of the beam axis.

The racetrack shaped aperture acts to improve the asymmetry with respect to the circular aperture along the early stages of each linac section before some mismatch becomes evident. The effect of the asymmetry of the quarter-wave resonators is most noticeable in the low energy section, which mismatches the beam at entry to the high energy section. The 95 % beam envelopes are shown in Figure 6.21, in which cavities with the racetrack beam port and the modified drift-tube are compared to the nominal and symmetric case. The mismatch is manageable without the need to significantly modify the drift-tube and

the envelopes remain sufficiently matched through the short linac that the modification to the geometry of the inner conductor was not deemed worthwhile. In the absence of space-charge the mismatch arising from the asymmetry does not cause significant emittance growth.

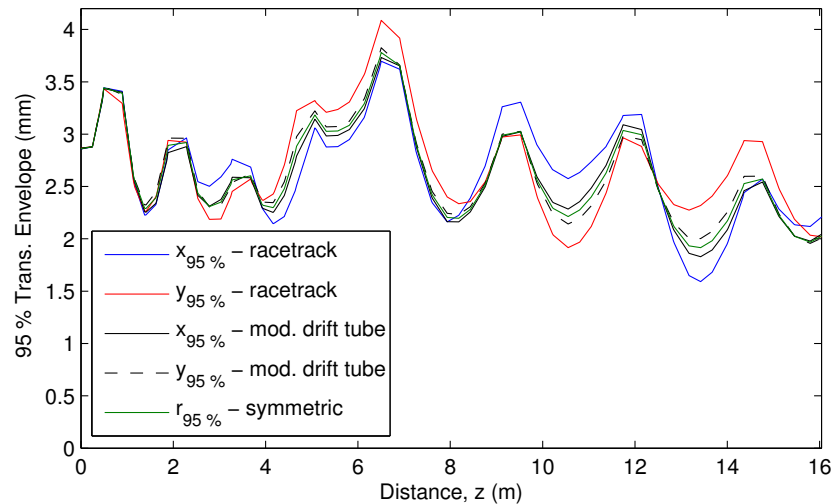


Figure 6.21: The horizontal and vertical beam envelopes along the entire HIE linac with different modifications to the cavity geometry in the vicinity of the beam axis.

## 6.6 Removal of Cavity Noses

The feasibility of removing the beam port noses on some of the high- $\beta$  cavities was investigated with the objective of simplifying and reducing the costs of manufacturing the cavity. If necessary, the noses could be removed from the high- $\beta$  cavities in the final cryomodule with a negligible effect. The study is summarised in Appendix F.2.

## 6.7 Misalignment and Error Studies

The sensitivity of the beam to misalignment and rf instabilities was investigated in order to understand the robustness of the design to imperfections. The study resulted in the specification of the alignment tolerances required in the design and assembly of the cryomodules, along with the specification to which the phase and amplitude of the electromagnetic fields in the cavities should be controlled by the low-level rf system.

The linac was subjected to misalignment in two different models that both used the realistic field maps of the cavities and solenoids. The first model used a linear parameterisation of the realistic fields in a matrix formalism, facilitating both the benchmarking of other codes and fast, systematic studies with many error seeds. The second model was implemented in TRACK to understand the effect on the beam emittance from both misalignment and rf errors. The following imperfections were investigated:

- Transverse misalignment of the cavities and solenoids:  $\sigma_{x,y,\text{cav}}$  and  $\sigma_{x,y,\text{sol}}$ .
- Longitudinal misalignment of the cavities:  $\sigma_{z,\text{cav}}$ .
- Phase and voltage instability in the cavities:  $\sigma_{\Delta\phi}$  and  $\sigma_{\Delta V}$ .

The beam is about 5 times more sensitive to the misalignment of the solenoids than to the misalignment of the cavities, see the results presented in [189]; owing to this dominance and the axial symmetry of the solenoid, skew errors (rotations about the beam axis) were neglected. The effect of a variation in the longitudinal position of the cavities was investigated to understand the tolerance to which the cavities must be aligned to avoid having to re-phase the linac. Static field errors and longitudinal misalignment of the solenoids were ignored.

Unlike in a fixed-velocity linac where the fields are scaled and the effect of misalignment is independent of  $A/q$ , in a superconducting linac the full accelerating voltage is delivered to all beams and those with lower  $A/q$  are usually more sensitive to misalignment; beams with  $A/q = 2.5$  were shown to be 15 % more sensitive than  $A/q = 4.5$  to misalignment [190]. The high energy section of the linac in Stage 2a was simulated with  $A/q = 2.5$  to provide the specification of the alignment tolerances for the ongoing development of the high energy cryomodule. The nominal beam parameters after the 9GP, presented in Chapter 4, were used as input at an injection energy of 3 MeV/u. The specified tolerances were then applied to the low energy section and the study concluded with end-to-end simulations of the completed linac in Stage 2b.

### 6.7.1 Misalignment with a Matrix Model

The beam dynamics in the realistic fields of the cavities and solenoids was linearised by tracking eigenvectors through the field maps using a numerical tracking routine to reconstruct the transverse transfer matrix. For a given beam velocity, synchronous phase and field level one can write the linearised motion of a single particle as,

$$\vec{X}_1 = R_{\text{cav}}(\beta, \phi_s, V_0)\vec{X}_0 + \vec{K}_{\text{cav}}(\beta, \phi_s, V_0), \quad (6.7.1)$$

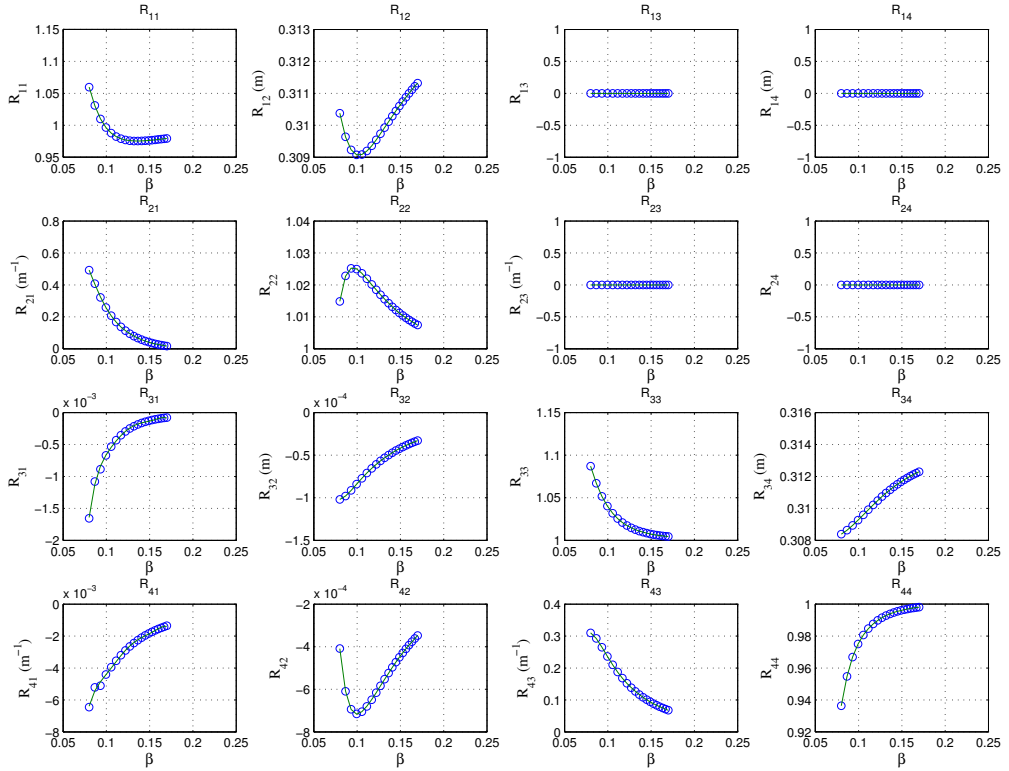
where  $\vec{K}_{\text{cav}}$  describes the beam-steering kick given to the centroid entering the cavity on and parallel to the beam axis. In the high- $\beta$  cavity the beam axis in the cavity is defined at  $\delta = 2.5$  mm from the centre of the racetrack aperture, as discussed. The model assumes that there is no coupling between the transverse and longitudinal dynamics, which was shown in [190] to be a good approximation in a strong focusing channel. The same can be written for the solenoid in terms of the peak field inside the solenoid,

$$\vec{X}_1 = R_{\text{sol}}(\beta, B_0)\vec{X}_0, \quad (6.7.2)$$

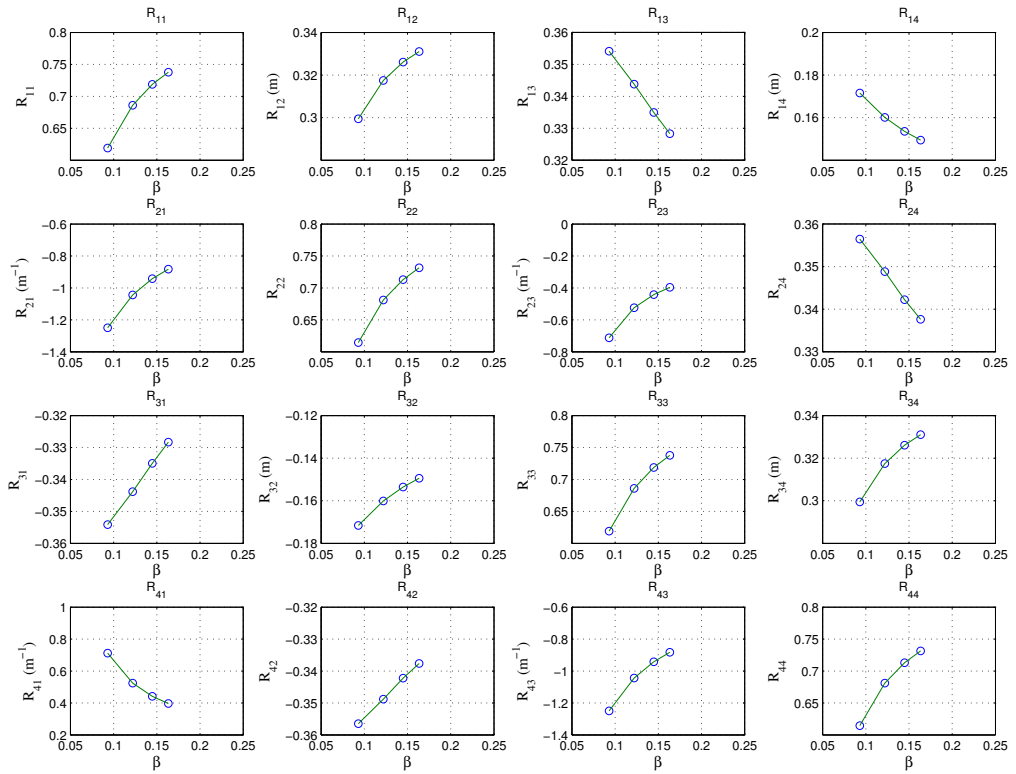
where the centroid receives no kick when aligned with the magnetic axis. The transverse transfer matrix elements of each of the 20 cavities and 4 solenoids of Stage 2a are shown in Figure 6.22 for a beam with  $A/q = 2.5$  operating at a synchronous phase of  $-20^\circ$  and a transverse phase advance of  $\pi/2$  per focusing period.

The linearised motion can be easily perturbed with a random misalignment to each matrix and the trajectory of the centroid tracked throughout the accelerator. The misalignment acts as a dipole kick to leading-order and for each active element in the accelerator one can generate a vector  $\vec{K}$  that represents the effect of a random misalignment, see Appendix G. In the case of the quarter-wave cavity,  $\vec{K}$  includes both the kick due to misalignment and the beam-steering kick. The tracking of a particle from before element  $n$  to after element  $n + 1$  can be expressed as,

$$\vec{X}_{1,n+1} = R_{\text{el},n+1}(R_{\text{el},n}\vec{X}_{0,n} + \vec{K}_n) + \vec{K}_{n+1}, \quad (6.7.3)$$



(a) The transfer matrices of the cavities as a function of reduced velocity,  $R_{\text{cav}}(\beta, \phi_s = -20^\circ, V_0 = 1.8 \text{ MV})$ .



(b) The transfer matrices of the solenoid, as a function of reduced velocity,  $R_{\text{sol}}(\beta)$ .

Figure 6.22: The linearised beam dynamics in Stage 2a,  $A/q = 2.5$ .

and the coordinates of a single particle tracked from before element  $j$  to after element  $n$  can be written more generally as,

$$\vec{X}_{1,n} = R(n|j)\vec{X}_{0,j} + \underbrace{\sum_{i=j}^{n-1} R(n|i+1)\vec{K}_{i+1}}_{\text{centroid trajectory}}, \quad (6.7.4)$$

where  $R(n|i) = R_n R_{n-1} R_{n-2} \dots R_{i+1}$  and  $R(n|n) = I$ . Using this formalism the centroid trajectory was tracked quickly through a large number of randomly misaligned linacs.

### 6.7.1.1 Generation of Random Errors

For any given error seed, the transverse misalignment of each element was generated with four random numbers that, together with a probability distribution function, parameterise the offset of the entry and exit positions:  $\Delta x_i$ ,  $\Delta y_i$ ,  $\Delta x_f$  and  $\Delta y_f$ . The distribution of the randomly generated numbers was either uniform or Gaussian and parameterised by the rms value ( $\sigma$ ), where the Gaussian distribution was truncated at  $\Sigma = \pm 3\sigma$ .

### 6.7.1.2 Injection Errors

The error in the position and divergence of the beam at injection was assumed to be small and correctable with steerer magnets placed upstream of the upgrade; the injection error was neglected. In the longitudinal plane, the jitter of the REX beam was already included in the value for the time-averaged longitudinal emittance measured in Chapter 5, which was used as input for the simulations.

### 6.7.1.3 Correction Routine

It is foreseen to install warm steerer magnets and beam position monitors (BPMs) in the spaces between the cryomodules. The implementation of cold steerers on the superconducting solenoids was also investigated and shown to provide a much improved control of the centroid excursion. In fact, the centroid excursion is reduced by over a factor of 4 and the steering strength demanded from the correctors is reduced by over 30 % in the high energy section of the linac. The improvement is shown in the four cryomodules of the high energy section of Stage 2a in Figure 6.23. Moving the corrector magnets inside

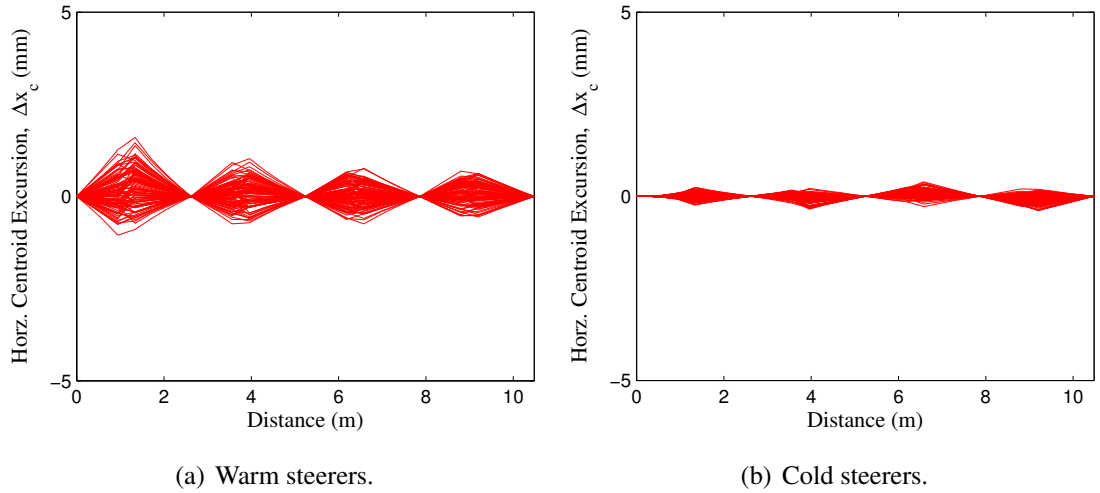


Figure 6.23: Comparison between the centroid excursions of 250 error seeds with warm and cold steerers in Stage 2a for tolerances:  $\sigma_{x,y,cav} = \pm 0.30$  mm and  $\sigma_{x,y,sol} = \pm 0.15$  mm.

the cryomodule could increase the packing factor of the linac by freeing up space in the already congested regions between the cryomodules. Although the use of cold steerers is still under consideration for the low energy section, the immediate technical challenges that they posed led to the decision to pursue conventional warm corrector magnets for the high energy cryomodules in the first stages of the upgrade.

In the case of warm steerers the correction routine is bracketed over each cryomodule, with a corrector located before and a BPM after each cryomodule. A phase advance of close to  $\pi/2$  between the corrector and BPM is optimum for an orbit correction system [191]. The correctors will consist of two steering elements capable of kicking the beam in the horizontal and vertical directions and were modelled as thin lenses. The corrector strength is determined by calculating the transfer matrix of each misaligned cryomodule ( $R_{n,cryo}$ ) and running a test particle to calculate the kick to the centroid in each cryomodule ( $\vec{K}_{n,cryo}$ ). In the test case the correctors are switched off and the position of the centroid at the BPM is expressed by,

$$\vec{X}_{n+1,BPM} = R_{n,cryo}\vec{X}_{n,BPM} + \vec{K}_{n,cryo} \quad (6.7.5)$$

The position at the BPM can then be set to zero and the transfer matrix inverted in order to derive the corrector strengths. As a result of the coupled motion in the solenoid focusing

channel the corrector strength in each orthogonal plane is coupled to the dynamics in the other plane.

#### 6.7.1.4 Transverse Cavity Misalignment

The effect of cavity misalignments on the likely centroid trajectory is shown in Figure 6.24, with and without correction, for 1000 linac error seeds and a tolerance on the alignment of  $\sigma_{x,y,cav} = \pm 0.5$  mm. There is no error in the BPM or misalignment of the solenoids. The larger spread of the centroid trajectories in the vertical plane in the first cryomodule arises from the correction scheme compensating for the vertical beam-steering force imparted by the cavities. The effect is strongest at low energy and quickly becomes negligible with acceleration along the linac.

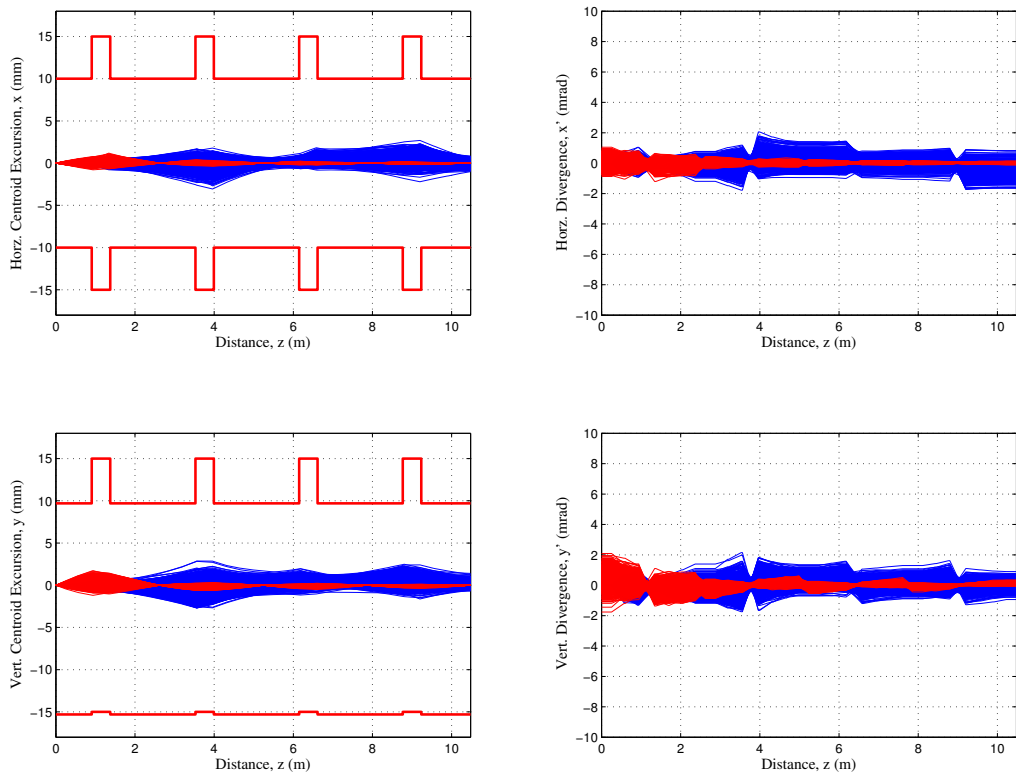


Figure 6.24: The centroid trajectory and divergence for 1000 linac error seeds with (red) and without correction (blue) for  $\sigma_{x,y,cav} = \pm 0.5$  mm. The physical aperture of the beam pipe is shown as a solid red line on the plots.

#### 6.7.1.5 Transverse Solenoid Misalignment

In a similar fashion, the centroid trajectories in 1000 randomly misaligned linacs are presented in Figure 6.25 for a solenoid alignment tolerance of  $\sigma_{x,y,sol} = \pm 0.5$  mm. There

is no error on the BPM or on the alignment of the cavities. The increased sensitivity to misalignment of the solenoids is evident and the beam centroid excursions even reach the aperture in some of the uncorrected cases. The correction routine is well illustrated. The asymmetry of the distribution in vertical steering kicks in the correction procedure is observable, however the dominance of the solenoid largely masks the effect.

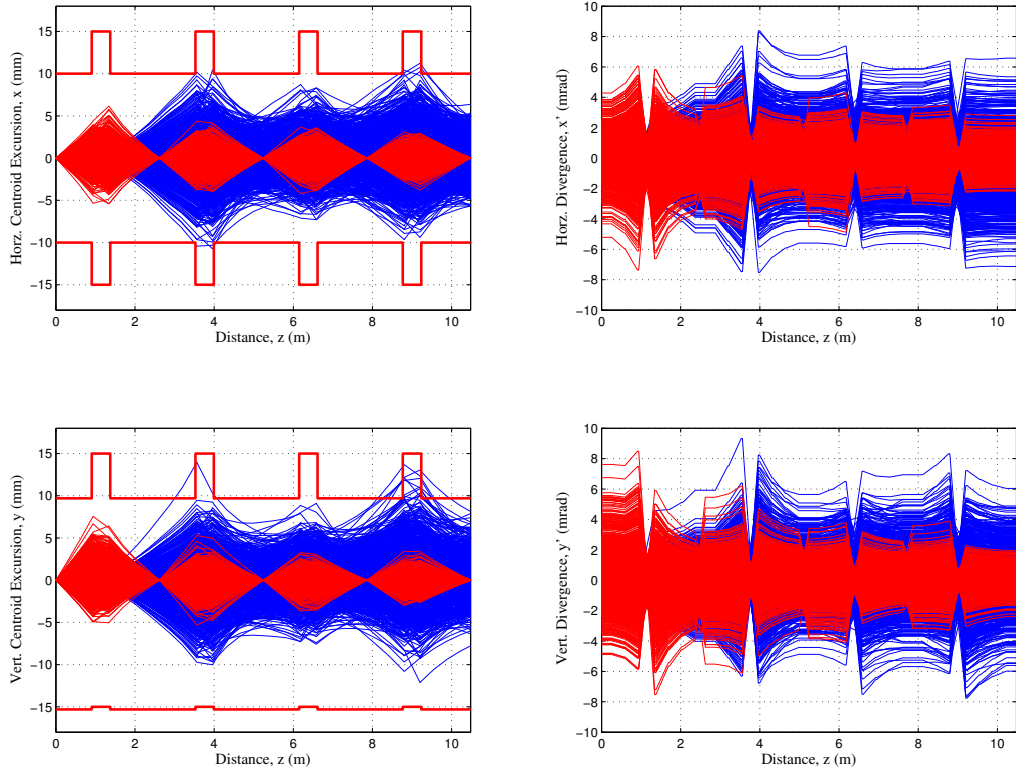


Figure 6.25: The centroid trajectory and divergence for 1000 error seeds with correction, in red, and without correction, in blue for  $\sigma_{x,y,\text{sol}} = \pm 0.5$  mm.

### 6.7.1.6 BPM Error

The precision of the BPM has important implications for the effectiveness of the correction routine. The error in the measurement of the beam position made by the BPM was simulated by superimposing a random error onto the beam position used to calculate the corrector strengths. Therefore,  $\vec{X}_{n+1,\text{BPM}}$  would not be set identically to zero but to  $\Delta\vec{X}_{n+1,\text{BPM}}$ . Hence, the corrector settings can be determined for each error seed as shown,

$$\vec{\Delta}_n = R_{n,\text{cryo}}^{-1}(\Delta\vec{X}_{n+1,\text{BPM}} - \vec{K}_{n,\text{cryo}}) - \vec{X}_{n,\text{BPM}}. \quad (6.7.6)$$

An example of the correction procedure with and without a BPM error of  $\sigma_{x,y,\text{BPM}} = \pm 0.5$  mm is shown in Figure 6.26 for the horizontal plane. The accuracy of the BPM has a significant effect on the efficacy of the correction routine.

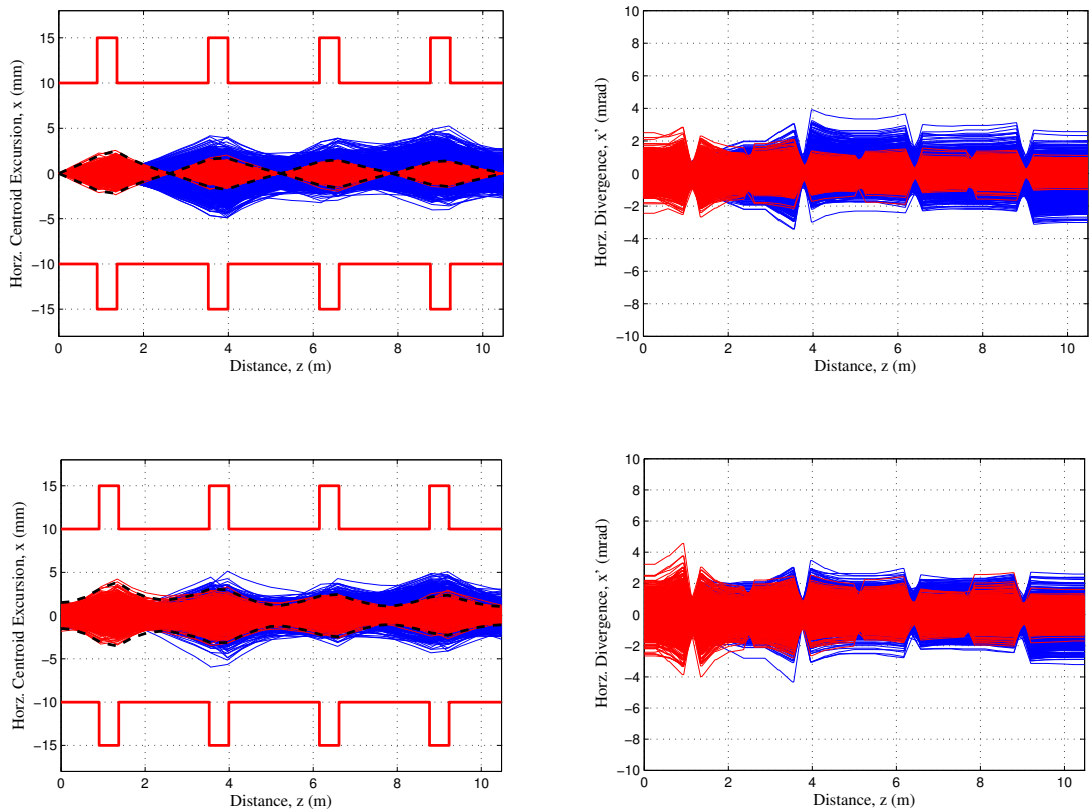


Figure 6.26: The centroid trajectory and divergence in the horizontal plane with (bottom) and without (top) a BPM error of  $\pm 0.5$  mm for  $\sigma_{x,y,\text{cav}} = \pm 0.5$  mm and  $\sigma_{x,y,\text{sol}} = \pm 0.2$  mm. The corrected centroid distribution is shown in red and enveloped at  $\pm 3\sigma$  by the black dashed line. The uncorrected centroid trajectories are shown in blue.

### 6.7.1.7 Transverse Acceptance

The transverse acceptance of the linac is determined by both the physical aperture and the strength of the focusing channel, and is strongly affected by the machine alignment and correction procedure. A stronger focusing channel tightly constrains the beam envelope, but the accompanying strength of the transverse fields increases the sensitivity to misalignment. The misalignment acts to move the beam centroid away from the axis and toward the aperture, which reduces the effective transverse acceptance of the linac. In addition, the probability of emittance degradation increases. Using the statistical approach detailed above, the centroid trajectories in phase space can be used to calculate the loss of

acceptance for a specified set of tolerances, and with an associated likelihood.

Enveloping the rms spatial extent of the centroid trajectories with  $\sigma_c$  one can express the loss in acceptance  $\Delta A/A$  using Equation 3.4.50 that was introduced in Chapter 3. The loss in acceptance is surveyed in Stage 2a operating at a transverse phase advance of  $\pi/2$  per focusing period for different solenoid and cavity misalignments and accuracies on the BPM in Figure 6.27. The acceptances were calculated by truncating the random centroid trajectories at  $\pm 3\sigma_c$ , accounting for roughly 997 error seeds in 1000.

The focusing strength that maximises the acceptance depends on the alignment tolerances of the linac elements. The focusing strength at which the acceptance is maximised was calculated in Stage 2a for different alignment tolerances by comparing the overall beam size to the aperture. This was done by adding the beam envelope to the envelope of possible centroid trajectories parameterised by  $\sigma_c$ . For example, in Stage 2a the beam size in the presence of misalignment is minimised at transverse phase advances of  $55^\circ$ ,  $65^\circ$  and  $85^\circ$  per period for  $\sigma_{x,y,\text{sol}}$  of  $\pm 0.50$  mm,  $\pm 0.25$  mm and  $\pm 0.10$  mm, respectively. In the absence of misalignment the acceptance starts to reduce when the focusing strength becomes very strong because the beam envelope function becomes large and 'spiked' inside the focusing elements, albeit remaining very small in the regions between. As discussed above, a phase advance of  $\pi/2$  or  $90^\circ$  per focusing period is preferred for beam quality concerns and, in order to optimise the acceptance at this focusing strength, the alignment of the solenoids should be achieved to better than  $\sigma_{x,y,\text{sol}} = \pm 0.1$  mm.

The alignment tolerances for the linac were specified such that in the worst case the loss in acceptance will not exceed 25 % (at a certainty of 99.7 %), demanding the tolerances  $\sigma_{x,y,\text{sol}} = \pm 0.15$  mm,  $\sigma_{x,y,\text{cav}} = \pm 0.30$  mm and  $\sigma_{x,y,\text{BPM}} = \pm 0.20$  mm. This can be contrasted to the loss of 20 % of the acceptance used at ISAC II, see [192]. The centroid should remain within 15 % of the aperture, i.e.  $3\sigma_c/R_{\text{ap}} \lesssim 15$  %.

## 6.7.2 Emittance Growth

The matrix model described above does not take into consideration the coupling between the longitudinal and transverse dynamics, which would increase the emittance growth if the beam-steering force is not well compensated or if the non-linearities in the fields of

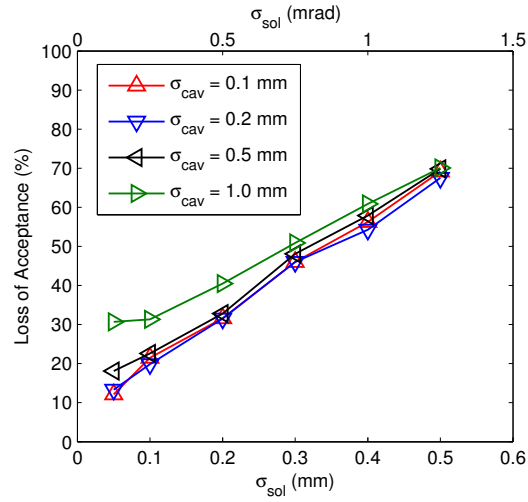
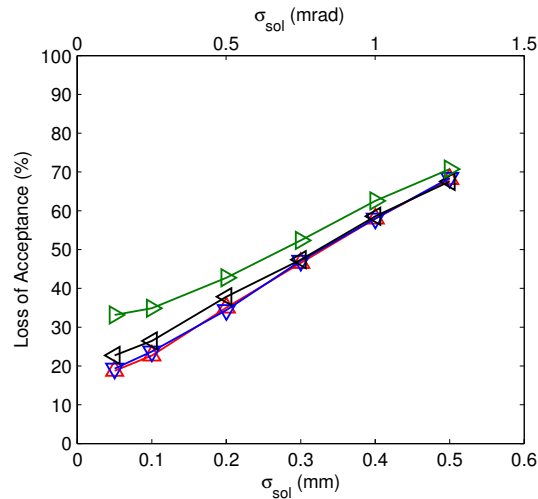
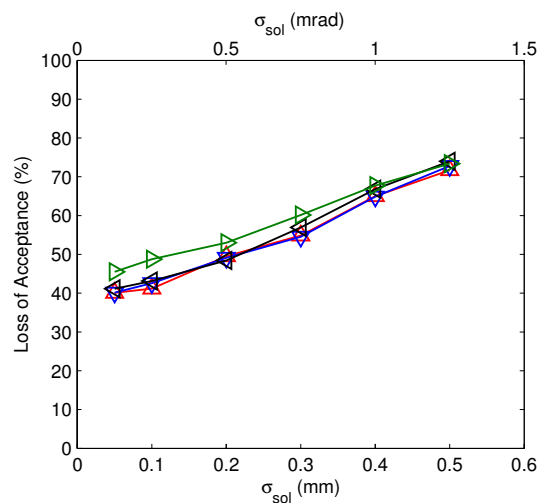
(a)  $\sigma_{x,y,BPM} = \pm 0.1$  mm.(b)  $\sigma_{x,y,BPM} = \pm 0.2$  mm.(c)  $\sigma_{x,y,BPM} = \pm 0.5$  mm.

Figure 6.27: A survey of the loss in acceptance ( $\Delta A/A$ ) in Stage 2a as a function of the solenoid alignment tolerance, for BPM error tolerances in the range  $\pm 0.1 - 0.5$  mm and cavity alignment tolerances in the range  $\pm 0.1 - 1.0$  mm.

the optical elements are significant off-axis. The likelihood of emittance growth caused by misalignment was investigated using the error module in TRACK. An ensemble of 250 error seeds was used with each seed containing 2000 particles in the bunch. The TRACK code uses a uniform probability distribution for transverse misalignment and a Gaussian probability distribution truncated at  $\pm 3\sigma$  for rf phase and amplitude jitter. The rms values are used to compare errors generated with different probability distributions. In the case of an uniform distribution, the maximum value ( $\Sigma$ ) is related to the rms value by,

$$\Sigma = \sqrt{3}\sigma. \quad (6.7.7)$$

The emittance growth relative to the nominal case, with and without orbit correction, for a transverse cavity alignment tolerance of  $\Sigma_{x,y,cav} = \pm 2.0$  mm is shown in Figure 6.28 in the horizontal plane. The growth of the longitudinal emittance, which mainly arises from the radial dependence of the transit-time factor, is an order of magnitude lower than the transverse emittance growth. For some error seeds the transverse emittance was smaller than in the nominal case because a path was found through the cavities that better compensated the beam-steering in the cavities; the beam-steering compensation was not optimised for one particular beam but for all beams inside the  $A/q$  acceptance.

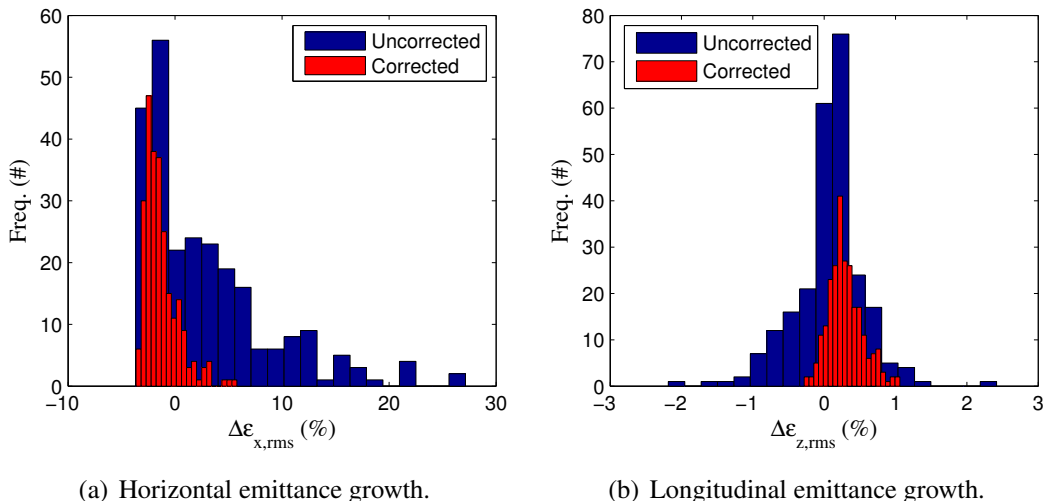


Figure 6.28: The emittance growth from 250 error seeds of the Stage 2a linac with  $\Sigma_{x,y,cav} = \pm 2.0$  mm.

### 6.7.2.1 Cavity: Transverse Misalignment

The probability of transverse emittance growth relative to the nominal case is shown in Figure 6.29, with and without correction using warm steerers. The probability of the emittance growth exceeding 10 % is less than 1 in 100 with correction, for a tolerance as large as  $\Sigma_{x,y,cav} = \pm 2.0$  mm on the exit and entry position of the cavity.

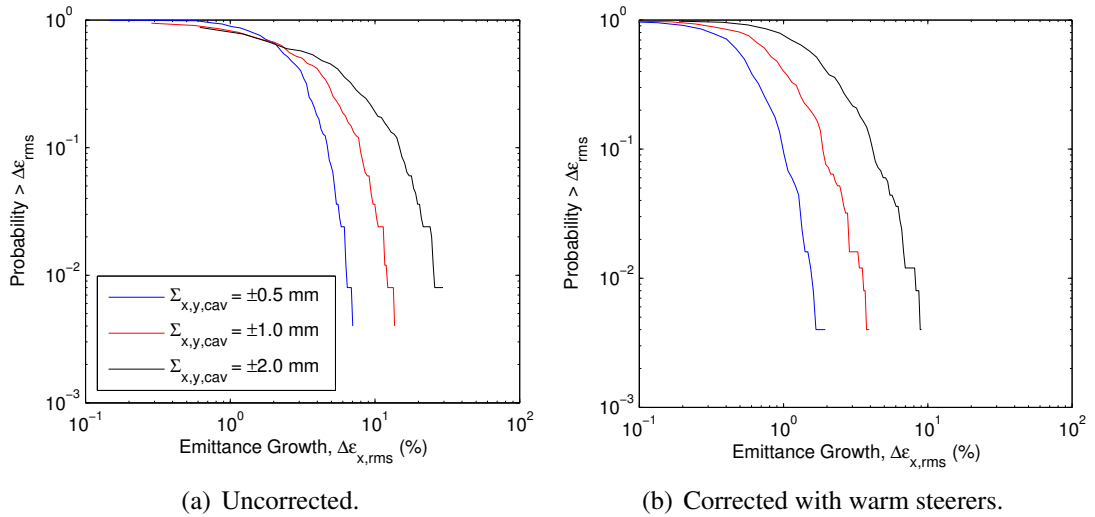


Figure 6.29: The probability of emittance growth in Stage 2a with transverse misalignment of the cavities.

### 6.7.2.2 Cavity: Longitudinal Misalignment

The stability of the longitudinal alignment of the cavities is important to ensure that the linac does not need re-phasing. The most likely cause of changes to the longitudinal

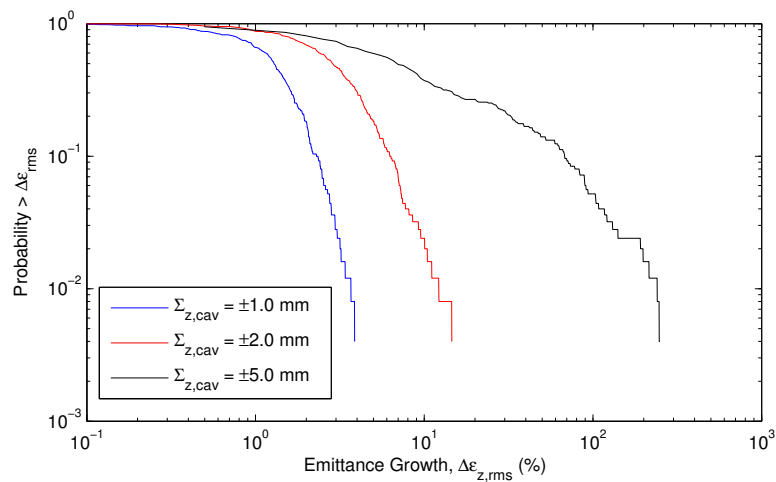


Figure 6.30: The probability of emittance growth in Stage 2a with longitudinal misalignment of the cavities.

position of the cavities will be the mechanical stresses involved in the thermal cycling of the cryomodule during shutdown and maintenance periods. As shown in Figure 6.30, the longitudinal emittance is only significantly affected if the longitudinal position of the cavities cannot be controlled to better than  $\Sigma_{z,\text{cav}} = \pm 2$  mm.

### 6.7.2.3 Solenoid: Transverse Misalignment

The probability of transverse emittance growth relative to the nominal case is shown in Figure 6.31, with and without correction using warm steerers. The probability of the emittance growth exceeding 10 % is less than 1 in 100 with the orbit corrected for a tolerance as large as  $\Sigma_{x,y,\text{sol}} = \pm 0.5$  mm on the exit and entry position of the solenoid.

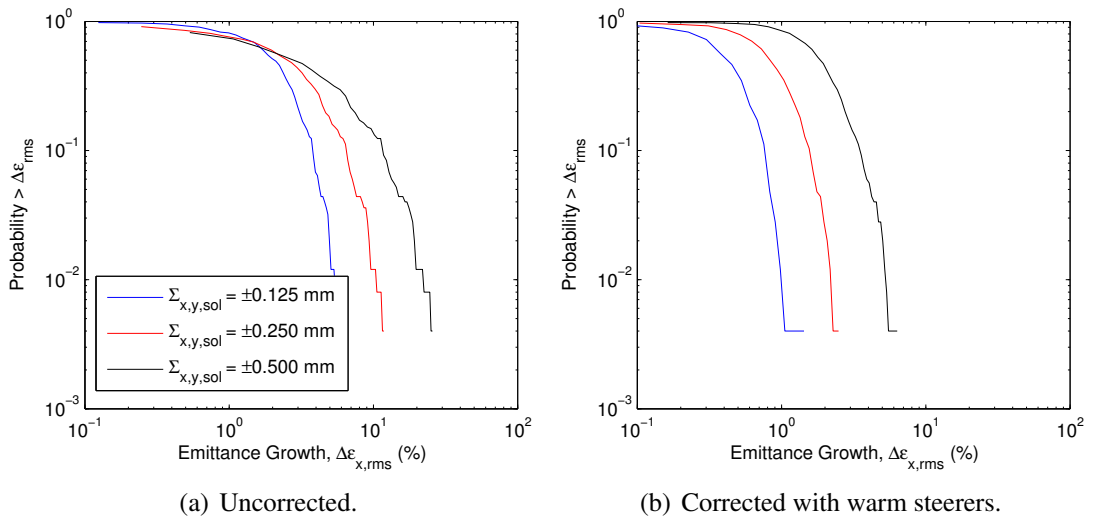


Figure 6.31: The probability of emittance growth in Stage 2a with transverse misalignment of the solenoids.

### 6.7.2.4 RF Jitter

The stability of the rf power sources in independently phased superconducting linacs has already been shown to be one of the most significant causes of effective longitudinal emittance growth, even in linacs with high beam currents that also experience the disruptive effects of beam-induced higher-order cavity modes [193].

The effect of fast jitter of the rf amplitude ( $\sigma_{\Delta V}$ ) and phase ( $\sigma_{\Delta\phi}$ ) of the cavities on the time-averaged longitudinal beam emittance was surveyed using TRACK for beams with  $A/q = 2.5$  and 4.5, as shown in Figure 6.32. At each data point of the contour plot surveys

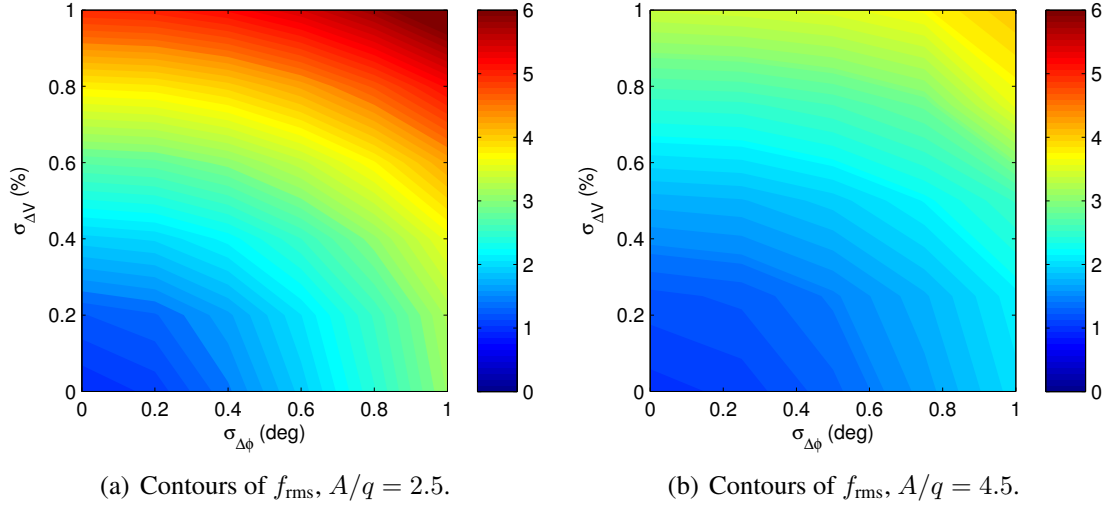


Figure 6.32: The time-averaged longitudinal emittance growth factor ( $f_{\text{rms}}$ ) at output from Stage 2a as a function of the rms voltage ( $\sigma_{\Delta V}$ ) and rms phase ( $\sigma_{\Delta\phi}$ ) stability.

100 error seeds were used with 1000 particles in each, contributing  $10^5$  particles in the time-averaged phase space. The plot shows the factor ( $f_{\text{rms}}$ ) by which the time-averaged rms emittance grows in the presence of jitter, i.e.,

$$f_{\text{rms}} = \frac{\epsilon_{\text{rms,jittered}}}{\epsilon_{\text{rms,nominal}}}. \quad (6.7.8)$$

The sensitivity of the emittance growth to the amplitude and phase stability is approximately equal in units of percent and degrees. The effect of rf instability is strong and has most impact on beams with low  $A/q$ . In order to keep the time-averaged emittance

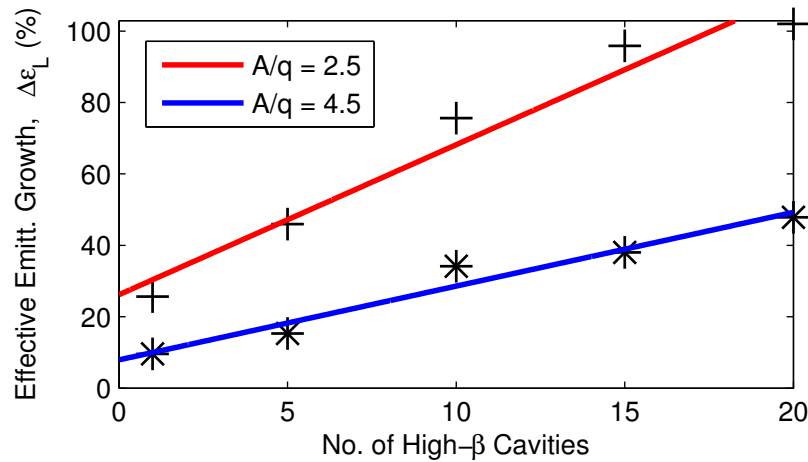


Figure 6.33: The time-averaged rms longitudinal emittance growth in Stage 2a as a function of cavity number for  $\sigma_{\Delta\phi} = \pm 0.33^\circ$  and  $\sigma_{\Delta V} = \pm 0.33\%$ .

growth below 50 % for all beams the rms phase and amplitude stability must be controlled

to better than  $0.2^\circ$  and  $0.2\%$ . The evolution of the time-averaged longitudinal emittance along the linac is closely linear with cavity number as shown in Figure 6.33.

### 6.7.3 Specification of Corrector

The integrated dipole field strength of the corrector magnets was specified from the simulated ensemble of corrector kicks for a given alignment tolerance, which for small angles and in the non-relativistic limit can be expressed as,

$$B_0[\text{T}]L[\text{mm}] = \frac{1}{32} \frac{A}{q} \beta_z[\%] \Delta[\text{mrad}], \quad (6.7.9)$$

where  $L$  is the length of the corrector field and  $\Delta$  is the steering angle. The distribution of the ensemble of corrector kicks was closely Gaussian and for misalignment tolerances resulting in a  $25\%$  loss of acceptance an integrated dipole field strength of  $\pm 4 \text{ T mm}$  is needed to correct the orbit of  $99.7\%$  of error seeds. The specification was validated by comparing the results of both the matrix and TRACK models, see [190]. As the specification is a strong function of the level of misalignment itself, some contingency was built into the design to allow a margin of error if in practice the specified alignment tolerances are not attained. The field quality was investigated by adding higher-order field components to the corrector kicks, with significant emittance growth observed only for sextupole components contributing some  $10\%$  of the field at a radius of  $10 \text{ mm}$ . Nonetheless, the

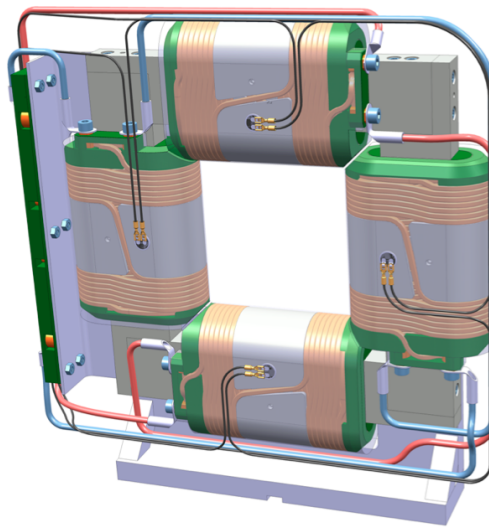


Figure 6.34: The compact warm inter-cryomodule orbit corrector magnet [194].

integrated field homogeneity was more tightly specified at 1 % out to a radius corresponding to 75 % of the mechanical aperture. The design of the compact normal conducting air-cooled steerer magnet based on the above specification is shown in Figure 6.34 and more details of the can be found in [194].

#### 6.7.4 Design of Cryomodule and Alignment System

The beam dynamics study had a strong impact on the design of the high energy cryomodule, which was recently presented in [195], see Figure 6.35. The solenoid is supported on an independently adjustable support that is separate from the cavities to ensure the alignment tolerances can be attained. An optical alignment system based on the Brandeis Camera Angle Monitor (BCAM) system [196] is under development to both align the beam line elements before installation in the cryomodule and to monitor their alignment online through view-ports on the side of the cryomodule.

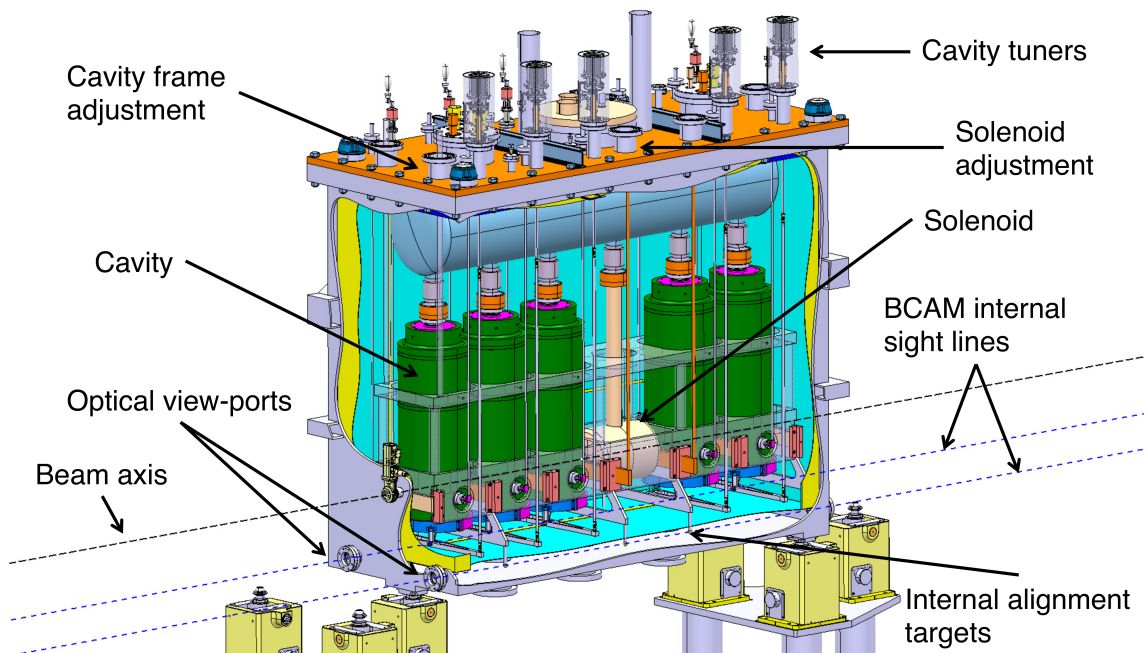


Figure 6.35: The high energy cryomodule [195].

#### 6.7.5 Misalignment in the Low Energy Section

The transverse beam quality is optimised close to a focusing strength corresponding to a phase advance per focusing period of  $\pi/2$  in the low energy section, however operating the

linac with this tune is problematic in the presence of misalignment using a warm correction system situated outside the low energy cryomodule, which contains two focusing periods. The phase advance between the steerer and BPM is close to  $\pi$ , i.e.  $R_{12} \approx R_{34} \approx 0$ , and as a result the response of the beam centroid to the corrector measured at the BPM is strongly suppressed. The linac should be tuned to a lower phase advance in order that a warm correction system located in the diagnostic boxes outside the cryomodule is capable of correcting misalignments. A phase advance of  $70^\circ$  per period was deemed acceptable for accelerating the beam. As was shown for the high energy section, cold steerers placed inside the cryomodule are a better solution to warm steerers and are being investigated, see Figure 6.36.

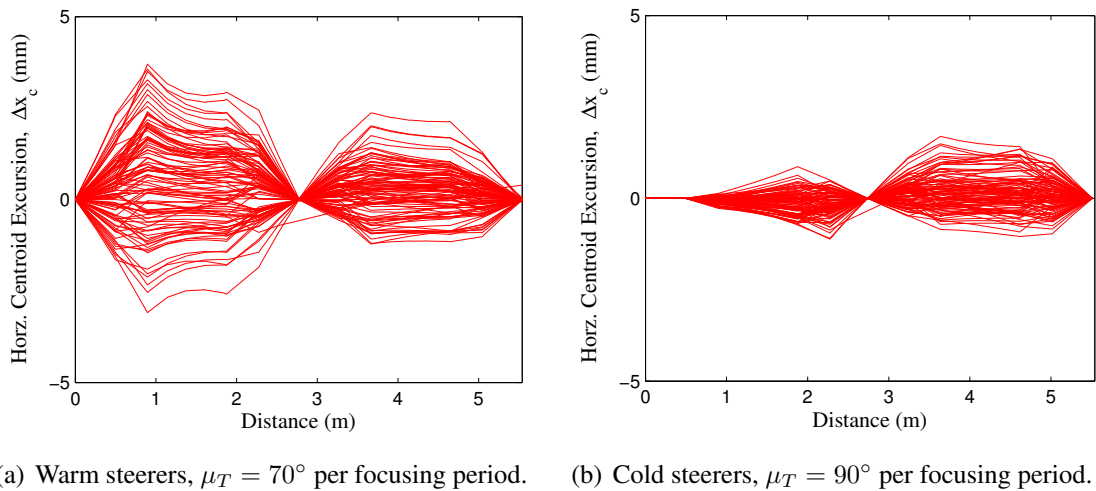


Figure 6.36: Comparison between the centroid excursions with warm and cold steerers in the low energy section for tolerances:  $\sigma_{\text{cav}} = \pm 0.30$  mm and  $\sigma_{\text{sol}} = \pm 0.15$  mm.

### 6.7.6 Summary and End-to-end Beam Dynamics Simulations

End-to-end simulations were carried out for the complete linac in Stage 2b with all the errors discussed above also applied to the low energy section:

- Transverse solenoid misalignment of  $\pm 0.15$  mm ( $\pm\sigma$ , truncated at  $\Sigma = \pm 3\sigma$ ).
- Transverse cavity misalignment of  $\pm 0.30$  mm ( $\pm\sigma$ , truncated at  $\Sigma = \pm 3\sigma$ ).
- Rf jitter of  $\pm 0.2^\circ$  and  $\pm 0.2\%$  ( $\pm\sigma$ , truncated at  $\Sigma = \pm 3\sigma$ ).

The realistic particle distribution was used with a beam of  $A/q = 4.5$  after tracking it through the IHS. Over 9000 particles were simulated in each of 250 error seeds. The focusing strength in the low energy section was relaxed to  $70^\circ$  per period and as a consequence the average transverse emittance growth is 10 % larger than if the focusing strength was kept at  $90^\circ$ . The transverse emittance growth with correction using warm steerers is on average 18 %, with just over 1 % rms variation in the presence of the errors simulated, see Table 6.4. The time-averaged longitudinal emittance in this scenario grows by just 22 %. No particles were lost in any of the 250 runs, even with the orbit correction procedure turned off. A doubling of the error tolerances showed rare cases of particle losses in the absence of orbit correction.

Table 6.4: RMS emittance growth in end-to-end simulations of Stage 2b in the presence of misalignment and rf jitter.

$\Delta\epsilon_{x,\text{rms}}^{\text{nominal}} \pm \langle \Delta\epsilon_{x,\text{rms}} \rangle [\%]$	$\Delta\epsilon_{y,\text{rms}}^{\text{nominal}} \pm \langle \Delta\epsilon_{y,\text{rms}} \rangle [\%]$	$\langle \Delta\epsilon_{z,\text{rms}} \rangle_{\text{time avg.}} [\%]$
$15.8 \pm 1.4$	$20.5 \pm 1.3$	21.6

## 6.8 Deceleration in Low Energy Section

Presently, beam energies in the range 0.3 - 1.2 MeV/ $u$  cannot be delivered to experiments because of the fixed velocity profile of the IHS. Although the IHS was originally designed with flexibility in its output energy, from 1.2 - 1.1 MeV/ $u$ , which would permit further deceleration in the 7G1 down to 0.8 MeV/ $u$ , manufacturing problems of its drift-tubes, previously discussed in Chapter 4.3, prevented the tilting of the gap voltage profile and variability in its output energy.

The low energy section of the superconducting linac could be used to decelerate beams after the IHS into an energy range never previously available at ISOLDE, which has particular relevance for the investigation of certain nuclear astrophysics reactions that demand beam energies close to 0.5 MeV/ $u$ , see e.g. [8, 22]. The geometric velocity of the low- $\beta$  cavity was chosen primarily to ensure efficient and cost-effective acceleration; however, the flexibility of the quarter-wave resonator permits deceleration to low energies. The main challenge of providing decelerated beams with good quality and transmission is

the increased strength of the rf (de)focusing and beam-steering forces below the geometric velocity of the quarter-wave resonators in a lattice designed nominally for acceleration. The formalism used to calculate the energy change and stable synchronous phase in cavities at low velocity is discussed and compared to numerical techniques. The attainable beam energy and expected beam quality are presented along with the foreseen limitations.

### 6.8.1 Characteristics of Deceleration Below $\beta_g$

From the second-order analytic expression for the energy change in an accelerating cavity,

$$\Delta W = qV_0 T(\beta) \cos \phi + \frac{(qV_0)^2}{W} (T^{(2)}(\beta) + T_s^{(2)}(\beta) \sin 2\phi), \quad (6.8.1)$$

which takes into account the changing beam velocity inside a cavity and was discussed in Chapter 3.3.4, one can discern a few characteristics of the longitudinal beam dynamics when decelerating in a linac composed of short and independently phased resonators. For reference, see the transit-time factors of the low- $\beta$  cavity presented in Figure 3.6:

- All three transit-time factors  $T$ ,  $T^{(2)}$  and  $T_s^{(2)}$  are positive in the velocity range  $\beta_g/2 < \beta < \beta_g$ .
- In this velocity range the rate of deceleration and the effective potential available for deceleration is reduced with respect to the first-order expression in the phase-stable region of  $-\pi < \phi < -\pi/2$ .
- It is possible to decelerate through the zero of  $T$ .
- The phase dependence of the energy gain is not sinusoidal at low velocity and the extrema of  $\Delta W$  versus  $\phi$  vary significantly from first-order estimates.

### 6.8.2 Limitations of Analytic Calculations

As was discussed in Chapter 3, simple analytic expressions for the second-order transit-time factors can be derived by assuming that the accelerating field is constant in the gaps and has the form of a square-wave. In terms of  $T(\beta)$ , which was given in Equation 3.3.26,

they can be expressed,

$$T^{(2)}(\beta) = -\frac{T(\beta)}{4} \left[ \cos \frac{\pi g}{\beta \lambda} \sin \frac{\pi \beta_g}{2\beta} + \frac{\beta_g \lambda}{2g} \sin \frac{\pi g}{\beta \lambda} \cos \frac{\pi \beta_g}{2\beta} - T(\beta) \right], \quad (6.8.2)$$

and,

$$T_s^{(2)}(\beta) = \frac{\pi \beta_g}{16\beta \sin^2 \frac{\pi \beta_g}{2\beta}} T^2(\beta) + \frac{\beta \lambda}{16\pi g} \cos \frac{\pi \beta_g}{\beta} \left[ \frac{T(2\beta)}{\sin \frac{\pi \beta_g}{4\beta}} - 1 \right]. \quad (6.8.3)$$

The validity of the analytic approximation at low velocity was investigated. The differences between the transit-time factors of the low- $\beta$  cavity produced using the realistic field profile and those produced with the analytic square-wave field are compared in Figure 6.37.

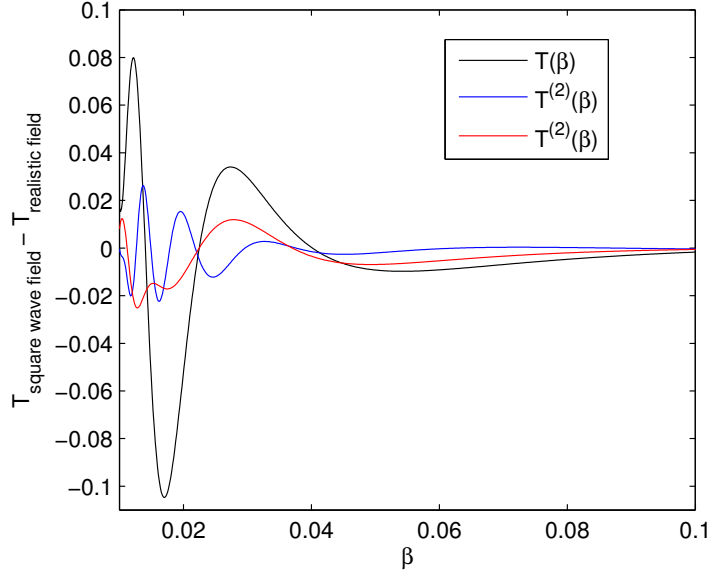


Figure 6.37: Difference between transit-time factors of the low- $\beta$  cavity calculated using the realistic field profile and the square-wave approximation.

For  $\beta \gg \beta_g$  the square-wave field approximates very well the realistic field and the difference is negligible. The second-order transit-time factors are well described by the analytic expressions derived using the square-wave approximation and it is the first-order transit-time factor that is most sensitive to the shape of the field at low velocity. Therefore, it is the first-order transit-time factor that limits the use of the square-wave analytic approximation for accurate calculations of the energy change in the low- $\beta$  cavity below its geometric velocity. The second-order approximation can be effectively applied if the realistic field profile is used to generate the transit-time factors and is accurate to a few per-

cent down to  $\beta_g/3$ , below which higher-order approximations or numerical calculations are required. All transit-time factors used in the following calculations were calculated numerically with the realistic field profile.

### 6.8.3 Phasing the Cavities

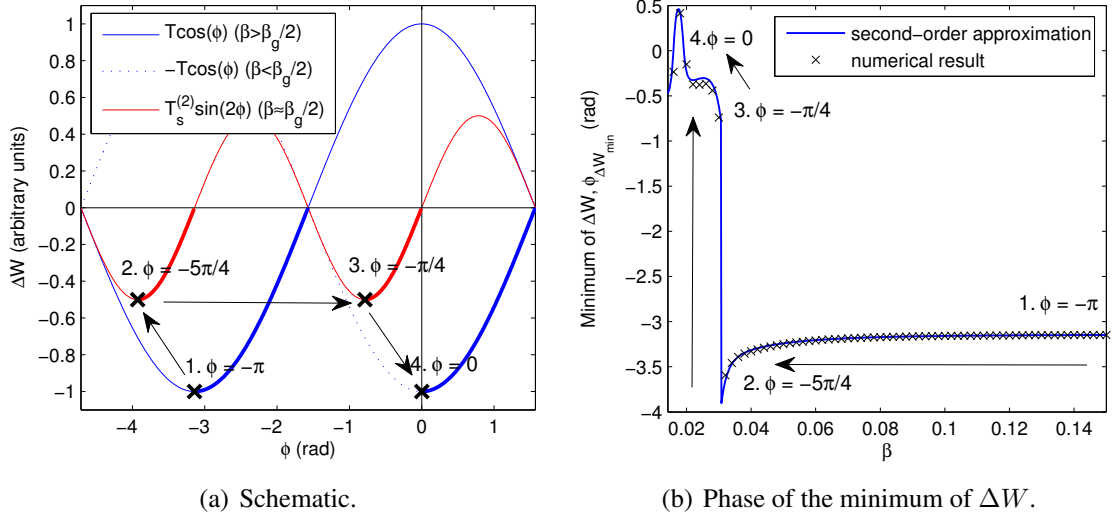
Phase-stable deceleration through the zero of the first-order transit-time factor is possible by smoothly varying the synchronous phase from the within the range  $-\pi < \phi < -\pi/2$  to the range  $-5\pi/4 < \phi < -\pi$  as the  $\sin 2\phi$  term dominates close to  $\beta_g/2$ , requiring a phase shift of  $\pi/2$ . The phase must then be switched rapidly by  $\pi$  into the range  $-\pi/2 < \phi < 0$  and eventually into the range  $0 < \phi < \pi/2$  as the sign of the first-order transit-time factor switches and starts to dominate again below  $\beta_g/2$ . The above listed regions of phase stability that are compatible with deceleration are shown in bold in Figure 6.38(a) and the shifting phase of the minimum of the energy gain shown in Figure 6.38(b). The shift in phase required to maintain the longitudinal phase stability of the beam can be described analytically by calculating the extrema of the second-order approximation for the energy gain; setting its derivative with respect to  $\phi$  to zero,

$$\left. \frac{\partial W}{\partial \phi} \right|_{\phi=\phi_{\Delta W_{\min}}} = -q\Delta V_0 T(\beta) \sin \phi_{\Delta W_{\min}} + \frac{2(q\Delta V_0)^2}{W} T_s^{(2)}(\beta) \cos 2\phi_{\Delta W_{\min}} = 0, \quad (6.8.4)$$

one can write the phase at which the energy gain is minimised as,

$$\phi_{\Delta W_{\min}}(\beta) = \arcsin \left( \frac{\pm \sqrt{1 + 32 \left( \frac{q\Delta V_0}{W} \right)^2 \left( \frac{T_s^{(2)}(\beta)}{T(\beta)} \right)^2 - 1}}{8 \left( \frac{q\Delta V_0}{W} \right) \frac{T_s^{(2)}(\beta)}{T(\beta)}} \right), \quad (6.8.5)$$

where the root should be chosen depending on the velocity of the particle. The phase of the minimum in the second-order approximation is compared to numerical calculations in Figure 6.38(b), alongside a schematic illustrating the phase shifts. The phase independent term of the second-order approximation is neglected in the schematic of Figure 6.38(a). An analytic understanding of the phase dependence of the energy gain at low velocity is important for maintaining the phase stability of the beam.

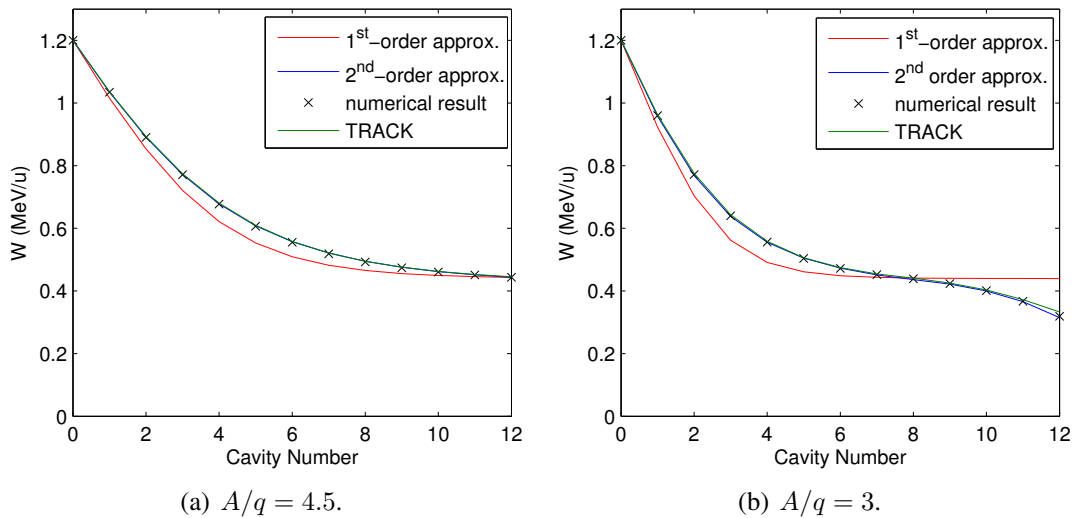

 Figure 6.38: Phasing the low- $\beta$  cavity for deceleration ( $A/q = 4.5$  and  $E_0 = 6$  MV/m).

### 6.8.4 Achievable Energies

The heaviest beams with  $A/q = 4.5$  can be decelerated down to 0.45 MeV/u, close to the zero of  $T$ , at a synchronous phase with respect to the minimum of the energy gain of  $\phi_s = +20^\circ$ , where,

$$\phi(\beta) = \phi_{\Delta W_{\min}}(\beta) + \phi_s, \quad (6.8.6)$$

which is equivalent to  $-160^\circ$  in the first-order approximation. The deceleration in this case is limited by the number of low- $\beta$  cavities. In principle, lighter beams can be decelerated though the zero of  $T$  to close the gap in energy between 1.2 MeV/u and 0.3


 Figure 6.39: Deceleration in the low energy section ( $E_{\text{acc}} = 6$  MV/m and  $\phi_s = +20^\circ$ ).

MeV/ $u$ , however severe deterioration of the beam quality is expected as the zero of  $T$  is traversed. The 12 superconducting low- $\beta$  cavities provide an effective deceleration potential of 3.4 MV for  $A/q = 4.5$  and 3.0 MV for  $A/q = 3$ , as opposed to 10.8 MV for acceleration. The beam energy after each cavity is shown in Figure 6.39 using the first and second-order approximations with a comparison made to the numerical result and the TRACK code for two beams with  $A/q = 4.5$  and 3.

TRACK is programmed to set the synchronous phase with respect to the maximum of the energy gain, not the minimum, and so a routine was written using the second-order result in Equation 6.8.5 to adjust the input synchronous phases relative to  $\phi_{\Delta W_{\min}}$ . The phase dependence of the energy gain in the cavities is shown explicitly in Figures 6.40 and 6.41 for decelerating beams with  $A/q = 4.5$  and 3, respectively. The linear regions become much smaller as the velocity tends towards  $\beta_g/2$ , which is the limiting factor for the longitudinal beam quality when decelerating. The final subplot in each figure shows an expanded scale highlighting the reliability of the second-order approximation, even at low velocity.

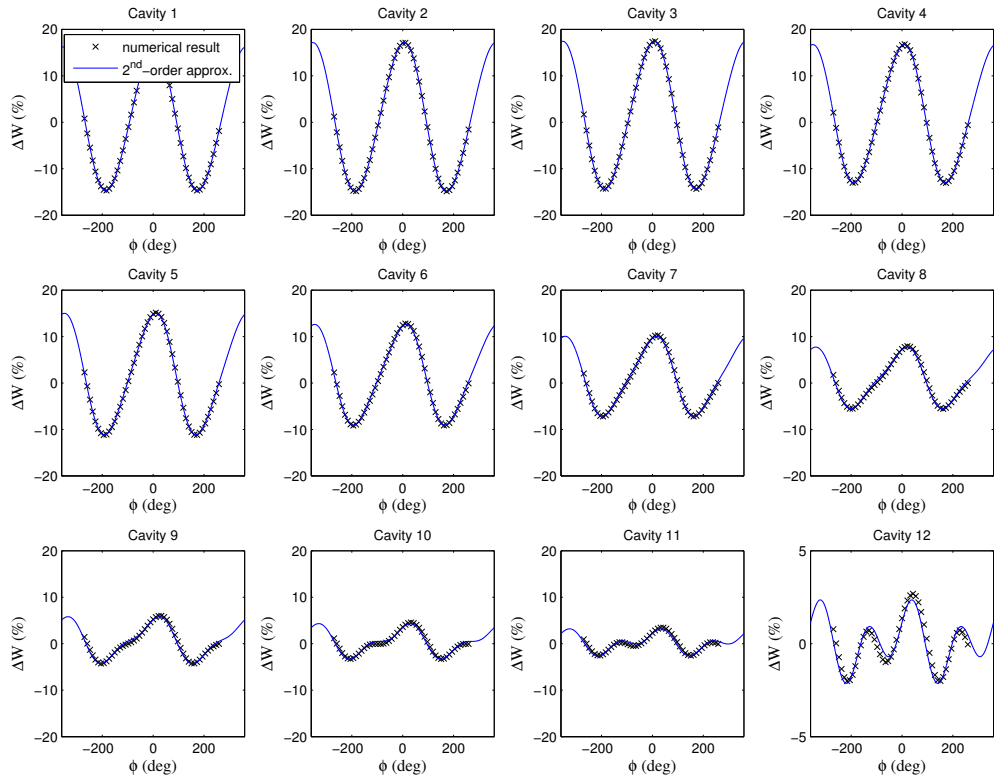


Figure 6.40:  $\Delta W$  vs.  $\phi$  in the low energy section for deceleration with  $A/q = 4.5$ .

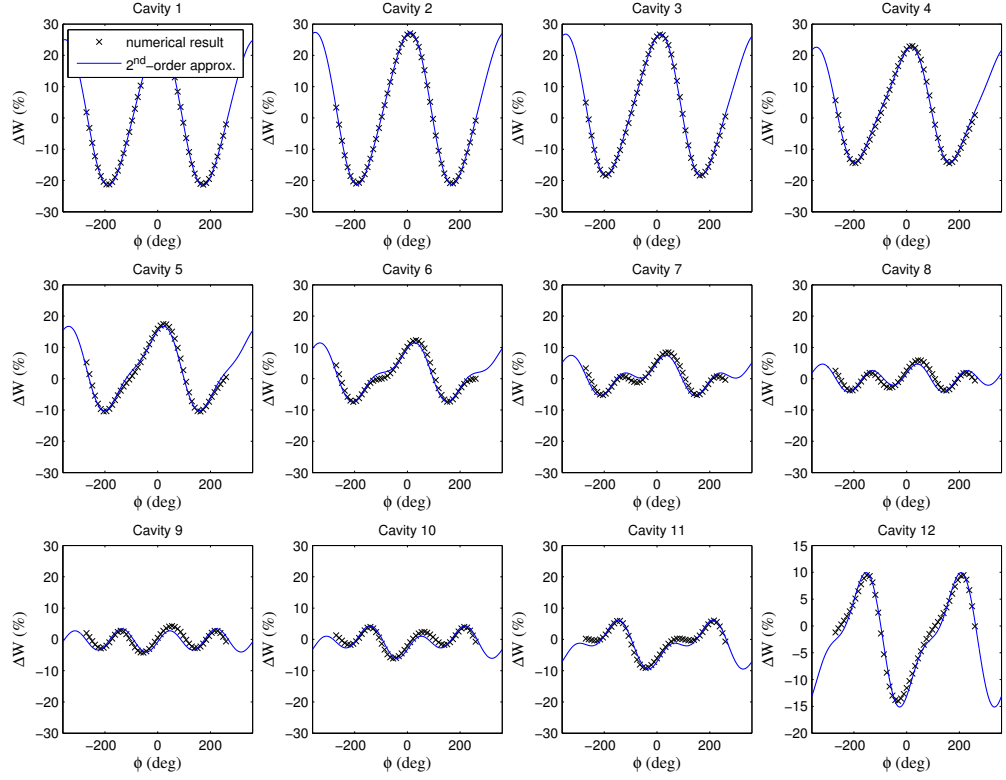


Figure 6.41:  $\Delta W$  vs.  $\phi$  in the low energy section for deceleration with  $A/q = 3$ .

### 6.8.5 Beam-steering Effects at Low Velocity

The analytic expression for the beam-steering,

$$\Delta y'_{\text{steering}} = \frac{qE_0 L_a T(\beta)}{A\gamma u c} \left[ \underbrace{\frac{\kappa_B(y_0)}{\beta}}_{\text{magnetic}} - \underbrace{\frac{\kappa_E(y_0)}{c\beta^2} \cot \frac{\pi\beta_g}{2\beta}}_{\text{electric}} - \underbrace{\delta \frac{\pi}{\lambda} \frac{1}{c\gamma^2 \beta^3}}_{\text{rf (de)focusing}} \right] \sin \phi_s, \quad (6.8.7)$$

is invariant under the phase shift introduced to decelerate because,

$$\sin(\pi - \phi_s) = \sin \phi_s, \quad (6.8.8)$$

and,

$$\Delta y'_{\text{steering}}(\phi_s) = \Delta y'_{\text{steering}}(\pi - \phi_s). \quad (6.8.9)$$

Therefore, one would expect the beam-steering to be well compensated during deceleration. However, the expression is only valid when the change in velocity inside the cavity is

small, which is not the case at low velocity. Numerical calculations of the beam-steering are shown in Figure 6.42 with the synchronous phase set at  $\pm 20^\circ$  with respect to  $\phi_{\Delta W_{\max}}$  and  $\phi_{\Delta W_{\min}}$  in the accelerating and decelerating cases, respectively. The beam-steering calculated numerically for acceleration, labelled  $\phi_s = -20^\circ$ , and for deceleration, labelled  $-160^\circ$ , is compared to the analytic result, which is invariant under the shift in the synchronous phase. The symmetry of the analytic result is broken at low velocity but

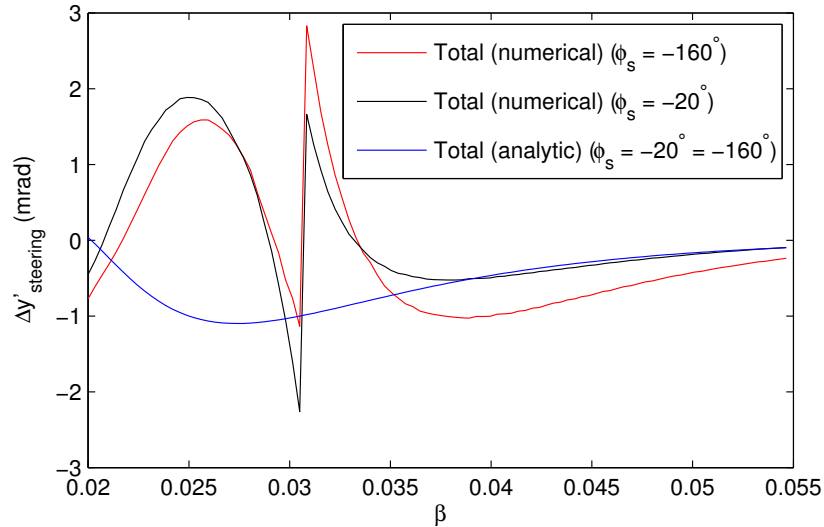


Figure 6.42: Beam-steering in the low energy section ( $\beta_g = 0.063$ ) phased to decelerate ( $A/q = 4.5$  and  $\delta = 0.6$  mm).

the steering behaves in a similar fashion whether accelerating or decelerating. The beam-steering becomes very large as  $\beta \rightarrow \beta_g/2$  because of the steering contribution from the electric dipole component, which adds in each gap and limits the transverse beam quality on decelerating through the zero of  $T$ , especially for lighter beams.

The optimisation of the beam-steering compensation offset ( $\delta$ ) for acceleration does not significantly hinder the beam quality when the linac is operated as a decelerator; the two are compatible.

### 6.8.6 Beam Characteristics after Deceleration

The phase and effective voltage of each accelerating gap was calculated numerically and implemented into a TRACE 3-D model to tune the solenoids. The TRACE 3-D model is only effective down to velocities just above  $\beta_g/2$  because at low velocity the cavities cannot be modelled by thin accelerating gaps. Nonetheless, drastic deterioration in the

beam quality was observed on decelerating through  $\beta_g/2$ , which limits the energy of decelerated beams to 0.45 MeV/u. The deterioration arises from the strength of the beam-steering at  $\beta_g/2$  and the non-linearity of the energy gain as a function of phase. The velocity of the beam is too low to use the high- $\beta$  cavities to keep the beam bunched at 101.28 MHz through the high energy section. If the bunch spacing was increased to 100 ns, a dedicated low energy rebuncher operating at a harmonic of 10 MHz could be used to keep the micro-bunch structure to the experiments. Error studies were also carried out with the tolerances specified for the nominal case and no significant problems were observed.

## 6.9 Summary of Beam Parameters

The beam parameters from realistic field TRACK simulations of the superconducting linac are presented here at the output of the last cryomodule at 5.9 MeV/u for Stage 1, and at 0.45 MeV/u and 10 MeV/u for Stage 2b. The realistic particle distribution from the RFQ was used and initially either tracked through the realistic fields of the IHS or through a LANA model of REX with  $A/q = 4.5$  and without the imperfections discussed in Chapter 6.7. The input parameters can be found in Tables 4.1, 4.2 and 4.3, which are consistent with a 90 % normalised transverse emittance of  $0.3 \pi$  mm mrad and the measured longitudinal emittance. The beam parameters at the exit to the linac are summarised in Tables 6.5, 6.6 and 6.7.

Table 6.5: Summary of the simulated horizontal HIE beam parameters<sup>a</sup>

Stage	Simulation Code	Energy [MeV/u]	$\tilde{\alpha}_x$	$\tilde{\beta}_x$ [mm/mrad]	$\epsilon_{x \text{ rms}}^{\text{geom}}$ [ $\pi$ mm mrad]	$\epsilon_{x \text{ rms}}^{\text{geom}}$ [ $\pi$ mm mrad]	$\epsilon_{x \text{ rms}}^{\text{norm}}$ [ $\pi$ mm mrad]	$\epsilon_{x \text{ rms}}^{\text{norm}}$ [ $\pi$ mm mrad]
Stage 1	TRACK	5.9	0.27	1.00	0.81	3.95	0.09	0.45
Stage 2b	TRACK	10.2	0.30	1.55	0.60	3.14	0.09	0.46
Stage 2b	TRACK	0.45	-0.32	0.51	3.40	20.2	0.11	0.62

Table 6.6: Summary of the simulated vertical HIE beam parameters<sup>a</sup>

Stage	Simulation Code	Energy [MeV/u]	$\tilde{\alpha}_y$	$\tilde{\beta}_y$ [mm/mrad]	$\epsilon_{y \text{ rms}}^{\text{geom}}$ [ $\pi$ mm mrad]	$\epsilon_{y \text{ rms}}^{\text{geom}}$ [ $\pi$ mm mrad]	$\epsilon_{y \text{ rms}}^{\text{norm}}$ [ $\pi$ mm mrad]	$\epsilon_{y \text{ rms}}^{\text{norm}}$ [ $\pi$ mm mrad]
Stage 1	TRACK	5.9	-0.04	1.03	0.80	3.68	0.09	0.42
Stage 2b	TRACK	10.2	0.00	1.21	0.60	3.16	0.09	0.47
Stage 2b	TRACK	0.45	-0.37	0.80	3.56	19.6	0.11	0.61

Table 6.7: Summary of the simulated longitudinal HIE beam parameters<sup>a</sup>

Stage	Simulation Code	Energy [MeV/u]	$\tilde{\alpha}_z$	$\tilde{\beta}_z$ [ns/(keV/u)]	$\tilde{\beta}_z$ [ $^\circ/\%$ ] <sup>b</sup>	$\epsilon_{z \text{ rms}}$ [ $\pi$ ns keV/u]			
Stage 1	TRACK	5.9	-0.49	0.004	8.7	0.58	3.8	0.36	2.34
Stage 2b	TRACK	10.2	0.88	0.003	12.0	0.30	2.12	0.11	0.76
Stage 2b	TRACK	0.45	11.9	14.9	2450	0.35	2.60	2.84	21.1

<sup>a</sup> The input files to all the simulation codes can be found on the CERN Engineering and Equipment Data Management Service (EDMS) under the HIE-ISOLDE project.

<sup>b</sup> At 101.28 MHz.

### 6.9.1 Stage 1: 5.9 MeV/u

The non-linearity in the longitudinal phase space, which is introduced by the 9GP, noticeably increases the energy spread of the beam at output, see Figure 6.43. The energy spread at output is  $\pm 0.6\%$  ( $\approx \pm\sqrt{6}\sigma$ , where  $\text{FWHM} \approx \sqrt{6}\sigma$ ). The 95% longitudinal emittance is approximately  $4\pi$  ns keV/u but the normalised transverse emittance remains largely unaffected.

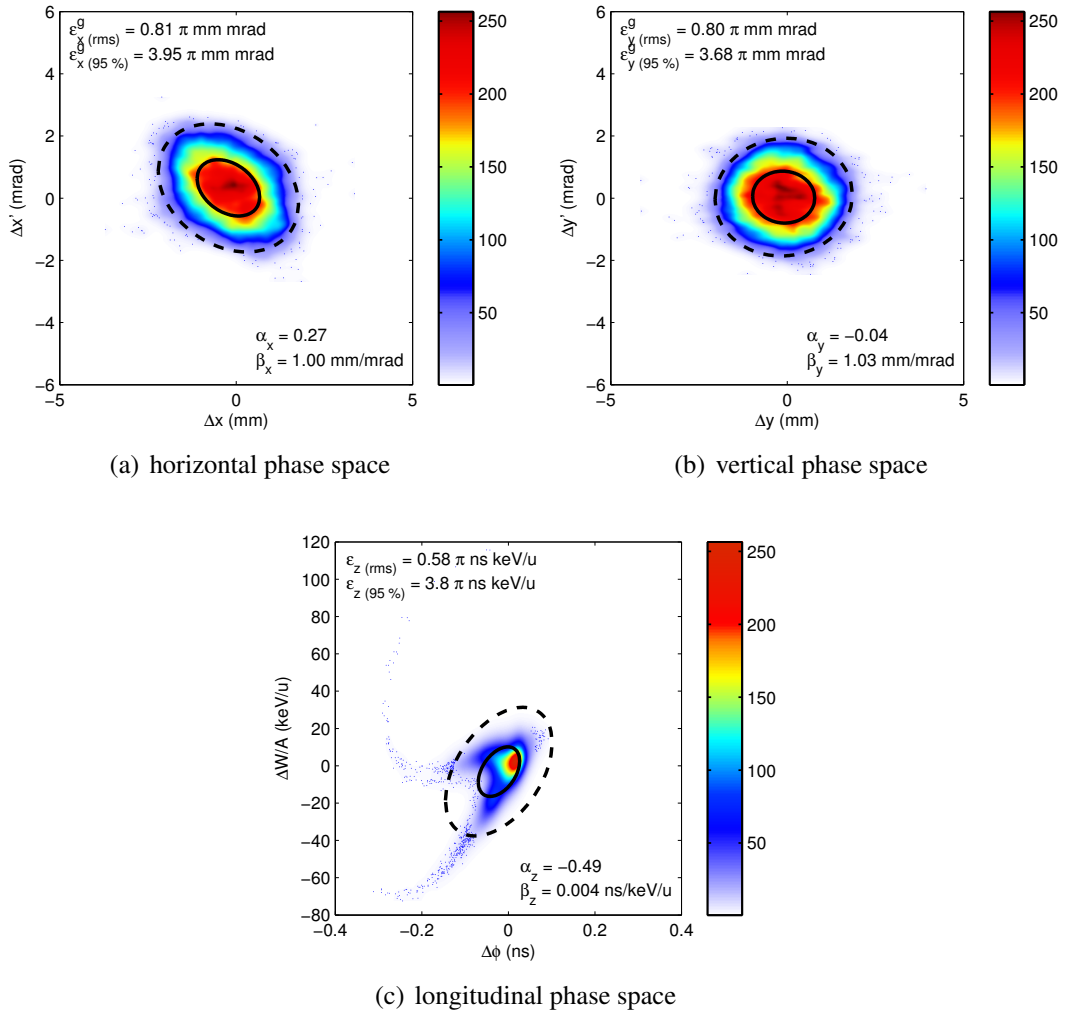


Figure 6.43: Beam phase space distribution at exit to the second high energy cryomodule in Stage 1 at 5.9 MeV/u, simulated with TRACK ( $A/q = 4.5$ ).

### 6.9.2 Stage 2b: 10.2 MeV/u

The installation of the low energy superconducting section significantly reduces the tails of the longitudinal phase space distribution and the energy spread at output can be expected as  $\pm 0.3\%$  ( $\approx \pm\sqrt{6}\sigma$ ), see Figure 6.44. The 95% longitudinal emittance is approximately  $2\pi$  ns keV/u.

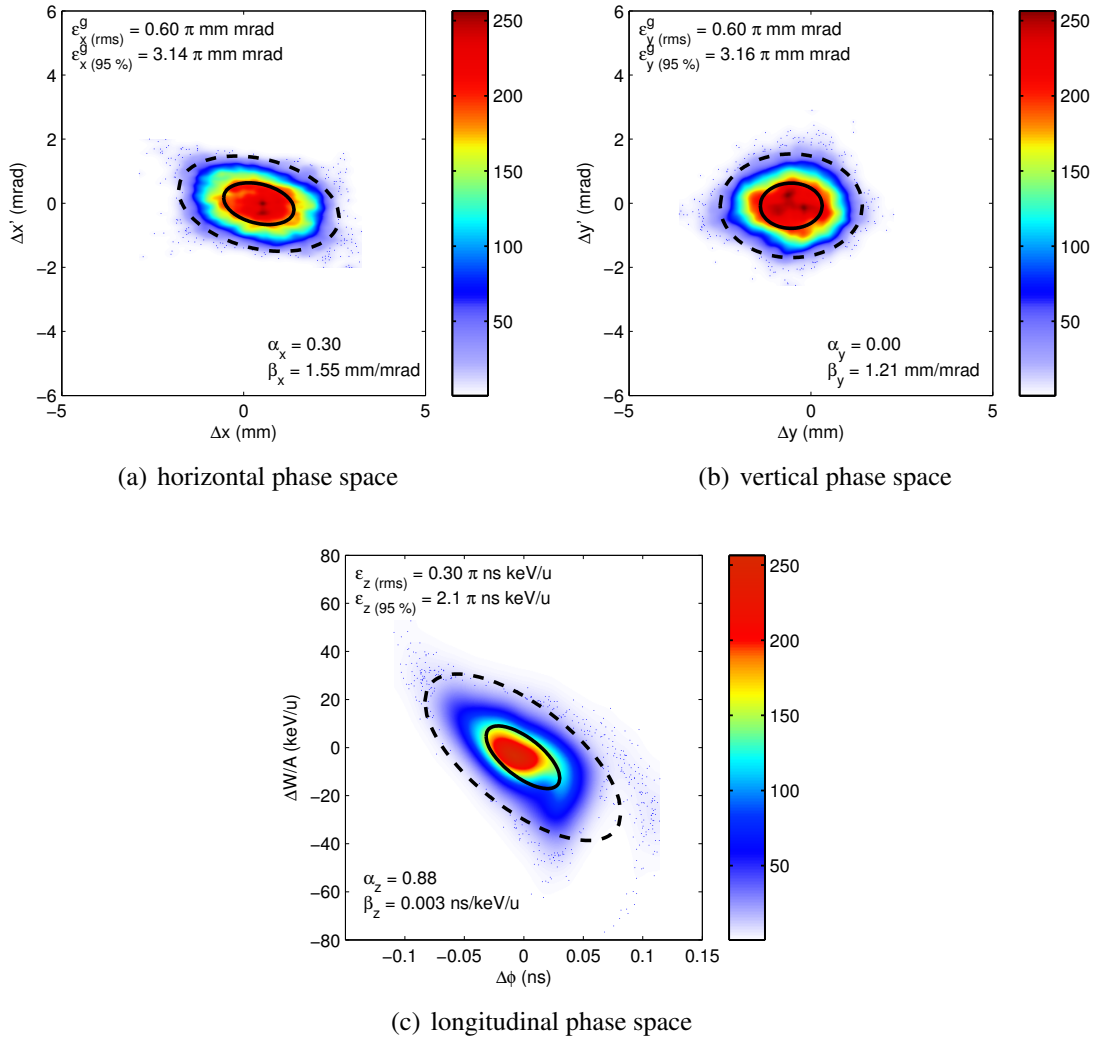


Figure 6.44: Beam phase space distribution at exit to the final high energy cryomodule in Stage 2b at 10.2 MeV/u, simulated with TRACK ( $A/q = 4.5$ ).

### 6.9.3 Stage 2b: 0.45 MeV/u

The energy spread at output will be close to  $\pm 1.1\%$  ( $\approx \pm\sqrt{6}\sigma$ ) and bunches at 101.28 MHz will have started to coalesce, see Figure 6.45. There is significant growth in the geometric transverse emittance.

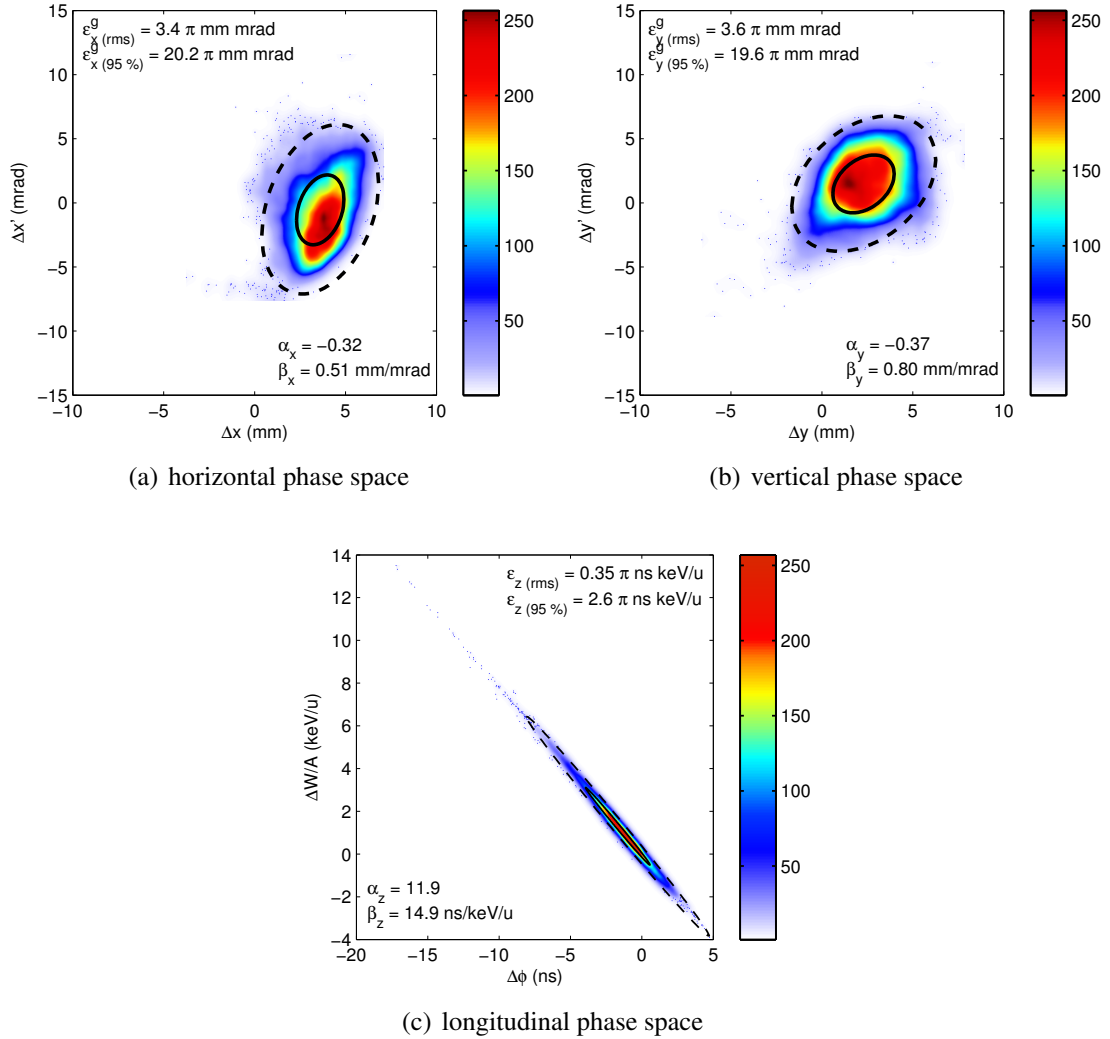
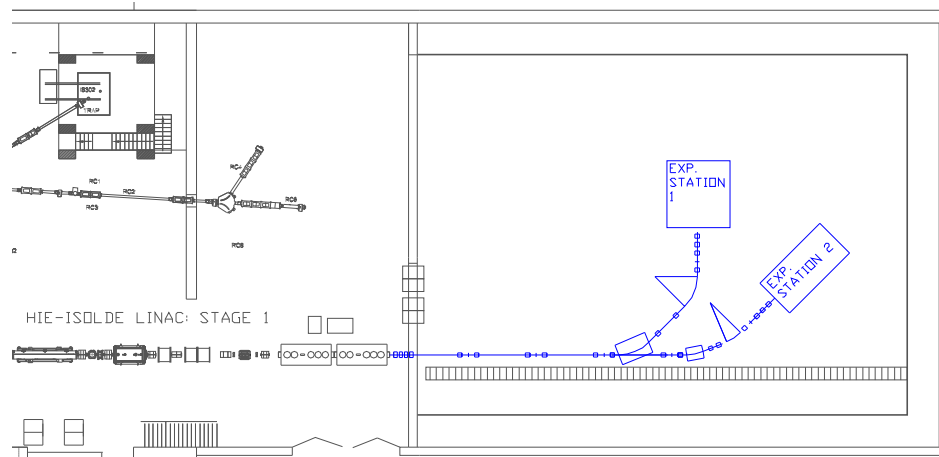


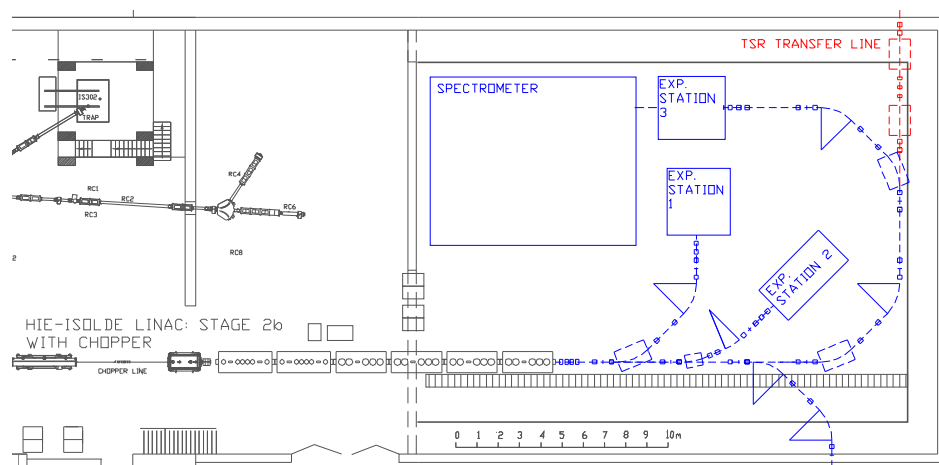
Figure 6.45: Beam phase space distribution at exit to the final high energy cryomodule in Stage 2b at 0.45 MeV/u, with the low energy section phased to decelerate, simulated with TRACK ( $A/q = 4.5$ ).

## 6.9.4 HEBT

A preliminary outline of the HEBT for Stage 1 and 2b is presented in Figures 6.46(a) and 6.46(b). TRACE 3-D solutions of the HEBT can be found in Appendix I. The proposed transfer line to a storage ring located in a second floor extension to the hall is also shown in red. Further details of the technical design of the storage ring can be found in [197]. The HEBT will need to transfer beams to up to four experimental stations over



(a) HEBT for Stage 1.



(b) HEBT for Stage 2b.

Figure 6.46: HEBT layout in the extension of the ISOLDE experimental hall.

a wide range of energies from 0.45 MeV/ $u$  to 10 MeV/ $u$ , which equates to a maximum beam rigidity of 2 Tm for  $A/q = 4.5$ . The HEBT is composed of a periodic quasi-FODO structure that can be removed in a modular fashion as cryomodules are added to the upgrade, leaving the double bend achromat sections that transfer the beam to the experiments in fixed positions. Note that before Stage 2b, a third and fourth high energy cryomodule will be installed. Experiment Stations 1 and 2, which are expected to house

respectively the Miniball and HELIOS experiments, will accompany the first stages of the upgrade. The U-bend along the back wall to Experiment Station 3 and a spectrometer will be added with the final stage. In addition, the option to transfer the beam into an extension of the experimental hall where the car park currently resides is available before the U-bend. A phase advance of  $\pi/2$  results in quadrupole gradients of 11.1 T/m at 10 MeV/ $u$  with quadrupoles of an effective length of 200 mm. The gradients do not exceed this value at any point in the double bend achromats except for in the matching section. The beam optics calculations show that all beams can be kept inside an aperture with a radius of 10 mm, and an aperture diameter of 40 mm is specified for the quadrupoles.

Only the beam parameters at Experiment Stations 1 and 2 are discussed here. The beam spot size and divergence are compatible with those requested at 5.5 and 10 MeV/ $u$ , however the specification for the spectrometer is not attainable with the input emittance that was assumed. The growth in the geometric emittance caused by deceleration will also make meeting the Miniball specification at 0.45 MeV/ $u$  challenging. It should be commented that the upgrade is not the limiting factor but rather it is the transverse emittance developed in the ion source and REX front-end that limits the geometrical beam parameters at the experiments. The energy spread at the linac exit is somewhat higher than the  $\pm 0.1\%$  requested by the users, however the longitudinal emittance is compatible with the users' request and a rebuncher could be used in the HEBT to suitably reduce the energy spread and bunch length at the experiments.

During the first stages of the upgrade the longitudinal beam properties will be limited by the non-linearities introduced by the 9GP cavity. Without a rebuncher the bunch length at Experiment Stations 1 and 2 during Stage 1 at 5.5 MeV/ $u$  will be  $< \pm 1.6$  ns ( $\approx \pm \sqrt{6}\sigma$ ) and the energy spread  $< \pm 0.6\%$  ( $\approx \pm \sqrt{6}\sigma$ ). A rebuncher could reduce the energy spread to below  $\pm 0.2\%$  ( $\approx \pm \sqrt{6}\sigma$ ) and focus the bunch length to less than  $\pm 0.5$  ns ( $\approx \pm \sqrt{6}\sigma$ ).

After the linac upgrade is completed the energy spread and bunch length at Experiment Station 1 will be limited to  $\pm 0.3\%$  ( $\approx \pm \sqrt{6}\sigma$ ) and  $\pm 0.6$  ns ( $\approx \pm \sqrt{6}\sigma$ ) at 10 MeV/ $u$  without a rebuncher. If the maximum beam energy is not needed then some cavities in the main linac could be used as rebunchers for the experiments. The next chapter will summarise the development of a solid-state detector for use at HIE-ISOLDE.

## DEVELOPMENT OF A SILICON DETECTOR FOR PHASING THE HIE LINAC

The installation of the 32 independently phased cavities will require an efficient tuning procedure in order to minimise the amount of time spent setting up the linac between the delivery of different beams. Currently at REX the phase working points of the cavities are set by using the switchyard magnet to measure the relative average beam energy as a function of phase; such a procedure is robust and reliable but inherently time consuming and very difficult to automate. To resolve this issue a diagnostics system based on silicon detector technology was researched and developed with a view to measuring the longitudinal beam properties in a quick and accurate way that could eventually be automated. In this chapter the system will be outlined, its performance assessed and the results of proof-of-principle tests using the 7G3 cavity will be presented; more details can be found in [40].

### **7.1 Longitudinal Beam Diagnostics**

The diagnostic systems available for low intensity non-relativistic ion beams typically involve destructive or semi-destructive techniques that directly impinge the beam; other non-destructive techniques that use capacitive pick-ups to measure the beam energy by time-of-flight (ToF) were ruled out based on the challenges posed by the low beam intensity. Semi-destructive ToF monitors, such as those based on measuring secondary electrons emitted from a wire placed in the beam [198], were also ruled out as a primary tool for cavity phasing because of the difficulties introduced by the short bunch spacing

of 9.87 ns at 101.28 MHz. In addition, low energy beams cannot be phased using ToF detectors located downstream of the linac because the temporal structure of these beams will be lost before exiting the linac.<sup>1</sup>

Therefore, a particle detector monitor based on semiconductor technology was developed, capable of directly measuring the energy of the beam and phasing all of the cavities with a single monitor downstream of the linac. A semiconductor detector can also identify the beam components by spectroscopy and provide temporal information to complement the energy measurements.

## 7.2 Diagnostic System Setup

Two partially-depleted PIPS detectors manufactured by Canberra, with thicknesses of 300 and 500  $\mu\text{m}$ , were chosen based on experience of their reliable operation in beam diagnostics systems at TRIUMF [198]. The two detectors have active areas of 50 and 25  $\text{mm}^2$ , respectively. The detector delivers a pulse of charge proportional to the energy deposited by a charged particle passing through it, requiring that the particle is stopped by the silicon so that all of its energy is deposited inside. SRIM [199] calculations showed that a thickness of 500  $\mu\text{m}$  was sufficient to stop all beams from beryllium to uranium at typical beam energies expected at HIE-ISOLDE of up to 10  $\text{MeV}/u$ . A thickness of 100  $\mu\text{m}$  is capable of stopping all beams from helium to uranium at 3  $\text{MeV}/u$ , which is the maximum beam energy currently available at REX.

The detector with a 300  $\mu\text{m}$  thickness and active area of 50  $\text{mm}^2$  is shown in Figure 7.1 along with its position on the beam line in DB5. The silicon detector was placed on the second actuator normally used to move the aluminium plate of the MCP low intensity beam profiler. In this position it could be protected by moving the Faraday cup into the beam. The detector was fitted securely on a custom built mechanical support, which also provided the grounding of the detector housing to the diagnostic box.

---

<sup>1</sup>ToF techniques could still be used at 101.28 MHz to measure the absolute energy of beams downstream of the linac, provided they can be kept bunched. In addition to the standard measurement with two pick-ups, an additional pick-up could be placed very close to the first to uniquely identify bunches. This type of monitor could provide the experiments with an absolute measurement of the beam energy that is independent of the spectrometer calibration and with an accuracy in the order of 0.1 % [169, 198], however such a measurement would take some time to set up and is not ideal for cavity phasing.

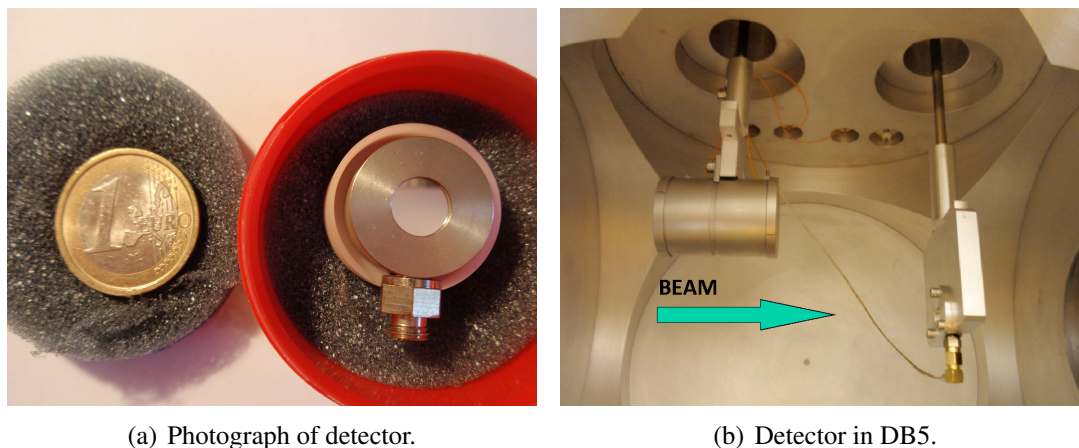


Figure 7.1: The  $300\ \mu\text{m}$  and  $50\ \text{mm}^2$  PIPS detector.

The electronics behind the silicon detector and the data acquisition system is summarised in the schematic of Figure 7.2. The detector hardware is only summarised in this thesis; for an extensive description see [200]. A charge-sensitive pre-amplifier provides simultaneous energy and timing output signals. The energy signal is a positive pulse characterised with a rise time of less than  $12\ \text{ns}$  followed by an exponential decay with a time constant of some  $250\ \mu\text{s}$ . The time signal, which is a negative pulse with a fast rise time of less than  $3\ \text{ns}$ , is derived from the energy signal via electronics internal to the pre-amplifier. The rising edge of the time signal is only very weakly dependent on the incident particle energy.

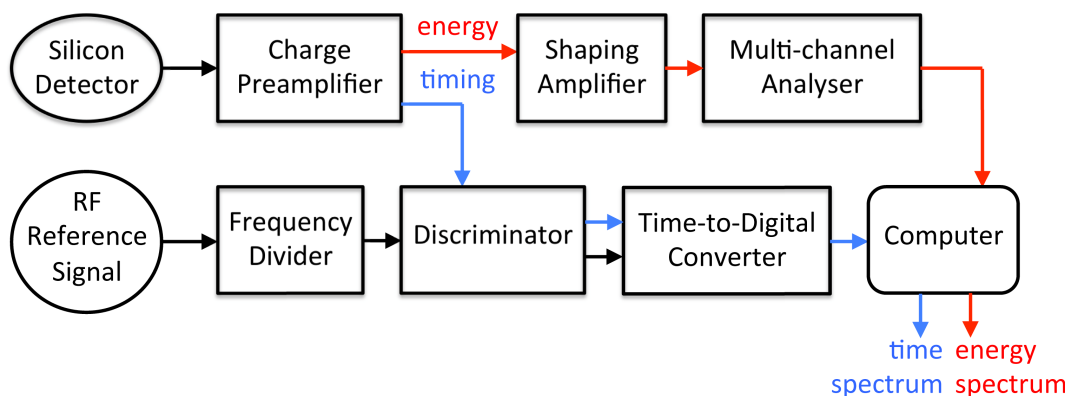


Figure 7.2: Schematic of the silicon detector electronics and data acquisition system.

For the energy signals a shaping amplifier was used to amplify and convert the exponentially decaying output pulses into semi-Gaussian signals with an optimised signal-to-noise ratio. The shaper also included a baseline correction feature that allowed pulses arriving in close succession to be accurately analysed in a Multi-Channel Analyser (MCA),

as demonstrated in Figure 7.3. The pulse height analysis was done using an MCA with 1024 channels located on a PCI card in a local computer. Later, a VME standard MCA was also tested for improved compatibility of the system with standard beam instrumentation at CERN.

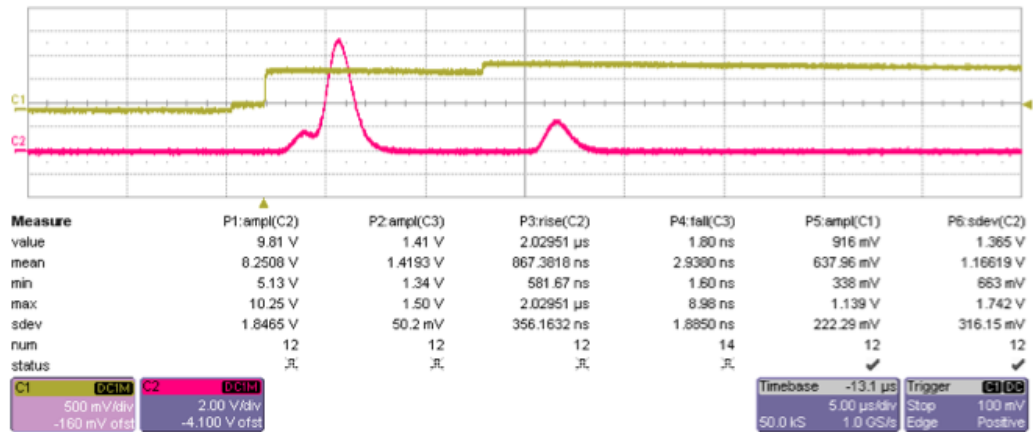


Figure 7.3: Demonstration of pile-up and baseline correction. Pre-amplifier output signal (yellow) and corresponding signal from the shaper amplifier (pink). The second pulse ( $^{16}\text{O}^{4+}$ ) piles-up on the first ( $^4\text{He}^+$ ) and dominates its signal. The third event is well defined even though it is located on the decaying signal from the second event.

For the time signals a Time-to-Digital Converter (TDC) was used to compare the time of arrival of particles at the detector with the rf master clock that determines the phase of the cavities in the linac. A VME standard TDC based on the time-stamping of multiple events was used rather than a more traditional TDC operating with ‘start-stop’ signals. The TDC works with an internal counter looping in 25 ps increments and a time-stamp is given from this clock to events fed to it through up to 16 input channels. The events are stored to memory for later recovery. The maximum data rate that the TDC could reliably accept was estimated at 7 MHz and so the rf signal was divided by a factor of 14 to give a reference signal at 7.23 MHz. The time-stamped events recorded from the silicon detector were compared to the rf signal offline. A LabVIEW program was written to control the data acquisition of the TDC and a MATLAB program was written to analyse the saved data. The discriminator was used to convert the signals into the NIM standard for input to the TDC.

## 7.3 Control of Beam Intensity

With good baseline correction and pile-up rejection techniques silicon detectors can typically accept events at rates in the order of a few kHz. An important functionality of the diagnostic system is to be able to rapidly and reproducibly attenuate the beam intensity to levels that facilitate the use of the silicon detector. The pulsed time structure of the EBIS leads to relatively high instantaneous beam intensities, even though the average beam intensities for pilot beams are typically only a few tens of pA. Presently the ion throughput of the source is limited by the space-charge capacity of the Penning trap at about  $10^8$  ions per pulse with a 50 Hz repetition rate [54]. Depending on the extraction mode, beam pulses ejected from the EBIS can range in length from 50 to 800  $\mu\text{s}$  and attenuation factors of up to  $10^8$  are needed to attain instantaneous rates in the range of a few kHz. A technique often used to attenuate the beam is to Rutherford scatter beam particles from a thin foil into the detector [201]. However, to keep the design of the prototype as simple as possible, it was decided to place the detector directly into the beam and instead, either adjust the intensity by modifying the parameters of the ion source or by inserting attenuator foils upstream of the detector. Space-charge effects are negligible even at full intensity, therefore it is valid to tune the accelerator when strongly attenuating the beam intensity. With the characteristically low average beam currents at REX the risk of radiation damage to the detector was not a major concern, although precautions were taken to ensure the detector was only inserted into the beam after attenuator foils had been inserted.

### 7.3.1 Modification of the EBIS Parameters

The beam measurements were made with the EBIS in an offline mode and light elements of either residual gas or leaked buffer gas from REXTRAP were ionised and accelerated. The pulsed time structure of the beam from the EBIS was removed by flattening the voltage profile of its drift-tube electrodes at 700 V and holding them constant throughout the entire cycle of the EBIS, including during extraction. The time structure of the ejected pulse was probed by offsetting the time at which the linac rf was triggered with respect to the EBIS timing cycle and measuring the beam intensity accelerated to the detector. Figure 7.4 shows that the flattening of the drift-tube potentials removes the time structure

of the ejected pulse and the beam intensity remains low on average throughout the pulse. The intensity can be reduced even with a fast-extracted pulse of some  $50 \mu\text{s}$  in length if the linac rf is delayed with respect to the time at which the pulse is ejected, in order that only those particles in the tail of the pulse are accelerated. The time structure of the EBIS and REX linac is shown in Figure A.1 of Appendix A.

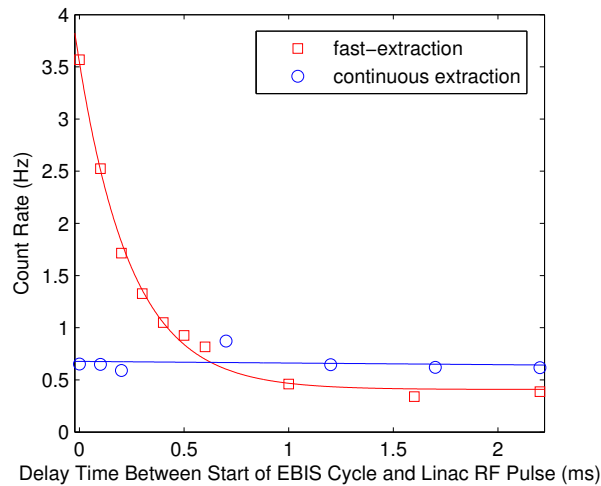


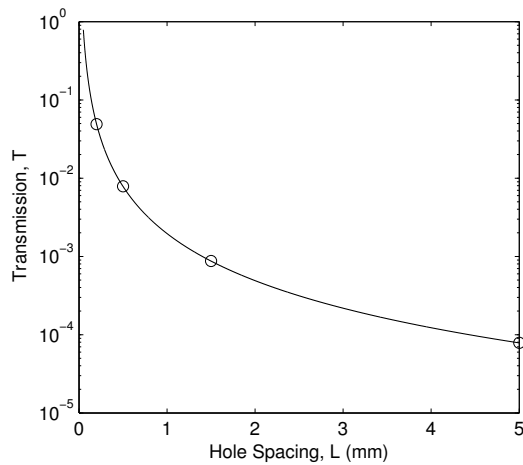
Figure 7.4: Time structure of extracted EBIS pulse probed by delaying the linac rf pulse with respect to the extraction time.

The average beam current could be reduced by a factor of 1000 by also turning off the Einzel lens that provides transverse focusing for the beam extracted from the EBIS. In addition, collimators were put along the beam line to further reduce the intensity. The use of the ion source to control the beam intensity for the diagnostic system is not ideal, especially if running with radioactive beam, therefore attenuator foils were investigated to ensure the diagnostic system could operate in a decoupled manner and independent of the machine parameters.

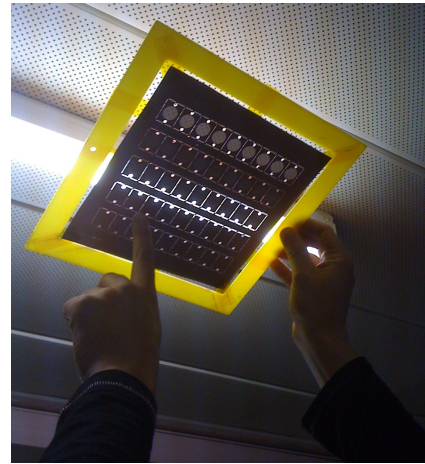
### 7.3.2 Attenuator Foils

The ion source had to be used to control the beam intensity for the first beam measurements with the silicon detector because of the poor performance of the first attenuator foils used. During the first tests the attenuators, consisting of perforated copper foils, were placed on the collimator wheel in the same diagnostic box in front of the silicon detector at a distance of approximately 15 cm. The results were disappointing and the energy spectra were dominated with a background arising from the direct scattering of

particles from the foils into the detector [200]. The foils were originally used for tests of a diamond detector at REX [202] in early 2009 and looked visibly aged. The foils also had to be stacked on top of each other to achieve a range of attenuation strengths, which was inherently unpredictable and difficult to calibrate. Therefore, new foils were fabricated in-house at CERN by the chemical etching of thin copper foils. They were placed at low energy, either side of the RFQ in DB2 (5 keV/ $u$ ) and DB3 (300 keV/ $u$ ), in order that any heavily scattered particles would be filtered by the rf of the cavities before reaching the detector.



(a) Transmission calculation for the attenuators.



(b) Inspection of the foils after etching.

Figure 7.5: Attenuators made with transmissions of approximately: 5 %, 1 %, 0.1 % and 0.01 %.

In general, a good quality etch with steep and well defined edges can only be attained with holes that have a radius comparable to or larger than the thickness of the substrate, which limits how small the holes can be made. At lower energy the thickness of the foils can be reduced and smaller holes etched with improved quality. A simple repeated pattern was employed with holes of radius  $R$  being placed on each corner of a square grid with dimension  $L$ . The transmission of the foils was varied by changing the spacing of the holes and assuming a simple optical model, the transmission  $T$  of the foils was calculated as,

$$T = \pi \frac{R^2}{L^2}. \quad (7.3.1)$$

At 300 keV/ $u$  all ions should be stopped in 5  $\mu\text{m}$  of copper, with 15  $\mu\text{m}$  required for 3 MeV/ $u$ . Therefore, foils of 15  $\mu\text{m}$  thickness were made with holes of 25  $\mu\text{m}$  radius.

Table 7.1: Calibration of attenuator foils (the reference intensity without foil was measured as 34.9 pA)

Foil Transmission [%]	Current [pA]	Measured Transmission [%]
5	2.08	6
1	0.28	0.8
0.1	0.03	0.09
0.01	n/a	n/a

A range of foils with different transmissions was made from 5 % to 0.01 %, as shown in Figure 7.5(a); the attenuators are shown being inspected in Figure 7.5(b). The transmission of each foil was calibrated by measuring the beam intensity with a Faraday cup. The beam intensity with the foil of an estimated transmission of 0.01 % was below the sensitivity of the Faraday cup and could not be measured, see Table 7.1. The attenuation can be reliably calibrated for a single foil, however if two foils are combined it becomes difficult to predict the overall attenuation factor. The attenuation through two foils depends very sensitively on their geometrical alignment and the exact position at the second foil of each individual ‘beamlet’ created by the first. Nonetheless, with enough different types of foil one can quickly find a combination that gives the required attenuation factor. The background was no longer observed after the installation of the new attenuators at low energy and clean spectra could be acquired, examples of which are shown in Figure 7.6.

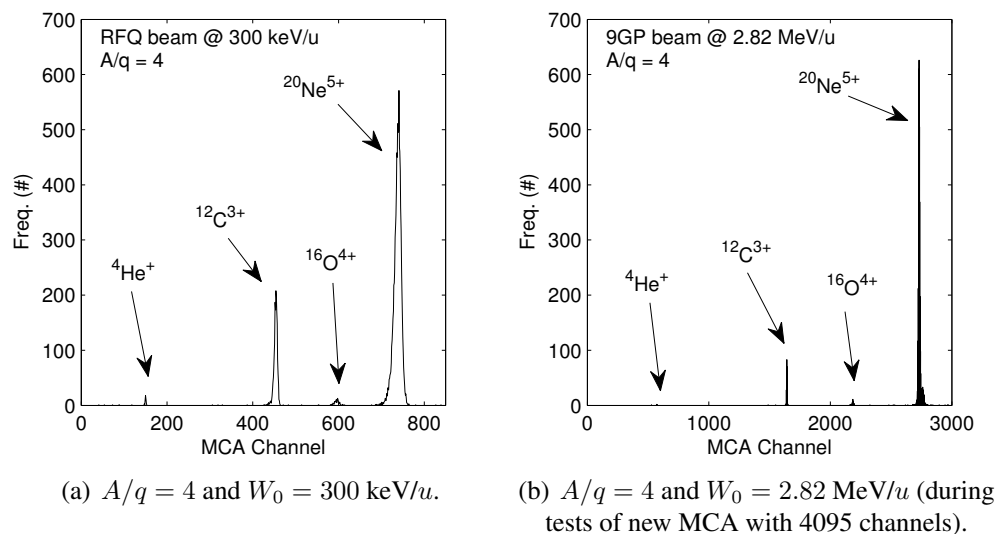


Figure 7.6: Example spectra taken using the attenuators to reduce the beam intensity.

Measurements of the silicon detector’s energy resolution showed no significant differ-

ence whether the ion source or the attenuators were used to reduce the beam intensity.

## 7.4 Resolution

The system must resolve the sinusoidal variation with phase of the beam energy in each cavity. The amplitudes of the  $\Delta W(\phi)$  curves decrease with acceleration from  $\pm 15\%$  of the beam energy in the first low- $\beta$  cavity to  $\pm 3.5\%$  in the last high- $\beta$  cavity, as shown by in Figure 7.7(a). With deceleration in the low energy section the amplitude of the energy gain curve decreases to  $\pm 2\%$  in the last low- $\beta$  cavity, as shown in Figure 7.7(b).

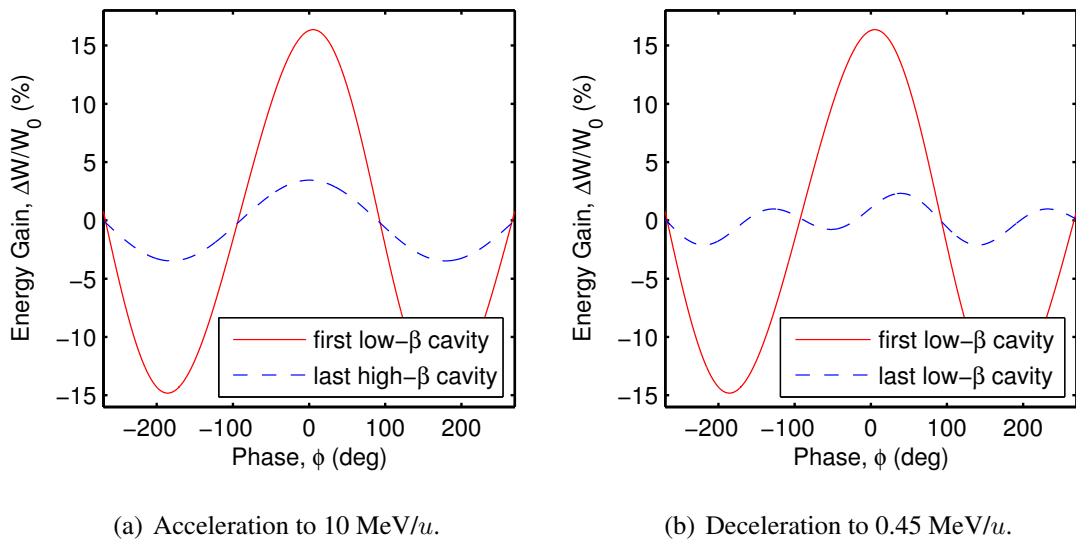


Figure 7.7: Simulated phasing curves for the first and last cavities with a beam of  $A/q = 4.5$ .

In principle, the average beam energy can be found to an accuracy limited only by the channel width of the MCA with a long enough acquisition, regardless of the resolution of the detector. In practice, one would like to make quick measurements, therefore the energy spread of the beam convoluted with the detector's resolution will limit the accuracy to which the average energy can be measured. The energy spread of the beam will only significantly affect the measurement at low energy when the beam is decelerated. Otherwise, the resolution of the detector will be the limiting factor and it should be ensured that it is smaller than the amplitude of the sinusoidal oscillation of the energy gain at the very worst.

### 7.4.1 Electronic Noise

The electronic noise of the system was measured by injecting a test pulse produced by a precision pulse generator into the designated test port on the pre-amplifier and acquiring the test signal on the MCA. The line width is dominated by the electronic noise contribution, which was measured as 11 and 6 keV FWHM at an optimum shaping time of  $0.5 \mu\text{s}$  for the  $300 \mu\text{m}$ ,  $50 \text{ mm}^2$  and the  $500 \mu\text{m}$ ,  $25 \text{ mm}^2$  detectors, respectively. Even for low energy beams the electronic noise contribution is small, e.g. 11 keV represents just 0.18 % of the energy of a  $300 \text{ keV/u } ^{20}\text{Ne}$  beam.

### 7.4.2 Measurement with Standard $\alpha$ -source

The resolution of the  $300 \mu\text{m}$ ,  $50 \text{ mm}^2$  detector was measured as 0.4 % FWHM (0.2 % rms) using a standard triple- $\alpha$  source containing three isotopes: plutonium ( $^{239}\text{Pu}$ ), americium, ( $^{241}\text{Am}$ ) and curium ( $^{244}\text{Cm}$ ), see e.g. [203]. A spectrum was grown on the MCA with the  $\alpha$ -source fixed on the collimator wheel inside the diagnostic box, under vacuum, at a very low average data rate of 0.5 Hz. The acquired spectrum is shown in Figure 7.8. Each isotope produced characteristic double peaks corresponding to  $\alpha$  decays at two different energies, which were fitted with a double Gaussian fit to extract the width of the main peaks.

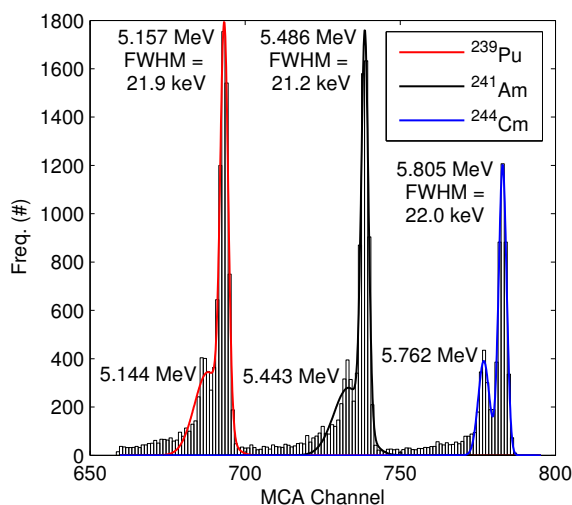


Figure 7.8:  $\alpha$ -source measurements of the  $300 \mu\text{m}$ ,  $50 \text{ mm}^2$  detector's energy resolution.

### 7.4.3 Measurements with Beam

The energy resolution was probed at 300 keV/u and 2.82 MeV/u. At RFQ energy the rebuncher was used to investigate the resolution by varying its voltage and measuring the energy spread with both the spectrometer and the silicon detector. For the 300  $\mu\text{m}$ , 50 mm<sup>2</sup> detector the resolution of the silicon detector was estimated as 1.4 % rms (3.3 % FWHM) by subtracting the resolution in quadrature, which was described in Chapter 5.5, until the measurements agreed with the spectrometer measurement and simulation, as shown in Figure 7.9(a). The instantaneous count rate at the detector was 7 kHz. A similar exercise was performed with the 500  $\mu\text{m}$ , 25 mm<sup>2</sup> detector without the rebuncher but varying the energy spread by adjusting the voltage of the RFQ, as shown in Figure 7.9(b), giving an estimated resolution of 1.1 % rms (2.6 % FWHM) at an instantaneous count rate of 2 kHz. The improvement was attributed to the better noise performance, thinner entrance window of the second detector and the lower count rate in the second experiment.

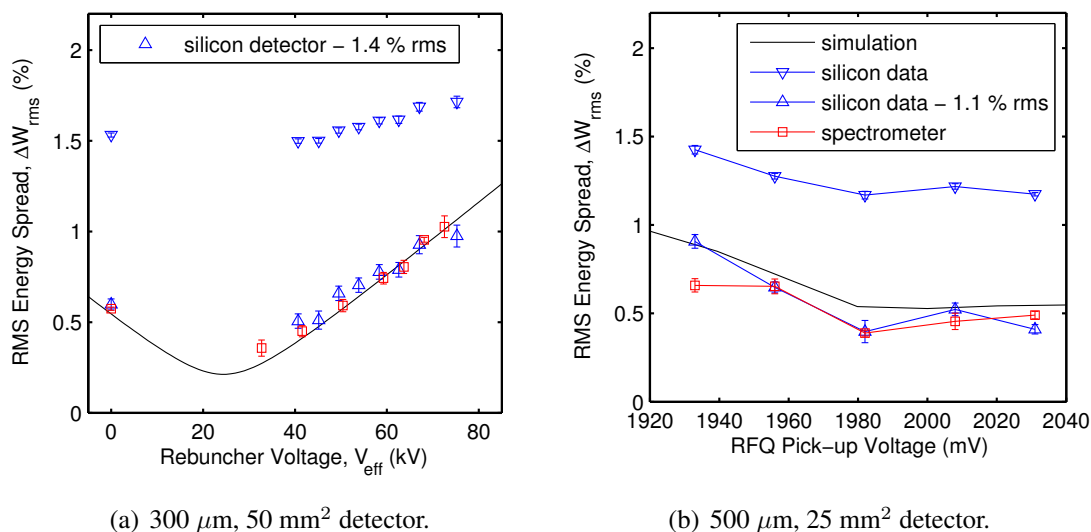


Figure 7.9: Beam-based estimation of the resolution of the silicon detectors at a beam energy of 300 keV/u.

The relative energy resolution improved as the beam energy increased, whilst still being strongly dependent on the beam intensity. At 2.8 MeV/u and with an instantaneous beam intensity of 3 kHz the resolution was estimated at 0.5 % rms (1.2 % FWHM) after the 9GP for the 500  $\mu\text{m}$ , 25 mm<sup>2</sup> detector.

As was commented in Chapter 5, the silicon detector is not well suited for accurate longitudinal emittance measurements because of its resolution. Although the energy and

timing signals could be correlated on acquisition to directly measure the longitudinal beam phase space parameters, the energy resolution of the detector would limit such a measurement. Nonetheless, the resolution does not prevent measuring relative changes in the energy spread and the monitor will be very useful for beam tuning, e.g. the voltage of the minimum in Figure 7.9(a) is independent of the resolution and well defined even in the silicon detector measurement.

The resolution estimated with the beam was significantly worse than with the  $\alpha$ -source, even though at 300 keV/u the dominant beam component ( $^{20}\text{Ne}^{5+}$ ) had an energy comparable to that of the  $\alpha$ -particles. However, the instantaneous count rates were significantly different, ranging from a few kHz with the beam to just 0.5 Hz with the  $\alpha$ -source, and was attributed as the cause of the disparity. The shaper amplifier does well to allow events at a few kHz to be counted, however there is an associated and inevitable loss in the resolution as a consequence of the moving baseline from which the pulse height analysis is made. The effect of the count rate at a few kHz degrades the resolution of the system by approximately a factor of 6. Acquiring data at slower rates is not practical. Even in the worst case, at 1.4 % rms, the resolution of the system is satisfactory for phasing the cavities of the HIE linac.

#### 7.4.4 Time Resolution

The time structure of the REX beam was measured for the first time after the 9GP at 2.82 MeV/u. The bunch structure measured in DB5 at a position of 9.5 m downstream of the 9GP is shown in Figure 7.10, with a bunch length of 2.5 ns, which is consistent with that expected from simulation. The jitter on the divided rf reference signal was measured by analysing the stability of the time period of the signal. The jitter was measured as 42 ps rms (98 ps FWHM), which includes contributions from the 25 ps resolution of the TDC and the discriminator. The stability of the rf reference signal itself was assumed as negligible. The time resolution of the detector is quoted as 140 ps by Canberra, which can be used to estimate the time resolution of the entire system as better than 200 ps rms.

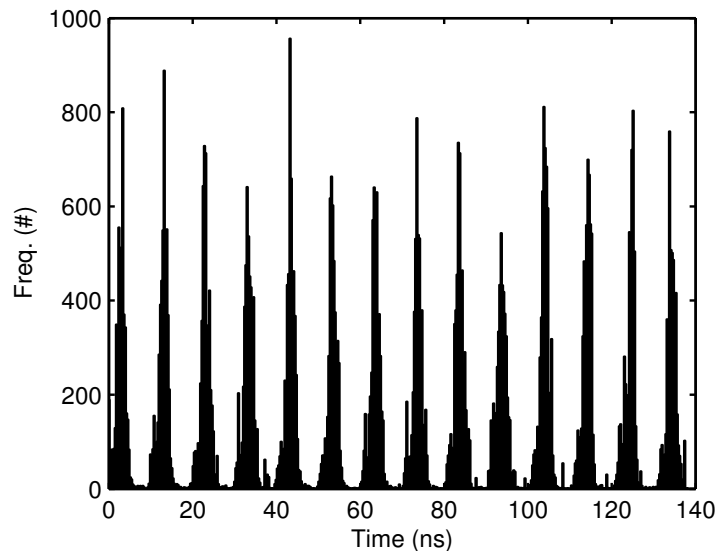


Figure 7.10: Measured time structure of the REX beam 9.5 m downstream of the 9GP at 2.82 MeV/u.

## 7.5 Phasing with Energy

The 7G3 was phased with a beam of  $A/q = 4$  at 1.92 MeV/u to prove that the silicon detector can be used to phase cavities. The channel number of the dominant peak in a beam composed primarily of  $^{16}\text{O}^{4+}$  was measured at 25 different phases. The channel number was calibrated and is plotted in Figure 7.11 with error bars that represent the rms width of the peak measured by the detector. The results from the silicon detector are consistent with the spectrometer measurements and simulation. In this case the amplitude of the energy gain is  $\pm 15\%$  with respect to the resolution estimated at between 0.5 and 1%. The energy spread was observed to vary throughout the measurement and is largest at the longitudinally unstable phases on the right-hand side of the crest, which indicates that the measured energy spread had a significant contribution from the beam and was not completely dominated by the resolution. The data was fitted with expressions of the form,

$$\Delta W = a(\beta) \cos \phi + b(\beta) \sin 2\phi + c(\beta), \quad (7.5.1)$$

where the constants  $a$ ,  $b$  and  $c$  are related to the transit-time factors discussed in Chapter 3.3.4 and [110]. The linac duty cycle reduces the data rate from a few kHz to typically 10-100 Hz, however reliable spectra could be grown within a minute. Longer acquisition

times were needed only close to the minimum of the curve in Figure 7.11 where the transmission was poor. As shown in the Figure 7.11, the curve can be reliably fitted with only 5 or 10 randomly chosen data points and the tuning done considerably quicker.

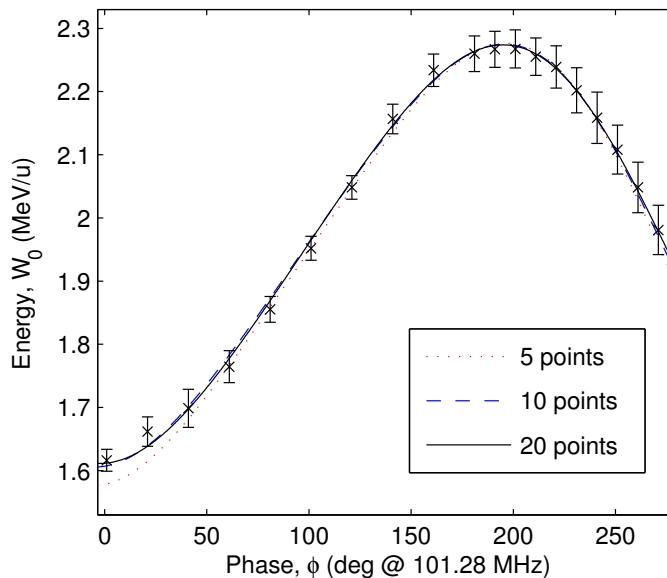


Figure 7.11: Proof-of-principle of phasing the 7G3 with the energy signal from the silicon detector.

## 7.6 Phasing with Time-of-Flight

The 7G3 cavity was also phased with ToF measurements using the silicon detector. The velocity modulation imparted on the beam varies its time-of-flight between the cavity and the detector by up to 100 ns over the 10.6 m drift distance. Due to the beam frequency of 101.28 MHz, the bunches could only be uniquely identified and their changing arrival time measured if the phase was varied in small increments, which kept the change in the arrival time below the 9.87 ns bunch spacing. Consequently, the measurement was particularly time consuming and was only made easier with the prior knowledge gained from phasing measurements made with the energy information. The measurements are shown in Figure 7.12, alongside a calculation made using the energy modulation data that was presented in Figure 7.11. At an instantaneous beam intensity of few kHz the average number of particles arriving per EBIS pulse is only of the order of 1. Therefore, instead of acquiring the rf reference signal throughout the entire rf duty cycle, the TDC

was programmed to trigger on the timing signal coming from events in the detector. An acquisition window of 500 ns was centred on the particle that triggered the TDC in order to acquire at the same time the rf reference signal.

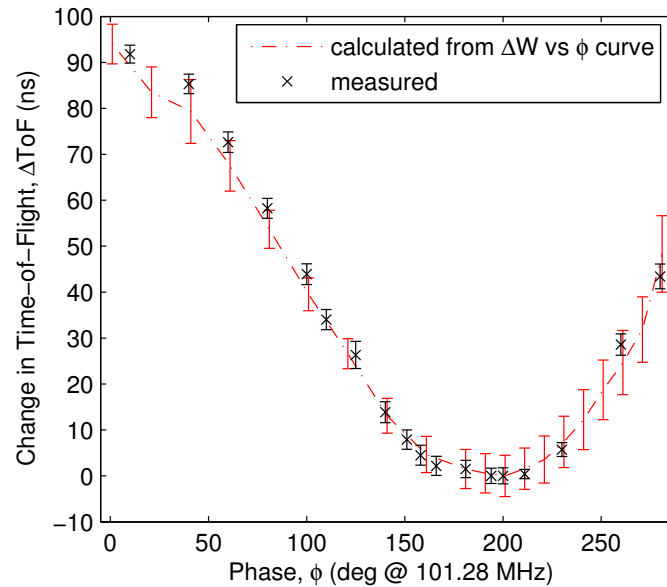


Figure 7.12: Proof-of-principle of phasing the 7G3 with the time signal from the silicon detector.

In principle, the silicon detector could be used to phase cavities with time-of-flight, however the procedure would only be efficient if the bunch spacing was increased significantly.

## 7.7 Summary

A solid-state longitudinal diagnostic system was developed and its resolution characterised. The system has been shown to be a viable tool for tuning the phases of the superconducting cavities of the upgrade, which could potentially be automated with further software development.

## CONCLUSION

### 8.1 Summary

A beam dynamics study was presented in two main sections with the common goal of providing post-accelerated radioactive ion beams of higher energy and quality at ISOLDE. The first section focused on establishing beam dynamics simulation tools of the REX linac that were benchmarked with rf and beam measurements, using both existing and new diagnostics systems developed as part of this thesis. The second section focused on the design studies of the HIE-ISOLDE superconducting linac upgrade with the objective of delivering all beams at over 10 MeV/ $u$  with a concomitant low dilution of emittance.

The investigation of the REX linac identified sources of emittance degradation and yielded techniques to check the working points of the two main accelerating structures, the RFQ and IHS, which will remain even after the addition of the superconducting linac. A highlight of the measurements was the development of a technique to measure the energy spread of low intensity beams at an estimated resolution of below 0.2 % using the switchyard magnet, allowing the phase and amplitude of the above mentioned accelerating cavities to be set reliably. The high resolution of the spectrometer also permitted the performance of the solid-state diagnostic system in its development stages to be evaluated. The beam dynamics models of the IHS were verified with numerical tracking in the realistic field map attained from new rf simulations that were validated with rf bead-pull measurements of the cavity. The 86 % longitudinal emittance was measured for the first time at REX at  $1.5 \pm 0.2 \pi$  ns keV/ $u$ , corresponding to the 4.4-rms emittance, at locations

both before and after the IHS to further confirm its performance and working point. An analytic formalism was developed to facilitate the emittance measurement with the multi-gap 7G3 cavity after the IHS, resulting in the publication of the technique in [38]. The emittance was put into context with the longitudinal acceptance of the superconducting linac and as a result the design of the matching sections could be advanced, most critically after the 9GP cavity in the first stages of the upgrade.

The design studies of the HIE-ISOLDE linac, published in [39], focused on the high energy section that will be installed and commissioned first. A first-order design was augmented to include end-to-end simulations using the realistic field maps of all of the linac components. A parametric resonance induced by the coupling of the transverse and longitudinal motions in the cavities was suppressed with a suitable choice of focusing strength, which led to the specification of the solenoid that has since entered prototyping. In particular, a compensation scheme was developed to minimise the beam-steering effects in the quarter-wave cavities and the cavity geometry was optimised with these considerations in mind. By deliberately offsetting the beam axis inside a racetrack-shaped aperture the emittance growth arising from beam-steering could be suppressed and the loss of transverse acceptance caused by the offset minimised. The racetrack also improves the transverse field asymmetry in an energy range consistent with normal operation. Rf error studies showed significant growth in the time-averaged longitudinal emittance in the independent cavity linac and a tight specification was made on the rf jitter to suppress the growth. Although significant modifications of the internal conductor of the cavity were investigated to improve the field asymmetry, it was deemed unnecessary after weighing up the small improvement in the beam quality with the difficulties involved in the surface sputtering. The misalignment studies that were carried out had a direct influence on the mechanical design of the cryomodule with a separately adjustable solenoid mounting and an optical system capable of monitoring the positions of the linac components online. The orbit correction scheme that was proposed and implemented in the misalignment studies formed the basis of the specification of the steerer magnets that are now under prototyping. The low energy section and its cavities were implemented into the simulations without any significant problems, except with regards to the orbit correction routine using

external steering elements, which was ameliorated by changing the focusing strength of the linac. Cold steering elements inside the cryomodule and on top of the superconducting solenoids were shown to offer a much improved orbit correction. Deceleration in the low energy section of the superconducting linac was studied and a second-order analytic formalism was used to complement numerical studies that showed reasonable beam quality could be attained for beams decelerated from 1.2 MeV/ $u$  to as low as 0.45 MeV/ $u$ .

The development of the solid-state diagnostics system and its associated attenuation system not only helped to improve the input parameters for the beam dynamics simulations of the upgrade, but also represents a system capable of the fast and eventually automated tuning of the 32 superconducting cavities that will accompany the upgrade. The proof-of-principle was achieved with the successful phasing of the 7G3 cavity and published in [40].

## 8.2 Future of HIE-ISOLDE

The prototyping activities of the high- $\beta$  cavities, solenoids, cryomodule, diagnostic systems and corrector magnet are ongoing, with the installation and commissioning of the first two cryomodules looking realistic for the long shutdown period during 2013/14. Further development is required to increase the quality of the niobium sputtered cavity surface, but the infrastructures are now in place to test the cavity performance at CERN quickly and in step with changes to the parameters involved in the sputtering process. The possibility of hurrying the cavity production without noses in some of the cryomodules has been considered and still remains an option, see Appendix F.2. The beam optics design of the HEBT is currently being validated and integrated with the experiments and a decision on the requirement for bunchers is pending. The development of the low energy section and completion of the linac upgrade is currently foreseen for the long shutdown during 2017/18. In addition to the installation of the low energy section, funding has been made available to investigate the option of increasing the bunch spacing by a factor of 10 to 100 ns, which will permit time-of-flight experiments at HIE-ISOLDE.

## BIBLIOGRAPHY

- [1] M. A. Fraser, “A survey of the introduction of rare-earth nuclei into the Beta-Beam accelerator chain in order to attain a monochromatic neutrino beam”, EURISOL DS task note 12-25-2008-0011 (CERN, Geneva, 2007).
- [2] P. Zucchelli, *Phys. Lett. B* **532**, pp. 166–172 (2002).
- [3] O. Kofoed-Hansen, K. O. Nielsen, *Phys. Rev.* **82**, pp. 96–97 (1 1951).
- [4] I. Tanihata, *Nucl. Instrum. Meth. B* **266**, pp. 4067–4073 (2008).
- [5] E. Kugler, *Hyperfine Interact.* **129**, pp. 23–42 (1 2000).
- [6] M. Huyse, in *The Euroschool Lectures on Physics with Exotic Beams, Vol. I*, ed. by J. Al-Khalili, E. Roeckl (Springer Berlin / Heidelberg, 2004), vol. 651, pp. 1–32.
- [7] B. Frois (chairman), “Report of the Working Group on Nuclear Physics”, tech. rep. (OECD Megascience Forum, 1999).
- [8] P. Decrock, T. Delbar, P. Duhamel, W. Galster, M. Huyse, P. Leleux, I. Licot, E. Liénard, P. Lipnik, M. Loiselet, C. Michotte, G. Ryckewaert, P. Van Duppen, J. Vanhorenbeeck, J. Vervier, *Phys. Rev. Lett.* **67**, pp. 808–811 (7 1991).
- [9] S. Hofmann, W. Reisdorf, G. Münzenberg, F. P. Heüberger, J. R. H. Schneider, P. Armbruster, *Z. Phys. A - Hadron Nucl.* **305**, pp. 111–123 (2 1982).
- [10] I. Tanihata, H. Hamagaki, O. Hashimoto, Y. Shida, N. Yoshikawa, K. Sugimoto, O. Yamakawa, T. Kobayashi, N. Takahashi, *Phys. Rev. Lett.* **55**, pp. 2676–2679 (24 1985).
- [11] B. Jonson, *Phys. Rep.* **389**, pp. 1–59 (2004).

- [12] A. Ozawa, T. Kobayashi, T. Suzuki, K. Yoshida, I. Tanihata, *Phys. Rev. Lett.* **84**, pp. 5493–5495 (24 2000).
- [13] H. L. Ravn, *Philos. T. Roy. Soc. A* **356**, pp. 1955–1984 (1998).
- [14] D. J. Morrissey, B. M. Sherrill, *Philos. T. Roy. Soc. A* **356**, pp. 1985–2006 (1998).
- [15] R. E. Laxdal, *Nucl. Instrum. Meth. B* **204**, pp. 400–409 (2003).
- [16] F. Wenander, *Nucl. Phys. A* **746**, pp. 40–46 (2004).
- [17] J. Aysto (chairman) *et al.*, “Radioactive Nuclear Beam Facilities”, tech. rep. (NuPECC Working Group on Radioactive Nuclear Beam Facilities, 2000).
- [18] M. Lindroos, *Proc. of EPAC’04*, pp. 45–49 (Lucern, 2004).
- [19] J. C. Cornell, *Proc. of CYCLOTRONS’04*, pp. 513–517 (Tokyo, 2004).
- [20] H. Sakurai, *Nucl. Instrum. Meth. B* **266**, pp. 4080–4085 (2008).
- [21] Y. Blumenfeld, *Proc. of EPAC’08*, pp. 41–45 (Genoa, 2008).
- [22] M. Huyse, R. Raabe, *J. Phys. G Nucl. Partic.* **38**, p. 024001 (2011).
- [23] J. R. Beene, D. W. Bardayan, A. G. Urbarri, C. J. Gross, K. L. Jones, J. F. Liang, W. Nazarewicz, D. W. Stracener, B. A. Tatum, R. L. Varner, *J. Phys. G Nucl. Partic.* **38**, p. 024002 (2011).
- [24] G. C. Ball, L. Buchmann, B. Davids, R. Kanungo, C. Ruiz, C. E. Svensson, *J. Phys. G Nucl. Partic.* **38**, p. 024003 (2011).
- [25] P. Van Duppen, K. Riisager, *J. Phys. G Nucl. Partic.* **38**, p. 024005 (2011).
- [26] A. Navin, F. de Oliveira Santos, P. Roussel-Chomaz, O. Sorlin, *J. Phys. G Nucl. Partic.* **38**, p. 024004 (2011).
- [27] D. Rifuggiato, L. Calabretta, L. Celona, F. Chines, L. Cosentino, G. Cuttone, P. Finocchiaro, A. Pappalardo, M. Re, A. Rovelli, *J. Phys. Conf. Ser.* **267**, p. 012007 (2011).
- [28] “Roadmap for Construction of Nuclear Physics Research Infrastructures in Europe”, tech. rep. (NuPECC, 2005).
- [29] G. Rosner (chair) *et al.*, “Perspectives of Nuclear Physics in Europe – NuPECC Long Range Plan 2010”, tech. rep. (ESF and NuPECC, 2010).

- [30] D. J. Morrissey, *J. Phys. Conf. Ser.* **267**, p. 012001 (2011).
- [31] L. Merminga *et al.*, *Proc. of IPAC'11*, pp. 1917–1919 (St Sebastian, 2011).
- [32] T. Suda, *J. Phys. Conf. Ser.* **267**, p. 012008 (2011).
- [33] W. F. Henning, *Nucl. Instrum. Meth. B* **214**, pp. 211–215 (2004).
- [34] “Final Report of the EURISOL Design Study (2005-2009): A design study for a european isotope-separation-on-line radioactive ion beam facility”, tech. rep. (European Commission Contract No. 515768 RIDS, 2009).
- [35] P. Van Duppen, *Nucl. Instrum. Meth. B* **204**, pp. 9–16 (2003).
- [36] G. Prete, A. Andrighetto, L. Biasetto, M. Manzolaro, F. Gramegna, A. Lombardi, A. Pisent, J. Esposito, E. Fagotti, M. Cinausero, P. Mastinu, L. Calabretta, SPES Collaboration, *J. Phys. Conf. Ser.* **168**, p. 012022 (2009).
- [37] M. Lewitowicz, *J. Phys. Conf. Ser.* **312**, p. 052014 (2011).
- [38] M. A. Fraser, F. Zocca, R. M. Jones, M. Pasini, P. A. Posocco, D. Voulot, F. Wenander, *Nucl. Instrum. Meth. A* **663**, pp. 1–9 (2012).
- [39] M. A. Fraser, R. M. Jones, M. Pasini, *Phys. Rev. ST Accel. Beams* **14**, p. 020102 (2011).
- [40] F. Zocca, M. A. Fraser, E. Bravin, M. Pasini, D. Voulot, F. Wenander, *Nucl. Instrum. Meth. A* **672**, pp. 21–28 (2012).
- [41] *CERN in a Nutshell* (cited 26 December 2011; <http://public.web.cern.ch/public/en/About/>).
- [42] *The LHC* (cited 26 December 2011; <http://public.web.cern.ch/public/en/lhc/>).
- [43] R. Kirchner, *Nucl. Instrum. Meth. B* **204**, pp. 179–190 (2003).
- [44] V. I. Mishin, V. N. Fedoseyev, H. J. Kluge, V. S. Letokhov, H. L. Ravn, F. Scheerer, Y. Shirakabe, S. Sundell, O. Tengblad, *Nucl. Instrum. Meth. B* **73**, pp. 550–560 (1993).
- [45] D. Forkel-Wirth, G. Bollen, *Hyperfine Interact.* **129** (1 2000).
- [46] D. Habs *et al.*, *Nucl. Instrum. Meth. B* **139**, pp. 128–135 (1998).

- [47] F. Ames, J. Cederkäll, T. Sieber, F. Wenander, *The REX-ISOLDE Facility: Design and Commissioning Report* (CERN, Geneva, 2005).
- [48] R. Rao, O. Kester, T. Sieber, D. Habs, K. Rudolph, *Nucl. Instrum. Meth. A* **427**, pp. 170–176 (1999).
- [49] H. Wollnik, *Optics of charged particles* (Academic Press, Orlando, 1987).
- [50] O. Kester *et al.*, *Nucl. Instrum. Meth. B* **204**, pp. 20–30 (2003).
- [51] P. Schmidt, F. Ames, G. Bollen, O. Forstner, G. Huber, M. Oinonen, J. Zimmer, *Nucl. Phys. A* **701**, pp. 550–556 (2002).
- [52] F. Ames, G. Bollen, P. Delahaye, O. Forstner, G. Huber, O. Kester, K. Reisinger, P. Schmidt, *Nucl. Instrum. Meth. A* **538**, pp. 17–32 (2005).
- [53] F. Wenander, B. Jonson, L. Liljeby, G. H. Nyman, “REXEBIS the Electron Beam Ion Source for the REX-ISOLDE project”, tech. rep. CERN-OPEN-2000-320 (CERN, Geneva, 1998).
- [54] F. Wenander, *J. Instrum.* **5**, p. C10004 (2010).
- [55] F. Wenander, P. Delahaye, R. Scrivens, R. Savreux, REX-ISOLDE Collaboration, *Rev. Sci. Instrum.* **77** (2006).
- [56] T. Sieber, D. Habs, O. Kester, *Proc. of LINAC’04*, pp. 318–320 (Lubeck, 2004).
- [57] T. Sieber, PhD thesis, Ludwig-Maximilians University (Munich, 2001).
- [58] A. Schempp, H. Deitinghoff, M. Ferch, P. Junior, H. Klein, *Nucl. Instrum. Meth. B* **10-11 Part 2**, pp. 831–834 (1985).
- [59] J. Friedrich, A. Schempp, H. Deitinghoff, U. Bessler, H. Klein, R. Veith, *Proc. of PAC’91*, pp. 3044–3046 (San Francisco, 1991).
- [60] C.-M. Kleffner, M. Grieser, D. Habs, R. von Hahn, J. Liebmann, R. Repnow, M. Stampfer, H. Deitinghoff, A. Schempp, E. Jaeschke, S. Papureanu, *Proc. of EPAC’92*, pp. 1340–1342 (Berlin, 1992).
- [61] K.-U. Kühnel, MA thesis, Institute for Applied Physics, Goethe University (Frankfurt, 1999).
- [62] S. Emhofer, MA thesis, Ludwig-Maximilians University (Munich, 1999).

- [63] S. Emhofer, PhD thesis, Ludwig-Maximilians University (Munich, 2004).
- [64] U. Ratzinger, *Proc. of CAS: RF Engineering*, pp. 374–375 (Seeheim, 2000).
- [65] U. Ratzinger, *Proc. of PAC’01*, pp. 567–571 (San Francisco, 1991).
- [66] R. Tiede, U. Ratzinger, H. Podlech, C. Zhang, G. Clemente, *Proc. of HB’08*, pp. 223–230 (Nashville, 2008).
- [67] T. Sieber, MA thesis, Ruprecht-Karls University, Heidelberg (1999).
- [68] R. von Hahn, M. Grieser, D. Habs, E. Jaeschke, C.-M. Kleffner, J. Liebmann, S. Papureanu, R. Repnow, D. Schwalm, M. Stampfer, *Nucl. Instrum. Meth. A* **328**, pp. 270–274 (1993).
- [69] H. Bongers, MA thesis, Ludwig-Maximilians University (Munich, 2003).
- [70] D. Habs *et al.*, *Nucl. Instrum. Meth. B* **204**, pp. 739–745 (2003).
- [71] P. A. Posocco, *Private Communication* (2011).
- [72] D. Voulot, F. Wenander, E. Piselli, R. Scrivens, M. Lindroos, H. Jeppesen, L. Fraile, S. Sturm, P. Delahaye, *Nucl. Instrum. Meth. B* **266**, pp. 4103–4107 (2008).
- [73] H. B. Jeppesen, A. M. Moro, *et al.*, *Phys. Lett. B* **642**, pp. 449–454 (2006).
- [74] J. V. Roosbroeck, C. Guénaut, *et al.*, *Phys. Rev. Lett.* **92**, p. 112501 (2004).
- [75] J. Bonn, G. Huber, H.-J. Kluge, L. Kugler, E. Otten, *Phys. Lett. B* **38**, pp. 308–311 (1972).
- [76] A. Petts, P. A. Butler, T. Grahn, *et al.*, *AIP Conf. Proc.* **1090**, ed. by J. Jolie, A. Zilges, N. Warr, A. Blazhev, pp. 414–418 (2009).
- [77] K. Wimmer *et al.*, *Phys. Rev. Lett.* **105**, p. 252501 (25 2010).
- [78] M. Lindroos, P. Butler, M. Huyse, K. Riisager, *Nucl. Instrum. Meth. B* **266**, pp. 4687–4691 (2008).
- [79] Y. Blumenfeld (chair), “Minutes of the 1st HIE-ISOLDE Physics Steering Committee: Investigating how HIE-ISOLDE technical developments meet the physics requirements”, (2010).
- [80] K. Riisager, P. Butler, M. Huyse, R. Krücken, *HIE-ISOLDE: the scientific opportunities* (CERN, Geneva, 2007).

- [81] M. Lindroos, T. Nilsson, *HIE-ISOLDE: the technical options* (CERN, Geneva, 2006).
- [82] K. Hanke *et al.*, *Proc. of IPAC'11*, pp. 2526–2528 (St Sebastian, 2011).
- [83] M. Vretenar *et al.*, *Proc. of IPAC'11*, pp. 900–902 (St Sebastian, 2011).
- [84] F. Wenander, T. Lamy, A. C. Müller, “Report on Beam Purification at REX-ISOLDE and ISOLDE PHOENIX charge breeder”, T-J03-5 (EURONS and CERN-ISOLDE, Geneva, 2008).
- [85] H. Frånberg, P. Delahaye, J. Billowes, K. Blaum, R. Catherall, F. Duval, O. Gianfrancesco, T. Giles, A. Jokinen, M. Lindroos, D. Lunney, E. Mane, I. Podadera, *Nucl. Instrum. Meth. B* **266**, pp. 4502–4504 (2008).
- [86] I. P. Aliseda, T. Fritioff, T. Giles, A. Jokinen, M. Lindroos, F. Wenander, *Nucl. Phys. A* **746**, pp. 647–650 (2004).
- [87] A. C. Müller, R. E. Laxdal, O. Kester, “International Advisory Board for the REX-ISOLDE Linac Energy Upgrade”, tech. rep. (CERN, Geneva, 2006).
- [88] M. Kelly, *Proc. of PAC'09*, pp. 699–703 (Vancouver, 2009).
- [89] *Computer Simulation Technology - Microwave Studio (CST - MWS)* (cited 26 December 2011; <http://www.cst.com/>).
- [90] A. D’Elia, R. M. Jones, M. Pasini, *Proc. of SRF'09*, pp. 609–613 (Berlin, 2009).
- [91] G. Lanza, S. Calatroni, L. Marques Antunes Ferreira, A. Gustafsson, M. Pasini, P. Trilhe, V. Palmieri, *Proc. of SRF'09*, pp. 801–805 (Berlin, 2009).
- [92] G. Lanza, S. Calatroni, O. Capatina, B. Delaup, L. Marques Antunes Ferreira, M. Pasini, M. Therasse, *Proc. of SRF'11* (Chicago, to be published).
- [93] J. K. Chambrillon, O. Brunner, P. Maesen, O. Pirotte, M. Therasse, B. Vullierme, W. Weingarten, *Proc. of SRF'11* (Chicago, to be published).
- [94] M. Pasini, S. Calatroni, O. Capatina, M. Therasse, A. D’Elia, M. A. Fraser, *Proc. of SRF'11* (Chicago, to be published).
- [95] M. Pasini, R. E. Laxdal, “ISAC-II: Beam Studies with Multi-charge Beams”, tech. rep. TRI-DN-01-08 (TRIUMF, Vancouver, 2001).

- [96] R. Wideröe, *Arch. Elektrotech.* **21**, pp. 387–406 (4 1928).
- [97] L. W. Alvarez, H. Bradner, J. V. Franck, H. Gordon, J. D. Gow, L. C. Marshall, F. Oppenheimer, W. K. H. Panofsky, C. Richman, J. R. Woodyard, *Review of Scientific Instruments* **26**, pp. 111–133 (1955).
- [98] T. P. Wangler, *RF linear accelerators; 2nd rev. version* (Wiley, Weinheim, 2008).
- [99] *ANSYS High Frequency Structure Simulator (HFSS)* (cited 26 December 2011; <http://www.ansoft.com/products/hf/hfss/>).
- [100] J. Miles, Ed., *CAS - CERN Accelerator School : RF Engineering for Particle Accelerators*, CERN-2005-003, CERN (CERN, Geneva, 2000).
- [101] J. R. Delayen, *Nucl. Instrum. Meth. A* **259**, pp. 341–357 (1987).
- [102] I. Ben-Zvi, J. Brennan, *Nucl. Instrum. Methods* **212**, pp. 73–79 (1983).
- [103] L. M. Bollinger, *Annu. Rev. Nucl. Part. S.* **36**, 475–503 (1986).
- [104] H. Padamsee, T. Hays, J. Knobloch, *RF superconductivity for accelerators; 2nd ed.* (Wiley, Weinheim, 2008).
- [105] N. Delruelle, *Private Communication* (2011).
- [106] H. Wiedemann, *Particle Accelerator Physics; 3rd ed.* (Springer, Berlin, 2007).
- [107] K. Crandall, D. Rusthoi, “TRACE 3-D Documenation”, tech. rep. (LANL, Los Alamos, 1997).
- [108] V. N. Aseev, P. N. Ostroumov, E. S. Lessner, B. Mustapha, *Proc. of PAC’05*, pp. 2053–2055 (Knoxville, 2005).
- [109] F. Gerigk, “The Effect of Phase Slippage in Multicell Cavities on Longitudinal Beam Dynamics”, tech. rep. PS/RF Note 2001-009, CERN-NUFACT-NOTE 2001-072 (CERN, Geneva, 2001).
- [110] J. R. Delayen, *Nucl. Instrum. Meth. A* **258**, pp. 15–25 (1987).
- [111] H. Goldstein, C. Poole, J. Safko, *Classical mechanics; 3rd ed* (Addison-Wesley, Reading, 2002).
- [112] R. L. Gluckstern, *IEEE T. Nucl. Sci.* **16**, pp. 194–201 (1969).

- [113] R. L. Gluckstern, “Transverse Beam Growth Due to Longitudinal Coupling in Linear Accelerators”, Accelerator Dept. Internal Report AADD-120 (BNL, Upton, 1966).
- [114] Y. Senichev, A. Bogdanov, R. Maier, *Phys. Rev. ST Accel. Beams* **6**, p. 124001 (12 2003).
- [115] M. Reiser, *Theory and Design of Charged Particle Beams; 2nd ed.* (Wiley, Weinheim, 2008), chap. 3.3.1, pp. 61–63.
- [116] E. M. McMillan, *Phys. Rev.* **80**, p. 493 (3 1950).
- [117] A. Facco, V. Zviagintsev, *Proc. of PAC’01*, pp. 1095–1097 (Chicago, 2001).
- [118] A. Facco, V. Zvyagintsev, *Phys. Rev. ST Accel. Beams* **14**, p. 070101 (7 2011).
- [119] E. D. Courant, M. S. Livingston, H. S. Snyder, *Phys. Rev.* **88**, pp. 1190–1196 (5 1952).
- [120] T. P. Wangler, *RF linear accelerators; 2nd rev. version* (Wiley, Weinheim, 2008), chap. 7.6, pp. 209–211.
- [121] M. Eshraqi, G. Franchetti, A. M. Lombardi, *Phys. Rev. ST Accel. Beams* **12**, p. 024201 (2 2009).
- [122] G. Franchetti, *Phys. Rev. ST Accel. Beams* **4**, p. 074001 (7 2001).
- [123] V. Kumar, *Am. J. Phys.* **77**, pp. 737–741 (2009).
- [124] L. Smith, R. L. Gluckstern, *Rev. Sci. Instrum.* **26**, pp. 220–228 (1955).
- [125] E. A. Wadlinger, *IEEE T. Nucl. Sci.* **26**, pp. 3511–3513 (1979).
- [126] P. M. Lapostolle, A. L. Septier, Eds., *Linear accelerators* (North-Holland, Amsterdam, 1970), chap. 1.2d, pp. 797–804.
- [127] I. M. Kapchinskiy, *Theory of resonance linear accelerators*, transl. from the Russian (Harwood, 1985).
- [128] K. Wille, *The physics of particle accelerators: An introduction* (Oxford Univ. Press, Oxford, 2000), chap. 3.10, pp. 83–87.
- [129] H. Wiedemann, *Particle Accelerator Physics; 3rd ed.* (Springer, Berlin, 2007), chap. 5.1.1, p. 155.

- [130] T. P. Wangler, *RF linear accelerators; 2nd rev. version* (Wiley, Weinheim, 2008), chap. 6.5, pp. 182–186.
- [131] R. Duperrier, *Proc. of HB'10*, pp. 576–579 (Morschach, 2010).
- [132] M. J. Rhee, *Phys. Fluids* **29**, pp. 3495–3496 (1986).
- [133] D. V. Gorelov, P. N. Ostroumov, “The LANA Computer Code for Beam Dynamic Simulation in a Multi Cavity Linac”, tech. rep. (INR, RAS, Moscow, 1995).
- [134] M. Reiser, *Theory and Design of Charged Particle Beams; 2nd ed.* (Wiley, Weinheim, 2008), chap. 5.3.4, p. 323.
- [135] T. P. Wangler, *RF linear accelerators; 2nd rev. version* (Wiley, Weinheim, 2008), chap. 9, pp. 282–340.
- [136] B. Carlsten, “Emittance of a Rotated Asymmetric Beam”, Memorandum AT-7:90-233 (LANL, Los Alamos, 1990).
- [137] M. Weiss, “Bunching of intense proton beams with six-dimensional matching to the linac acceptance”, tech. rep. CERN-MPS-LIN-73-2 (CERN, Geneva, 1973).
- [138] R. Baartman, “RMS Emittance Growth due to Intrinsic Solenoid Aberrations”, addendum to TRI-DN-99-8 (TRIUMF, Vancouver, 2006).
- [139] A. P. Fateev, P. N. Ostroumov, *Nucl. Instrum. Methods* **222**, pp. 420–427 (1984).
- [140] Los Alamos Accelerator Code Group, *LAACG Design Codes* (cited 26 December 2011; <http://laacg1.lanl.gov/>).
- [141] R. Tiede, G. Clemente, H. Podlech, U. Ratzinger, A. Sauer, S. Minaev, *Proc. of EPAC'10*, pp. 2194–2196 (Edinburgh, 2006).
- [142] A. Perrin, J. F. Amand, T. Mütze, “Travel v4.07 User Manual”, tech. rep. (CERN, Geneva, 2007).
- [143] T. Sieber, O. Kester, D. Habs, S. Emhofer, K. Rudolph, H. Bongers, A. Schempp, U. Ratzinger, *Nucl. Phys. A* **701**, pp. 656–660 (2002).
- [144] T. Sieber, H. Bongers, S. Emhofer, D. Habs, O. Kester, K. Rudolph, A. Schempp, C. Welsch, K.-U. Kühnel, *Proc. of PAC'99*, pp. 3516–3518 (New York, 1999).

- [145] S. Emhofer, O. Kester, D. Habs, T. Sieber, H. Bongers, K. Rudolph, U. Ratzinger, *Maier-Leibnitz-Laboratorium Annual Report*, p. 74 (1999).
- [146] O. Kester, D. Habs, T. Sieber, S. Emhofer, K. Rudolph, R. von Hahn, H. Podlech, R. Repnow, D. Schwalm, U. Ratzinger, A. Schempp, REX-ISOLDE Collaboration, *Proc. of LINAC'00*, pp. 351–355 (Monterey, 2000).
- [147] T. Sieber, F. Ames, J. Cederkäll, S. Emhofer, D. Habs, O. Kester, K. Reisinger, K. Rudolph, R. von Hahn, B. Wolf, REX-ISOLDE Collaboration, *Proc. of LINAC'02*, pp. 291–295 (Gyeongju, 2002).
- [148] S. Emhofer, F. Ames, J. Cederkäll, D. Habs, O. Kester, K. Rudolph, T. Sieber, *Proc. of PAC'03*, pp. 2869–2871 (Portland, 2003).
- [149] O. Kester, T. Sieber, H. Bongers, S. Emhofer, K. Rudolph, W. Carli, D. Habs, *Proc. of PAC'03*, pp. 2872–2874 (California, 2003).
- [150] O. Kester, D. Habs, S. Emhofer, K. Rudolph, T. Sieber, F. Wenander, F. Ames, P. Delahaye, M. Lindroos, P. Butler, R. von Hahn, H. Scheit, R. Repnow, D. Schwalm, REX-ISOLDE Collaboration, *Proc. of LINAC'04*, pp. 18–22 (Lubeck, 2004).
- [151] R. von Hahn, M. Grieser, R. Repnow, D. Schwalm, O. Kester, S. Emhofer, T. Sieber, H. Podlech, *Proc. of EPAC'02*, pp. 975–977 (Paris, 2002).
- [152] M. A. Fraser, P. A. Posocco, M. Pasini, “Benchmarking of the REX-ISOLDE RFQ Beam Dynamics Simulations”, tech. rep. CERN-BE-Note (CERN, Geneva, to be published).
- [153] A. D’Elia, *Private Communication* (2010).
- [154] J. C. Slater, *Microwave Electronics* (Van Nostrand, 1950), pp. 80–81.
- [155] L. C. Maier, J. C. Slater, *J. Appl. Phys.* **23**, pp. 68–77 (1952).
- [156] S. W. Kitchen, A. D. Schelberg, *J. Appl. Phys.* **26**, pp. 618–621 (1955).
- [157] G. D. Michele, S. Ramberger, “An Automated Test Bench for the Long. E Field Measurements in DTL, CCL and other Cavities”, CERN-sLHC Project Note (CERN, Geneva, to be published).

- [158] A. P. French, *Vibrations and Waves* (Norton, New York, 1971).
- [159] M. Marchetto, J. Berring, R. E. Laxdal, *Proc. of EPAC'08*, pp. 3440–3442 (Genoa, 2008).
- [160] D. Voulot, “REX-linac Emittance Measurements”, tech. rep. CERN-BE-Note-2009-012 (CERN, Geneva, 2009).
- [161] M. A. Fraser, R. M. Jones, M. Pasini, D. Voulot, *Proc. of IPAC'10*, pp. 4701–4703 (Kyoto, 2010).
- [162] S. Emhofer, *Private Communication* (2010).
- [163] U. Raich, “The Pepperpot Measurement Bench”, tech. rep. CERN-BE-Note-2010-003 (CERN, Geneva, 2010).
- [164] T. Milosic, P. Forck, *Proc. of DIPAC'09*, pp. 330–332 (Basel, 2009).
- [165] A. Pisent *et al.*, *Proc. of LINAC'06*, pp. 227–229 (Knoxville, 2006).
- [166] D. H. Dowell, P. R. Bolton, J. E. Clendenin, S. M. Gierman, C. G. Limborg, B. F. Murphy, J. F. Schmerge, T. Shaftan, *Nucl. Instrum. Meth. A* **507**, pp. 331–334 (2003).
- [167] J. Rodnizki, A. Perry, L. Weissman, *Proc. of LINAC'10* (Tsukuba, 2010).
- [168] Y. V. Bylinsky, A. V. Feschenko, P. N. Ostroumov, *Proc. of PAC'91*, pp. 3062–3063 (San Francisco, 1991).
- [169] P. Forck, *Lecture Notes on Beam Instrumentation and Diagnostics* (Presented at JUAS, Archamps, 2009).
- [170] P. N. Ostroumov, *ESS Bilibao Initiative Workshop* (Bilbao, 2009).
- [171] P. Strehl, *Beam Instrumentation and Diagnostics* (Springer, Berlin, 2006).
- [172] F. Wenander, *Private Communication* (2011).
- [173] J.-C. Gayde *et al.*, “ISOLDE: Survey of the Existing REX Linac”, tech. rep. EDMS Doc. No. 738489 (CERN, Geneva, 2006).
- [174] K. Kruglov, L. Weissman, P. Van den Bergh, A. Andreyev, M. Huyse, P. Van Duppen, *Nucl. Instrum. Meth. A* **441**, pp. 595–604 (2000).

- [175] E. Piselli, *Private Communication* (2010).
- [176] O. Kester, A. Bechtold, *Private Communication* (1998).
- [177] M. A. Fraser, R. M. Jones, M. Pasini, D. Voulot, *Proc. of LINAC'10*, pp. 950–952 (Tsukuba, 2010).
- [178] G. Deferne *et al.*, “Single Stretched Wire Magnetic Measurements of the MTQ6/MQT7 Triplet of the ISOLDE Facility”, tech. rep. EDMS Doc. No. 1119870 v.1 (CERN, Geneva, 2010).
- [179] U. Rohrer, W. Joho, *Introduction of 2-Dimensional Beam Tomography for Monitoring Transverse Beam Emittances at SIN (Annual Report, PSI, 1982)* (cited 26 December 2011; [http://aea.web.psi.ch/Urs\\_Rohrer/MyWeb/ment.htm](http://aea.web.psi.ch/Urs_Rohrer/MyWeb/ment.htm)).
- [180] G. Minerbo, *Comput. Vision Graph.* **10**, pp. 48–68 (1979).
- [181] C. T. Mottershead, *IEEE T. Nucl. Sci.* **32**, pp. 1970–1972 (1985).
- [182] P. N. Ostroumov, *New J. Phys.* **8**, p. 281 (2006).
- [183] N. W. McLachlan, *Theory and application of Mathieu functions* (Clarendon Press, Oxford, 1951).
- [184] P. N. Ostroumov, *Proc. of LINAC'02*, pp. 64–66 (Gyeongju, 2002).
- [185] M. Pasini, M. A. Fraser, R. M. Jones, D. Voulot, *Proc. of LINAC'08*, pp. 127–129 (Victoria, 2008).
- [186] M. A. Fraser, M. Pasini, “Beam Dynamics Studies of the HIE-LINAC at CERN”, CERN-BE-Note (CERN, Geneva, to be published).
- [187] P. N. Ostroumov, K. W. Shepard, *Phys. Rev. ST Accel. Beams* **4**, p. 110101 (2001).
- [188] P. N. Ostroumov, K. W. Shepard, *Proc. of LINAC'02*, pp. 473–475 (Gyeongju, 2002).
- [189] M. A. Fraser, R. M. Jones, M. Pasini, *Proc. of PAC'09*, pp. 3753–3755 (Vancouver, 2009).

- [190] M. A. Fraser, M. Pasini, “Misalignment and Error Studies of the High Energy Section of the HIE-ISOLDE Linac”, tech. rep. CERN-BE-Note (CERN, Geneva, to be published).
- [191] K. Wille, *The physics of particle accelerators: An introduction* (Oxford Univ. Press, Oxford, 2000), chap. 10.4.2, pp. 281–287.
- [192] M. Pasini, R. E. Laxdal, A. Bandyopadhyay, “Misalignment Studies of the Medium Beta Section of the ISAC-II Superconducting Linac”, tech. rep. TRI-DN-03-03 (TRIUMF, Vancouver, 2003).
- [193] M. Schuh, F. Gerigk, J. Tückmantel, C. P. Welsch, *Phys. Rev. ST Accel. Beams* **14**, p. 051001 (2011).
- [194] J. Bauche, *Proc. of MT-22* (Marseille, to be published).
- [195] L. Williams, A. Bouzoud, N. Delruelle, J.-C. Gayde, Y. Leclercq, M. Pasini, J.-P. Tock, G. Vandoni, *Proc. of IPAC’11*, pp. 319–321 (St Sebastian, 2011).
- [196] K. Hashemi, *BCAM Home Page*, Brandeis University (cited 26 December 2011; <http://alignment.hep.brandeis.edu/Devices/BCAM/>).
- [197] K. Blaum *et al.*, “TDR: Storage Ring Facility at HIE-ISOLDE”, tech. rep. (CERN, Geneva, to be published).
- [198] V. A. Verzilov, R. E. Laxdal, M. Marchetto, W. R. Rawnsley, *Proc. of DIPAC’07*, pp. 247–249 (Venice, 2007).
- [199] J. F. Ziegler, *SRIM - The Stopping Range of Ions in Matter* (cited 26 December 2011; <http://www.srim.org/>).
- [200] F. Zocca, M. A. Fraser, E. Bravin, M. Pasini, D. Voulot, F. Wenander, *Proc. of DIPAC’11*, pp. 131–133 (Hamburg, 2011).
- [201] P. Forck, F. Heymach, U. Meyer, P. Moritz, P. Strehl, *Proc. of DIPAC’99*, pp. 186–189 (Chester, 1999).

- [202] E. Griesmayer, H. Pernegger, D. Dobos, F. Wenander, J. Bergoz, H. Bayle, H. Frais-Kölbl, J. Leinweber, T. Aumeyr, “High-Resolution Energy and Intensity Measurements with CVD Diamond at REX-ISOLDE”, BE-Note-2009-028 (CERN, Geneva, 2009).
- [203] G. Espinosa, R. Silva, *J. Radioanal. Nucl. Ch.* **248**, pp. 575–578 (3 2001).
- [204] J. van de Walle, PhD thesis, Katholieke Universiteit Leuven (Leuven, 2006).
- [205] J. R. Delayen, *Private Communication* (2009).
- [206] I. S. Gradshteyn, A. Jeffrey, I. M. Ryzhik, *Table of integrals, series, and products; 5th ed.* transl. from the Russian (Academic Press, San Diego, 1994).
- [207] M. A. Fraser, M. Pasini, A. D’Elia, R. M. Jones, *Proc. of SRF’09*, pp. 604–608 (Berlin, 2009).
- [208] M. Pasini, R. E. Laxdal, P. N. Ostroumov, *Proc. of EPAC’02*, pp. 933–935 (Paris, 2002).
- [209] S. M. Lund, C. J. Wootton, E. P. Lee, *Nucl. Instrum. Meth. A* **606**, pp. 56–63 (2009).

REX-ISOLDE TIME STRUCTURE

With reference to Figure A.1:

- **A** - Proton bunches strike the ISOLDE target at a rate dependent on the supercycle.
- **B** - Release of radionuclides from the target is heavily modulated by the PSB cycle.
- **C** - REXTRAP accumulates, bunches and cools the quasi-continuous beam.
- **D** - REXEBIS breeds synchronously with REXTRAP at e.g. 10 Hz.
- **E** - Linac is synchronised to the timing of the REXEBIS with a duty cycle permitting an rf pulse of up to  $1000 \mu\text{s}$  at 100 Hz.
- **F** - Extracted beam from the REXEBIS:
  - **Self-extraction** - the pulse length is typically  $50 \mu\text{s}$ , decaying exponentially.
  - **Slow extraction** - the pulse length is typically as long as 1 ms.

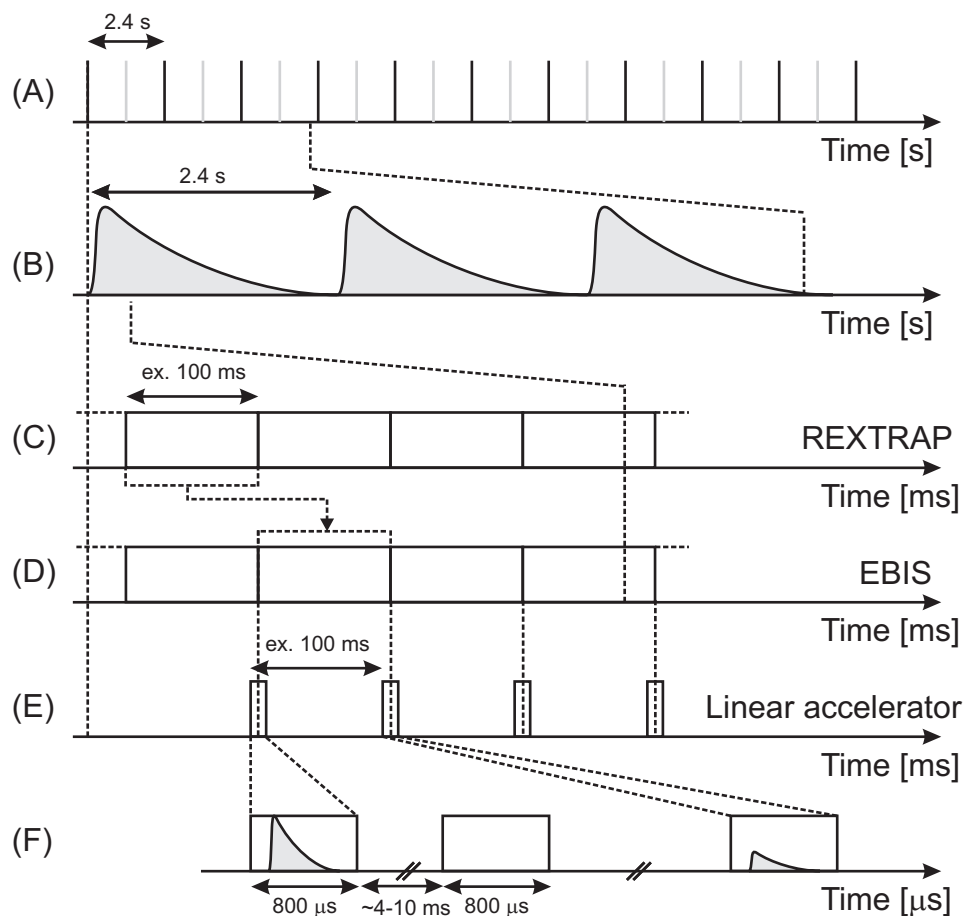


Figure A.1: REX beam time structure. Figure courtesy of J. van de Walle. Reprinted with permission from Figure 3.11 of [204].

SECOND-ORDER TRANSIT-TIME FACTORS

As was introduced in Chapter 3.3.4, the energy gain in a cavity can be written to second-order as,

$$\Delta W = qV_0 T(\beta) \cos \phi + \frac{(qV_0)^2}{W} (T^{(2)}(\beta) + T_s^{(2)}(\beta) \sin 2\phi). \quad (\text{B.0.1})$$

In this appendix analytic expressions for the transit-time factors  $T^{(2)}$  and  $T_s^{(2)}$  will be derived for a two-gap cavity operating in  $\pi$ -mode, assuming that the field level is constant throughout each gap, i.e. in the square-wave approximation.

## B.1 Derivation of $T^{(2)}$ for a Two-gap Resonator

The expression for the first-order transit-time factor can be written in a simpler form:

$$T(x) = \text{sinc} x \sin \alpha x \quad \text{where,} \quad x = \frac{\pi g}{\beta \lambda} \quad \text{and} \quad \alpha = \frac{\beta_g \lambda}{2g} = \frac{L}{g}.$$

The derivation is straightforward using the result published in [110],

$$T^{(2)}(x) = -\frac{x}{4} T(x) T'(x),$$

and one can write,

$$T^{(2)}(x) = -\frac{T(x)}{4} [\cos x \sin \alpha x + \alpha \sin x \cos \alpha x - T(x)].$$

## B.2 Derivation of $T_s^{(2)}$ for a Two-gap Resonator

Starting from the result published in [110],

$$T_s^{(2)} = -\frac{x}{8\pi} \int_{-\infty}^{+\infty} \frac{T'(x+x')T(x-x') - T(x+x')T'(x-x')}{x'} dx',$$

the integral can be split into two parts, I and II,

$$T_s^{(2)} = -\frac{x}{8\pi} \int_{-\infty}^{+\infty} \underbrace{\frac{T'(x+x')T(x-x')}{x'}}_I - \underbrace{\frac{T(x+x')T'(x-x')}{x'}}_{II} dx'.$$

By simplifying the expressions inside the integral, part I can be expressed,

$$\begin{aligned} I &= \underbrace{\frac{1}{x'(x^2-x'^2)} \sin(x-x') \cos(x+x') \sin(\alpha(x+x')) \sin(\alpha(x-x'))}_a \\ &\quad + \underbrace{\frac{\alpha}{x'(x^2-x'^2)} \sin(x-x') \sin(x+x') \sin(\alpha(x-x')) \cos(\alpha(x+x'))}_b \\ &\quad - \underbrace{\frac{1}{x'(x+x')(x^2-x'^2)} \sin(x-x') \sin(x+x') \sin(\alpha(x-x')) \sin(\alpha(x+x'))}_c. \end{aligned}$$

Similarly, part II can be expressed,

$$\begin{aligned} II &= \underbrace{\frac{1}{x'(x^2-x'^2)} \sin(x+x') \cos(x-x') \sin(\alpha(x+x')) \sin(\alpha(x-x'))}_a \\ &\quad + \underbrace{\frac{\alpha}{x'(x^2-x'^2)} \sin(x-x') \sin(x+x') \sin(\alpha(x+x')) \cos(\alpha(x-x'))}_b \\ &\quad - \underbrace{\frac{1}{x'(x-x')(x^2-x'^2)} \sin(x-x') \sin(x+x') \sin(\alpha(x-x')) \sin(\alpha(x+x'))}_c. \end{aligned}$$

Considering pairs of terms separately and using the trigonometric identities quoted, one can write,

$$\begin{aligned} \text{I.a} - \text{II.a} &= \frac{\overbrace{\sin(\alpha(x-x')) \sin(\alpha(x+x'))}^{\frac{\cos(2\alpha x') - \cos(2\alpha x)}{2}}}{x'(x^2-x'^2)} \\ &\quad \times \underbrace{[\sin(x-x') \cos(x+x') - \sin(x+x') \cos(x-x')]}_{\sin(-2x')} \\ &= \frac{\cos(2\alpha x) \sin(2x')}{2x'(x^2-x'^2)} - \frac{\sin(2x') \cos(2\alpha x')}{2x'(x^2-x'^2)}. \end{aligned}$$

$$\begin{aligned}
 \text{I.b} - \text{II.b} &= \frac{\overbrace{\alpha \sin(x-x') \sin(x+x')}^{\frac{\cos(2x') - \cos(2x)}{2}}}{x'(x^2 - x'^2)} \\
 &\quad \times \underbrace{[\sin(\alpha(x-x')) \cos(\alpha(x+x')) - \sin(\alpha(x+x')) \cos(\alpha(x-x'))]}_{\sin(-2\alpha x')} \\
 &= \frac{\alpha \cos(2x) \sin(2\alpha x')}{2x'(x^2 - x'^2)} - \frac{\alpha \sin(2\alpha x') \cos(2x')}{2x'(x^2 - x'^2)}.
 \end{aligned}$$

$$\text{I.c} - \text{II.c} = \left[ \frac{1}{x-x'} - \frac{1}{x+x'} \right] \frac{\overbrace{\sin(x-x') \sin(x+x')}^{\frac{\cos(2x') - \cos(2x)}{2}} \overbrace{\sin(\alpha(x-x')) \sin(\alpha(x+x'))}^{\frac{\cos(2\alpha x') - \cos(2\alpha x)}{2}}}{x'(x^2 - x'^2)}$$

$$\begin{aligned}
 &= \frac{\overbrace{\cos(2x') \cos(2\alpha x')}^{\frac{\cos(2(1+\alpha)x') + \cos(2(1-\alpha)x')}{2}}}{2(x^2 - x'^2)^2} - \frac{\cos(2\alpha x) \cos(2x')}{2(x^2 - x'^2)^2} \\
 &\quad - \frac{\cos(2x) \cos(2\alpha x')}{2(x^2 - x'^2)^2} + \frac{\cos(2x) \cos(2\alpha x)}{2(x^2 - x'^2)^2} \\
 &= \frac{\cos(2(1+\alpha)x')}{4(x^2 - x'^2)^2} + \frac{\cos(2(1-\alpha)x')}{4(x^2 - x'^2)^2} - \frac{\cos(2\alpha x) \cos(2x')}{2(x^2 - x'^2)^2} \\
 &\quad - \frac{\cos(2x) \cos(2\alpha x')}{2(x^2 - x'^2)^2} + \frac{\cos(2x) \cos(2\alpha x)}{2(x^2 - x'^2)^2}
 \end{aligned}$$

These expressions can be integrated using the standard integrals collected in Appendix B.4,

$$\begin{aligned}
 -\frac{x}{8\pi} \int_{-\infty}^{+\infty} (\text{I.a} - \text{II.a}) dx' &= \frac{x}{16\pi} \underbrace{\int_{-\infty}^{+\infty} \frac{\sin(2x') \cos(2\alpha x')}{x'(x^2 - x'^2)} dx'}_{f \#3(b>a)} \\
 &\quad - \frac{x \cos(2\alpha x)}{16\pi} \underbrace{\int_{-\infty}^{+\infty} \frac{\sin(2x')}{x'(x^2 - x'^2)} dx'}_{f \#4} \\
 &= \frac{x}{16\pi} \left[ \frac{\pi \sin 2x \sin 2\alpha x}{x^2} \right] - \frac{x \cos 2\alpha x}{16\pi} \left[ \frac{\pi(1 - \cos 2x)}{x^2} \right] \\
 &= \frac{1}{16x} [\sin 2x \sin 2\alpha x - (1 - \cos 2x) \cos 2\alpha x]. \quad (\text{B.2.1})
 \end{aligned}$$

$$\begin{aligned}
 -\frac{x}{8\pi} \int_{-\infty}^{+\infty} (\text{I.b} - \text{II.b}) dx' &= \frac{\alpha x}{16\pi} \underbrace{\int_{-\infty}^{+\infty} \frac{\sin(2\alpha x') \cos(2x')}{x'(x^2 - x'^2)} dx'}_{f \#3(a>b)} \\
 &\quad - \frac{\alpha x \cos(2x)}{16\pi} \underbrace{\int_{-\infty}^{+\infty} \frac{\sin(2\alpha x')}{x'(x^2 - x'^2)} dx'}_{f \#4} \\
 &= \frac{\alpha x}{16\pi} \left[ \frac{\pi(1 - \cos 2x \cos 2\alpha x)}{x^2} \right] - \frac{\alpha x \cos 2x}{16\pi} \left[ \frac{\pi(1 - \cos 2\alpha x)}{x^2} \right] \\
 &= \frac{\alpha}{16x} [1 - \cos 2x]. \tag{B.2.2}
 \end{aligned}$$

$$\begin{aligned}
 -\frac{x}{8\pi} \int_{-\infty}^{+\infty} (\text{I.c} - \text{II.c}) dx' &= -\frac{x}{32\pi} \underbrace{\int_{-\infty}^{+\infty} \frac{\cos(2(1+\alpha)x')}{(x^2 - x'^2)^2} dx'}_{f \#5} + \underbrace{\int_{-\infty}^{+\infty} \frac{\cos(2(1-\alpha)x')}{(x^2 - x'^2)^2} dx'}_{f \#5} \\
 &\quad + \frac{x \cos(2\alpha x)}{16\pi} \underbrace{\int_{-\infty}^{+\infty} \frac{\cos(2x')}{(x^2 - x'^2)^2} dx'}_{f \#5} \\
 &\quad + \frac{x \cos(2x)}{16\pi} \underbrace{\int_{-\infty}^{+\infty} \frac{\cos(2\alpha x')}{(x^2 - x'^2)^2} dx'}_{f \#5} \\
 &\quad - \frac{x \cos(2x) \cos(2\alpha x)}{16\pi} \underbrace{\int_{-\infty}^{+\infty} \frac{1}{(x^2 - x'^2)^2} dx'}_{f \#6} \\
 &= -\frac{x}{32\pi} \left[ \frac{\pi}{2x^3} \{ \sin(2(1+\alpha)x') - (2(1+\alpha)x') \cos(2(1+\alpha)x') \} \right] \\
 &\quad - \frac{x}{32\pi} \left[ \frac{\pi}{2x^3} \{ \sin(2(1-\alpha)x') - (2(1-\alpha)x') \cos(2(1-\alpha)x') \} \right] \\
 &\quad + \frac{x \cos(2\alpha x)}{16\pi} \left[ \frac{\pi}{2x^3} \{ \sin(2x) - 2x \cos(2x) \} \right] \\
 &\quad + \frac{x \cos(2x)}{16\pi} \left[ \frac{\pi}{2x^3} \{ \sin(2\alpha x) - 2\alpha x \cos(2\alpha x) \} \right] \\
 &= -\frac{x}{32\pi} \left[ \frac{\pi}{x^3} \{ -2\alpha x \cos(2\alpha x) \cos(2x) + \sin(2\alpha x)(\cos(2x) + 2x \sin(2x)) \} \right] \\
 &\quad + \frac{x \cos(2\alpha x)}{16\pi} \left[ \frac{\pi}{2x^3} \{ \sin(2x) - 2x \cos(2x) \} \right] \\
 &\quad + \frac{x \cos(2x)}{16\pi} \left[ \frac{\pi}{2x^3} \{ \sin(2\alpha x) - 2\alpha x \cos(2\alpha x) \} \right]
 \end{aligned}$$

$$= \frac{1}{16x^2} \left[ \frac{\sin 2x \cos 2\alpha x}{2} - x(\sin 2x \sin 2\alpha x + \cos 2x \cos 2\alpha x) \right]. \quad (\text{B.2.3})$$

Finally, the derivation is completed by putting together all of the terms in parts I and II and summing Equations B.2.1, B.2.2 and B.2.3,

$$T_s^{(2)}(x) = \frac{\alpha x \sin^2 x}{8 x^2} + \frac{\cos 2\alpha x}{16x} \left[ \frac{\sin 2x}{2x} - 1 \right].$$

### B.3 $T^{(2)}$ and $T_s^{(2)}$ for a Single Gap Resonator

The second-order transit-time factors for a two-gap resonator can be compared to those for a single gap shown below [205],

$$T^{(2)}(x) = -\frac{T(x)}{4} [\cos x - T(x)] \quad \text{and} \quad T_s^{(2)}(x) = \frac{1}{8x} [1 - T(2x)],$$

where,

$$T(x) = \frac{\sin x}{x}.$$

### B.4 Standard Integrals

The standard integrals were found in the tables of [206]. The equation reference numbers are quoted.

$$\int \#1 : [206] (3.741.2):$$

$$\int_{-\infty}^{+\infty} \frac{\sin(ax) \cos(bx)}{x} dx = \begin{cases} \pi & \text{if } a > b \geq 0 \\ \frac{\pi}{2} & \text{if } a = b \geq 0 \\ 0 & \text{if } b > a \geq 0 \end{cases}$$

$\int$  #2 : [206] (3.742.7):

$$\int_{-\infty}^{+\infty} \frac{x \sin(ax) \cos(bx)}{c^2 - x^2} dx = \begin{cases} -\pi \cos(ac) \cos(bc) & \text{if } a > b > 0 \\ -\frac{\pi}{2} \cos(2ac) & \text{if } a = b \geq 0 \\ \pi \sin(ac) \sin(bc) & \text{if } b > a > 0 \end{cases}$$

$\int$  #3 :

$$\begin{aligned} \int_{-\infty}^{+\infty} \frac{\sin(ax) \cos(bx)}{x(c^2 - x^2)} dx &= \frac{1}{c^2} \underbrace{\int_{-\infty}^{+\infty} \frac{\sin(ax) \cos(bx)}{x} dx}_{f \#1} \qquad \qquad \qquad \text{(B.4.1)} \\ &\quad + \frac{1}{c^2} \underbrace{\int_{-\infty}^{+\infty} \frac{x \sin(ax) \cos(bx)}{c^2 - x^2} dx}_{f \#2} \\ &= \begin{cases} \frac{\pi}{c^2} (1 - \cos(ac) \cos(bc)) & \text{if } a > b > 0 \\ \frac{\pi}{c^2} \sin(ac) \sin(bc) & \text{if } b > a > 0 \\ -\frac{\pi}{4} \cos(2ac) & \text{if } a = b \geq 0 \end{cases} \end{aligned}$$

$\int$  #4 : [206] (3.725.2):

$$\int_{-\infty}^{+\infty} \frac{\sin(ax)}{x(b^2 - x^2)} dx = \frac{\pi}{b^2} (1 - \cos ab).$$

$\int$  #5 : [206] (3.728.5):

$$\lim_{c \rightarrow b} \int_{-\infty}^{+\infty} \frac{\cos(ax)}{(b^2 - x^2)(c^2 - x^2)} dx = \int_{-\infty}^{+\infty} \frac{\cos(ax)}{(b^2 - x^2)^2} dx = \frac{\pi}{2b^3} [\sin(ab) - ab \cos(ab)].$$

$\int$  #6 : [206] (2.172) and (2.173.1):

$$\int_{-\infty}^{+\infty} \frac{1}{(a^2 - x^2)^2} dx = 0.$$

LONGITUDINAL TRANSFER MATRICES FOR  
BUNCHER CAVITIES

The transfer matrix description of the bunching cavity is discussed. The thin lens result is derived before the transfer matrix for a multi-gap buncher is approximated.

## C.1 Thin Lens Buncher Cavity

Using Equation 3.3.29, the energy spread of the beam after a thin cavity can be written,

$$\Delta W_1 = qV_{\text{eff}} (\cos \phi - \cos \phi_s) + \Delta W_0.$$

If the bunch length is small, i.e. if  $\Delta\phi_0 \ll 1$ , then the equation can be approximated as,

$$\Delta W_1 = -qV_{\text{eff}} \sin \phi_s \Delta\phi_0 + \Delta W_0, \quad (\text{C.1.1})$$

and written in matrix form,

$$X_1 = R_{\text{buncher}} X_0, \quad (\text{C.1.2})$$

as,

$$\begin{pmatrix} \Delta\phi_1 \\ \Delta W_1 \end{pmatrix} = \begin{pmatrix} 1 & 0 \\ -qV_{\text{eff}} \sin \phi_s & 1 \end{pmatrix} \begin{pmatrix} \Delta\phi_0 \\ \Delta W_0 \end{pmatrix} \quad (\text{C.1.3})$$

The longitudinal transfer matrix for a thin buncher cavity can therefore be expressed simply as,

$$R_{\text{buncher}} = \begin{pmatrix} 1 & 0 \\ \mp qV_{\text{eff}} & 1 \end{pmatrix} \text{ given } \phi_s = \pm 90^\circ. \quad (\text{C.1.4})$$

## C.2 Multi-gap Buncher Cavity

One can show by expanding out Equation 5.2.14 that the longitudinal transfer matrix describing the dynamics between the first and last gaps of an  $N$ -gap buncher cavity with

a constant geometric velocity operating in  $\pi$ -mode can be written,

$$R_{\text{buncher}}^{N\text{gaps}} = \sum_{i=1}^N \begin{pmatrix} f_{i,11}(N) \left(\frac{\pi}{2} \sin \phi_s\right)^{i-1} \left(\frac{qV_{\text{eff}}}{W_0}\right)^{i-1} & -\frac{\pi}{2W_0} f_{i,12}(N) \left(\frac{\pi}{2} \sin \phi_s\right)^{i-2} \left(\frac{qV_{\text{eff}}}{W_0}\right)^{i-2} \\ -qV_{\text{eff}} \sin \phi_s f_{i,21}(N) \left(\frac{\pi}{2} \sin \phi_s\right)^{i-1} \left(\frac{qV_{\text{eff}}}{W_0}\right)^{i-1} & f_{i,22}(N) \left(\frac{\pi}{2} \sin \phi_s\right)^{i-1} \left(\frac{qV_{\text{eff}}}{W_0}\right)^{i-1} \end{pmatrix}.$$

where the beam energy ( $W_0$ ) is matched the the geometric velocity. The matrix equation can also be written,

$$R_{\text{buncher}}^{N\text{gaps}} = \sum_{i=1}^N R_i. \quad (\text{C.2.1})$$

If  $qV_{\text{eff}} \ll W_0$  then  $R_{\text{buncher}}^{N\text{gaps}}$  can be approximated and the polynomial series truncated to a given order.  $R_{\text{buncher}}^{N\text{gaps}}$  must be expanded up until  $i = 3$  to include terms up to second-order in  $\frac{qV_{\text{eff}}}{W_0}$ ,

$$R_{\text{buncher}}^{N\text{gaps}} \approx R_1 + R_2 + R_3, \quad (\text{C.2.2})$$

where,

$$R_1 = R_{\text{buncher}} = \begin{pmatrix} 1 & 0 \\ -qV_{\text{eff}} \sin \phi_s & 1 \end{pmatrix}, \quad (\text{C.2.3})$$

and the next two matrices in the expansion are,

$$R_2 = \begin{pmatrix} f_{2,11}(N) \left(\frac{\pi}{2} \sin \phi_s\right) \left(\frac{qV_{\text{eff}}}{W_0}\right) & -\frac{\pi}{2W_0} f_{2,12}(N) \\ -qV_{\text{eff}} \sin \phi_s f_{2,21}(N) \left(\frac{\pi}{2} \sin \phi_s\right) \left(\frac{qV_{\text{eff}}}{W_0}\right) & f_{2,22}(N) \left(\frac{\pi}{2} \sin \phi_s\right) \left(\frac{qV_{\text{eff}}}{W_0}\right) \end{pmatrix}, \quad (\text{C.2.4})$$

and,

$$R_3 = \begin{pmatrix} f_{3,11}(N) \left(\frac{\pi}{2} \sin \phi_s\right)^2 \left(\frac{qV_{\text{eff}}}{W_0}\right)^2 & -\frac{\pi}{2W_0} f_{3,12}(N) \left(\frac{\pi}{2} \sin \phi_s\right) \left(\frac{qV_{\text{eff}}}{W_0}\right) \\ -qV_{\text{eff}} \sin \phi_s f_{3,21}(N) \left(\frac{\pi}{2} \sin \phi_s\right)^2 \left(\frac{qV_{\text{eff}}}{W_0}\right)^2 & f_{3,22}(N) \left(\frac{\pi}{2} \sin \phi_s\right)^2 \left(\frac{qV_{\text{eff}}}{W_0}\right)^2 \end{pmatrix}. \quad (\text{C.2.5})$$

The first set of coefficients  $f_1$  are independent of  $N$ ,

$$f_1 = \begin{pmatrix} 1 & 0 \\ 1 & 1 \end{pmatrix}. \quad (\text{C.2.6})$$

Depending on the voltage distribution across the gaps simple expressions for the coefficients  $f_{i>1}$  can be derived. For a flat voltage distribution the voltage on each gap is identical,

$$V_{i,\text{eff}} = \frac{V_{\text{eff}}}{N}, \quad (\text{C.2.7})$$

and the next sets of coefficients can be expressed as,

$$f_2(N) = \begin{pmatrix} \frac{N-1}{2} & N-1 \\ \frac{N^2-1}{6N} & \frac{N-1}{2} \end{pmatrix}, \quad (\text{C.2.8})$$

and,

$$f_3(N) = \begin{pmatrix} \frac{(N-2)(N^2-1)}{24N} & \frac{(N-2)(N-1)}{6} \\ \frac{(N^2-4)(N^2-1)}{120N^2} & \frac{(N-2)(N^2-1)}{24N} \end{pmatrix}. \quad (\text{C.2.9})$$

In the case of a flat voltage distribution with grounded external drift-tubes, the first and last gaps have a voltage,

$$V_{1,\text{eff}} = V_{N,\text{eff}} = \frac{V_{\text{eff}}}{2(N-1)}, \quad (\text{C.2.10})$$

and the internal gaps,

$$V_{2,\text{eff}} = V_{3,\text{eff}} = \dots = V_{N-1,\text{eff}} = \frac{V_{\text{eff}}}{N-1}, \quad (\text{C.2.11})$$

and the next sets of coefficients can be expressed as,

$$f_2(N) = \begin{pmatrix} \frac{N-1}{2} & N-1 \\ \frac{3-4N+2N^2}{12(N-1)} & \frac{N-1}{2} \end{pmatrix}, \quad (\text{C.2.12})$$

and,

$$f_3(N) = \begin{pmatrix} \frac{N(N-2)}{24} & \frac{N(N-2)}{6} \\ \frac{(N-1)^4-1}{120(N-1)^2} & \frac{N(N-2)}{24} \end{pmatrix}. \quad (\text{C.2.13})$$

This analytic approximation can be used to describe an  $N$ -gap buncher when the beam velocity is matched to the geometric velocity of the structure.

By truncating the expansion at  $i = 2$ , such that  $R_{\text{buncher}}^{N_{\text{gaps}}} = \sum_{i=1}^2 R_i = R_1 + R_2$ , the energy spread downstream of a multi-gap buncher can be approximated to orders linear in  $\frac{qV_{\text{eff}}}{W_0}$  as a cubic function of  $V_{\text{eff}}$ ,

$$\left(\frac{\Delta W_1^2}{A^2}\right) = a_3 \sin^3 \phi_s V_{\text{eff}}^3 + a_2 \sin^2 \phi_s V_{\text{eff}}^2 + a_1 \sin \phi_s V_{\text{eff}} + a_0, \quad (\text{C.2.14})$$

where,

$$\frac{a_3}{\epsilon_0} = \left(\frac{q}{A}\right)^3 \frac{\pi}{W_0/A} f_{2,21} \beta_0, \quad (\text{C.2.15})$$

$$\frac{a_2}{\epsilon_0} = \left(\frac{q}{A}\right)^2 \left[ \beta_0 + \frac{\pi}{W_0/A} (f_{2,21} + f_{2,22}) \alpha_0 \right], \quad (\text{C.2.16})$$

$$\frac{a_1}{\epsilon_0} = \left(\frac{q}{A}\right) \left[ 2\alpha_0 + \frac{\pi}{W_0/A} f_{2,22} \gamma_0 \right], \quad (\text{C.2.17})$$

$$\frac{a_0}{\epsilon_0} = \gamma_0. \quad (\text{C.2.18})$$

By truncating the expansion at  $i = 3$ , the energy spread can be calculated to second-order in  $\frac{qV_{\text{eff}}}{W_0}$  as a quartic polynomial in  $V_{\text{eff}}$ ,

$$\left(\frac{\Delta W_1^2}{A^2}\right) = a_4 \sin^4 \phi_s V_{\text{eff}}^4 + a_3 \sin^3 \phi_s V_{\text{eff}}^3 + a_2 \sin^2 \phi_s V_{\text{eff}}^2 + a_1 \sin \phi_s V_{\text{eff}} + a_0, \quad (\text{C.2.19})$$

where,

$$\frac{a_4}{\epsilon_0} = \left(\frac{q}{A}\right)^4 \frac{\pi^2}{4W_0^2/A^2} (f_{2,21}^2 + 2f_{3,21}) \beta_0, \quad (\text{C.2.20})$$

$$\frac{a_3}{\epsilon_0} = \left(\frac{q}{A}\right)^3 \frac{\pi}{W_0/A} \left[ f_{2,21} \beta_0 + \frac{\pi}{2W_0/A} (f_{2,21} f_{2,22} + f_{3,21} + f_{3,22}) \alpha_0 \right], \quad (\text{C.2.21})$$

$$\frac{a_2}{\epsilon_0} = \left(\frac{q}{A}\right)^2 \left[ \beta_0 + \frac{\pi}{W_0/A} (f_{2,21} + f_{2,22}) \alpha_0 + \frac{\pi^2}{4W_0^2/A^2} (f_{2,22}^2 + 2f_{3,22}) \gamma_0 \right], \quad (\text{C.2.22})$$

$$\frac{a_1}{\epsilon_0} = \left(\frac{q}{A}\right) \left[ 2\alpha_0 + \frac{\pi}{W_0/A} f_{2,22} \gamma_0 \right], \quad (\text{C.2.23})$$

$$\frac{a_0}{\epsilon_0} = \gamma_0. \quad (\text{C.2.24})$$

REB AND 7G3 CALIBRATIONS

The calibration of the ReB and 7G3 cavities used to measure the longitudinal emittance is outlined briefly in this appendix.

## D.1 Setting the Synchronous Phase

The switchyard magnet was used to measure the average beam energy with an error close to that of the intrinsic energy spread of the beam. The cavity being calibrated was first turned off, the reference energy corresponding to no energy gain recorded and then the cavity was powered and the phase rotated to bring the beam back to the reference energy close to either  $\phi_s = \pm 90^\circ$ , with respect to the maximum of the energy gain. The energy gain as a function of phase taken during a calibration for the 7G3 is shown in Figure D.1, where the change in the phase of the maximum energy gain is plotted at two different values of the voltage signal on the pick-up ( $A_{pu}$ ). The plots are fitted with the second-order approximation for the energy gain. The synchronous phase was set at a moderate value of  $A_{pu}$ .

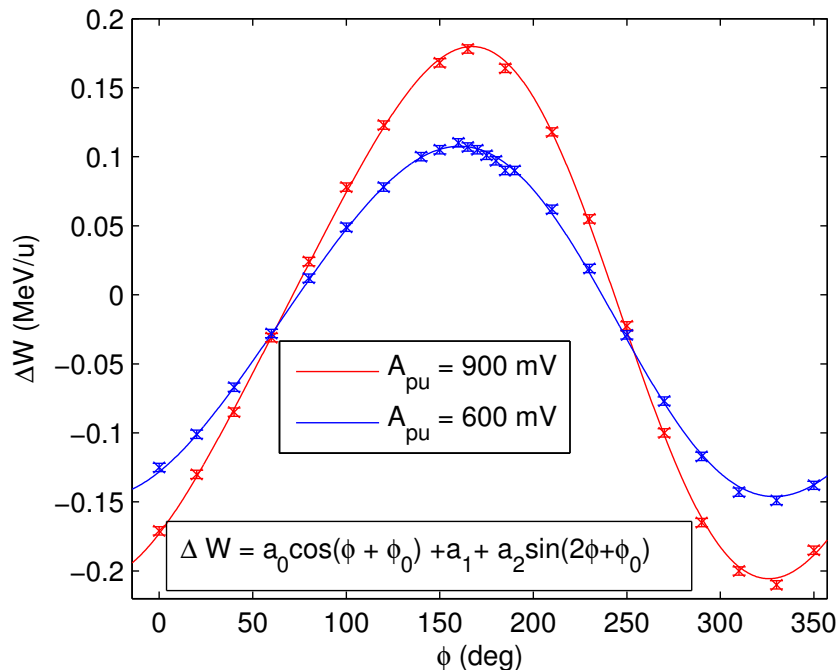


Figure D.1: Beam-based phasing of 7G3.

## D.2 Pick-up Calibration

The pick-up ports of the cavities were calibrated by measuring the average beam energy as a function of  $A_{\text{pu}}$  with the cavity operating at a synchronous phase of  $0^\circ$ . The calibration curves are plotted in Figures D.2(a) and D.2(b) using a beam with  $A/q = 4$  that can be summarised for the ReB as,

$$V_{\text{eff,ReB}} [\text{kV}] = (0.0442 \pm 0.004) A_{\text{pu,ReB}} [\text{mV}], \quad (\text{D.2.1})$$

and for the 7G3 as,

$$V_{\text{eff,7G3}} [\text{kV}] = (0.739 \pm 0.015) A_{\text{pu,7G3}} [\text{mV}]. \quad (\text{D.2.2})$$

The variations in the calibration data about the linear fit for the 7G3 arise from the dependence of the synchronous phase on the  $A_{\text{pu}}$ , as shown in Figure D.1.

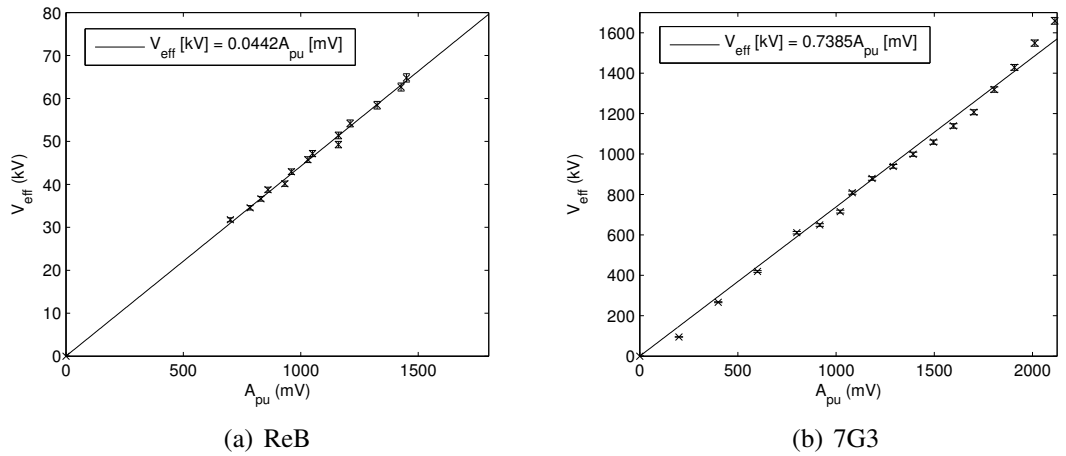


Figure D.2: Calibration curves for the ReB and 7G3 pick-up ports.

PHASE SPACE TOMOGRAPHY

The results of the MENT Beam Tomography Program [179] for the 7G3 longitudinal emittance measurement are collected in this appendix.

## E.1 7G3 Measurement

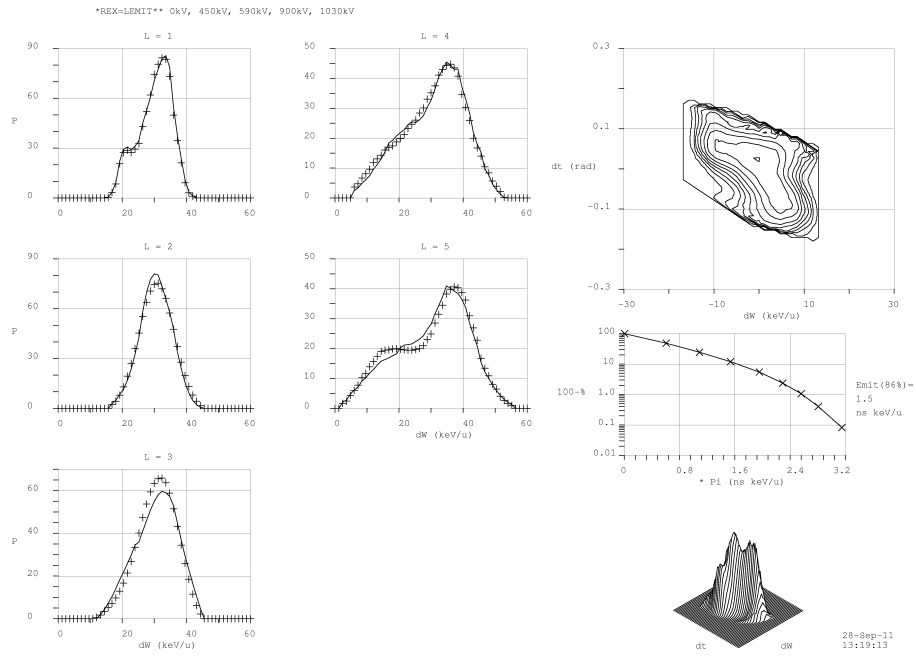


Figure E.1: MENT Beam Tomography Program [179] analysis for the 7G3 measurement.

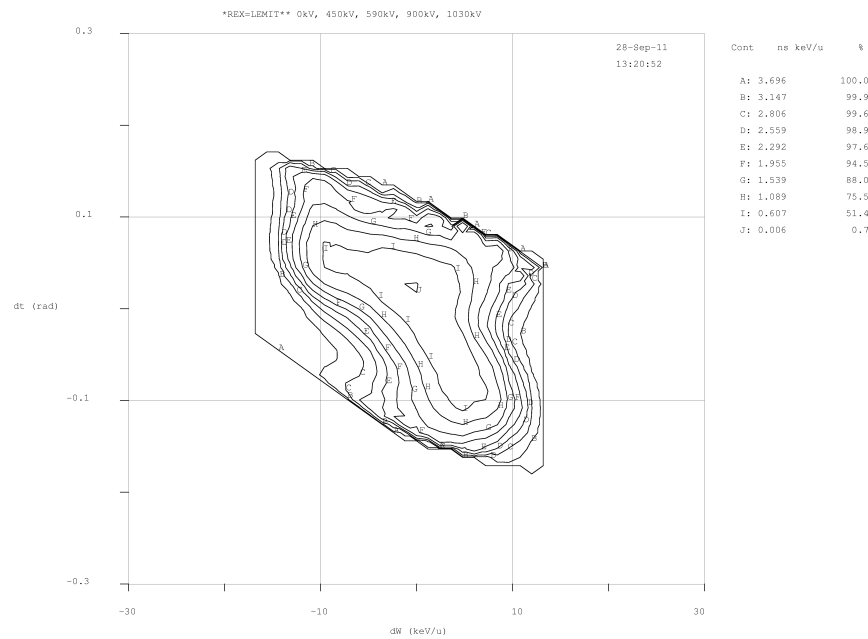


Figure E.2: Contour plot from MENT Beam Tomography Program [179] for the 7G3 measurement.

CAVITY VARIANTS

Two major modifications to the geometry of the quarter-wave cavities are briefly discussed in this appendix. In the first modification the axial symmetry of the drift-tube of the quarter-wave resonator is improved. In the second modification the noses on the high- $\beta$  cavity are removed.

## F.1 Modification to the Drift-Tubes

The axial symmetry of the electric fields at the beam axis was improved by modifying the shape of the inner conductor, as presented in Figure F.1 [207]. The modification was made compatible with the sputtering process required to coat the cavity substrate with niobium. In particular, sharp edges were avoided and all surfaces were made with a clear line-of-sight to the niobium cathode to ensure a smooth deposition of the film. The modification

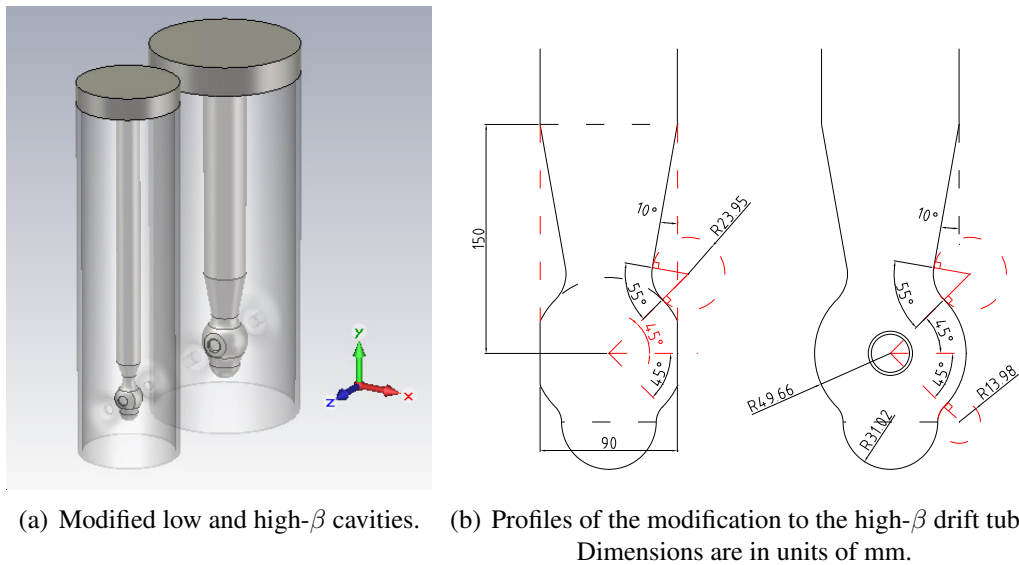


Figure F.1: Modifications to the drift-tubes of the low and high- $\beta$  cavities.

reflects the shape of the noses and is achieved by tapering a flattened sphere onto the shaft. An extension to the bottom of the sphere is required to move the site of peak electric field away from the beam axis, such that an effective compensation of beam-steering can be achieved. With the exception of the flattened faces, the modification has cylindrical symmetry about the resonator axis and would present an acceptable surface for sputtering. Other classic 'donut' type drift-tubes were ruled out [208]. The modification reduces the capacitive loading and, in order to maintain the resonant frequency of 101.28 MHz, the cavity must be lengthened.

Table F.1: Basic Parameters of the Modification to the High- $\beta$  Cavity.

Parameter	Nominal Cavity	Modified Cavity
$T_{\max}(\beta_{\text{opt}})$	0.902	0.904
$\beta_g(\beta_{\text{opt}})$ [%]	10.3 (11.3)	10.3 (11.3)
Mechanical height [mm]	785	807
$E_{\text{pk}}/E_0$	5.4	6.6
$B_{\text{pk}}/E_0$ [Oe/(MV/m)]	96	93
$R_{\max}/Q$ [ $\Omega$ ]	548	585
$\Gamma = R_s Q$ [ $\Omega$ ]	30.6	31.3
$U/E_0^2$ [J/(MV/m) <sup>2</sup> ]	207	196
$\delta_{\text{opt}}$ [mm]	2.5	2.2

The reduction in the radius of curvature of the end of the inner conductor causes the peak electric field to rise by 20 %. The rf parameters for the modified the high- $\beta$  cavity are compared to the nominal cavity with a racetrack aperture in Table F.1. The effect on the symmetry of the (de)focusing is shown in Figure 6.19.

## F.2 High- $\beta$ Cavity with Beam Port Noses Removed

The parameters of the high- $\beta$  cavity design without beam port noses are compared to the nominal design in Table F.2.

Table F.2: Parameters of the high- $\beta$  cavity without beam port noses

Cavity Design	$g$ [mm]	$\beta_g$	$L_g = \beta_g \lambda / 2$ [mm]	$\beta_{\text{opt}}$	$R_{\max}/Q$ [ $\Omega$ ]
Without noses	105	11.4	169	13.1	510
Nominal	85	10.3	153	11.4	554

The change to  $Q$  and the peak fields inside the cavity is negligible; the change in resonant frequency is  $\sim +0.5$  MHz. The removal of the noses increases both the length of the gaps and the separation of their electric centres, as shown by the comparison of the accelerating field profiles in Figure F.2(a). The geometric velocity increases and the transit-time factor drops causing the shunt impedance to lower by  $\sim 10$  %, shown as a function of velocity in Figure F.2(b). The loss of shunt impedance is significant below the optimum velocity of the modified cavity, ruling out the removal of the noses in the cavities of the first few cryomodules; the enhancement of the acceleration efficiency for  $\beta \gtrsim 0.15$  facilitates the modification of the cavities in the final high energy cryomodule. The design velocity for  $A/q = 4.5$  on entry to the final cryomodule is  $\beta = 0.135$ , at

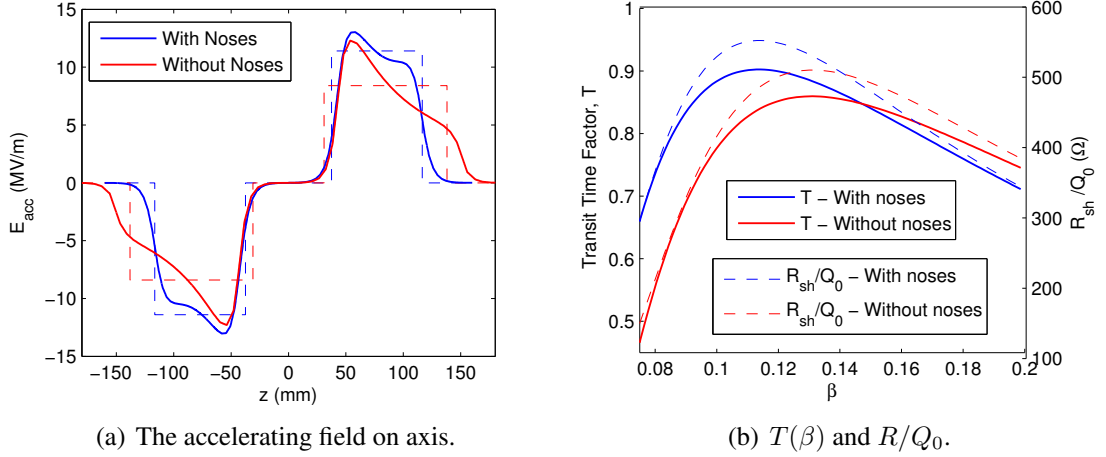


Figure F.2: A comparison of the accelerating field and shunt impedance of the high- $\beta$  cavity, with and without noses.

which the difference in  $R/Q$  is less than 2 % and the effect on the maximum energy gain is negligible; operating the modified cavities at the same average gradient of 6 MV/m causes a drop in the energy gain of just 0.2 % at the linac output. For  $A/q = 2.5$  the maximum output energy of the linac is actually increased by a similar margin.

The beam-steering force increases with the gap length but the rf (de)focusing force differs very little to the nominal cavity at high energy, as presented in Figure F.3. No significant deterioration in the beam quality was observed by implementing the field map of the cavity into TRACK.

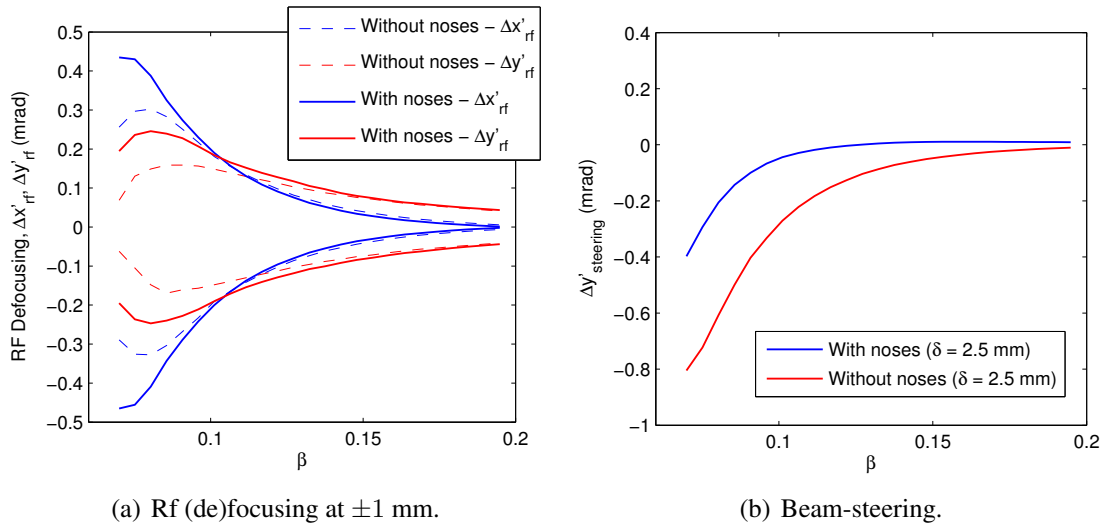


Figure F.3: A comparison of the rf (de)focusing and beam-steering in the high- $\beta$  cavity with and without beam ports ( $A/q = 2.5$ ,  $\phi_s = -20^\circ$  and  $\delta = 2.5$  mm).

The modification is limited by the rise in the electric field at the adjacent cavity, which

could cause cross-talk between the cavities, and would likely require the cryomodule to be adjusted and the inter-cavity space to be increased, however this requires further investigation.

MISALIGNMENT IN THE MATRIX DESCRIPTION

In order to track a particle through a misaligned element, one has to first transform the particle coordinates from the global system representing the accelerator hall ( $\vec{x}_{\text{hall}}$ ) and the ideal beam axis to the coordinate system of the misaligned element ( $\vec{x}_{\text{el}}$ ). The particle can then be tracked through the transfer matrix of the element ( $R_{\text{el}}$ ) and transformed back into the global coordinate system afterwards. By parameterising the misalignment of the entry position of the element with displacements  $\Delta x_i$ ,  $\Delta y_i$  and  $\Delta z_i$  and the rotation of the element with respect to the cartesian coordinate axes of the global system with  $\phi_x$ ,  $\phi_y$  and  $\phi_z$ , one can write the coordinate transformation from the hall to the misaligned element as,

$$\vec{x}_{\text{el}} = R_{\text{rot}}(\phi_x, \phi_y, \phi_z)(\vec{x}_{\text{hall}} - \vec{\Delta}_i) \quad (\text{G.0.1})$$

where  $\vec{\Delta}_i = (\Delta x_i, \Delta y_i, \Delta z_i)$  describes the displacement of the entry position of the element and  $R_{\text{rot}}$  describes the rotation of the misaligned element in a 3-dimensional cartesian coordinate system. The divergence of the particle transforms as,

$$\vec{x}'_{\text{el}} = R_{\text{rot}}(\phi_x, \phi_y, \phi_z)\vec{x}'_{\text{hall}}. \quad (\text{G.0.2})$$

$R_{\text{rot}}$  can be written in a right-handed coordinate system and in the small angle approximation, i.e.  $\phi_x, \phi_y \ll 1$ , to first-order as,

$$R_{\text{rot}} \approx \begin{pmatrix} 1 & 0 & \phi_y \\ 0 & 1 & -\phi_x \\ -\phi_y & \phi_x & 1 \end{pmatrix}, \quad (\text{G.0.3})$$

where  $\phi_x$  and  $\phi_y$  are counter-clockwise rotations about the denoted axis when viewed looking back toward the origin and skew rotations about the beam axis are neglected, i.e.  $\phi_z = 0$ . Following through the algebra using Eqs. G.0.1 and G.0.2 the transverse phase space coordinates of the particle at entry to the element can be expressed in the reference frame of the element as,

$$\vec{X}_{0,\text{el}} = \vec{X}_{0,\text{hall}} + \vec{X}_i \quad (\text{G.0.4})$$

where,

$$\vec{X}_i = \begin{pmatrix} -\Delta x_i \\ \phi_y \\ -\Delta y_i \\ -\phi_x \end{pmatrix}, \quad (\text{G.0.5})$$

at,

$$z_{\text{el}} = 0. \quad (\text{G.0.6})$$

After tracking the particle through the transfer matrix of the element the particle coordinates can be transformed back into the coordinate system of the accelerator hall using,

$$\vec{x}_{\text{hall}} = R_{\text{rot}}^{-1} \vec{x}_{\text{el}} + \vec{\Delta}_i \quad (\text{G.0.7})$$

and,

$$\vec{x}'_{\text{hall}} = R_{\text{rot}}^{-1} \vec{x}'_{\text{el}}, \quad (\text{G.0.8})$$

The final transformation can be written for an element of length  $L$  as,

$$\vec{X}_{1,\text{hall}} = \vec{X}_{1,\text{el}} + \vec{X}_f, \quad (\text{G.0.9})$$

where,

$$\vec{X}_f = \begin{pmatrix} \Delta x_f \\ -\phi_y \\ \Delta y_f \\ \phi_x \end{pmatrix}, \quad (\text{G.0.10})$$

and, in the small angle approximation,

$$\Delta x_f \approx L\phi_y + \Delta x_i, \quad (\text{G.0.11})$$

$$\Delta y_f \approx -L\phi_x + \Delta y_i. \quad (\text{G.0.12})$$

at,

$$z_{\text{el}} = L. \quad (\text{G.0.13})$$

Finally, the transverse dynamics through the element can be written in the coordinate system of the accelerator hall and in terms of the misalignment at the entry and exit positions as,

$$\vec{X}_{1,\text{hall}} = R_{\text{el}}\vec{X}_{0,\text{hall}} + \vec{K}, \quad (\text{G.0.14})$$

where,

$$\vec{K} = \vec{X}_f - R_{\text{el}}\vec{X}_i. \quad (\text{G.0.15})$$

The tracking of a particle from before element  $n$  to after element  $n + 1$  can be expressed as,

$$\vec{X}_{1,n+1} = R_{\text{el},n+1}(R_{\text{el},n}\vec{X}_{0,n} + \vec{K}_n) + \vec{K}_{n+1}, \quad (\text{G.0.16})$$

and the position of a single particle tracked from before element  $j$  to after element  $n$  can be written more generally as,

$$\vec{X}_{1,n} = R(n|j)\vec{X}_{0,j} + \underbrace{\sum_{i=j}^{n-1} R(n|i+1)\vec{K}_{i+1}}_{\text{centroid trajectory}}, \quad (\text{G.0.17})$$

where  $R(n|i) = R_n R_{n-1} R_{n-2} \dots R_{i+1}$  and  $R(n|n) = I$ . The reader is referred to [209] for further details on linearising the effect of small misalignments of axially symmetric beam line elements.

MATCHED LINAC PARAMETERS

---

The linac parameters, including the matching conditions for the input transverse Twiss parameters and the matched solenoid settings, are tabulated in this appendix for beams with mass-to-charge states on the extremes of the machine's acceptance. In particular, the linac parameters used in the systematic studies of the parametric resonance are collected in Tables H.3 and H.5. The matched transverse beam parameters are given at a plane 25 cm before the first cavity, which is equivalent to the mid-point between cryomodules spaced by 50 cm and the solenoid field values are given for hard-edge solenoids with an effective length of 20 cm. The TRACK code requires a realistic field map of the solenoid normalised such that the peak field is 1 T, i.e.,

$$B(z = 0, r = 0) = 1 \text{ T}. \quad (\text{H.0.1})$$

The square of the normalised longitudinal magnetic field integrated along the axis of the HIE-ISOLDE prototype solenoid is  $0.140 \text{ T}^2\text{m}$ , which is proportional to its focusing strength, i.e.,

$$N = \frac{1}{B^2(z = 0, r = 0)} \int_{-\infty}^{+\infty} B^2(z, r = 0) dz = 0.140 \text{ T}^2\text{m}. \quad (\text{H.0.2})$$

To convert the tabulated values for a hard-edge solenoid for use with the realistic solenoid field map implemented in TRACK, one has to scale the normalised field map with the factor  $\sqrt{B_{\text{T3D}}^2 L_{\text{eff}}/N}$  such that,

$$B(z = 0, r = 0) = \sqrt{\frac{B_{\text{T3D}}^2 L_{\text{eff}}}{N}}. \quad (\text{H.0.3})$$

The longitudinal beam dynamics is fixed by the lattice operating at a synchronous phase of  $-20^\circ$  and the cavities operating with the design gradient of 6 MV/m.

## H.1 Stage 1 and 2a

All the cavities were set to a synchronous phase of  $-20^\circ$ . The injection energy for stage 1 and 2a was 2.8 MeV/u for  $A/q = 4.5$ . Table H.1 summarises the settings for  $A/q = 4.5$ .

Table H.1: Linac settings for the high energy section in stage 1 and 2a,  $A/q = 4.5$  and  $E_{\text{in}} = 2.8$  MeV/u.

<b>Phase Advance</b> $\mu_{\text{T}}$ [deg]	$\tilde{\alpha}_{\text{x,y}}$	$\tilde{\beta}_{\text{x,y}}$ [mm/mrad]	$B_{5,\text{T3D}}$ [T]	$B_{6,\text{T3D}}$ [T]	$B_{7,\text{T3D}}$ [T]	$B_{8,\text{T3D}}$ [T]
30	0.06	3.04	4.96	5.10	5.06	4.99
50	-0.12	2.14	5.30	5.63	5.83	5.97
70	-0.12	1.43	5.72	6.30	6.74	7.10
90	-0.15	1.08	6.17	6.98	7.66	8.22
110	-0.22	0.62	6.59	7.61	8.49	9.21
130	-0.24	0.48	6.95	8.12	9.16	10.01

For  $A/q = 2.5$  the injection energy was 3.0 MeV/u. Table H.2 summarises the settings for  $A/q = 2.5$ .

Table H.2: Linac settings for the high energy section in stage 1 and 2a,  $A/q = 2.5$  and  $E_{\text{in}} = 3.0$  MeV/u.

<b>Phase Advance</b> $\mu_{\text{T}}$ [deg]	$\tilde{\alpha}_{\text{x,y}}$	$\tilde{\beta}_{\text{x,y}}$ [mm/mrad]	$B_{5,\text{T3D}}$ [T]	$B_{6,\text{T3D}}$ [T]	$B_{7,\text{T3D}}$ [T]	$B_{8,\text{T3D}}$ [T]
30	-0.19	3.18	3.45	3.44	3.32	3.25
50	-0.11	1.88	3.61	3.79	3.88	3.98
70	-0.09	1.26	3.81	4.22	4.53	4.78
90	-0.10	0.89	4.03	4.52	4.98	5.60
110	-0.12	0.62	4.23	5.08	5.76	6.31
130	-0.16	0.42	4.41	5.42	6.23	6.88

## H.2 Stage 2b

### H.2.1 Low Energy Section

The first and the sixth cavities were re-phased to  $-40^\circ$ . The longitudinal beam parameters at injection were those given in Chapter 4.7. Table H.3 summarises the settings for  $A/q = 4.5$ .

Table H.3: Linac settings for the low energy section,  $A/q = 4.5$  and  $E_{\text{in}} = 1.2 \text{ MeV}/u$ .

Phase Advance $\mu_{\text{T}}$ [deg]	$\tilde{\alpha}_{\text{x,y}}$	$\tilde{\beta}_{\text{x,y}}$ [mm/mrad]	$B_{1,\text{T3D}}$ [T]	$B_{2,\text{T3D}}$ [T]	$B_{3,\text{T3D}}$ [T]	$B_{4,\text{T3D}}$ [T]
30	-0.05	1.92	4.29	4.47	4.01	4.03
50	-0.07	1.14	4.56	4.96	4.72	4.97
70	0.02	0.78	4.94	5.56	5.55	6.03
90	0.04	0.56	5.31	6.18	6.36	7.05
110	0.07	0.40	5.67	6.75	7.08	7.96
130	0.10	0.29	5.97	7.21	7.66	8.68

For  $A/q = 2.5$  the gradient of the first cavity should be halved to capture the beam at a synchronous phase of  $-40^\circ$ . Table H.4 summarises the settings for  $A/q = 2.5$ .

Table H.4: Linac settings for the low energy section,  $A/q = 2.5$  and  $E_{\text{in}} = 1.2 \text{ MeV}/u$ .

Phase Advance $\mu_{\text{T}}$ [deg]	$\tilde{\alpha}_{\text{x,y}}$	$\tilde{\beta}_{\text{x,y}}$ [mm/mrad]	$B_{1,\text{T3D}}$ [T]	$B_{2,\text{T3D}}$ [T]	$B_{3,\text{T3D}}$ [T]	$B_{4,\text{T3D}}$ [T]
30	-0.41	1.15	2.63	3.04	2.64	2.64
50	-0.25	0.98	2.76	3.32	3.10	3.12
70	-0.16	0.68	2.93	3.66	3.63	4.09
90	-0.10	0.49	3.11	4.02	4.15	4.71
110	-0.05	0.36	3.27	4.35	4.62	5.32
130	-0.01	0.25	3.41	4.62	4.99	5.80

### H.2.2 High Energy Section

All the cavities were phased nominally at  $-20^\circ$  and the longitudinal beam parameters at injection were set to those after the low energy superconducting section. Table H.5 summarises the settings for  $A/q = 4.5$  at an injection energy of  $3.6 \text{ MeV}/u$ .

Table H.6 summarises the settings for  $A/q = 2.5$  at an injection energy of  $5.2 \text{ MeV}/u$ .

Table H.5: Linac settings for the high energy section,  $A/q = 4.5$  and  $E_{\text{in}} = 3.6$  MeV/u.

<b>Phase Advance</b> $\mu_{\text{T}}$ [deg]	$\tilde{\alpha}_{\text{x,y}}$	$\tilde{\beta}_{\text{x,y}}$ [mm/mrad]	$B_{1,\text{T3D}}$ [T]	$B_{2,\text{T3D}}$ [T]	$B_{3,\text{T3D}}$ [T]	$B_{4,\text{T3D}}$ [T]
30	0.04	3.29	5.09	5.08	5.02	4.97
50	0.00	1.81	5.52	5.75	5.91	6.07
70	-0.05	1.30	6.07	6.55	6.96	7.32
90	-0.13	0.95	6.64	7.36	8.00	8.54
110	-0.22	0.66	7.17	8.10	8.93	9.62
130	-0.32	0.48	7.61	8.71	9.68	10.49

Table H.6: Linac settings for the high energy section,  $A/q = 2.5$  and  $E_{\text{in}} = 5.2$  MeV/u.

<b>Phase Advance</b> $\mu_{\text{T}}$ [deg]	$\tilde{\alpha}_{\text{x,y}}$	$\tilde{\beta}_{\text{x,y}}$ [mm/mrad]	$B_{1,\text{T3D}}$ [T]	$B_{2,\text{T3D}}$ [T]	$B_{3,\text{T3D}}$ [T]	$B_{4,\text{T3D}}$ [T]
30	-0.19	3.74	3.47	3.34	3.26	3.22
50	-0.13	2.18	3.77	3.89	3.96	4.08
70	-0.12	1.46	4.16	4.47	4.76	5.03
90	-0.13	1.03	4.56	5.08	5.54	5.93
110	-0.15	0.72	4.93	5.63	6.23	6.73
130	-0.21	0.49	5.23	6.08	6.79	7.38

### H.2.3 Complete Linac

The settings for the complete linac are summarised in Table H.7 with the phase advance at  $90^\circ$  per period in the high energy section. The two cases show the nominal case in which the emittance growth was shown to be minimised and a second case in which  $90^\circ$  per period in the low energy section is avoided to ensure that any misalignment can be efficiently corrected with steerers placed outside the cryomodules.

Table H.7: Solenoid settings and matched beam parameters for the complete stage 2b linac

$A/q$	Low Energy Section $\mu_T$ [deg]	High Energy Section $\mu_T$ [deg]	$\tilde{\alpha}_{xy}$	$\tilde{\beta}_{xy}$ [mm/mrad]	$B_{1,T3D}$ [T]	$B_{2,T3D}$ [T]	$B_{3,T3D}$ [T]	$B_{4,T3D}$ [T]	$B_{5,T3D}$ [T]	$B_{6,T3D}$ [T]	$B_{7,T3D}$ [T]	$B_{8,T3D}$ [T]
4.5	70	90	-0.1	0.90	4.94	5.04	5.36	5.68	6.64	7.36	8.00	8.54
4.5	90	90	0.04	0.56	5.31	5.39	5.62	6.37	6.64	7.36	8.00	8.54
2.5	70	90	-0.16	0.68	2.93	3.44	3.56	4.38	4.56	5.08	5.54	5.93
2.5	90	90	-0.10	0.49	3.11	3.55	3.44	3.98	4.56	5.08	5.54	5.93

---

APPENDIX

**I**

---

HEBT

The TRACE 3-D solutions for the preliminary design of the HEBT are collected for Stage 1 at 5.9 MeV/u and for Stage 2b at 10 MeV/u and 0.45 MeV/u.

## I.1 Stage 1: 5.9 MeV/u - Experiment Station 1

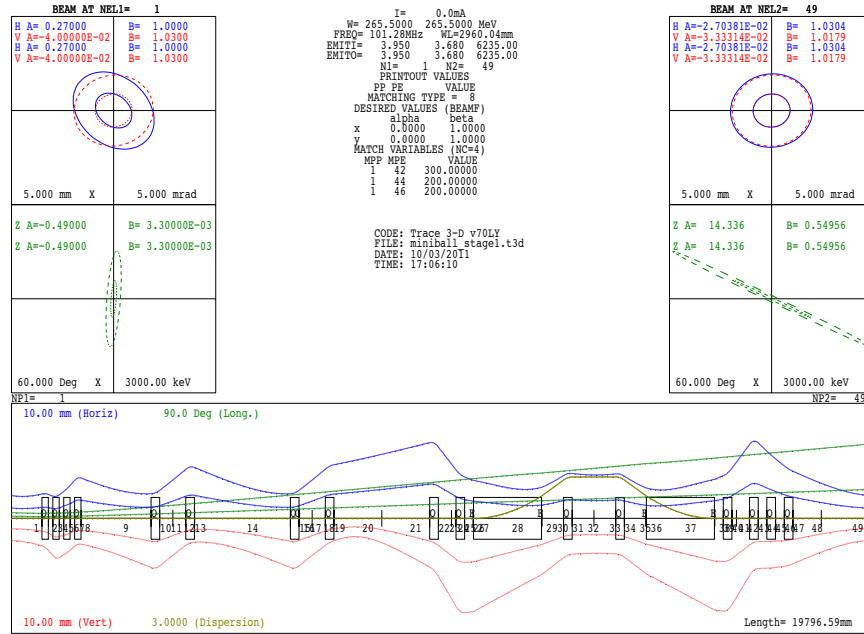


Figure I.1: HEBT to Experiment Station 1 at 5.9 MeV/u ( $\epsilon_{rms}$  and  $6\epsilon_{rms}$  envelopes).

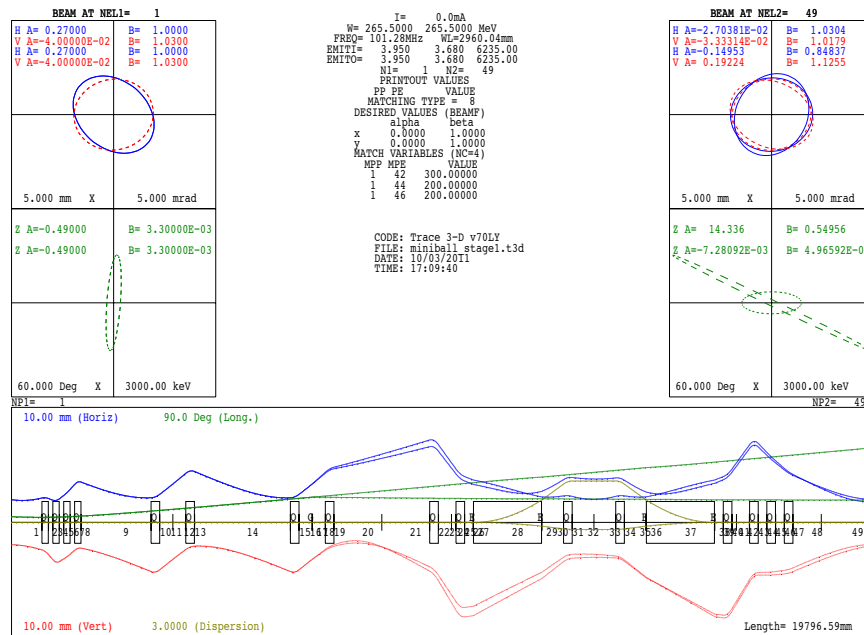


Figure I.2: HEBT to Experiment Station 1 at 5.9 MeV/u with and without rebuncher ( $6\epsilon_{rms}$  envelopes).

## I.2 Stage 1: 5.9 MeV/u - Experiment Station 2

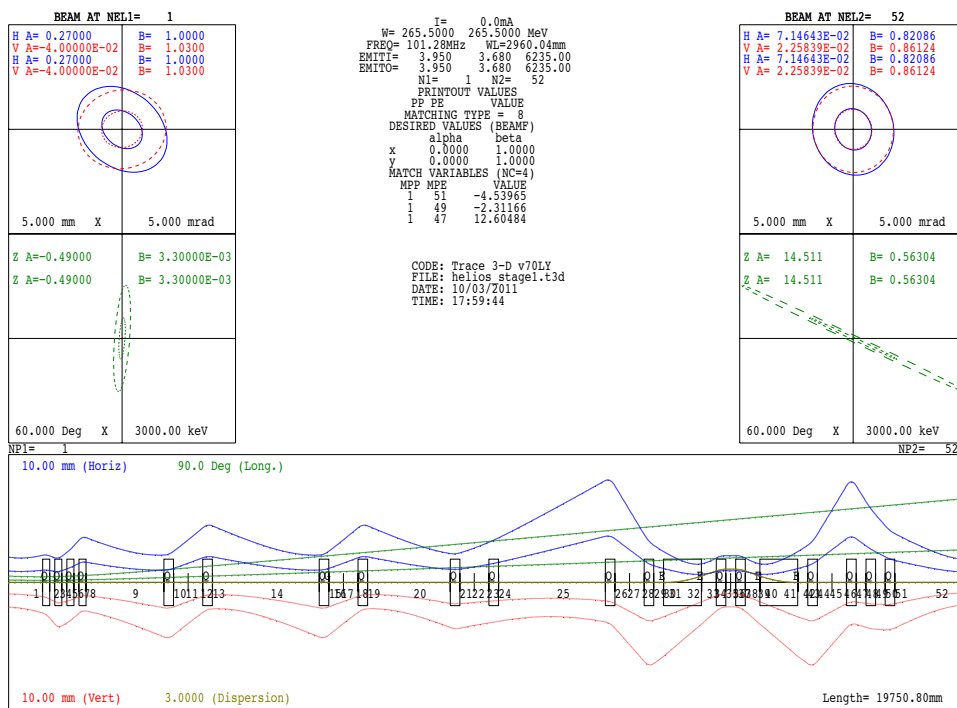


Figure I.3: HEBT to Experiment Station 2 at 5.9 MeV/u ( $\epsilon_{rms}$  and  $6\epsilon_{rms}$  envelopes).

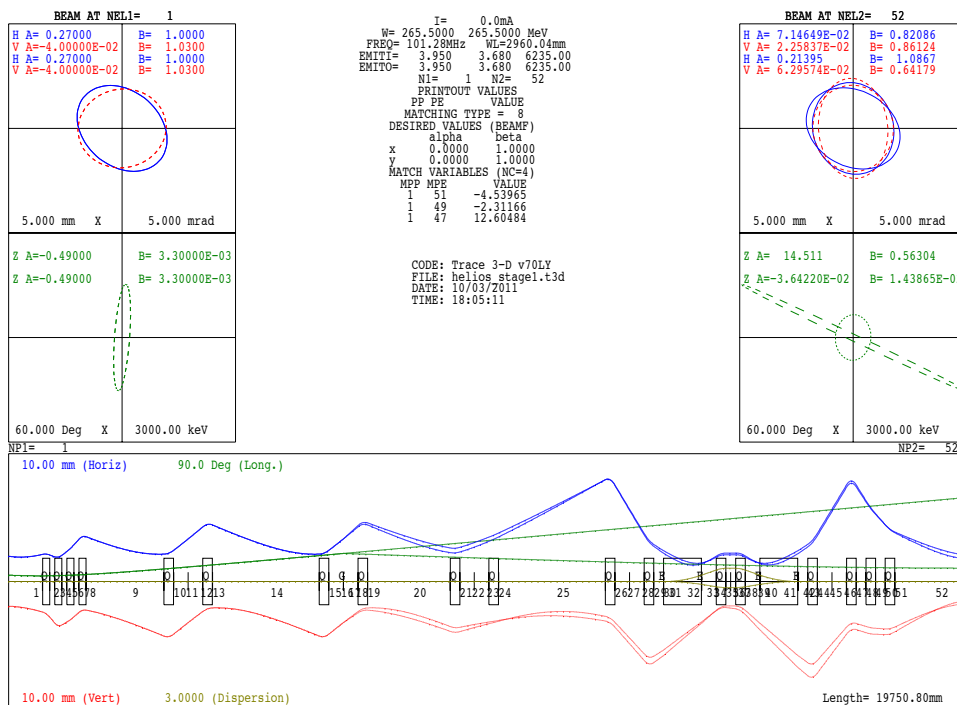


Figure I.4: HEBT to Experiment Station 2 at 5.9 MeV/u with and without rebuncher ( $6\epsilon_{rms}$  envelopes).

### I.3 Stage 2b: 10 MeV/u - Experiment Station 1

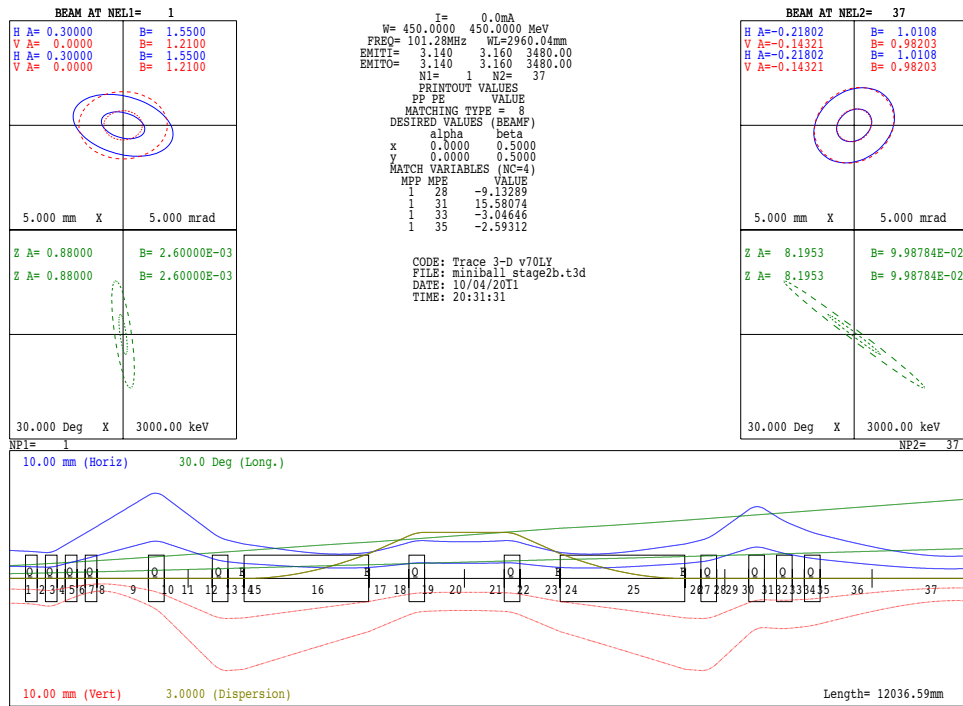


Figure I.5: HEBT to Experiment Station 1 at 10 MeV/u ( $\epsilon_{rms}$  and  $6\epsilon_{rms}$  envelopes).

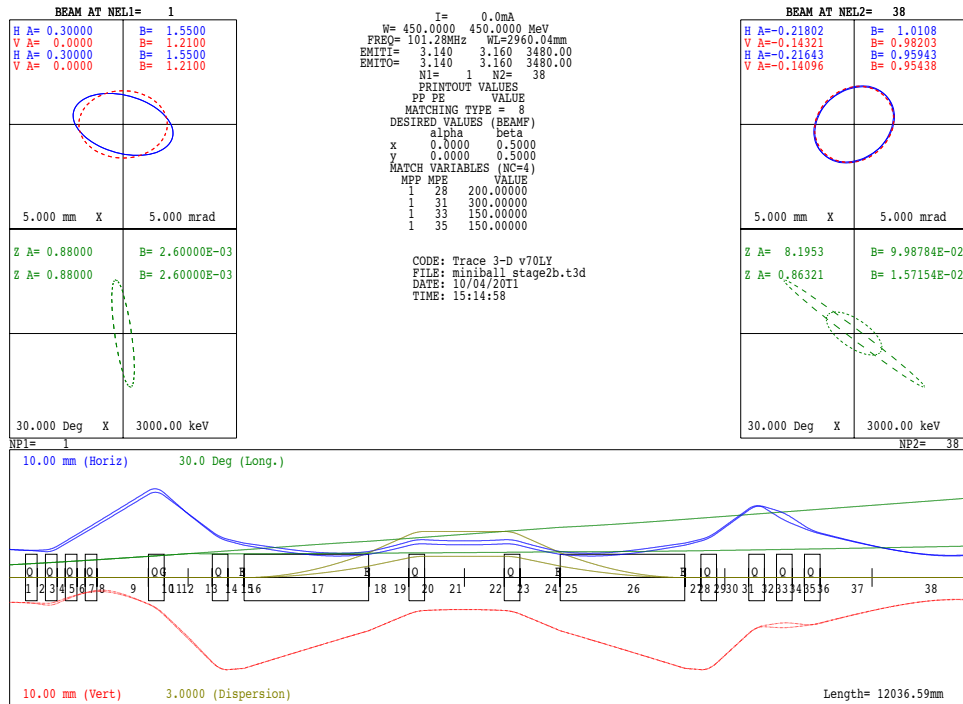


Figure I.6: HEBT to Experiment Station 1 at 10 MeV/u with and without rebuncher ( $6\epsilon_{rms}$  envelopes).

## I.4 Stage 2b: 10 MeV/u - Experiment Station 2

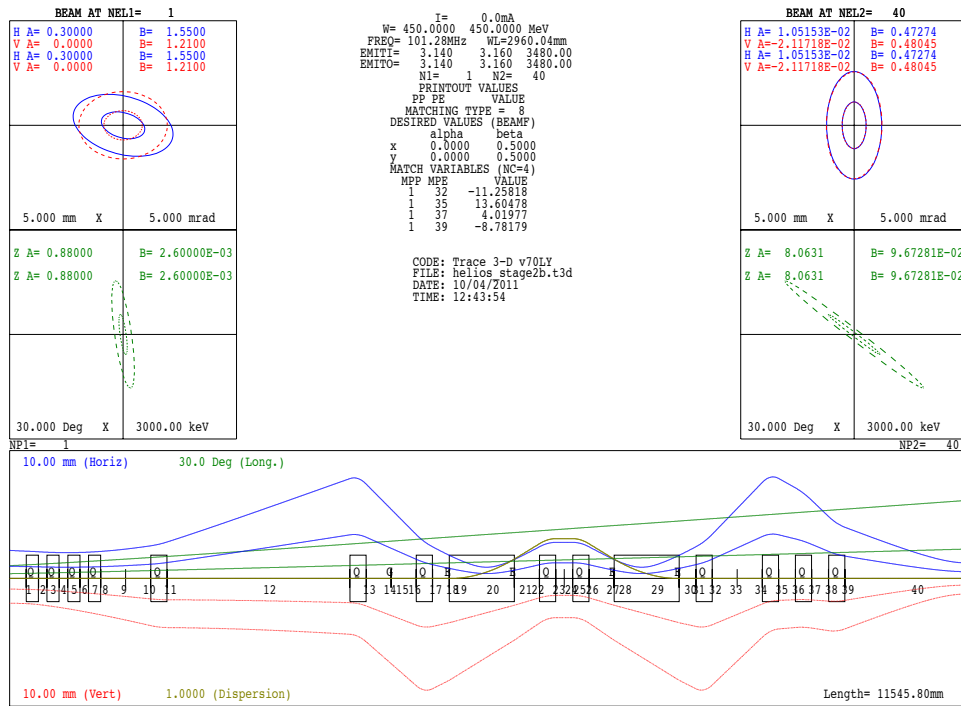


Figure I.7: HEBT to Experiment Station 2 at 10 MeV/u ( $\epsilon_{rms}$  and  $6\epsilon_{rms}$  envelopes).

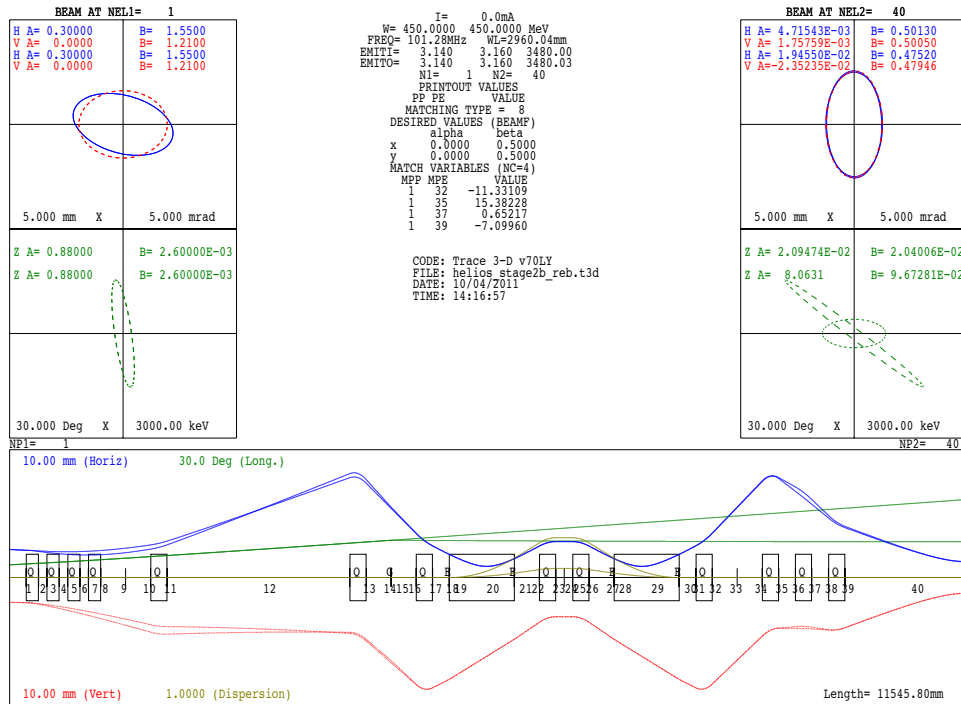


Figure I.8: HEBT to Experiment Station 2 at 10 MeV/u with and without rebuncher ( $6\epsilon_{rms}$  envelopes).

## I.5 Stage 2b: 0.45 MeV/u - Experiment Station 1

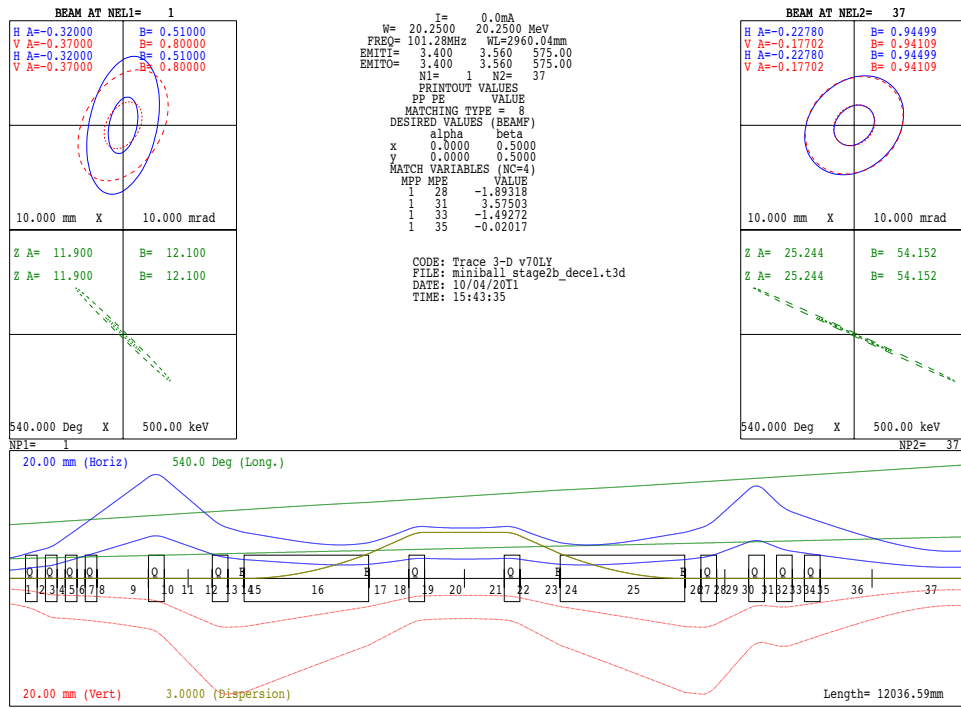


Figure I.9: HEBT to Experiment Station 1 at 0.45 MeV/u ( $\epsilon_{rms}$  and  $6\epsilon_{rms}$  envelopes).